Novel Soft Chemistry Synthesis of TiO_2 for Applications in Dye–Sensitized Solar Cells and Photocatalysis

by

Aiat Hussein El-Foly Hegazy

A thesis

presented to the University of Waterloo

in fulfillment of the

thesis requirement for the degree of

Doctor of Philosophy

in

Chemical Engineering–Nanotechnology

Waterloo, Ontario, Canada, 2012

Author's Declaration

I hereby declare that I am the sole author of this thesis. This is a true copy of the thesis, including any required final revisions, as accepted by my examiners.

I understand that my thesis may be made electronically available to the public.

Abstract

Although the high cost of solar cells prevents them being a primary candidate for energy production, great attention has been paid towards them because of the depletion of the conventional energy sources–fossil fuels–and the global warming effect, and the need to provide power to remote communities disconnected from the power grid. To reduce the cost, thin film technologies for silicon solar cells have also been investigated and commercialized, but dye sensitized solar cells (DSSC) have been considered as a promising alternative even for the silicon thin films with efficiency exceeding 10%.

Compared with silicon-based photovoltaic devices, DSSCs are quite complex systems that require an intimate interaction among components. Within the last few years, conclusive smart solutions have been provided to improve the efficiency of these cells, with solar efficiency that makes them potential competitors against silicon devices. The most successful systems use titanium oxide as a core material tuned to collect and transmit the electrons generated by the photo-excitation of dye molecules. However, most of the solutions demonstrated so far require a thermal treatment of the TiO_2 photoelectrodes at temperatures that preclude using any flexible organic substrate. This treatment prevents development of any roll-to-roll manufacturing process, which would be the only way to achieve cost effective large scale production.

In order to overcome this major drawback, a novel synthesis of TiO_2 at room temperature is described in the present document. This synthesis leads to 4-6 nm nanocrystalline anatase, the desired phase of titanium oxide for photoactive applications. An intensive study was carried out to explore the properties of these nanoparticles, via a mixture design study designed to analyze the influence of the starting composition on the final TiO_2 structure. The influence of a post-synthesis thermal treatment was also explored. This 4 nm nanocrystalline TiO_2 exhibits a high specific surface area and a good porosity that fulfills the requirements for an efficient photoanode; a high surface area allows high dye loading, and, hence, increases photocurrent and photo-conversion efficiency. Another important result of this study is the band gap, as it confirmed that nanocrystalline anatase has an indirect band gap and a quantum confinement for

a crystal size of less than 10 nm. This result, well-known for bulk materials, had been discussed in some previous publications that claimed the effectiveness of a direct band gap.

Following this synthesis and the structural and spectroscopic analyzes carried out in parallel, photocatalytic study was an important tool to further explore the semiconducting properties of this material. Additionally, our material gave very promising results in photocatalytic dye degradation, compared to the commercial products, even if it was not initially synthesized for this application. We assign these performances to the improved crystallinity resulting from thermal activation, without changing the crystal size, and to the ability to optimize the surface.

This photocatalytic study gave us insights into the methods that optimize the electronic structure of the titanium oxide. Hence, we decided to thermally activate the nanoparticles before the preparation of films to be inserted into DSSCs. At this stage, as the thermal activation applies to the powder, the resulting material can still be used with flexible substrates.

We have successfully integrated these nanoparticles in dye sensitized solar cells. Various organic additives were added to the TiO_2 paste used to prepare photoelectrode films, to increase the porosity of the film and have a crack–free film with good attachment to the substrate. We demonstrated that the dye was chemically attached to the TiO_2 surface, which led to better electron transport. Different treatment methods (UV and thermal) were applied to the film to cure it from organic additives and improve the electronic connectivity between the particles. When the UV treatment was applied as a single method, i.e. without thermal treatment, the cell performance was lower, but a combination of thermal treatment and UV enhanced this performance. We compared our nanoparticles to the reference material used in most of the studies on DSSC, that is, TiO_2 Degussa, with cells prepared the same way. Our nanoparticles revealed higher overall conversion efficiency. As the dye attachment to the TiO_2 surface is an important parameter that enhances the cell efficiency, so we checked *via* ATR-FTIR how the dye attached to the TiO_2 surface. In addition, FTIR, UV-Vis, and IV measurements revealed that the amount of dye adsorbed was increased through HCl treatment of the photoelectrode. We also checked the internal resistance of the cell using impedance spectroscopy, and the analysis proved a successful integration of the nanoparticles in dye–sensitized solar cells as there was an increase in both the electron life time and the

recombination resistance, and a decrease in the charge transfer resistance compared to the commercial powder.

Acknowledgments

First and foremost, all praise to Allah the lord of all the universe. He who taught human beings everything new and unknown before.

I would like to express my sincere gratitude and appreciation for my supervisor Eric Prouzet for allowing me to explore new scientific areas, and for his support, discussions, advice, and patience throughout this study.

I deeply appreciate the prayers, support, and sacrifice from my family, especially my sister (Eman) who has been taking care of our family during my Master's and PhD studies. I dedicate all my success to her.

I would also like to thank my committee members (Prof. Sivoththaman, Prof. Mario Ioannidis, and prof. Ting Tsui) for their help, advice, and their critical review of my work. My sincere thanks to Prof. Ioannidis for his valuable advice and continuous encouragement during my committee meetings that helped me to continue doing this challenge work. Many thanks to Prof. Sivoththaman for allowing me to use his instruments for cell characterization, and many thanks to his students Bahrain and Roohen for training me on the instruments. My sincere thanks to Prof. Tsui for the use of the UV furnace and his help with the SEM imaging instrument. Thanks to Zeinab for giving me the training sessions.

Sincere thanks to my colleague Ian Hussein for his continues help and invaluable discussion throughout this work. Moreover, I would like to thank all my lab-mates Manal, Haleema, Natacha, Edgar, and Andrew for their help and support .

I would like also to thank Prof. Eric Croiset for allowing me to use the impedance spectroscopy and special thanks to my friend Asmida who gave me the training sessions and helped me in the measurements.

My great thanks to all my friends–Manzi, Noorlisa, Raina Lawindy, Ahlam, Amal, Sanaa, Ghada, Throe–for their support and encouragement over the years I spent in Canada

I owe special thanks to my Master's thesis supervisor (Dr. Eman Bellah) for her advice and help in applying for my Ph.D scholarship. Many thanks to my supervisors (Dr. Omar Elfarouk

and Dr. Nagwa Khattab), and colleagues in Egypt, the Solar Energy Department in the National Research Centre for their help and support.

Finally, I would like to thank the Egyptian Ministry of Higher Education for giving me the opportunity to continue my graduate studies in Canada and also for their financial support.

Dedication

To my beloved parents,

To my beloved sister….. Eman

To my beloved twin….. Amged

Table of Contents

List of Figures

List of Tables

List of Appreviations

ATR-FTIR	Attenuated-Total-Reflection- Fourier Transform Infra Red
BIPV	Building Integrated Photovoltaic Window
CIE	Charge injection efficiency
CPE	Constant phase element
CVD	Chemical Vapor Deposition
DSSCs	Dye Sensitized Solar Cells
EDX	Energy-Dispersive X-Ray Spectroscopy
EG	Ethylene Glycol
EIS	Electrochemical Impedance Spectroscopy
EMIDCA	1-ethyl-3-methylimidazolium dicyanamide
EQE	External Quantum Efficiency
EVA	Ethyl Vinyl Amine
FF	Fill Factor
FTO	Flourine doped tin oxide
fsec	Femto second
FWHM	Full width at Half Maximum
HLB	Hydrophilic Lipophilic Balance
HOMO	Highest occupied molecular orbital
HPLC	High- Performance Liquid Chromatography
IEP	Iso Electrical Point
IMPS	Intensity-Modulated Photocurrent Spectroscopy
IMVS	Intensity-Modulated Voltage Spectroscopy
IPCE	Icident photon to light harvesting efficiency

IQE	Internal Quantum Efficiency
ITO	Indium doped Tin Oxide
LHE	Light harvesting efficiency
LOMO	Lowest unoccupied molecular orbital
MB	Methylene Blue
MLCT	Metal to Ligand Charge Transfer
PEN	polyethylene-naphthalate
PEO	Polyethylene-oxide
PET	polyethyleneterephethalate
PSCs	Photoelectrochemical Solar Cells
psec	Peco second
RSM	Response Surface Methodology
RTILs	Room Temperature Ionic Liquids
SAXS	Small Angel X-Ray Scattering
SEM	Scanning Electron Microscope
ss	specific surface area
TBAHO	tetra-butyl ammonium hydroxide
TBP	4-tert-butylpyrridine
TCO	Transparent conductive oxide
TEM	Transmission Electron Microscope
TP-XRD	Temperature Programed X-Ray Diffraction
UV	Ultraviolet
WAXS	Wide Angel X-Ray Scattering
XRD	X-Ray Diffraction

Nomenclature

A	absorbance
A_A	integrated intensity of anatase
A_B	integrated intensity of brookite
c	concentration of the dye
C_0	methylene blue concentrations at t = 0
C_t	methylene blue concentrations at t
d	interparticle d-spacing
D	crystal diameter in nm
D_e	Diffusion coefficient of the electron
D_v	mass fractal dimension
E_g	anatase bandgap
E_{in}	incident irradiation power
ΔE_g	theoretical variation of the band gap shift, eV
E_{Ry}^*	effective Rydberg energy , 4.3 10^{-39} J
f_A	anatase weight fraction
ΔG_{mix}	Free energy of mixing
h	Plank's constant, $6.62*10^{-34}$ (m^2.kg/s)
Imax	Current at maximum power point
I_R	integrated intensity of rutile
I_A	integrated intensity of anatase
J	current density
J_{inj}	injected electron current density
J_s	saturation current density
J_r	surface recombination current

J_{sc}	Short circuit current
k_A	experimental coefficient (anatase) (0.886)
k_B	experimental coefficient (brookite)(2.721)
k	the reaction rate constant
k_{re}	rate constant for the reduction of triiodide
l	thickness of the solution
Ln	Diffusion length
L	crystal size
m or n	diode ideality factor (has a value between 1 and 2)
m^*_e	effective mass of the electron,10 m_e ($m_e = 9.11.10^{-31}$ Kg)
m^*_h	the effective mass of the hole, 0.8 m_e
n_{cb}	concentration of electron at the surface of the electrode
N	coordination number
P	film porosity
P_{in}	Photon flux (1000W/m^2 for AM 1.5)
Q	The percentage removal of MB
R	radius of the particle, nm
r	degradation rate of the methylene blue
Re	Reflection of light
R_r	Recombination resistance
R_s	series resistance
R_{sh}	shunt resistance
Rstot	Total series resistance, Ω
Rs	ohmic resistance, proportional to the sheet resistance of FTO
R_t	Charge transfer resistance
ΔS_{mix}	Entropy of mixing

T	the ratio of transmitted light to the incident one
V	Voltage
V_{oc}	Open circuit voltage
W_B	weight fraction of brookite
Vmax	Voltage at maximum power point
Ws	Warburg diffusion resistance
Θ	the angular position of the diffraction peak
α_0	absorbance of the MB solutions in the 664 nm wavelength at initial time
α_t	absorbance of the MB solutions in the 664 nm wavelength at any time
e	Electron charge, $1.6021*10^{-19}$ C
μ	reduced mass of the exciton
Δτ	the Full Width at Half Maximum (FWHM) (in rds),
υ	Frequency
α	the absorption coefficient in cm^{-1}
λ	the X-ray wavelength (0.154 nm)
τ	Electron lifetime
ω_{min}	Minimum frequency
ω_r	Frequency corresponding to charge transfer
ω_d	Frequency corresponding to diffusion (electron transport)
Z	impedance
η_c	efficiency of collecting electrons at the back contact
Γ	dye coverage
εmax	molar absorbance of the ruthenium polypyridyl dyes , $1.4 * 10^4$ M^{-1} cm^{-1}
ε	dielectric constant

Chapter 1: Introduction

1.1. Motivation

The market for silicon solar cells with different applications has been growing–from small–scale distribution of power to megawatt power plants. However, the high cost of solar cells in terms of energy, material, and processing time has limited their large scale production.

An efficient alternative to silicon solar cells is Dye-Sensitized Solar Cells (DSSCs), which have attracted interest since the pioneering work of Graetzel and coll.[1] The core design of these cells depends on obtaining a short path length for the collection of the photogenerated electron-hole pairs from the generation sites to their collection sites, and on obtaining a long optical path length for the incident photons through reflection and scattering. DSSCs are considered one of the thin film technologies with the highest potential, among all types of organic solar cells: dye-sensitized, polymer, and molecular. The efficiency of this technology has exceeded 11%, and it is also theoretically expected to reach 20%[2] compared to the efficiency of the traditional thin film silicon technique, which is commercially available at efficiencies of 12% and 15%. Due to the low cost of raw materials, low production cost, and high conversion efficiency from light to electrical energy, DSSCs have attracted great attention over the past years, but progress must be made on both improving the components involved and the design and engineering for large-scale production.

Dye-sensitized solar cells convert photons into electrical energy through charge separation in a dye that acts as a sensitizer. As a result of the charge separation mechanism, the electron is transferred to a semi-conductor, and the holes are transferred to the electrolyte. Unlike silicon-based devices, these cells separate the two functions: the silicon acts as both the source of photoelectrons and as the provider of the electric field that separates the charges and creates a current, whereas the bulk of the semiconductor (called the photoanode) is used solely for charge transport in dye-sensitized solar cells, since the creation of the photoelectrons is due to the photosensitive dye molecule. The dye works as an antenna for photon capturing, so

adsorbing large amounts of dye on TiO_2 nanoparticles has been considered an important goal for enhancing the performance of the dye sensitized solar cells.

More generally, the requirements for high performance solar cells depend on three factors: efficiency, cost, and stability. Any research devoted to increasing the performance must take into account of such devices, these three factors, which are highly interrelated. Doing so can achieve not only high solar efficiency and good reliability, but also a manufacturing process that will allow for large scale manufacturing. The following schematic shows the overall view of the dye solar cell components. This flow diagram illustrates the requirements of each component and the interaction between the components that must be meet are illustrated to construct high performance dye-sensitized solar cells.

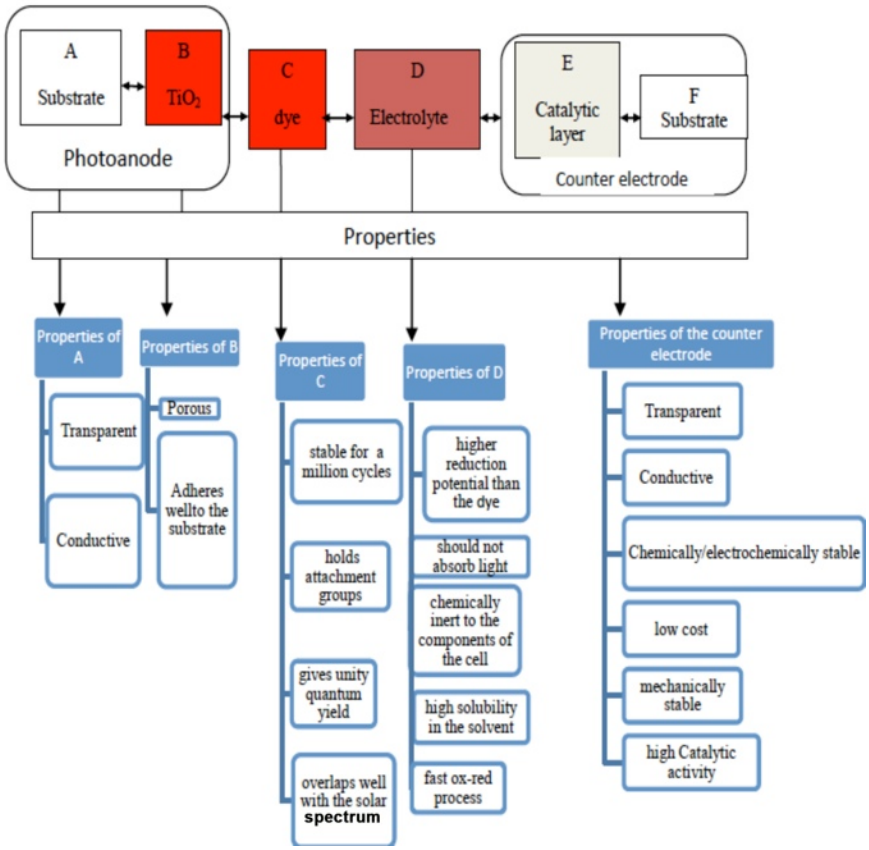

Figure 1.1: Flow Diagram schematic of the requirements for achieving efficient DSSCs

As can be seen from the flow chart, the high efficiency of dye solar cells must be obtained via the optimization of each component (the substrate, the photoanode, the photosensitizer, the counter electrode, and the electrolyte). For example, the substrate has to be transparent and conductive in order to allow the penetrating light to be absorbed by the sensitizer (dye). Furthermore, the photoanode, which is prepared by the deposition of the TiO_2 paste on the substrate, has to be conductive enough and porous in order to allow the penetration of the electrolyte into the pores up to the dye molecules adsorbed onto the surface of the photoanode. However, the porosity of the film has a significant effect on electron transport: as the porosity increases, the connection between particles can decrease, resulting in lengthening of the electron transport pathway. Another example deals with the size of the particles used for the photoanode: decreasing their size will allow us to increase the total surface area, hence the amount of dye that can be grafted, and optimize the porosity. However, too small size can prevent any light scattering within the photoanode, which reduces the efficiency of the light collection. A last example deals with the nature of the electrolyte that can be liquid for higher conductivity. However, there is a risk of leakage that will reduce the overall lifetime of the DSSC. It appears from these examples that the optimization of the components is not a one-way route as properties and structures are correlated within a complex network of interactions. Therefore, the improvement of one component must be validated as a function of its integration in the whole system.

As a result, proper integration and connectivity of all these components are compulsory. The intrinsic electrical conductivity of each component is not sufficient if the conductivity between components is weakened by bad adhesion or defective interfaces. As explained above, the structure of the photoanode plays an important role in enhancing the light harvesting efficiency: the photosensitizer (dye) has to be adsorbed on the large surface area of the semiconducting photoanode to increase the dye loading. The transfer of electrons depends on the area of interconnection between the particles, and the smaller the area of the interconnection, the slower the overall transport. However, increasing the density of the photoanode to increase the electron conduction will result in a decrease in dye loading. On the other hand, when a redox mechanism is involved in the hole capture and electron transfer at the

counter electrode, this electrode not only conducts electricity, but has an effective catalytic activity, speeding up the chemical reaction that allows one component of the electrolyte to capture the electron coming from the outer circuit and transfer it back to the dye molecule to balance the electron loss resulting from the photoreaction. Finally, if a liquid electrolyte is used, a good sealing material is important to ensure high stability of the cell by preventing leakage. The sealing material can also work as a spacer to prevent the cell from being short circuited. Consequently, the elements of the dye solar cell are related to each other, and great care should be taken in the selection of these elements to achieve high performance plastic dye-sensitized solar cells. In addition, their contribution cannot be evaluated without taking into account their correct integration.

1.2. Research Objectives

The initial objective of this study was to explore the possibility of using only room-temperature processes for the manufacturing of DSSCs in order to contribute to the development of high efficiency devices. Indeed, from an engineering point of view, performance of a solar cell is not only defined by its intrinsic efficiency, but as the ratio between the efficiency and the manufacturing cost. High efficiency and low production cost are important factors in making DSSC modules competitive with other products on the market, and reduction of the cost can be achieved by using specific processes that could more easily be scaled up to the industrial level.

Therefore, a manufacturing method based on multilayer roll-type processes would be a good candidate, but it implies the choice of flexible–plastic–supports, which precludes any high temperature operation during the assembly process. Usually, the photoanode of DSSC is prepared from a colloidal paste of TiO_2 nanoparticles glued with organic additives, and the connectivity between these particles is provided by a thermal treatment that creates a partial sintering between particles. This thermal treatment is also used to generate a suitable crystalline phase. Obviously, this process prevents the use of any flexible organic substrate, hence any roll-based manufacturing method. Therefore, our initial goal was to adapt room–temperature procedures developed for other domains to the preparation of titania to be used as

a photoanode, and to explore the requirements for the assembly and testing of DSSC made with soft organic substrates.

During the research, we managed to synthesize a new type of nanocrystalline TiO_2 at room temperature by a novel soft chemistry pathway is highly competitive with other preparation methods. As recommended by the PhD Thesis Committee along the work, it also became important to further explore the properties of this new type of nanomaterial, to see how it could be modified and optimized for photovoltaic applications. Therefore, we decided to focus on three topics, starting from the synthesis of the material, up to the validation of DSSCs using this material: (i) synthesis, characterization and optimization of a new nanocrystalline titania; (ii) exploration of the property/structure relationship, especially the semiconducting properties developed by the study of photocatalytic properties; (iii) integration and testing of this optimized material in DSSC devices.

1.3. Contributions

1.3.1. A New Material

Although the components of the dye solar cell play an important role in achieving high performance solar cells, the photoanode is considered the most important component of the cell. Recently, a lot of work has been done in order to commercialize dye-sensitized solar cells taking into considerations different factors that affect their performance. The recent reports of dye-sensitized solar cells have shown that high efficiency solar cells can be obtained with specific combinations of their components, such as nanostructured TiO_2 as a semiconductor, organic dyes as they have higher extinction coefficient, and electrolytes consisting of volatile organic solvents with an iodide/triiodide redox couple.[3] Except for some specific geometries[4, 5] , most of the studies use commercial powders that are not fully optimized for this application. Being able to synthesize nanocrystalline TiO_2 with the anatase structure using the room temperature method allowed us to propose a new material, and to explore in detail how the nanostructure of the material and crystallinity can affect semiconducting properties.

1.3.2. A Method for Material Development

Usually, the development of materials is based on trial-and-error methods where by different parameters are tested independently and randomly. This approach finds its limitations when the parameters are correlated. We used a mixture design method to explore how synthesis parameters modify the final material, and to be able to define *a priori* these parameters to achieve a specific final structure.

1.3.3. Parameters That Govern Photocatalysis of TiO_2

Titania has been a material largely studied for its photocatalytic properties. To increase our understanding of the structure/property of the new material we had synthesized, we used photocatalytic tests that are easier to undertake than assembling and testing of photovoltaic cells, which can depend on other parameters. Our room temperature synthesis of nanocrystalline anatase allowed us to expand the domain of study and identify the role of different parameters.

1.3.4. A New Material for DSSC

This new form of titania was tested in DSSCs, and the preparation of the thin film photoanode allowed us to compare different methods for an optimized integration and structure of the film. The cell preparation was modified by adding different organics (polyethyleneoxide-PEO 12000-, Pluronic P123, and Span 80/tween 80 with acetic acid). Two treatments (UV and thermal) were applied to the film, and their effect on the cell performance was studied. This study allowed us to compare these additional treatments (some had been published before, some are new).

1.4. Document Outline

This thesis is organized as follows:

- Chapter 1 presents the motivation, objectives and the contributions of this work.

- Chapter 2 illustrates the overall background on the Dye-Sensitized Solar Cell, how it works, the components of the cell, the theoretical concepts of the cell, and the research that has been done so far in this area.
- Chapter 3 explains the first step in manufacturing dye-sensitized solar cells and describes the novel soft chemistry synthesis of TiO_2 nanoparticles by sol-gel accompanied by phase separation.
- Chapter 4 optimizes the operating temperature as a crucial requirement for enhancing solar cell performance. Moreover, a photocatalytic behaviour for the synthesized nanoparticles is tested.
- Chapter 5 illustrates the steps of manufacturing dye sensitized solar cells and the different treatment methods that affect cell performance.
- Chapter 6 provides concluding remarks and introduces areas for future work.

Chapter 2: Literature review

2.1. Introduction

Dye-Sensitized Solar Cells (DSSCs) can be divided into three types according to the type of the electrolyte used:

DSSCs with liquid junction such as ionic liquid or other organic solvent

DSCs with quasi solid-state electrolyte such as polymer electrolytes

DSCs with hole conducting electrolytes such as p-type semiconductors

Although dye-sensitized solar cells have existed for a long time and their charge separation occurs at high efficiency, they have had traditionally low conversion efficiency below 1%. This low efficiency is due to the adsorption of the dyes onto a relatively flat surface of semiconductor electrodes. In 1991, in order to achieve high efficiencies in solar cells, O'Regan and Graetzel made drastic improvements in the performance of DSSC at the Swiss Federal Institute of Technology (EPFL) through two approaches. The first approach was to obtain high surface area of photoelectrodes, and the second was to promote new trends in photosensitizers (dyes) with broader absorption ranges.[1] For example, using a nanoporous TiO_2 photoelectrode that has a large surface area enhances the adsorption of a large amount of Ru terpyridine complex dyes that are capable of absorbing visible and infrared light from 400 to 900 nm. The resulting cell reached a photo-efficiency ή = 10.4% under AM1.5 with a short-circuit photocurrent density, J_{SC}, of 20.5 $mAcm^{-2}$, an open-circuit voltage, V_{OC}, of 0.72 V, and a fill factor (FF) of 0.70. High efficiency and low production costs are important factors in making DSSC modules competitive with other alternatives on the market. Several research groups have been working on developing DSSC products. Currently, the overall light conversion efficiency of the dye-sensitized solar cells is larger than 11%, a percentage which is still two times lower than that achieved with silicon technology. [2]

2.2. Components of Dye-Sensitized Solar Cells

Dye-sensitized solar cells, which are also known as photoelectrochemical solar cells (PSCs), consist of three basic components in addition to the photosensitizer: a photoanode, a redox mediator (electrolyte), and a counter electrode. Another essential component is a sealing material, and finally the solvent which plays an important role in increasing the cell efficiency. [1]. Other additives were found to be important in enhancing the efficiency of the cell by adding them to the electrolyte. Figure 2.1 illustrates the components of dye sensitized solar cell.

The energy conversion efficiency of the dye-sensitized solar cells interrelates with the effectiveness of the electron transport and transfer rates. The parameters that influence the rate of electron transport are: (i) the preparation method of TiO_2, in term of nature and particle size, (ii) the surface treatment of TiO_2, (iii) the annealing temperature of the TiO_2 film, (iv) the concentration of the redox couple and its cation, (v) the additives to the electrolytes, (vi) the nature and catalytic performance of the counter-electrode, and (vii) the solvent. Individual properties of the components of the solar cell and the processes can significantly affect the overall performance of the dye solar cell.

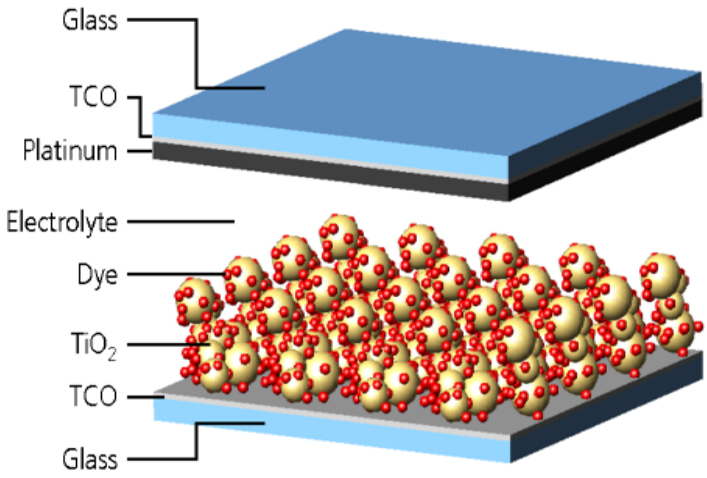

Figure 2.1 Cross-sectional area of the dye sensitized solar cell.

2.2.1. Photoanode

The morphology and the interfacial properties of the nanostructured electrode are the master keys to achieving high efficiency solar cells. The nanostructured anode must exhibit a large surface area to allow a high dye loading, but both the particle size distribution and interparticle pore size distribution affect also the ion diffusion and the optical properties. In addition, good interparticle electrical connectivity enhances the electron diffusion. The photoanode consists of three parts as follows:

* a transparent conducting oxide (TCO) on a substrate such as glass
* a thin layer of nanocrystalline TiO_2
* a layer of dye molecules adsorbed onto the surface of TiO_2 particles

In order to prepare TiO_2 nanoelectrode, two steps are required. The first step is to deposit a paste or a suspension of TiO_2 particles onto a glass substrate previously coated with a conducting layer. Different techniques can be used, such as chemical vapor deposition (CVD), spray pyrolysis,[6] DC sputtering, and precipitation. In the second step, sintering is used to form a continuous and porous body of TiO_2 nanoparticles that displays sufficient cohesion to stand mechanical stress and exhibit good electrical contact, but enough porosity to allow for a large adsorption of dye molecules and facile access of the electrolyte. Usually, in addition to nanoparticles that contribute to increase the total surface area, the TiO_2 film contains some larger particles (250 - 300nm) that allow for an improved internal light scattering, which results in a better light harvesting efficiency.

2.2.2. Substrate

The substrate usually is glass coated with a conductive layer. Glass is a cheap transparent support and efficient barrier against water and oxygen penetration into the cell. For high solar cell performance, the transparent conductive layer (TCO) must exhibit low electrical resistance and high transparency. Moreover, the resistance must be temperature independent, and the layer must stand temperatures higher than 500°C, the usual sintering temperature of TiO_2 nanoparticles. There are two types of TCO used in dye-sensitized solar cells: Indium-doped tin oxide (ITO) and fluorine doped tin oxide (FTO).The most commonly used TCO in solar cells is

fluorine-doped SnO_2 due to its optical and electrical properties, and compatibility with high temperature processing. However, because of the lack of flexibility, and brittleness of glass, plastic substrates are studied as a viable option. The choice of plastic substrates is more the result of being able to develop large scale roll-to-roll manufacturing processes, than a simple competitive cost between materials. Recently, flexible plastic substrates such as polyethylene-terephethalate (ITO/PET) and polyethylene-naphthalate (ITO/PEN) have been used in DSSC. In 2003, Murakami *et al*., fabricated a plastic film- based TiO_2 using the electrophoretical technique to deposit the TiO_2 layer on ITO-coated PET. In addition, they treated the film with CVD followed by UV light irradiation below $110C^{o}$.[5] This electrode bearing Ru complex (Ru 535-bis TBA) yielded 3.8% efficiency. If Roll-to-roll production techniques using plastic substrates could be applied, it would result a drastic reduction in production cost of DSSCs

2.2.3. Titanium Oxide

Titanium oxide remains the most used material for the preparation of photoanodes. Mesoporous TiO_2 materials have been extensively used in diverse areas such as catalysis, sensing electronics, solar cells, and separation science**.** TiO_2 has a high dielectric constant (ε=80) which enhances electrostatic shielding for the electrons injected by the dye, which slows down the recombination of these electrons until the oxidized dye is regenerated by the redox electrolyte. The light absorption is enhanced by the efficient diffuse scattering due to the high refractive index of the titanium oxide (n=2.5). Titania presents different crystalline phases, anatase and rutile being the two most important. Anatase is stable at low temperatures in the form of pyramid-like crystals and gives mesoscopic films transparency.[6] Rutile, in the form of needle- like crystals, is dominant at high temperatures. The densities of rutile and anatase are 4.26 and 3.89 g/ cm^3, respectively. Anatase has a more opened structure than rutile, with a different electronic structure that leads to a smaller band gap (3 eV) for anatase, compared with that of rutile (3.2 eV). The TiO_2 is weakly n-doped semiconductor because of oxygen vacancies in the lattice. The most stable lattice plane is (101).

2.2.4. Dye

Several criteria are recommended for the dyes used as photosensitizers in solar cells. Spectral properties are important in order to insure that the range of light absorption in the visible and near IR region is covered, that is, the dye spectrum overlaps effectively with the solar spectrum. Moreover, the sensitizer must hold attachment groups such as carboxylate or phosphonate groups to graft firmly onto the surface of TiO_2. The quantum yield should be unity to achieve a high injection rate of electrons from the excited state to the conduction band of the semiconductor, and the dye should be stable for many millions of cycles.[7] The most common and most successful dyes until now, are Ru complexes which have been used intensively in research because the excited states of the complexes have long lifetimes and that the oxidized dye (Ru (III)) has long-term chemical stability. Figure 2.2 shows the molecular structure of the most common types of Ru complex dyes that have been used in the research.

Figure 2.2 Molecular structures of typical Ru complex photosensitizers (Reprinted from 1 with permission from John Wiley and Sons copyright 2009)[1]

The currently used dyes, ruthenium complexes, have some limitations as their extinction coefficient is low. The molar absorbance of the ruthenium polypyridyl dyes is low ($\varepsilon max \approx 1.4 * 10^4\ M^{-1}\ cm^{-1}$), which is considered a basic limitation for their future use. As the amount of the adsorbed dye increases, the light harvesting efficiency of the solar cells increases in parallel. Other metal complexes that have metal centers other than Ru have been synthesized,

and organic dyes or metal free organic sensitizers as shown in Figure 2.3 have been investigated, which have shown promising results. They are low cost and have molar extinction coefficient higher than that of Ru dyes.[8]

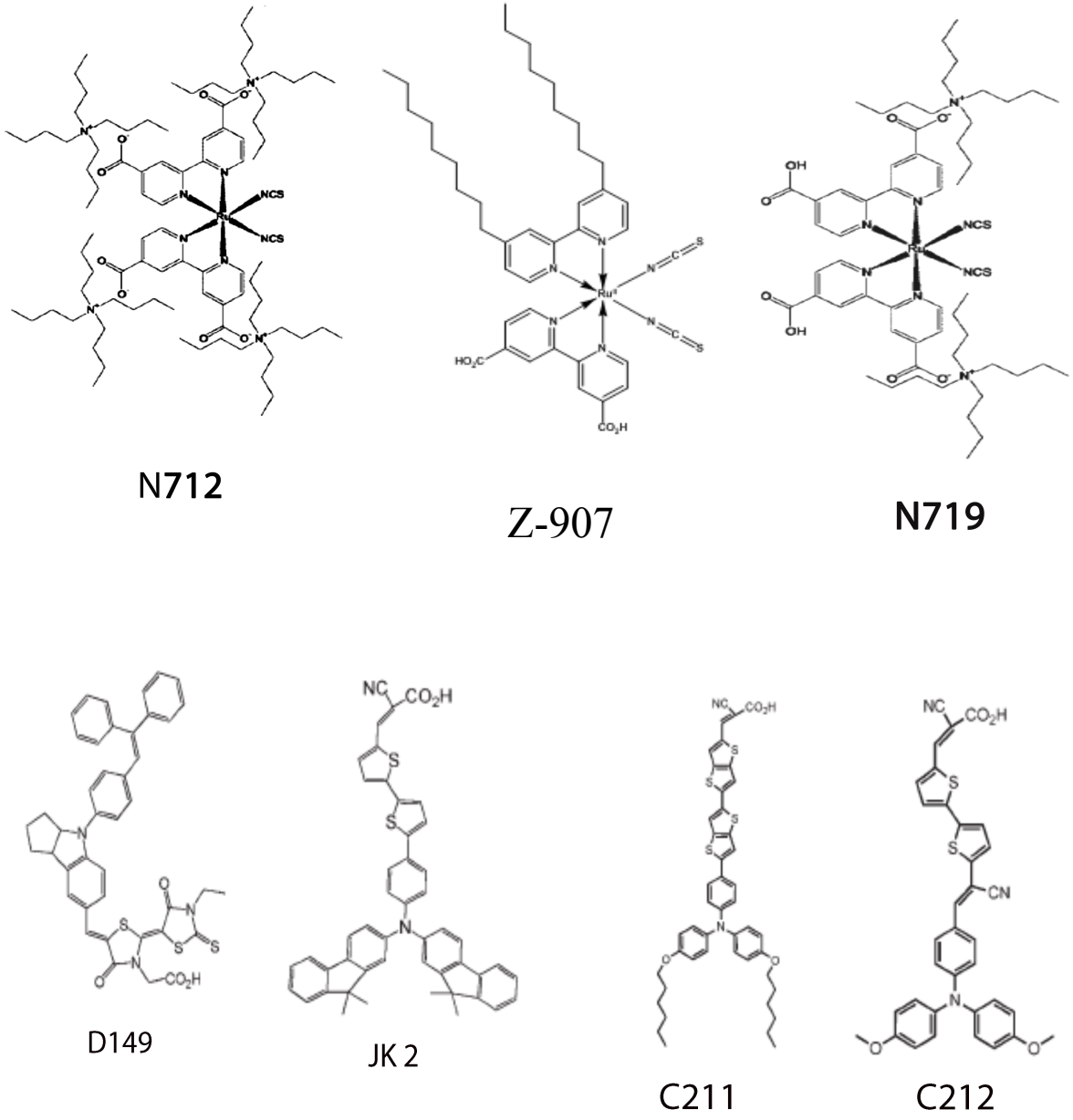

Figure 2.3 Molecular Structures of Metal Free Sensitizers used with Ionic Liquid (IL) Electrolytes [8]

Furthermore, Ru complex dyes have been tested with ionic liquids as the electrolyte for the cell and have shown good results. Table 2.1 displays the comparison between the most commonly used Ru metal complex dyes, Z907and N719, with ionic liquid electrolyte.[8]

Table 2.1 Comparison Between Z907 and N719 Dyes Using Ionic Liquid as Electrolyte[8]

Type of dye	Isc	Voc	FF	η	Electrolyte (ionic liquid)
Z907(Ru complex)	12.8mA/cm^2	707mV	0.727	6.6%	0.1 M iodine, 0.1 M LiI and 0.45 M NMB in a mixture of PMII and 1-ethyl-3-methylimidazolium dicyanamide (EMIDCA) (volume ratio, 13:7).
N719(Ru complex)	Showed lower conversion efficiency due to the faster back transfer reaction of electrons from the TiO_2 to the tri-iodide				

2.2.5. Redox Mediator and Electrolyte

2.2.5.1. Current Systems

The redox mediator is the second component of dye-sensitized solar cells. Its main function is to mediate electrons between the dye on the surface of the photoelectrode and the counter electrode. The most common redox mediator used in dye-sensitized solar cells is an iodide/ tri iodide solution I^-/I^-_3. One of the most important parameters that affect the selection of the redox mediator is its reduction potential relative to the reduction potential of the dye. Since the electron must be rapidly transferred from the mediator to the oxidized dye–to avoid the electron-hole recombination–, the reduction potential of the mediator must be higher in energy than the reduction potential of the dye. This mechanism is important to prevent recombination of the photoinjected electrons with the oxidized dye and to maximize the cell voltage. Furthermore, the electrolyte should not participate in the absorption of the incident light and has to be chemically inert toward all components of the cell. In order to have a high concentration of charge carriers, the solubility of the electrolyte in the solvent must also be

high. Finally, the reduction-oxidation must be very fast to facilitate the electron transfer and the reduced and oxidized species have to be stable to extend the lifetime of the cell. [9] The iodide / triiodide solution is prepared by adding the iodine solution to the solvent with iodine salt (KI, LiI, alkyl methylimidazolium iodide, and methyl-hexylimidazolium iodide MHImI). Performance of the cell is found to be influenced by the cation of the electrolyte salt. As the cation radius decreases, the photocurrent of the device increases linearly (Figure 2.4). Besides, another important factor that affects the performance of the cell, is the relative concentration of I_3^- to I^-. [9] The drawbacks of triiodide/iodide solution are as follows: limitation of the open circuit voltage due to low redox potential, absorption of visible light by triiodide, and the attack of the metal when silver is used as a current collector. In order to increase the stability of DSSCs, alternative redox couples have been investigated, such as Co^{II}/Co^{III}. Nusbaumer *et al*. reported that at low light intensity, Co^{II}/Co^{III} couple gave promising results, while Co^{II}/Co^{III} at high light intensity (1Sun) gave less promising results.[10]

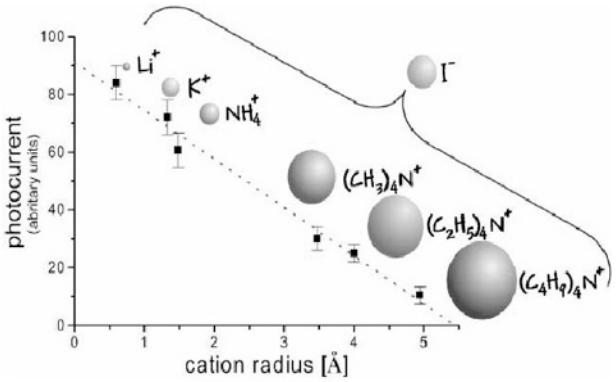

Figure 2.4 Effect of Cation Radius on the Photocurrent (Reprinted from 9 with the permission from Elsevier) [9]

Liquid electrolytes have shown some problems regarding the stability of the dye-sensitized solar cells. This instability is the result of the leakage of the electrolyte caused by the high volatility of the solvent used with the electrolyte, than a true chemical unsuitability. A better stability can be obtained by using a low vapor pressure solvent or using alternative electrolytes. A lot of research has been done in order to solve the problem of the volatile liquid electrolyte, and the research revealed that other alternatives can be used, as for example, ionic liquid, p-

type semiconductors, organic and inorganic hole transport materials, nanocomposites, and polymer gels.

In 2010, Moser *et.al* solved one of the major problems in the dye-sensitized solar cells by discovering a new redox couple as an alternative liquid electrolyte to the iodide/ triiodide redox couple: the disulfide/thiolate redox couple. This new redox couple has no absorption in the visible light. The efficiency of the solar cells achieved using this new redox couple reached 6.4% under standard conditions.[11]

2.2.5.2. Ionic liquids

Ionic liquids have been studied extensively as alternatives for liquid electrolytes in dye-sensitized solar cells. Ionic liquids are salts with melting points less than 100°C, and many of them are liquid at room temperature. Ionic liquids have unique properties such as low vapour pressure, wide electrochemical windows, ability to dissolve a wide range of organic and inorganic materials, high ionic conductivity, and high thermal and chemical stability. Room Temperature Ionic Liquids (RTILs) consist of cations and anions. Organic salts such as imidazolium, pyridinium or alkylammonium ions represent the cation, whereas halide or non-coordinating ions represent the anions. Figure 2.5 shows some general structure for the cations and anions of ionic liquids. At first, ionic liquids based on imidazolium salts were used as a solvent for the electrolyte in DSSCs, but the efficiency of the cells was low as a result of their high viscosity.[12] In order to reduce their viscosity, ionic liquids were mixed with organic solvents, and other types of low viscosity ionic liquids were synthesized.

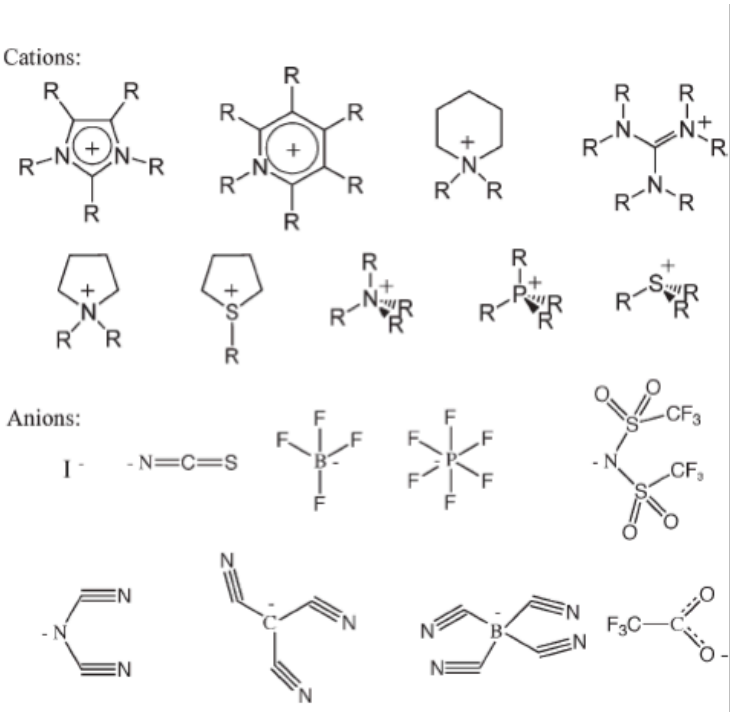

Figure 2.5 General Structure of Cations and Anions of Ionic Liquids.[8](Reprinted from 8 with permission from John Wiley and Sons)

2.2.6. Counter Electrode

The function of the counter electrode, which is the third component of the dye solar cell, is to conduct the electrons that were injected into the external circuit, back to the cell, and help to regenerate the oxidized mediator into its reduced state. Thus, the counter electrode has to be coated by a catalyst layer that has high electrocatalytic activity in order to reduce I^-_3. The material of the counter electrode will play an important role if it has a low charge transfer resistance, and if the platinum/electrolyte interface demonstrates good chemical and electrochemical stability during the iodide/triiodide reduction. Platinum is the most commonly used catalyst, and it is usually coated as nanoparticles to improve the catalytic efficiency. As a result, the electrochemical performance of the cell is strongly affected by the structure and morphology of the platinum catalyst. Good adhesion of the platinum nanoparticles on the substrate is also very important as non-adherent Pt particles move through the cell, adsorb on TiO_2 and cause a dark current at the TiO_2/electrolyte interface, leading to less conversion efficiency of solar cells.[13a,b]

Papageorgiou, *et.al*. came up with a range of a desirable exchange current density (0.01 to 0.2 $A.cm^{-2}$) related to the electrocatalytic activity for the reduction of tri-iodide ions.[14] Different methods have been used to deposit the catalyst layer on the surface of the TCO: spin coating, sputtering, and vapour deposition. Pt has high electrocatalytic activity and is chemically and mechanically stable, but it is expensive, which explains why much research has been done on the use of other materials such as activated carbon which has catalytic activity comparable to platinum.[14] By example, Kay and Grätzel demonstrated that a porous carbon made of carbon black, graphite powder, and nanocrystalline TiO_2.could be used as a catalytic counter-electrode. This carbon electrode shows high conductivity (for a 50μm thick layer the sheet resistance is 5Ω/sq).[15]

2.2.7. Sealing Materials

The function of a sealing material is to protect the cell from atmosphere, and to prevent leakage of the electrolyte solution and evaporation of solvents. An example of a sealing material is Surlyn™, which is a copolymer of ethylene and acrylic acid. Figure 2.6 is a photo of the sealing material taking directly from Dyesol catalogue. A good sealing material must be chemically inert with the components of the DSSC, adhere well to the substrate, be impermeable to water and oxygen, and do not break due to thermal expansion. Beside Surlyn, other types of sealing materials have been investigated such as epoxy glue, aluminum foil laminated with polymer foil, and a vacuum sealant named Torr Seal®.[16] In regard of the existing commercial products, there is not a clear research in this domain.

Figure 2.6 Surlyn (thermoplastic sealant) taking directly from Dysol (catalogue 2010).

2.2.8. Solvent

Selecting a good solvent for the liquid electrolyte that is used for high dye solar cell efficiency requires some criteria:[16]

* the viscosity of the solvent should be low to facilitate carrier diffusion,

* the solubility of the electrolyte (redox mediator) in the solvent should be high,

* the desorption of the sensitized dye into the solvent must be avoided,

* the decomposition of the solvent has to be very slow over a long period,

* the volatility of the solvent must be low, between the range of (40-80°C) to avoid freezing of the electrolyte.

Different types of solvents have been used for the electrolyte in dye-sensitized solar cells, such as acetonitrile, methoxyacetonitrile, methoxypropionitrile, glutaronitrile, and ethylene carbonate. Among these solvents, the one that has been used most intensively in research is acetonitrile as it meets most of the listed criteria. However, it has some limitations for long term stability of the cell due to its high volatility, which causes it to escape easily through the sealing of the cell. Furthermore, its boiling point is 82°C, a temperature equal to the temperature that a roof-top of solar cells can reach at full sun.

2.2.9. Electrical Contacts

The need for the electrical contacts in solar cells is due to the limited conductivity of the TCO layer. In 1996, Kay and Gratzel found that the losses related to ohmic contact in the TCO layer increases as the distance between the photoactive species and the current collector becomes longer than 1 cm. In addition, the Iodine-based electrolyte in the dye-sensitized solar cells attacks most metals (Al, Ag, Cu, Ni, and Au) due to the highly corrosive effect of this electrolyte. Thus, choosing an electrical contact and counter electrode that are compatible with the type of electrolyte is very important.[15]

2.2.10. Additives

Various compounds have been added to the liquid electrolyte (I^-/I^-_3). The most commonly used additives are 4-tert-butylpyrridine (TBP) and Li^+ ion. TBP is added to suppress the dark current; it is adsorbed on the uncovered TiO_2 surface. Addition of TBP results in a decrease in I_{sc} and an increase of Voc because the negative shift of the conduction band of TiO_2 [1]. Li+ ion has been shown to affect the conduction band of TiO_2 through either the adsorption or intercalation mechanisms. Consequently, this intercalation shifts the flat band potential positively. Furthermore, I_3^- absorbs light below 500nm[16]; therefore, tetra-butyl ammonium hydroxide (TBAHO) is added as a reducing agent for the light absorbing I_3^- complexes.

2.3. Operational Principles of DSSCs

The operation of a photovoltaic cell is divided into three processes: light harvesting, charge separation, and charge collection, and the efficiency of each step will affect the overall efficiency of the photovoltaic cell. According to the different kinds of photovoltaic cells and different materials used, the mechanisms of the three processes vary. In dye-sensitized solar cells, the incident light strikes the dye, shifting electrons from their fundamental state to an excited one (reaction 1). Instead of relaxing back to the fundamental state of the dye molecule, the vicinity of the TiO_2 substrate allows the excited electron to be injected into the conduction band of the oxide semiconductor (reaction 2). In parallel, the redox mediator regenerate the electron lost by the dye by reducing the molecule - the redox mediator is oxidized - (reaction

3). The injected electrons are transported in a narrow depletion region close to the particle, created by the interaction between the electrolyte and the surface of the solid, until they reach the TCO electrode. The electrons are injected into the external circuit, creating current, before they go back to the counter electrode. These charges are used to regenerate– reduce– ((reaction 4) the redox mediator, but the charge transfer must be catalytically activated, which justifies the need for a Pt nanostructure grown onto the counter-electrode. The following equations clarify the different reactions[1]:

$D + h\nu \longrightarrow D^*$	(1)	Dye sensitization	Anode (photoelectrode TiO_2)
$D^* \longrightarrow D^+ + e^-(TiO2)$	(2)	electron injection	
$3I^- + 2D^+ \rightarrow 2D + I_3^-$	(3)	Dye regeneration	
$I_3^- + 2e^-(Pt) \rightarrow 3I^-$	(4)	redox mediator regeneration	Cathode (counter electrode, Pt)
$e^-(Pt) + h\nu \rightarrow e^-(TiO2)$	(5)	***Cell reaction***	

As can be seen from the overall reaction (cell reaction), the cell operation is naturally regenerative: no chemical substances are produced or consumed.

2.3.1. Light Harvesting

As light must reach the dye molecules, any parasite absorption on its way will reduce overall the cell efficiency (calculated as the photovoltaic efficiency as a function of the light intensity). The light pathway uses the photoanode side, with the light being transmitted through the glass support, the FTO layer and within the semiconductor film. Hence, using wide-band gap semiconductors as a photoanode is appropriate for dye sensitization, because wide-band gap semiconductors have band gaps greater than 3 eV, which make them nearly transparent to the major part of the solar spectrum. In addition, the band structure of titanium oxide has the configuration required to make it a good candidate for its use in DSSC, because its conduction band is located slightly below the excited states of many dyes, which makes it the best host material for electron transfer and prevent electron-hole recombination after dye sensitization.

There are four energy levels (Figure 2.7) that define the performance of a dye solar cell: the first two are the excited state (LUMO: lowest unoccupied molecular orbital) and the ground state (HOMO: highest occupied molecular orbital) of the photosensitizer. The third one is the Fermi level of the TiO_2 electrode, and the fourth one is the redox potential of the electrolyte. The energy difference between LUMO and HOMO is critical for the photocurrent obtained from the cell: the smaller the difference between the two energy levels, the larger the photocurrent will be. With respect to the effectiveness of the electrons injection, the energy of LUMO must be above that of the conduction band of TiO_2 electrode (ΔE_1) to allow for spontaneous transfer. After the electron transfer from the LUMO to TiO_2, the hole in the dye HOMO must be filled by an electron transferred from the redox mediator. Therefore, the HOMO level must be below the potential of the redox mediator (ΔE_2). Finally, a minimum driving force for the electron-transfer reactions will require that the energy gaps, ΔE_1 and ΔE_2, must be at least 200mV.[1] The maximum voltage that can be obtained from the DSSC is the potential difference between the Fermi level of the TiO_2 (-0.5V/NHE) and the redox potential of the electrolyte (0.4V/NHE). This difference is expected to be 0.9V depending on the electrolyte components and their concentrations.

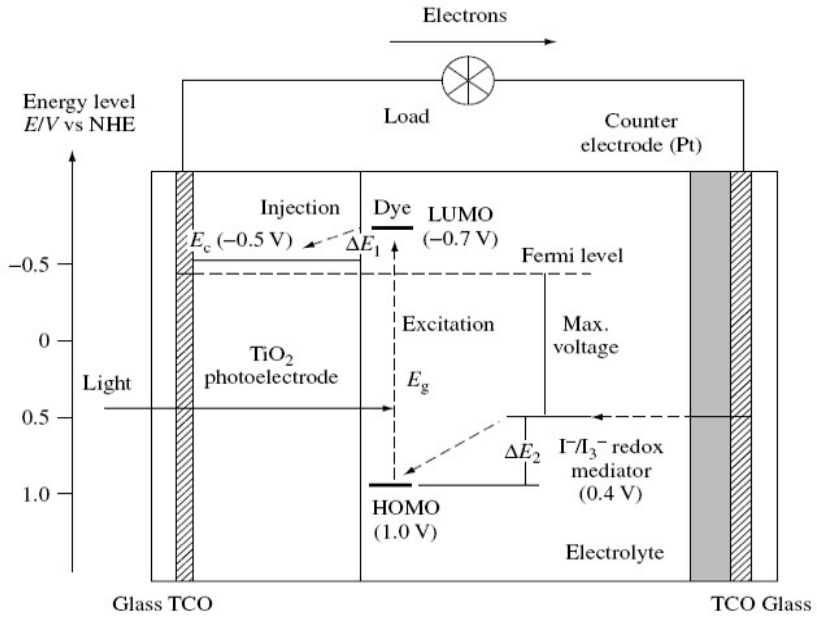

Figure 2.7 Schematic energy diagram and operating principles of DSSC (Reprinted from 1 with permission from John Wiley and Sons).[1]

2.3.1.1. Porosity and Nanostructure of the Semiconductor Film

The high surface area of the nanostructured semiconductor plays an important role in the performance of dye-sensitized solar cells for different reasons. A higher surface area will allow a larger amount of dye to be adsorbed, which facilitates high light absorption. On the other side, if the particle size is too small, the particles are depleted by the surrounding electrolyte solution, the depletion layer is no longer found. Hence, the semiconductor is considered as an intrinsic one. Furthermore, the nanoporous structure speeds up the interfacial charge transfer between the dye and the semiconductor.[17] Consequently, the amount of the injected electrons increases and the conductivity of the semiconductor increases.

2.3.1.2. Adsorption of the Dye Molecule

The adsorption of the dye molecule onto the surface of the semiconductor occurs via the anchoring groups attached to the dye molecule. The following example is for the N3 dye (Ru^{II} polypyridyl complexes with 4, 4'- $(COOH)_2$-2, 2'-bipyridine ligand. When it is adsorbed onto the surface of TiO_2, a dehydration reaction takes place, creating an ester group. The carboxyl

group can attach to the TiO_2 surface in different ways: physically through hydrogen bond or chemically through unidentate, dinette, or bridging linkage (Figure 2.8).

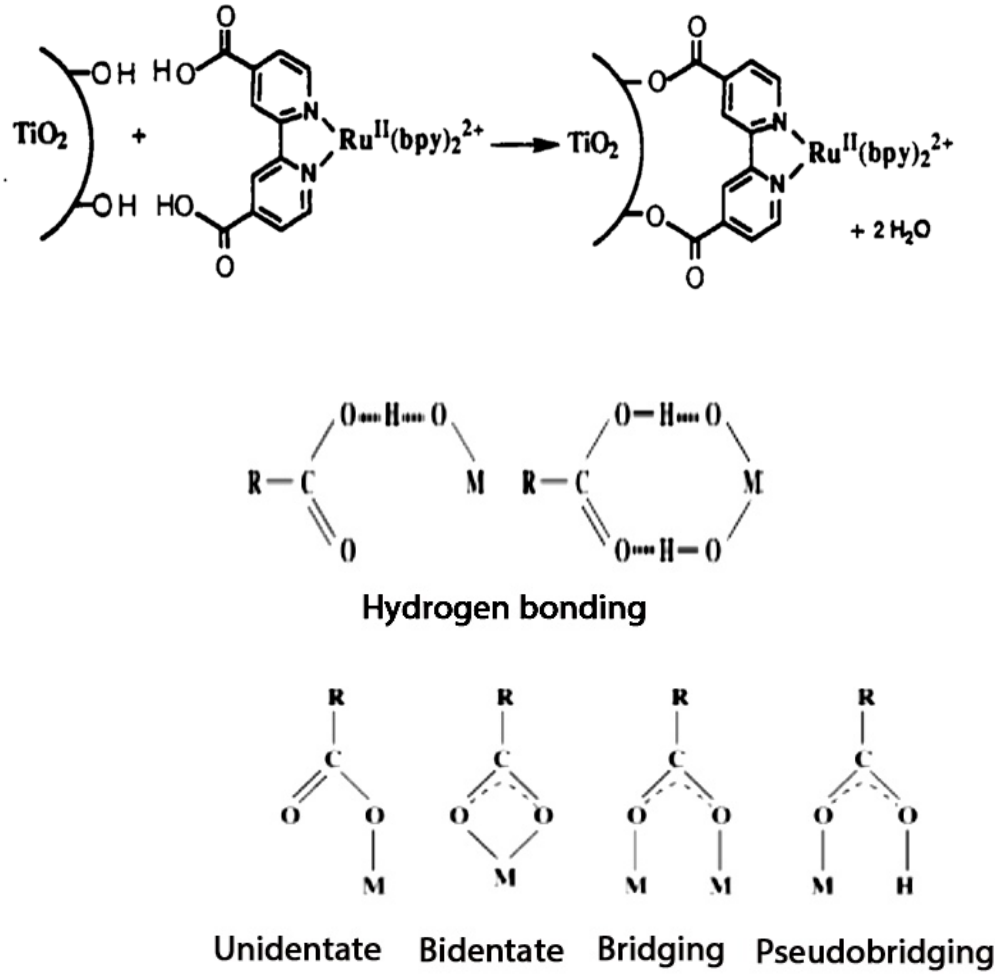

Figure 2.8 Different types of coordination: chemisorption (Reprinted from 18 with the permission from American Chemical Society)[18]
M: denotes to the metal The Spectral Response of dDifferent Types of Sensitized Dyes

Figure 2.9 illustrates the spectral response for cells sensitized with different dyes compared with TiO_2. As can be seen from the TiO_2 curve, the absorption spectrum of TiO_2 alone is restricted to a narrow band in the UV region.

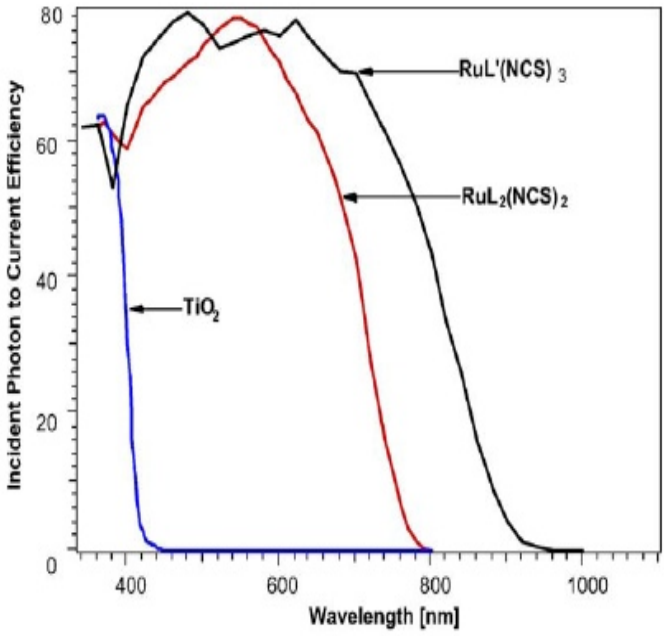

Figure 2.9 Photocurrent action spectra obtained with the N3 (ligand L) and the black dye (ligand L') as sensitizers (Reprinted from 19 with the permission of Elsevier)[19]
L= 4, 4'-COOH-2, 2'-bipyridine
L'= 4, 4', 4"-COOH-2, 2':6', 2"-terpyridine

2.3.1.3. Light Absorption via MLCT

Photon absorption induces a metal-to-ligand charge transfer (MLCT) transition from the highest occupied molecular orbital (HOMO) of Ru to the lowest unoccupied molecular orbital (LUMO) of the ligand. In addition, the redox potential of the sensitizer should be positive enough to be regenerated by the electrons donated from the redox electrolyte. Regarding stability, the dye should also sustain 10^8 turnover cycles.

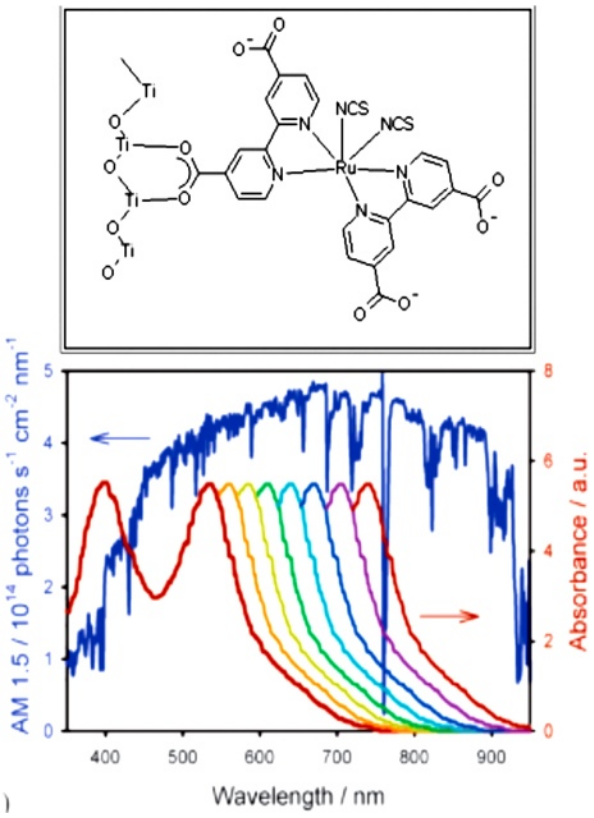

Figure 2.10 Top - Ruthenium based "N3" dye adsorbed onto a titanium dioxide surface; Bottom: Solar Spectrum and Ru-N3 dye (left-most red spectrum) Additional spectra are predicted overlap from changing dye energy gap[20]

Figure 2.10 (top) explains how the dye anchors onto the surface of titanium oxide. As can be seen from the spectrum shown in the above figure (bottom side), there is a red shift in the absorption property of the complex. This red shift occurs because NCS (-N=C=S) ligand shifts the HOMO level negatively (higher in energy).[1] In 1996, Rehm et al. measured the electron injection rate from N3 dye to the conduction band TiO_2 in femtoseconds using time-resolved laser spectroscopy, and they determined that the rate of injection was high ($5*10^{12}$ sec^{-1}).[21] Unlike TiO_2, it was observed that the injection rate of electrons from N3 dye into the conduction band of ZnO was low,[22] which means that the intrinsic semiconducting properties of the photoanode are not sufficient for material validation. Indeed, these results demonstrate that the rate constant for electron injection depends on the type of semiconductor used, and

ZnO, a potential good candidate cannot be kept because high energy conversion efficiency requires a high injection rate.[22]

2.3.2. Charge Creation and Transport

2.3.2.1. Charge Separation

In the photovoltaic energy conversion process, the photons of incident light excite the dye molecule, leading to the electron transfer from HOMO to LUMO. As these electrons access to a higher energy state, they leave holes in the ground state. As a result, electron-hole pairs are formed that tend to recombine if the system is left alone. Hence, the successful collection of electrons by the photoanode and that of holes by the counter electrode (actually via an electron transfer by the redox mediator) depend on the successful separation of the electron-hole pair for a time long enough to allow the other mechanisms to appear. In other words, recombination of the electron and holes after the separation has to be blocked. In p-n junction semiconductors, the separation of the electron-hole pair happens due to the effect of the electrical current formed in the space charge region. n-type and p-type semiconductors are formed by doping the semiconductor (Si) with electron donor (phosphorus) or electron acceptor (boron), respectively. If the two doped semiconductors are coupled, a p-n junction is formed, and the electrons in the n-type side will diffuse to the p-type side as a result of the electron concentration gradient between the two sides. The same phenomenon can be described with the holes in the p-type. Due to the diffusion of the electrons and holes, an electric field is built up.

In contrast, dye-sensitized solar cells have no significant depletion region or space charge. The particle size of the nanostructured semiconductor is too small to form a space charge layer inside the particles.[23] The depletion layer is created if there is transfer of mobile charge carriers between the electrolyte and the semiconductor. This charge transfer occurs with the assistance of electroactive species, which act as electron donors or acceptors in the bulk of semiconductors in contact with aqueous media, which results in the formation of an electric field at the interface between the semiconductor and the electrolyte. This electric field is formed by the adsorbed dye anchored to the surface of the semiconductor with the help of the carboxylic group. During the attachment of the $COOH^-$ group an H^+ is released making the

charge on the dye partially negative. Transport of carriers is due to the potential difference between cations in electrolyte and the negatively charged species (dye and iodide).[17] A dipole is formed across the Helmholtz layer and as a result, the difference in the electrical potential between the semiconductor and the solution will drop within the Helmholtz layer, inducing a shift in the position of the band edges of the semiconductor. This result was demonstrated by Hodes when the action spectra for the nanostructured film electrodes were recorded with the incident light on the interface between the electrode and either the substrate, or the electrolyte.[15]

The major charge separation for the electron and hole depends on the difference in energy levels between the conduction band of the semiconductor and the LUMO of the excited dye, and between the HOMO of the dye and the chemical potential of the electrolyte.

2.3.2.2. Charge Transport and Electron Transport Model

In order to figure out which elements affect the charge transport, the study of the whole system of the semiconductor and of the electrolyte should be considered. The electrons are transported in the semiconductor, while the ions and redox species are transported in the electrolyte. The charge separation occurs at the interface between the semiconductor and the electrolyte. Both electron transport and hole transport are very important mechanisms in dye-sensitized solar cells. The nanostructured semiconductor is at the core of this system as it is a supporting area for the sensitizer and a charge transport vector. The particles of TiO_2 are too small, to allow the creation of an electric field and a depletion layer.[24] Consequently, the transport of electron proceeds by diffusion not by drift. When electrons are injected into the metal oxide, positive ions move to the surface of the charged nanoparticles and neutralize long-range electrical fields. Therefore, the change in electrical field occurs right at the substrate interface, and electron transport occurs mainly by a concentration gradient, i.e., by diffusion. The diffusion coefficient of electrons was measured by several groups and all of them confirmed the same results:[25] the mechanism of charge transfer occurs by electron hopping via surface traps, which are localized energy states, just below the conduction band edge of the TiO_2.[18] This hopping

occurs because of the particle-based structure of the TiO_2 works as a network of individual particles.

It is worth mentioning that there is a relation between particle contact number and the porosity in nanoparticles film,[26] and a sufficient number of interparticle connections in the material network is required to allow for electrons to move readily from one particle to another. In parallel, the mechanical stability of a particle network requires that the average coordination number has to be at least 3.[27] For dye sensitized solar cells, the porosity should be typically in the 50-65% range which means more than half of the volume is voids. The redox electrolyte diffuses into these pores and is in contact with the nanoparticles. Lagemaat *et al*. simulated the relation between the film porosity and the coordination number of nanoporous films according to the following equation:[26, 28]

$$N = \frac{3.08}{P} - 1.13 \qquad 2.6$$

With

N: coordination number

P: film porosity

According to this equation the expected coordination numbers for a porosity range of 50-65% are 3.6-5, indicating that the nanostructured film is highly branched.

2.3.2.3. Charge Recombination

Recombination of the injected electron with the hole can occur during the injection process as well as *via* the transport of the electrons through the semiconductor to the back of the TCO. In p-n junction, the possibility of a recombination is high in the presence of impurities or high grain boundaries. In contrast, nanocrystalline dye-sensitized solar cells have a high surface area due to the nano-dimension and a lot of grain boundaries, but the probability of recombination is low.[17] This low recombination rate happens because injection of electrons occurs from the excited dye to the conduction band of the semiconductor (TiO_2) while the holes are being filled by electron transfer from the redox mediator in the electrolyte. The recombination occurs also

at different interfaces such as TiO_2-electrolyte interface, TiO_2-TCO, and TCO-electrolyte interface. In order to prevent charge recombination between the injected electron and the oxidized dye, the rate of charge recombination has to be very slow (nsec-msec). In contrast, the rate of charge injection from the excited dye to the conduction band of TiO_2 has to be very fast (fsec-psec). The only observed recombination reaction was between the tri-iodide solution and the electrons from the conduction band of TiO_2. The following figure (Figure 2.11) shows the reaction time of the different mechanisms at the semiconductor/dye/electrolyte interface.

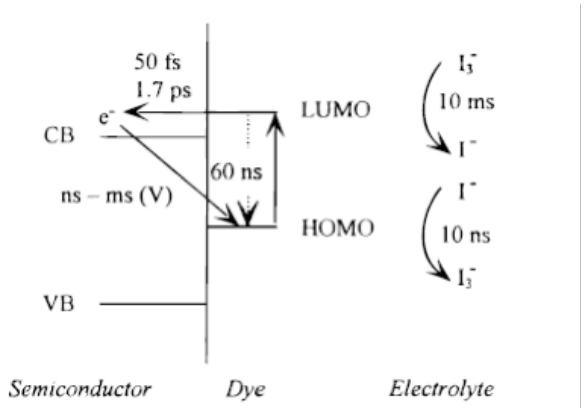

Figure 2.11 Kinetics in the DSSC, showing by arrows excitation of the dye from the HOMO to the LUMO level, relaxation of the exited state (60 nsec), electron injection from the dye LUMO level to the TiO_2 conduction band (50 fsec-1.7 psec), recombination of the injected electron with the hole in the dye HOMO level (nsec - msec), recombination of the electron in the TiO_2 conduction band with a hole (I_3^-) in the electrolyte (10 msec), and the regeneration of the oxidized dye by I^- (10 nsec).

2.3.2.4. Ion Transport in The Electrolyte Solution

The most commonly used electrolyte is the redox couple I^-/I_3^- . This electrolyte works as a hole conductor as it provides the oxidized dye with the electrons at the photoanode; I^- is oxidized to form I_3^- while I_3^- is reduced at the counter electrode to form I^-. The dye is continuously receiving the electrons from the fast redox reaction between I^-/I_3^- couple.

* At the photoanode $$3I^- + 2D^+ \rightarrow I_3^- + 2D \qquad (2.7)$$

* At the counter electrode $$I_3^- + 2e^- \rightarrow 3I^- \qquad (2.8)$$

The second reaction happens according to successive steps as follows[29] :

$I_3^- \rightarrow I_2 + I^-$ (Fast)

$I_2 + e^- \rightarrow I_2^-$ (Fast)

$2I_2^- \rightarrow I^- + I_3^-$ (Slow)

2.4. Device Construction and Manufacture

The construction of the DSSC device is shown in Figure 2.12. The cell consists of two FTO-coated glass substrates. The side of the top substrate is considered a photoanode on which a (10-15µm) porous-TiO_2 layer with the sensitized dye is deposited. More often, a catalytic Pt layer is deposited on the bottom substrate, this substrate being considered to be a cathode. The two electrodes are clamped together and a sealing material, which also acts as a spacer, is inserted between the two electrodes. The electrolyte solution, which contains usually the iodide/triiodide redox couple as a redox mediator, fills the voids within the nanostructuredTiO_2 film, and the space required between the two electrodes to prevent short circuit.[19] The steps for the cell manufacturing are illustrated in the following five sections.

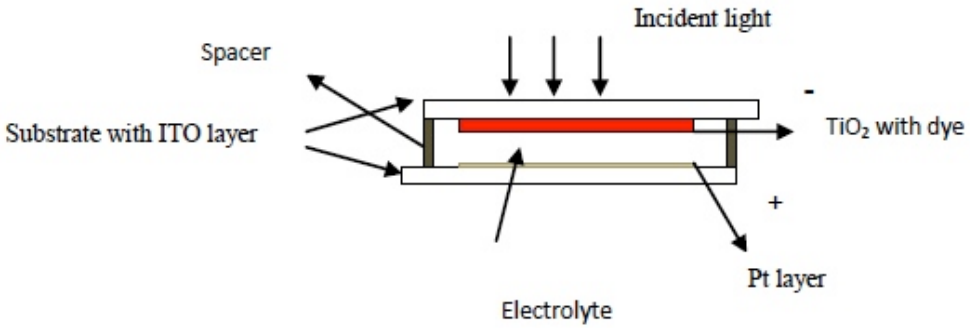

Figure 2.12 Schematic Construction of DSSC

2.4.1. Preparation of the TiO_2 Electrode

There are different methods to prepare the nanoparticles of TiO_2. The most effective method is the sol-gel (hydrolysis of aqueous $TiCl_4$, hydrolysis of titanium tetraisopropoxide in the presence of nitric acid); this is the method used to obtain particles of a desired size. The

hydrolysis and condensation kinetics must be controlled. The first step of preparing the titanium oxide photoelectrode is to prepare the paste of titanium oxide. Organic binders, surfactants, and porosity controlling agents are added to the suspension to optimize the microstructure of the nanocrystalline coating. If Ti-alkoxides have massive groups such as butoxide, they will hydrolyze slowly, and, as a result, slow condensation rates are achieved. Autoclaving of these sols (heating at 200-250°C for 12 h) allows controlled growth of the primary particles and, to some extent, the crystallinity. During this hydrothermal growth, smaller particles dissolve and blend with larger particles through a process known as 'Ostwald ripening'. After removal of the solvent and addition of a binder, the sol is ready for deposition on the substrate.[6] The usual preparation of TiO_2 colloids follows the successive steps:[1]

1. Precipitation by hydrolysis of Ti alkoxides using 0.1 M HNO_3
2. Peptization by heating at 80 ^oC for 8 h, followed by filtering
3. Hydrothermal growth by autoclaving at 200^o to 250^{o}C for 12 h
4. Sonication with an ultrasonic bath
5. Concentration with a rotary evaporator

Ti-alkoxide modified with acetic acid or acetyl acetone yields a colloid of a particle size of 5-7 nm with a large surface area of >200 m^2/g. The importance of the peptization is the ability to separate the agglomerates to initial particles. Autoclaving allows those primary particles to grow to 10-25 nm of the TiO_2 colloidal solution. Moreover, the crystallinity of the anatase increases. In order to avoid formation of the rutile, the autoclaving temperature should be from 200^o - 240^{o}C. Sonication is done after autoclaving in order to redisperse the precipitates because sedimentation occurs during the autoclaving. The rotary evaporator is used at 45^{o}C to concentrate the colloid solution so that it can reach the concentration of 11% wt TiO_2. Prior to the deposition, an organic filler such as carbowax is added to the sol in order to control the film porosity. The porosity of the film is important because the electrolyte must penetrate the film effectively to suppress the rate-determining step by diffusion of redox ions into the film. After preparing the paste, the second step is the preparation of the film by the deposition, done by either screen printing or doctor blade techniques on a substrate, which is usually glass. This step is followed by the sintering process at a temperature of 450°C, a temperature required to

allow the formation of low ohmic resistance contacts between particles, which leads to a good electronic percolation. Therefore, the injected electrons can move without being trapped within the layer.[3] The thickness of the film has to be optimized in order to increase the photocurrent and, hence, the efficiency, within a given thickness because a too thick layer will see its electrical resistivity increasing and, as a result, the photovoltage and the fill factor will decrease.[7] Therefore, typical film thicknesses are 5-20μm, with TiO_2 mass 1-4 mg/cm^2, film porosity 50-65%. The diffusion coefficient, D_{eff}, and the life time of the electron are affected by the crystal structure of the particles; the crystal size; surface structure; the interconnection between the particles; and the charge traps density and distribution. These parameters can differ according to the different preparation methods of TiO_2. The following table shows the effect of the previous parameters on the electron diffusion coefficient.[30]

Table 2.2 Electron Diffusion coefficients (D) in porous TiO_2 electrodes having various characteristics[30]

	Structure	**Shape**	**Size (nm)[a]**	**D(x10^{-5} cm^{2}s^{-1})**
S1	A*	Spheric	19	12
S2	A/Amor	Spheric	12	22.2
S2 $TiCl_4$	A/Amor	Spheric	12	2.2
A2	A	Cubic	12	0.3
A2 550	A	Cubic	12	2
A3	A	Rod-like	12/34	4
A4	A	Cubic	11	4.1
P25	A/R	Spheric	21	4
P25 large	A/R	Spheric	21	4
R1	R	Spheric	27	0.1
R1 $TiCl_4$	R	Spheric	27	0.4
R2	R	Rod-like	23/73	0.3

* A: Anatase; Amor: Amorphous; R: Rutile

As can be seen from Table 2.2 the highest diffusion coefficient, by far, was achieved with 19 nm average spherical particle size of crystalline anatase prepared by aqueous $TiCl_4$ solution. The rutile structure shows the lowest electron diffusion coefficient despite the preparation method, the shape of the particles, and their size.[21] The commercial P25 TiO_2, obtained from Nippon Aerogel, with different particle size shows the same diffusion coefficient. It can be observed that the annealing temperature modifies the value of the Diffusion Coefficient, as illustrated for the samples A2 (non annealed and annealed at 550°C), the diffusion coefficient being multiplied by seven. Sintering increases the diffusion coefficient by enlarging the interparticle necking. However, it is worth mentioning that this is opposite to the need for a large surface area that could accept a large amount of dye molecules. For plastic substrates the use of high temperature annealing for increasing the electron diffusion coefficient is obviously prohibited.

2.4.2. Fixation of the Dye

In this process, the dye is adsorbed onto the surface of TiO_2 surface film by anchoring with the carboxylate groups to form bidendate and ester groups, and the thiocyanate groups enhance the absorption of the visible light. The adsorption of the dye is obtained by immersing the TiO_2 electrode into (0.2-0.3 mM) dye solution, and, then the electrode is stored at room temperature for 12-18 h. Lastly, the electrode is washed by alcohol to remove the non-adsorbed dye.[1]

2.4.3. Redox Electrolyte

The most commonly used electrolyte in dye-sensitized solar cells is the iodide /tri-iodide redox couple. The redox electrolyte is responsible for the achievement of the electrical contact between the two electrodes: the TiO_2 photoanode and the counter electrode. It was found that the organic solvents that were used with the iodine electrolyte, such as acetonitrile, propionitrile, and methoxypropionitrile, have low viscosity; hence, high ionic conductivity is obtained. In recent studies, using the imidazolium derivatives decreases the resistance of the electrolyte solution.[1]

2.4.4. Counter Electrode

Fabrication of the counter electrode is considered one of the most important steps as the Fill Factor (FF) of the solar cell is influenced by the properties of the counter electrode. The counter electrode is fabricated from FTO-coated glass, but it should have higher electrocatalytic negativity to catalyze the reduction of the redox electrolyte. Therefore the addition of Pt as a catalyst is important. Platinum (200-nm thickness) is sputtered onto a FTO substrate. Droplets of the H_2PtCl_6 solution are added on the surface of the Pt electrode, which is heated at 350^{o}C for 10 min.[1] This process helps the reduction of metallic Pt, but the process does not work with plastic substrates. Another way to deposit the Pt layer is based on sputtering method, the commonly used method for thin film coating, and adapted to low temperature processing.[14]

2.4.5. Cell Assembly

The dye-coated TiO_2 electrode is covered by a spacer film (polyethylene), 15-30μm thickness, and one or two drops of the electrolyte solution is then added on the surface of the TiO_2 electrode. The counter electrode is placed on the top of the photoanode, and the two electrodes are fixed firmly with binder clips. The fabrication of the dye solar cell with long term stability requires sealing of the cell using a low melting point polymer (Surlyn) after packaging with a resin (EVA).[1]

2.5. Factors Affecting Cell Performance

Many factors contribute to low conversion efficiency. One of them is the poor electrical contact between the TiO_2 layer and the TCO layer, which occurs due to the inefficient preparation of the TiO_2 thin film by colloidal solution where incomplete dispersion and aggregation of particles is obtained. Many solutions have been proposed, such as adding a thin interfacial layer directly to the TCO layer before adding the thick nanocrystalline TiO_2.[31, 32] Another reason may be the insufficient amount of anchoring sites for the dye attachment, which limits dye adsorption. One possible mitigation is to protonate the TiO_2 surface before the dye adsorption step. The anchoring of the dye on the TiO_2 surface does increase cell efficiency. A

UV-treatment can be applied to the TiO_2 thin film to remove organic contaminants. In this method, the high energy of ultraviolet (UV) light directly or via photocatalysis of TiO_2 (UV treatment) gives a clean surface that favors dye adsorption.[33 34 35] Furthermore, the protonation of TiO_2 prior to dye anchoring has been used to improve the photocurrent generation of DSSCs because the protonation modifies TiO_2 surface to attract negatively charged dye molecules and, hence, the generation of the photocurrent. The TiO_2 electrode is immersed in hydrogen chloride (HCl) acid 0.1 M for surface protonation for 2 hrs and then washed with DI water (UV-HCl treatment)[35a]. The adsorption mechanism of the dye can be investigated by attenuated-total-reflection Fourier transform infrared absorption spectroscopy, whereby the dye molecules anchor on the surface of TiO_2 through one or two of their carboxylic groups.

2.5.1. I-V Characteristic Curve

A photovoltaic cell is a device which converts light to electricity. The capability of the photovoltaic device to produce voltage is characterized by the I-V curve under certain conditions. When the cell is short-circuited under illumination, the maximum current of the cell is the short circuit current (Isc), whereas the maximum voltage, i.e. the open circuit voltage (Voc), is obtained at no current flow. An important point on the I-V curve (Figure 2.13) is the point at which the product of the multiplication of the current and the voltage gives the maximum power. Another important parameter of the cell is the fill factor, which can be determined by the following equation

$$FF = \frac{V_{MPP} \bullet I_{MPP}}{V_{oc} I_{sc}} = \frac{P_{\max}}{V_{oc} I_{sc}} \qquad 2.9$$

with:

V max: Voltage at maximum power point

Imax : Current at maximum power point

Pmax or MPP : Maximum power point

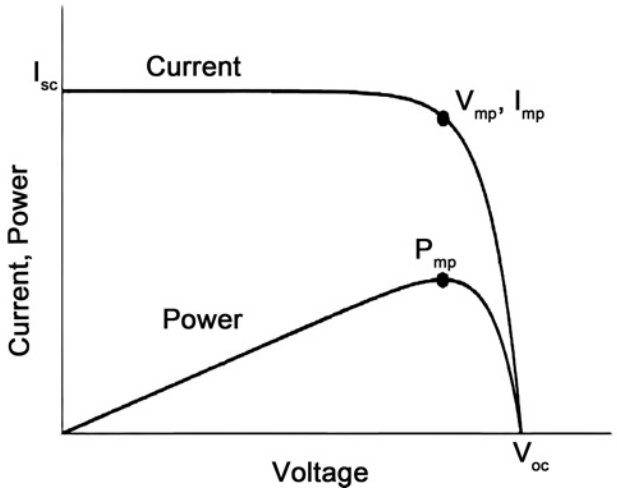

Figure 2.13 I-V Characteristic curve of solar cells.

The J-V equation of the solar cell is as follows

$$V = \frac{nkT}{q}\ln\left(\frac{J_{inj} - J_r}{J_s} - \frac{V + JR_s}{J_s R_{sh}} + 1\right) - JR_s \qquad 2.10$$

with:

V: Voltage

n: diode ideality factor (has a value between 1 and 2)

J: current density

J_{inj}: injected electron current density

R_s: series resistance

R_{sh}: shunt resistance

J_s: saturation current density

J_r: surface recombination current[7]

Note: Photocurrent density:

$$J_{ph} = J_{in} - J_r \qquad 2.11$$

$$J_r = n_{cb} k_{re} [I_3^-]_{22} \qquad 2.12$$

with

n_{cb}: concentration of electron at the surface of the electrode

k_{re} :the rate constant for the reduction of triiodide

2.5.2. Factors Affecting the Photocurrent

The photocurrent can be increased by the following factors:[17]

* High injection rate from the dye to the semiconductor to decrease the possibility of recombination between the semiconductor and the electrolyte.

* Fast removal of the injected electron by the back contact of the electrode to prevent excessive built up of electrons.

* High polarity of the Helmholtz field to reduce the recombination.

* High negative charged hole transport to reduce recombination by electron repulsion.

2.5.3. Factors Affect Photovoltage

The requirements for having maximum photovoltage are conflicting with that for photocurrent. Under dark current condition, the difference between the Fermi level of the semiconductor and the conduction band should be high. Any factor that reduces the recombination will increase the photovoltage. Therefore, optimization of open circuit voltage and the short circuit current is a crucial step. The conduction band of TiO_2 is known to have a Nernstian dependence on pH.

2.6. Cell characterization

2.6.1. Incident-light to Current Efficiency (IPCE)

The cell performance is determined by two factors: incident-light to current conversion efficiency (IPCE) and the overall light to electrical current (η). The IPCE is determined by three efficiencies, which are related to the components of the solar cell: the light harvesting efficiency (LHE), the charge injection (CIE), and the quantum yield of charge collection (CCE). LHE is defined as the ratio of absorbed photons to incident photons.

2.6.2. Light Harvesting Efficiency (LHE)

LHE can be improved by increasing the following:

* The absorption coefficient of dye

* The density of adsorbed dye

* The thickness of dye adsorbed nanoporous electrodes

2.6.3. Charge Injection Efficiency

CIE is determined by several factors:

* Potential difference between the conduction band edge of TiO_2 and lowest unoccupied molecular orbital (LUMO) of the adsorbed dyes

* Acceptor density in TiO_2

* Spatial distance between the surface of TiO_2 and the dye

Figure 2.14 demonstrates the path of the electron transfer inside the nanostructured material TiO_2 and the different types of efficiencies that affect the IPCE.

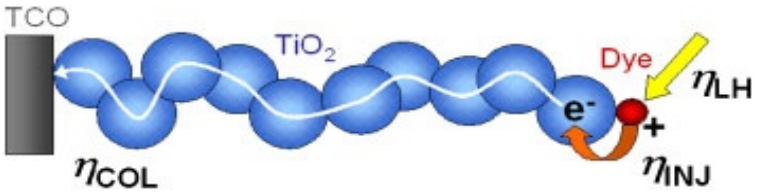

Figure 2.14 The path of the electron transfer inside the nanostructured TiO_2 (reprinted from 16 with permission from John Wiley and Sons)[16]

The rate of electron transfer from the dye into the conduction band of the TiO_2 depends on the surface configuration of the adsorbed dye onto the semiconductor as well as on the energy gab between the LUMO of the dye and the conduction band of the semiconductor. The incident-light to current conversion efficiency can be determined by the following equations [23]:

$$IPCE = \frac{\left[\left(1.25\times10^{3}\right)\times Photocurrent\ \text{density}\left[\mu A/cm^{2}\right]\right]}{\left[\text{wavelength}\,[nm]\times light\ \text{intensity}\left[W/m^{2}\right]\right]} \qquad 2.13$$

$$IPCE(\lambda) = \mathrm{LHE}(\lambda)\,\phi_{inj}\eta_c \qquad 2.14$$

The LHE can be determined by the following equation:

$$LHE = 1 - T = 1 - 10^{-A} = 1 - 10^{-\Gamma^*\sigma} \qquad 2.15$$

Where T is the transmittance, Φ_{inj} is the quantum yield of electron injection, and η_c is the efficiency of collecting electrons at the back contact is the dye coverage cm^{-2}, is the absorption cross section cm^2. The overall light to electrical current efficiency is defined as the power produced by the cell (P_{max}) divided by the incident power (P_{in}) on the representative area of the cell, and it can be obtained by the following equation:

$$\eta = \frac{P_{\max}}{P_{in}} \bullet 100 = J_{sc} \bullet V_{oc} \bullet {ff}/{I_o} \bullet 100 \qquad 2.16$$

with:

J_{sc} Short circuit current

V_{oc} Open circuit voltage

FF fill factor

P_{in} Photon flux ($1000W/m^2$ for AM 1.5)

The efficiency of the photovoltaic cell depends on the temperature and the intensity of the light and its spectral distribution; hence, a standard measurement condition has been developed (light intensity=$1000W/m^2$ or 1 sun, AM 1.5 global standard spectrum, and 25°C the temperature of the cell). This standard measurement facilitates the comparison of testing different solar cells at different laboratories. The output power of the cell under the standard conditions is the nominal power of the cell, W_p. An advantage of dye-sensitized solar cells is that their performance is insensitive to temperature change. For example, increasing the temperature from 20 to 60°C has no effect on conversion efficiency.[17]

2.6.4. Quantum Efficiency

Quantum efficiency is defined as the number of electron-hole pairs that is delivered to the external circuit to the number of photons striking the surface of the cell. It measures the spectral response of photovoltaic cells. Quantum efficiency can be useful in indicating the wavelengths at which the solar cell converts light efficiently.

$$EQE = (1 - R) * IQE \qquad 2.17$$

with:

* EQE : (External Quantum Efficiency)

* IQE: Internal Quantum Efficiency

* R: Reflection of light.

In order to achieve a high collecting efficiency of the charge carriers, an important key parameter which is the diffusion length should be taking into consideration; the diffusion length has to be greater than the thickness of the film. The diffusion length can be obtained from the following equation:

$$L_n = \sqrt{D_e \tau_e} \qquad 2.18$$

Where:

D_e: diffusion coefficient of the electron

τ_e : electron lifetime

2.6.5. Dark Current

The dark I-V measurement has been used to evaluate the electrical performance of photovoltaic cell, such as series resistance, shunt resistance, diode factor, and diode saturation current). In the dark I-V measurement, the the cell is covered to avoid the light generating current. The values of the voltage are predetermined to certain values. An electrical current, generated by the power supply, is forced from the positive contact to the negative contact. The current and voltage are recorded simultaneously. The direction of

the current flow is opposite to the one under light. The shape and the linearity of the measured curve can be used to determine the electrical parameters. At high current level, if the degree of the curvature is to the right, the magnitude of the series resistance is high, whereas at the low current level, a large curvature is an indication for low shunt resistance. The presence of non-ideal carrier recombination is represented by the inflection in the curve near mid current levels.

The recombination between the injected electrons and tri-iodide ions is a result of the dark current in dye-sensitized solar cells. This recombination happens because the incomplete coverage of the substrate (ITO layer) with TiO_2.

2.6.6. Electrochemical Impedance Spectroscopy (EIS)

In order to optimize the process of dye sensitized solar cells, characterization of the cathode plays crucial role to identify the limiting/defective element(s) of the total electrical circuit. The electrochemical impedance spectroscopy was used to study the interfacial properties, internal resistances, and the charge-transfer kinetics of the mesoporous TiO_2 films in DSSCs. Therefore, problems in the performance of contacts, or transport layers, can be detected with IS measurements. During an impedance measurement, the system is (ideally) kept at a fixed steady state by imposing DC voltage (stationary constraints), and the Z(v) is measured by scanning the frequency over several frequency ranges (0.01 Hz-100kHz).[36] The result may be represented graphically using two types of plots: complex plane Nyquist plots(a plot of Z" versus Z'). and Bode plots (a plot of log $|\mathbf{Z}|$ (magnitude) and phase-angle, ϕ, versus log(ω)). In general, the complex impedance may be written for any circuit:

- ***Resistor R in series with (capacitor) C (R-C circuit)***

The impedance is given by:

$$Z(j\omega) = Z' + Z'' = R + \frac{1}{j\omega C} = R - j\frac{1}{\omega C} \qquad 2.19$$

where the real part, Z'=R, the imaginary part, $Z'' = -\frac{1}{\omega C}$, characteristic frequency ω=1/RC which is equal to the inverse of time constant (1/τ). The phase-angle between the imaginary and real impedance equals $\phi \equiv \text{atan}(-1/\omega RC)$, which changes from 90° at low frequency to 0° at high frequency.

- ***Resistor Rs in series with the Parallel combination of R and capacitor C***

The impedance is written as:

$$Z(j\omega) = R_s + \frac{1}{1/R_{ct} + j\omega C_{dl}} \qquad 2.20$$

When the frequency tends to zero, the imaginary part tends to zero and the real part can be expressed by $R_s + R_{ct}$. On the other hand, the real part Z tends to R_s when the frequency $\omega \rightarrow \infty$

When mobile charges are present in a solution, physical processes occur and the total electrode impedance consists of diffusion, bulk generation-recombination effect, adsorption at electrode, and electrochemical reactions taking place on the electrode.[37]

- ***The Equivalent Circuit of the Dye Sensitized Solar Cell***

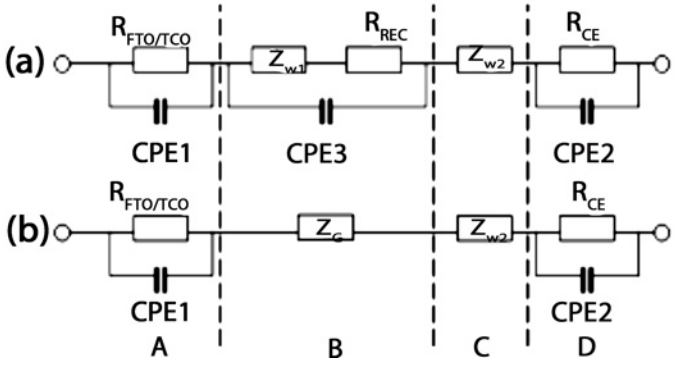

Figure 2.15 Equivalent circuits of DSC. (a) a cell showing quantitative collection of photoinjected electrons; (b) a cell showing incomplete collection of electrons. Bottom line shows the interpretation of the electrical elements of the equivalent circuit. (A) electron transfer at the FTO/TiO_2 interface; (B) electron transport and back reaction at the mesoscopic TiO_2/electrolyte interface; (C) diffusion of I_3^- in the

electrolyte; (D) charge transfer at electrolyte/Pt-FTO interface (Reprinted from 38 with the permission from American Chemical Society)[38]

Figure 2.15 can be used for simplicity to represent the equivalent circuit for modeling the DSSC at different states; either the quantitative collection efficiency of the photoinjected electrons (case (a)) or incomplete collection of electrons (case (b)). These two cases will be explained well hereinafter.

In the general EIS Nyquist diagram, DSC has three semicircles in the whole frequency range. the first semicircle in the high frequency range (frequency of about 10 -100 kHz) at the electrode/ electrolyte interface, refers to the resistance of the electron transfer at the counter electrode (the charge transfer resistance R_{Pt}) where the the reduction of triiodide (I_3^-) to iodide (I^-) occurs. In addition, an interfacial capacitance which is the Helmholtz capacitance C_{Pt}, is present at the same interface. The second semicircle, a larger one in the middle frequency range, represents the resistance about the electron diffusion across the TiO_2/dye/electrolyte interfaces and its recapture by triiodide. The change in the middle frequency range is closely related to the condition of dye-adsorbed TiO_2 surface: if the number of the adsorbed dye molecules increases, the resistive elements decreases.[39] The last semicircle in the low frequency range is related with the resistance about the ion transfer inside the electrolyte (the role of the electrolyte is not only transporting holes between electrodes but also facilitating the movement of electrons inside TiO_2 by the screening effect) which is governed by a finite-Warburg impedance.[36a] Other elements can be found such as the resistance and capacitance of the back layer that are corresponding to the electron recombination and the charge accumulation at the contact between the uncovered part of the substrate with the TiO_2 layer, the resistance Rs of the transparent conducting layer (TCO), and the resistance between the TCO/ TiO_2 interface.[40] There are different electrochemical parameters that can be determined from the impedance analysis:

* the ohmic resistance (R_s) is directly proportional to the sheet resistance of FTO, and it is considered that the resistance element Rs in the high-frequency range > 10^6 Hz is mainly due to the sheet resistance of FTO.

* the charge transfer resistance at the counter electrode (R_1), depends on the roughness factor of the Pt counter electrode.[41, 42]

* the constant phase element (CPE) reflects the interfacial capacitance, charge transfer resistance at the photoelectrode, electrolyte resistance at the Warburg diffusion W_s, minimum angular frequency (ω_{min}), and electron life time for recombination (τ_r).[14, 43, 38, 44] The impedance of the CPE is given by the following equation:

$$Z_{CPE} = T(j\omega)^{-p} \qquad (0 \le p \le 1) \qquad 2.21$$

with T and p frequency-independent parameters.

If p = 1 this will represent a perfect semicircle in the Nyquist plot where the CPE behaving as a capacitor because there is no charge transfer across the solution-electrode boundary.

The constant phase element (CPE) is often used in a model in place of a capacitor to compensate for non homogeneity in the system. When p approaches zero, a depression in the semicircle is observed which is assigned to electrode roughness. Rough or porous surface can cause a double-layer capacitance.[45] This is in contrast to a de levie pore finite length where the pores are non active (infinite polarization resistance) or in another words, the penetration depth of the ac signal is not sufficient to reach the bottom of the pore. However, if the material is thick enough, low frequencies will not fully penetrate the layer and an infinite Warburg effect is created. It is worth mentioning that de levie pore- semi-finite length element describes the impedance of a pore with conductive and reactive pore wall.[46]

Under illumination, new photogenerated electrons are injected into the conduction band of TiO_2, leading to a significant increase in the concentration of the electrons, hence, an increase of the Faraday current and a decrease of the charge transfer resistance R_{ct}.[8] In the dark under forward bias, electrons are injected from the FTO substrate into the conduction band of the TiO_2, and their motion is coupled to that of I^-/I_3^- ions in the electrolyte, leading to a tremendous increase of the R_{ct}. Fraction of the injected electrons reduce the I_3^- ions in the electrolyte.[47]

The frequency response of the electron transfer at the TiO_2/electrolyte interface is expressed by the following equation:[48, 40]

$$z = \left(\frac{R_t R_r}{1 + i\omega / \omega_r}\right)^{1/2} \coth[(\omega_r / \omega_d)^{1/2}(1 + i\omega / \omega_r)^{1/2}] \qquad 2.22$$

$\omega_d = D/L^2$, $\omega_r = 1/\tau$, $R_r = (\omega_d/\omega_r)\, R_t$

with R_t the diffusion or electron transport resistance in TiO_2 and and R_r the charge transfer resistance related to recombination, ω and ω_r are the corresponding characteristic frequencies, and L, D, τ the film thickness, electron diffusion coefficient, and electron lifetime, respectively. The shapes of the spectra are regulated by the factor relating the characteristic frequencies ω_r, recombination frequency, and ω_d diffusion frequency, so we can classify equation 2.21 as in the following cases:

* If $R_r > R_t$, this means that most injected electrons reach FTO without recombination. In this case Eq. (1) becomes:

$$z = \frac{1}{3} R_t + \frac{R_r}{1 + i\omega / \omega_r} \qquad 2.24$$

This is the case for efficient solar cells at a moderate forward bias[40], where two features can be seen in the spectrum: (i) at low frequency ($\omega << \omega_d$), a recombination arc appears which can be represented in the equivalent circuit as a parallel combination of a R_r and C_μ.; (ii) at high frequency ($\omega >> \omega_d$), the impedance spectrum on the Nyquist plot shows a short straight line with a slope close to 1 due to diffusion, and in the low frequency, the spectrum represents a large semicircle attributed to recombination. Bisquert and Wang have modeled the electron transport and recombination in the TiO_2 electrode.[49, 38] If [transport resistance R_t] < [recombination reaction R_r], the equivalent circuit is represented by Rr in series with a Warburg impedance and both in parallel with CPE.

From equation 2.22 , $\omega_{max} = 1/\tau$ and the dc series resistance $R_{dc} = \frac{1}{3} R_t + R_r$

* If $R_t >> R_r$, the equivalent circuit can be modeled by a single Gerischer impedance element.

When $R_r < R_t$, a strong recombination occurs in which many injected electrons are consumed by the reaction with I^-_3 before they reach FTO. A single Gerischer impedance element describes the diffusion of the electron in the TiO_2 film and their recapture by the triiodide ions in the electrolyte by the following equation:

$$Z = \left(\frac{R_t R_r}{1 + i\omega / \omega_r}\right)^{1/2} \qquad 2.25$$

The low frequency resistance is $R_t/3$. This is an important feature, since the electronic conductivity of the semiconductor layer can be directly extracted from R_t. For the opposite, The characteristic transport frequency, ω_d, is the reciprocal of the transit time through the layer of thickness, L :

$$\omega_d = \frac{D_o}{L^2} = \frac{1}{R_t C_\mu} = \frac{1}{\tau_n} \qquad 2.26$$

$$\tau_{r(TiO2/electrolyte)} = \frac{1}{\omega_{\min}} = \frac{1}{2\pi f_{\max}} \qquad 2.27$$

The electron diffusion length (L_n) is determined by the electron diffusion coefficient and the electron lifetime. Obviously, as the electron lifetime increases, the diffusion length becomes longer. The following equation reveals the relationship between the diffusion length and the electron lifetime:

$$L_n = \sqrt{D_n \tau}$$

$$D_n = \frac{L^2}{(R_t C_\mu)}$$

The total series resistance is given by

$$Rs_{total} = R_s + R_{pt} + \frac{1}{3} R_t + R_r$$

2.7. New Attempts for Manufacturing Dye-Sensitized Solar Cells

Many attempts have been made to prepare low-temperature TiO_2 film. We must consider several factors to obtain an efficient non-sintering electrode. For example, the physical and chemical bindings between particles are important to insure that electrons injected anywhere in the TiO_2 film can be collected at the underlying conductive substrate. This binding is better achieved by chemical means rather than high temperature sintering. In addition, the optimization of the film porosity can be achieved by building a porous hierarchical structure controlled by adding large aggregates.

Pichot et al. (2000) prepared TiO_2 film at temperatures <150°C without organic binders. The performance of this film was much lower than that of the high-temperature film because of the low electric interconnection between the particles and the substrate.[50]

Lindström et al. (2001) investigated a new method for manufacturing DSSCs by pressing a nanostructured porous layer of a semiconductor material at room temperature onto a conducting glass or plastic substrate. The overall efficiency was 5.2% at 0.1 Sun.[51]

Park et al. (2005) suggest that using ammonia with titanium oxide colloid lowers the temperature of the sintering and increases the efficiency of the cell to 3.52%. Another successful low-temperature sintering has also been successfully accomplished by applying mechanical compression to the photoelectrode.[52]

D. Zhang et al. (2006) described a new chemical method for the preparation of nanocrystalline photoelectrodes, a method considered a breakthrough in dye-solar cells. The authors came up with a solution for avoiding the high-temperature treatment of the photoelectrodes and for synthesizing a room-temperature titanium oxide film.[5] A mixture of titanium oxide dissolved in an ethanol solvent and titanium tetraisopropoxide ($Ti(OPr)_4$), which acts as a glue, improved the interconnection between the titania nanoparticles. Controlled amount of titanium oxide to titanium isopropoxide was added in order to obtain a good interparticle connectivity (Figure 2.16). This improvement in connectivity was confirmed by TEM analysis (Figure 2.17).

Moreover, the authors asserted that preheating the titanium oxide nanoparticles at higher temperatures and treating the titanium oxide film with the UV-ozone technique were ways to obtain a higher solar cell efficiency. Figure 2.18 illustrates the effect of the UV-Ozone treatment. This efficiency reaches 3.27% and 4% for plastic and glass substrates, respectively. Their explanation was that nanoparticles preheating removes water and carbon compounds formed during the titanium oxide preparation process; hence, increases the dye loading, whereas UV-ozone treatment removes the organic contaminants resulting from the hydrolysis of the Titanium isopropoxide. These organic contaminants, which act as surface states and recombination centers for electrons, affect the performance of solar cells. Two spectroscopic tests, intensity-modulated photocurrent spectroscopy (IMPS) and intensity-modulated photovoltage spectroscopy (IMVS), were carried out to study the effect of the post-UV-ozone treatment on film performance. These tests reveal the electron transport period in the titanium oxide film by measuring the electron lifetime. The results of these tests show an increase in the lifetime of the electrons.[5]. We used these results in the parameters for material and cell optimization in the current work.

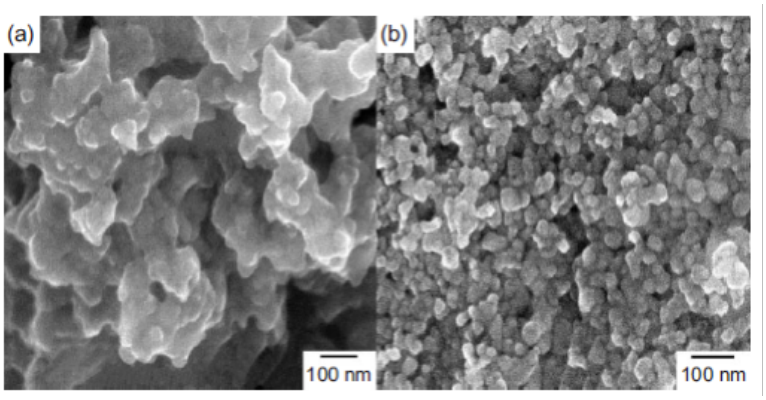

Figure 2.16 SEM images of TiO_2 films prepared at room temperature on ITO/PET with molar ratios TTIP: TiO_2 of a) 0.36 and b) 0.036 (Reprinted from 5 with the permission from John Wiley and Sons) [5]

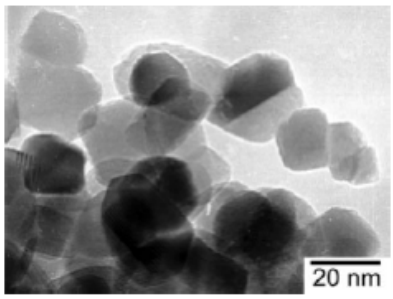

Figure 2.17 TEM image of a porous nanoparticulate TiO_2 film prepared at room temperature on ITO/PET (Reprinted from 5 with the permission from John Wiley and Sons)[5]

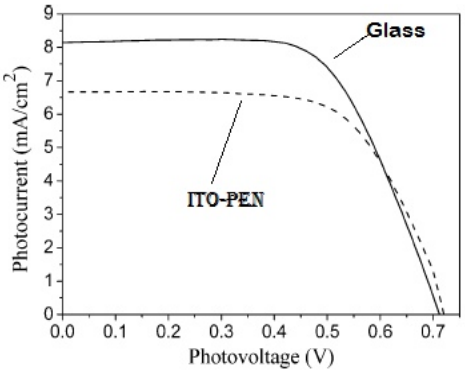

Figure 2.18 I–V curves of dye-sensitized TiO_2 films prepared at room temperature on FTO/glass (solid line) and ITO/PET (dashed line) after pre-heating of the TiO_2 nanoparticles and UV–ozone-treatment of the films (Reprinted from 5 with the permission from John Wiley and Sons)[5]

Zhang and Cao, in 2010, classified different nano structured photoelectrodes for dye sensitized solar cells and summarized their effects on cell performance.[53] Four nanostructures were described:

* Nano particles that offer high specific surface area for dye adsorption;

* Core-shell with the concept of forming a coating layer to decrease the possibility of charge recombination;

* One dimensional structures (nanowires and nanorod) that provide direct and fast pathway for electron transport;

* Three-dimensioned- nanostructure (branched nanowire or nanotube and oxide aggregates). The three-dimension structure has a bi-function that provides a large surface area, and enables more light scattering, thus providing high harvesting efficiency. These oxide aggregates are potential structure. This is illustrated in Figure 2.19, that shows how the electrolyte diffuse through the internal and the external pores.

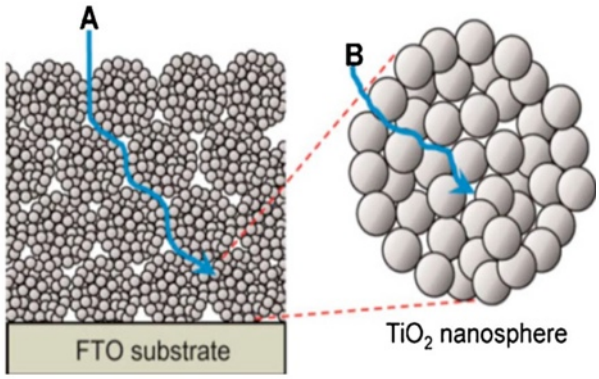

Figure 2.19 schematic diagram showing the electrolyte diffusion through the external (A) and internal (B) pores in the film made of nanoporous TiO_2 spheres. (Reprinted from 53 with permission from Elsevier)[53]

2.8. Synthesis of Monolithic Materials (TiO_2)

2.8.1. Sol-Gel Methods

The fabrication of bimodal porous nanocrystalline TiO_2 monoliths has been recently developed. The most recent method to obtain macro-mesoporous structures of TiO_2 is a template free sol-gel process accompanied by phase separation.[54] One application of this process is to use monolithic TiO_2 as a separation medium for high-performance liquid chromatography (HPLC) , because it was demonstrated that HPLC columns filled with porous monoliths instead of packed particles exhibited better properties.[55] The sol-gel technique has been known for a long time and is considered one of the most successful methods for preparing metal oxide monoliths at room temperature. The sol-gel process can be divided into the following steps:

1- Hydrolysis

2- Polycondensation

3- Aging

4- Drying

5- Calcination

The basic steps are the hydrolysis and polycondensation, both of which happen simultaneously. The reaction rate depends on the factors that contribute in the reaction such as pH, type of precursor, temperature, and ionic strength. The first step, hydrolysis of the alkoxy group, occurs as a result of the nucleophilic attack of the oxygen contained in water on the alkoxy group, followed by proton transfer. Reaction 1 represents the hydrolysis reaction. The second step is polycondensation, where by the metal hydroxide reacts either with metal alkoxide, as shown by reaction 2, or with another metal hydroxide, as shown in reaction 3. [56]

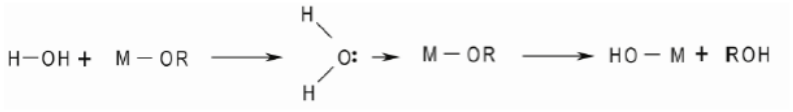

(1)

hydrolysis

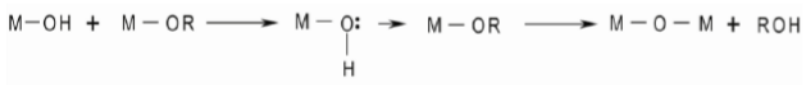

(2)

alcoxolation

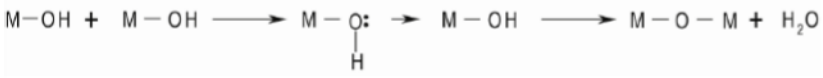

(3)

oxolation

2.8.2. Sol-Gel Method Accompanied by Phase Separation

Fabrication of monolithic materials with a bimodal pore structure via the phase separation route in alkoxy systems has been used for the preparation of macroporous silica, not for TiO_2. The problem related to the preparation of multiscale porous TiO_2 monoliths in alkoxy systems is that the reactivity of alkoxides is high; hence, reaction control is difficult during hydrolysis and polycondensation. Fujita et al. improved a method of preparing monolithic TiO_2 with controlled porosity, using a free template sol-gel process parallel to phase separation. Figure 2.20 depicts the coarsening of phase-separated domains. [54]

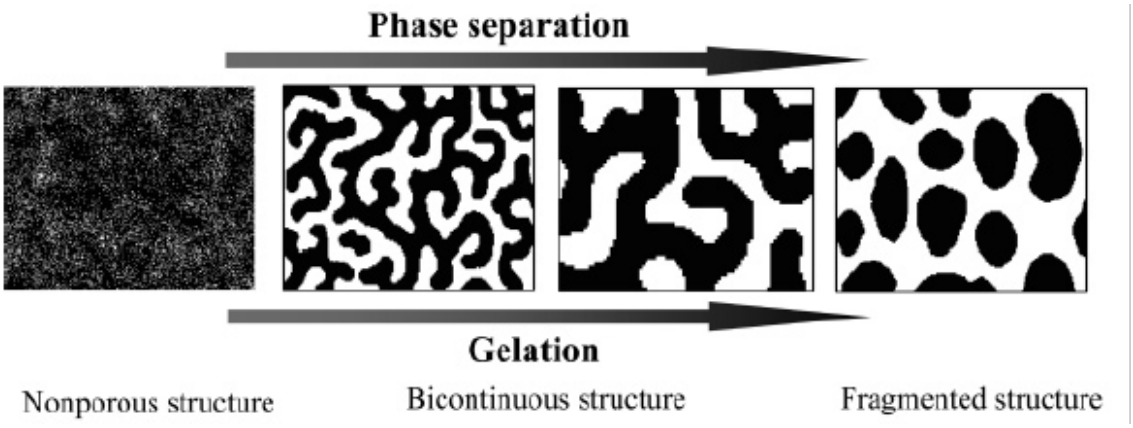

Figure 2.20 Schematic illustration of coarsening of phase-separated domains (Reprinted from 54 with permission from American Chemical Society).[54]

2.8.2.1. Spinodal Decomposition

Spinodal decomposition is observed in a variety of materials, from metals to liquids. The transition of a solid or liquid solution occurs by diffusion up against a concentration gradient (uphill diffusion) initiated by the spontaneous growth of local sinusoidal concentration fluctuations. This growth occurs uniformly throughout the material, not just at discrete nucleation sites without a thermodynamic barrier. In between the spinodal and coexistence curve, free energy barrier arises that is overcome by the nucleus of the new phase (nucleation) forming, leading to formation of a uniform-sized, periodic fine microstructure.

2.8.2.2. Thermodynamics of a Temperature- Induced Phase Separation

If we have a mixture of two phases, a phase diagram can provide information about the composition and temperature of the two phases under different conditions (Figure 2.21). Above a certain temperature (the critical temperature, Tc), the two phases form a homogenous solution at all compositions (Figure 2.21a). If we lower the temperature, the system is not stable and coexisting phases appear where there is a miscibility gap separated from the homogenous solution by the binodal curve or the coexistence curve.[57] When the system is exposed to large fluctuation by dropping the temperature from Ti to Tf, then the existing mixture will consist of solid and liquid phases, with A-rich and B-rich regions. The tie line cuts the phase boundary and the spinodal curve at Tf at points (1,2) and (3,4), respectively. In the region between the

coexistence curve and the spinodal curve, the liquid crystallizes by a nucleation mechanism and then continues to grow (point 5 on the curve), whereas in the region of the spinodal curve, the liquid is unstable and solidifies according to spinodal decomposition, no need to cross the energy barrier to form nuclei (point 6 on the curve).[58, 59]

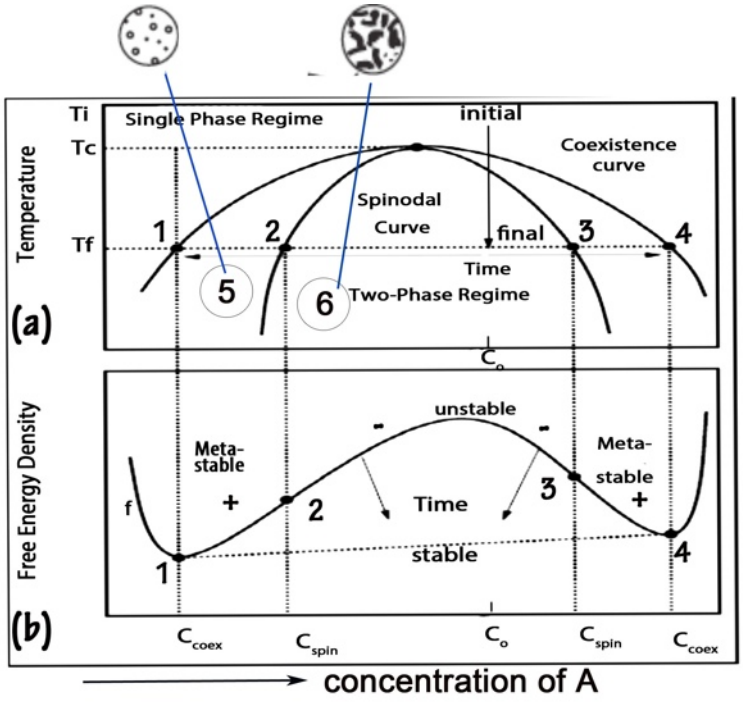

Figure 2.21 (a) The demixing area and (b) the Gibbs energy curve for a binary mixture. Spinodal decomposition takes place in the thermodynamic unstable region. Above the coexistence curve, the system is in a homogeneous or disordered state. Below the coexistence curve, the system is in a phase-separated state, characterized by A-rich and B-rich regions. The homogeneous system is metastable between the coexistence and spinodal curves and unstable below the spinodal lines.[57, 61](modified from 61)

The Gibbs free energy of a mixture is given by:

$$\Delta G_{mix} = \Delta H_{mix} - T\Delta S_{mix}$$

ΔG_{mix}:Free energy of mixing

ΔS_{mix}: Entropy of mixing

* In the stability region, the Gibbs free energy is negative and the second derivative is positive. In addition, the two components are completely miscible.

$\Delta G_{mix} < 0$ and $\frac{d^2 \Delta G_{mix}}{dX^2} > 0$

* For the unstable region, the Gibbs free energy of mixing is positive and the second derivative is negative

$\Delta G_{mix} > 0$ and $\frac{d^2 \Delta G_{mix}}{dX^2} < 0$

Any composition in the unstable region will spontaneously demix. For the composition in the spinodal region, the Gibbs free energy has reached maximum and the second derivative is zero. In the binodal region, the Gibbs free energy has reached a minimum and the first derivative is zero.

$$\frac{d\ \Delta G_{mix}}{dX} = 0$$

Any composition in the metastable region, which is between the binodal (coexistence) and spinodal regions, will be stable, and demixing is achieved by nucleation and growth.[59]

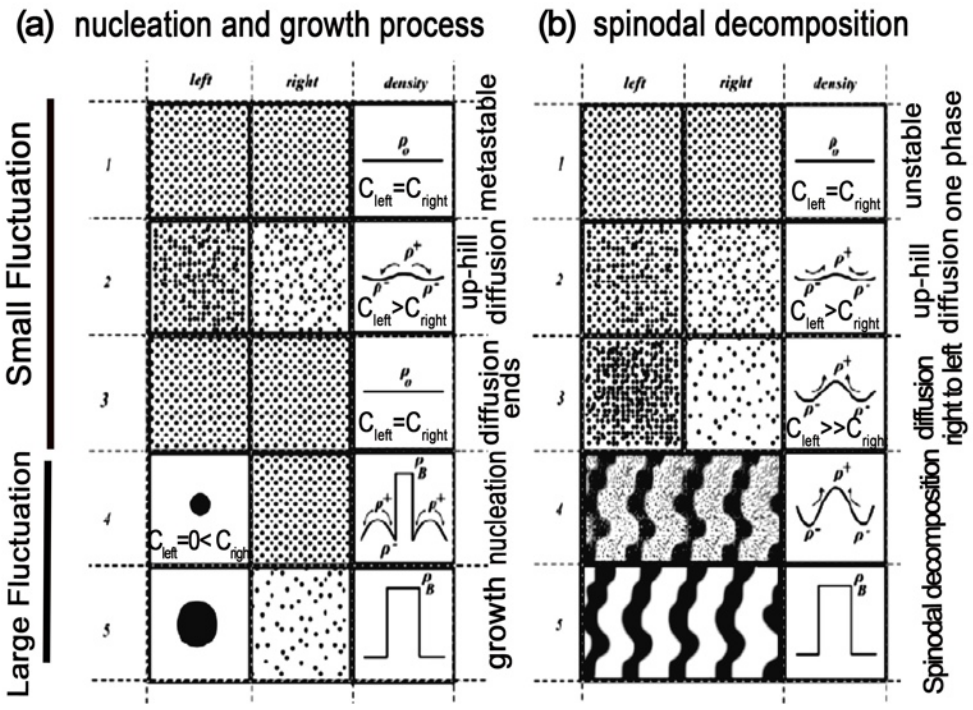

Figure 2.22 a) Nucleation and growth process b) Spinodal decomposition process (modified from 58)[58]

Figure 2.22 shows two different processes: a) nucleation and growth, and b) spinodal decomposition. The rows were divided into five stages: the first three show the effect of small perturbation and the last two show the effect of a large perturbation; we next describe the effect on one of the two components. The left and right columns exhibit two adjacent local regions of component A. In Figure 2.22.a, the first stage displays a metastable region where the concentration of the two components is equal. After small perturbation, the downhill diffusion takes place (from left to right) as the concentration in the left column is larger than the one in the right column ($C_A^{left} > C_A^{right}$) until the system comes back to the initial state where the concentration of left and right sides is equal (row 3). With greater perturbation, nucleation takes place, in which the formation of the critical size of a nucleus starts (row 4). Accordingly, the concentration of A on the left side depletes ($C_A^{right}=0$), so the diffusion takes place but from right to left (downhill diffusion). The Ostwald ripening occurs once some B reaches the left (row 5). Stages 4 and 5 represent the phase separation, which occurs through the nucleation and growth process. The fingerprint of this process is the downhill diffusion.[58]

In Figure 2.22.b, although the solution is in the unstable region, there is no difference in the local concentration between the left and right (row 1). Therefore, no diffusion takes place (one phase), so the density profile is flat. In row 2, the infinitesimal change causes a concentration difference, and the diffusion (downhill) is expected to occur from left, higher concentration, to right localities. Therefore, the density of the system has a wavy profile with maxima and minima that result in a higher increase in the concentration in the left to the right (row 3). The diffusion in this stage takes place from the right, lower concentration, to the left, higher concentration (uphill diffusion) not the opposite as, it can not reach the state where $C_A^{right}=C_A^{left}$, because doing so contradicts with the first stage of instability. The density is large in extent but small in degree. As the diffusion progresses, the density reaches to a point where it equals the density of the pure component (A) (row 3-5). The phase separation in this process is known as spinodal decomposition, which depends on local fluctuations in the concentration of the components. Its fingerprint is the uphill diffusion.[58]

2.9. Commercial DSSCs

Table 2.3 compares the new trends in dye-sensitized solar cells to traditional ones. [14]

Cell component	Traditional technology	New developments
substrate	glass	Plastic(PET, PEN), metal foil
Transparent conductive layer	FTO	ITO
photoanode	Porous TiO_2	Mixed oxides, nanorod or nanotube TiO_2
Counter electrode	pt	Carbon nanotubes, carbon black
dye	N3	Higher extinction coefficient dyes and other organic dyes
Sealing materials	Surlyn, epoxy glue	Lamination in polymer foils
Process technique	High temperature	Low temperature, room temperature

Stability of the dye-sensitized solar cells is an important aspect of their commercialization. The lifetime of dye-sensitized solar cells is determined according to certain degradation mechanisms. Furthermore, it is important to define the criteria for evaluating the stability of solar cells; the parameters that affect their performance should also be defined. Solar cell stability has been evaluated in many studies by aging tests run for 1000 h, such as light soaking tests at 60°C or 80°C at 100mw/cm^2, dark tests at 60°C or 80°C, humidity tests, UV tests, and heat-cycle durability tests.

Commercialization of DSCs has not been viable, unlike thin film silicon cells. Recently, some companies have launched a large production of flexible dye-sensitized solar cells, using a roll-to-roll process. For example, in October, 2009, G24 Innovations, Inc. in Great Britain shipped its first solar modules, which produce 0.5W under direct sunlight to Mascotte. Dyesol, the global leader in DSSC technology, opened a factory in Queanbeyan, Australia, to make tiles that can be integrated into building facades. In May 2010, Dyesol was selected to exhibit a building integrated photovoltaic (BIPV) window based on Dyesol's dye solar cell (DSC) technology in the Smithsonian Institution's Cooper-Hewitt, National Design Museum's Triennial series "Why Design Now?". Figure 2.23 shows some available applications of DSSCs.

Any other significant advances in this field have been limited and attempts at progress are kept under tight security. For example the author's request for details on one chemical concentration of the platisol T(transparent platinum catalyst paint) for Solaronix company was refused on the grounds of security.

Figure 2.23: (left) G24 Innovations DSC bags, (center) First product of G24i: light weight power supply for mobile phones, (right) Building Integrated Photovoltaic (BIPV) Window Based on Dyesol's Dye Solar Cell (DSC) Technology

Chapter 3:
Room temperature synthesis and thermal evolution of porous nanocrystalline TiO_2 anatase*

3.1. Overview

TiO_2 nanoparticles are a major component in many areas, and especially for Dye Sensitized Solar Cells (DSSC) as a result of their electronic structure that allows them to collect the electrons transferred from the dye molecules after sunlight irradiation, as well as of their semi-conducting properties, which provide the surface transport of these electrons up to the collecting electrode. However, for this application or others, the optimization of both structural and electronic properties of titanium oxide is still a challenge, because it depends on both crystalline structure and material nano/mesostructure. We report how small (< 6 nm) titanium oxide nanoparticles were synthesized by a single step method, with the anatase crystalline phase obtained at room temperature, and an open nanostructure. A mixture design method was required to identify the precise composition that led to the suitable material. Mesoporous materials made of pure anatase nanocrystals were obtained with the suitable porosity (5 nm pore diameter, 190 m^2/g, 0.3 mL/g porous volume) without any surfactant agent. Both the evolution of the crystal size and nature of the phases were studied as a function of heating temperatures ranging from 20°C to 800°C. These materials display a good thermal stability up to 400°C, in term of crystal size, and up to 700°C, regarding the crystalline phase. Finally, the study of their semiconducting properties as a function of the crystal size, allowed us to confirm the previous theoretical models regarding the crystal size-dependence of band gap, and to set the limit of the size quantum confinement effect around 7 nm.

3.2. Introduction

Nanocrystalline phases of titanium oxides are required in many domains that use the specific semi-conducting properties of this metal oxide. For example, Dye-Sensitized Solar Cells (DSSCs),[1] have attracted interest since the pioneering work of Grätzel and coll.,[2] and DSSC thin film-based solar cells technologies are currently considered one of the most promising candidates,[3] due to the low cost of raw materials, and potential high conversion efficiency.[1, 4] However, results have been demonstrated only at the laboratory scale, and a lot of development and processing have still to be developed. DSSCs are multifunctional systems where photons are initially collected by dye molecules that host photoconversion.[2c] The electrons generated by the dye molecule are extracted via an oxidation mechanism and injected into the conduction band of a semi-conducting material, named the photoanode, before being transferred to the electrical circuit through a charge migration into a small surface region (1.5 nm) of the photoanode,[5] as a result of a surface charge depletion induced by the surrounding electrolyte.[6] In parallel, the dye molecules are regenerated by reduction with a I_3^-/I^- based electrolyte, itself regenerated by the electrons coming from the external electrical circuit.

One of the most important challenges in DSSC devices is achieving synergy between all cell components, and the nature, morphology and interfacial properties of the photoanode are master keys to achieving high solar conversion efficiency. First, the material must possess a wide bandgap to allow for the electron transfer from the dye molecule and prevent any electron-hole recombination. Secondly, its nanostructure must allow for a high dye loading, and good connectivity for easy electron transport to the current collectors, a requirement that implies the existence of a hierarchical nanostructure.[7] Therefore, TiO_2 is one of the most commonly used photoanodes for DSSC.[8] Among the different crystalline phases of TiO_2 crystalline structures,. anatase has a more opened structure and a larger bandgap (3.2 eV) than rutile (3.0 eV). This wider bandgap not only slows down the electron-hole recombination, but it allows also the material to be transparent to most of the visible light spectrum, a compulsory requirement to the electrode,[2c] even though the porous structure of the electrode will allow it to reduce transparency and improve light scattering within, for a better photon capture by the dye

molecules. Therefore, a specific nanostructure can help to confine the incident photons through reflection and scattering and to increase the optical path length that favors a better absorption by the dye molecules. To date, several groups have developed specific syntheses to achieve an optimized nanostructure to better trap light within the photoanode,[4] including various nanostructures.[9] Since now, many experimental devices use rather large commercial powders.[10] With 85 nm anatase particles as in Degussa™ P-25,[11] a 1.5 nm depletion layer means that only 10% of the particle volume is actually used for the electron migration. With 10 nm particles, it would be 60%, and with 5 nm, 94% of the TiO_2 photoanode would be accessible for the electron migration. Finally, it is assumed that the best way to scale-up the production of these photovoltaic cells will be to use roll-to-roll manufacturing using organic soft substrates, which requires room temperature methods. As a result, a room temperature synthesis of pure anatase TiO_2, with crystallite size that would be small enough to allow the whole volume to be electronically depleted by the electrolyte, is still expected.

In addition to the specific structure, electronic properties are also extremely important for various applications involving TiO_2. Therefore, the ability to finely control the semiconducting properties of titania would help to improve overall, the process efficiency by controlling their semiconducting properties.[9a] It is now well known that the bandgap of semiconductors is modulated by size-induced quantum effects when the crystal size reaches nanometric dimensions,[11-12] as a result of an increase of the bandgap and the resulting blue-shift of the optical absorption.[13] This quantum size effect on titania has been already observed for small particles,[14] thin films,[15] and the prediction of the evolution was calculated for both rutile and anatase.[16] Surprisingly, the band gap structure of nanostructured TiO_2 anatase was reported in some reports, being a direct band gap instead of the indirect band gap of the bulk compound.[17]

We report hereinafter on a new route for the facile preparation at room temperature, of nanostructured titanium oxide made of 4 nm anatase nanoparticles that aggregate and form a mesoporous structure. This method allows for a single-step route that provides both the expected crystalline structure and the correct mesostructure. The fine optimization of the synthesis parameters was explored through mixture design, which we have demonstrated is a very powerful method for analyzing multi-parameter systems.[18] The nature, structure and

electronic features of these materials were explored by UV-vis spectroscopy, SAXS, Temperature-programmed XRD, N_2 isotherm adsorption, and Dynamic Light Scattering, and we took benefit from the large collection of pure anatase samples to explore more deeply the influence of the quantum size-modulation on this band gap of these nanocrystals.

3.3. Experimental Work

3.3.1. Materials

Titanium *n*-propoxide (Ti(O-*n*-Pr)$_4$, Aldrich) was used as the titanium source. Hydrochloric acid (HCl, 37wt%), and Formamide (FA: H_2N-CHO) were purchased from Sigma- Aldrich. All the chemicals were used as received without any further purification.

3.3.2. Synthesis

The preparation of TiO_2 nanoparticles was inspired by a synthesis initially developed by Konishi *et al.*,[19] for room temperature preparation of macroporous anatase monoliths. This method was modified in order to adjust the nucleation/growth mechanism to favor particle nucleation at the expense of crystal framework growth, which allowed us to obtain small crystallized nanoparticles. TiO_2 materials were prepared using different starting compositions defined relatively to the mixture design.

In a typical synthesis, 2.9ml HCl was added drop-by-drop within 5 minutes under vigorous stirring (200 rpm) to 5 mL of Ti(O-*n*-Pr)$_4$ left in an ice bath. 2.86 mL FA and 2.43 mL deionized water were mixed before being added drop-by-drop to the previous solution within 15 min. After full addition, the sample was left for aging in a thermostated bath at 30°C for 24 hours. The solution experienced a phase separation during this aging phase, with a physical gel formed at the bottom and a supernatant liquor on the top. The gel container was sealed with Parafilm™ and left at 60°C for one week before drying. Ammonium chloride, a by-product of the reaction, was removed by washing the sample three times with 100 mL of deionized water, the powder being recovered by filtration afterwards. At this stage, the gel could be easily

dispersed in water by sonication. The samples were finally calcined in air for 4 hours (100°C/h ramp) at different temperatures: 300°C, 400°C, 600°C and 700°C.

3.3.3. Methods

Samples were characterized by SEM, SAXS, Temperature Programmed XRD (TP-XRD), N_2 isotherm adsorption at 77K, and UV-Vis spectroscopy. SEM images were obtained on a Leo 1530 microscope at an EHT of 5 kV with gold-coated samples. TEM images were recorded at 100 kV with a JEOL 1200 XII microscope. SAXS measurements were recorded on an Anton Paar SAXSess system equipped with a 2.2 kW Copper anode (λ=1.54Å) and focusing multilayer optics. Collecting flux was enhanced by linear collimation, collected over a 0 to 40 (2 theta) angular range with a 2D Imaging Plate as detector. Scattering patterns are reported as a function of the wave vector $q=2\pi/d=4\pi\sin(\theta)/\lambda$,where d is the characteristic distance. SAXS patterns were corrected from linear collimation, and background-extracted using SAXSquant© and OptiQuant© as the interfacing programs. TP-XRD was performed with an Inel CPS120 equipped with a FUR1400 high temperature furnace. The sample was left to equilibrate for 20 minutes at the given temperature, before measurement (20 min recording time). The N_2 adsorption isotherms were measured with a Quantachrome AUTOSORB-1. The samples were outgassed at 150°C under vacuum for 12 h before the measurement. Surface area was determined by the BET method in a relative pressure range of 0.05-0.25.[20] Pore size distribution was calculated with the Broekhoff and deBoer Model applied to the desorption branch.[21] The size of the particle suspensions was studied by dynamic light scattering, using a Vasco-2 (Cordouan Technologies). A 60 mW monomode red laser (λ = 658 nm) with variable intensity was used, and measurements were carried out at different temperatures (from 25 to 70°C) with a detector set at 135°. The correlated parameters were adapted for each sample (sampling time x number of channels) to collect the whole autocorrelation curve. Accuracy and reproducibility of the results were checked with several measurements ran with various recording times. The autocorrelation curves were fitted with both a monodisperse cumulant and a polydisperse Padé-Laplace models.[22] UV-vis absorption spectra were collected with a Varian Cary 5000 UV-Vis-NIR spectrophotometer. Quartz cuvettes (Spectrosil, Starna Cells Inc.,

transparency 170-2700 nm) and the 1 cm optical path length were used to measure the electronic absorption spectra. The UV-vis spectra were corrected from non specific absorption before analysis. The band gap E_g was deduced from UV-vis spectra. The correspondence between the energy (in eV) and the wavelength λ (in nm) is given by:

$$E\ (eV) = 1{,}240/\lambda\ (nm) \qquad 3.1$$

As anatase is an indirect bandgap semiconductor with an absorption edge E_g around 3.2 eV, it has been demonstrated that the value of E_g can be obtained by plotting:[2b, 23]

$$(\alpha.h\upsilon)^{1/2} = f(E) \qquad 3.2$$

where α is the absorption coefficient in cm^{-1}, $h\upsilon$ is the photon energy, and h is the Planck constant (h = 41.34 10^{-16} eV.s). E_g is calculated from the extrapolation of a straight line to the abscissa axis, as $E_g = h\upsilon$ when $\alpha.(h\upsilon)=0$.[24]

3.3.4. Mixture Design of Experiments

The experimental design of a mixture is a subclass of the Response Surface Methodology (RSM) which can be used to study the relationships between responses and factors.[25] In another words, to study the effect of dependent variables, which related only to the proportion of the ingredient in the mixture not to the amount of the mixture, on the independent variables. The sum of all the components proportion must equal to 1. The RSM helps to obtain optimal responses for the data collected from the designed experiments by a regression analysis.

A mixture design study was carried out to analyze the influence of starting composition on the final TiO_2 structure after synthesis and after thermal treatment. The compositions of samples were defined within the (Ti(O-*n*-Pr)$_4$:FA:H_2O+HCl) ternary diagram. The lowest and highest level volume fractions were chosen to fit within a restricted domain: 0.3<Ti(O-*n*-Pr)$_4$<0.6; 0.1< FA <0.4; 0.3<HCl+H_2O <0.6 (Figure 3.1.a). Specific data points were selected within this restricted domain (Figure 3.1.b and Table 3.I).

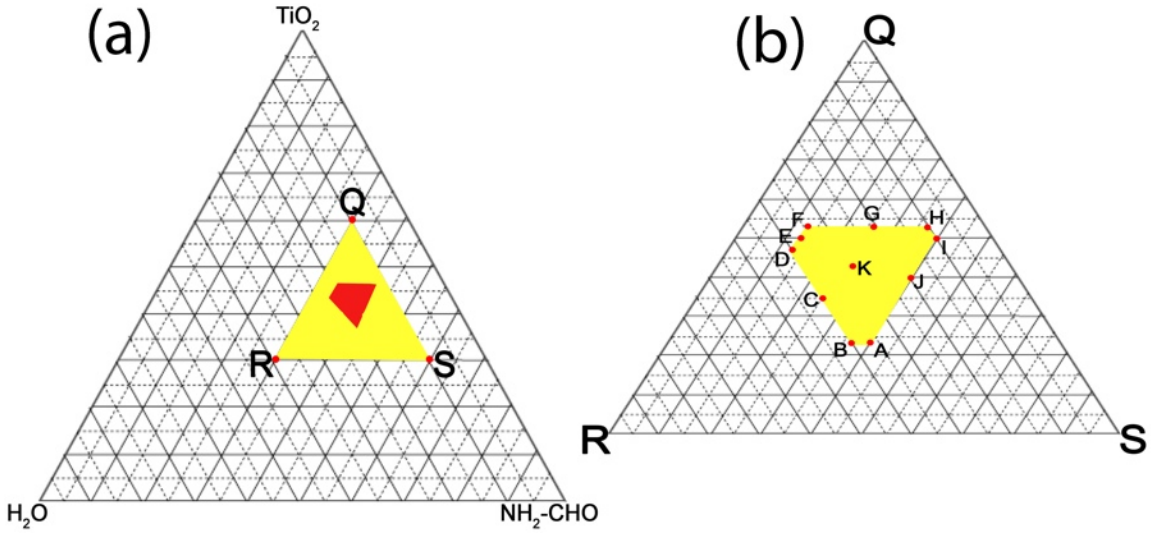

Figure 3.1 a) Q: (TiO_2-rich), R: (H_2O-rich) and S: (FA-rich) b) Data points selected for the experiment design study. For values of points, see Table 3.I.

Table 3.I. Sample composition (mL)

Sample	Ti(O-*n*-Pr)$_4$	HCl	H_2O	FA
A	5.00	2.9	2.45	2.85
B	4.62	2.9	2.20	2.30
C	5.00	2.9	2.60	2.80
D	5.95	2.9	2.60	1.80
E	6.10	2.9	2.45	1.85
F	6.21	2.9	2.30	1.83
G	6.22	2.9	1.85	2.20
H	6.10	2.9	1.40	2.75
I	6.10	2.9	1.40	2.85
J	5.56	2.9	1.91	2.86
K	5.56	2.9	2.05	2.50

The Design-Expert program V.8.0.4 (Stat-Ease Inc.) was used to define the optimum number of experiments according to the limits selected for this study. Significance of the regression model was tested by the "Prob(F)" statistics test, which tests the full model against a model with no variables, and with the estimate of the dependent variable being the mean of the values of the dependent variable. The value of Prob(F) is the probability that the null hypothesis for the full model is true (*i.e*. that all of the regression coefficients are zero). For example, if Prob(F) has a value of 0.01, then there is 1 chance out of 100 that all of the regression parameters are zero. This low value implies that at least some of the regression parameters are nonzero and that the regression equation does have some validity in fitting the data (*i.e*. the independent variables are not purely random with respect to the dependent variable).

3.4. Results and Discussions

3.4.1. Nature and Structure of the TiO_2 Nanocrystals

UV-vis spectra of specific samples selected across the phase diagram are displayed as examples in Figure 3.2 (for all spectra, see Figure 3.3). These spectra exhibit an absorption edge in the 3-to 3.5 eV range, characteristic of titanium oxide. The bandgap E_g was calculated according to eq.(2) (Figure 3.2(inset); Figure 3.4, Table A.I in Appendix A).

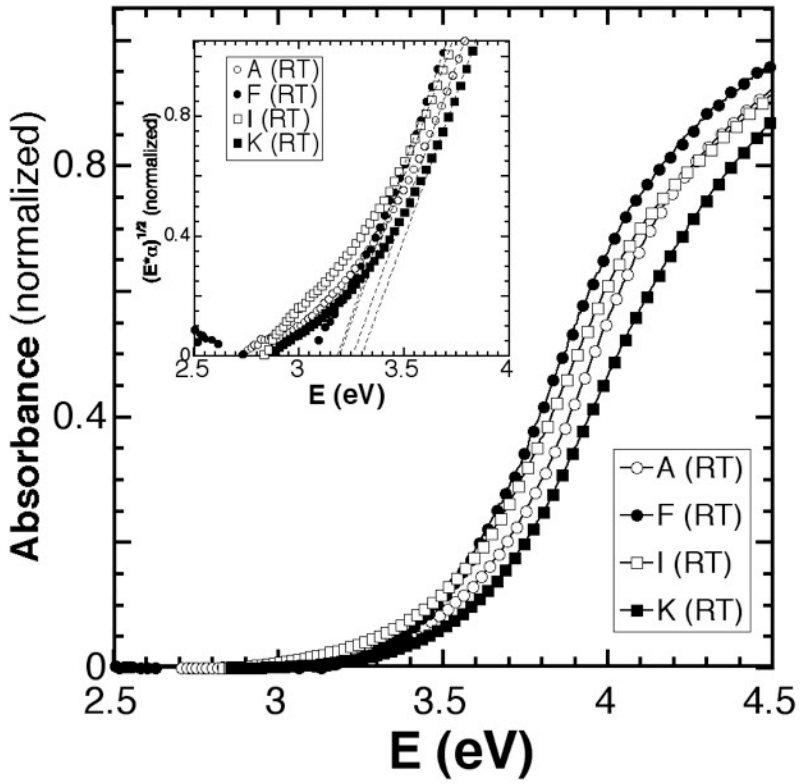

Figure 3.2. Representative UV-vis spectra for samples A, F, I, and K selected at representative locations in the phase diagram. After correction of the baseline, spectra intensity were normalized to ease comparison. inset: Evolution of $(\alpha.E)^{1/2}$ as a function of the energy. The extrapolation of the edge down to $\alpha = 0$ provides the value of the band gap Eg, for indirect band gaps.

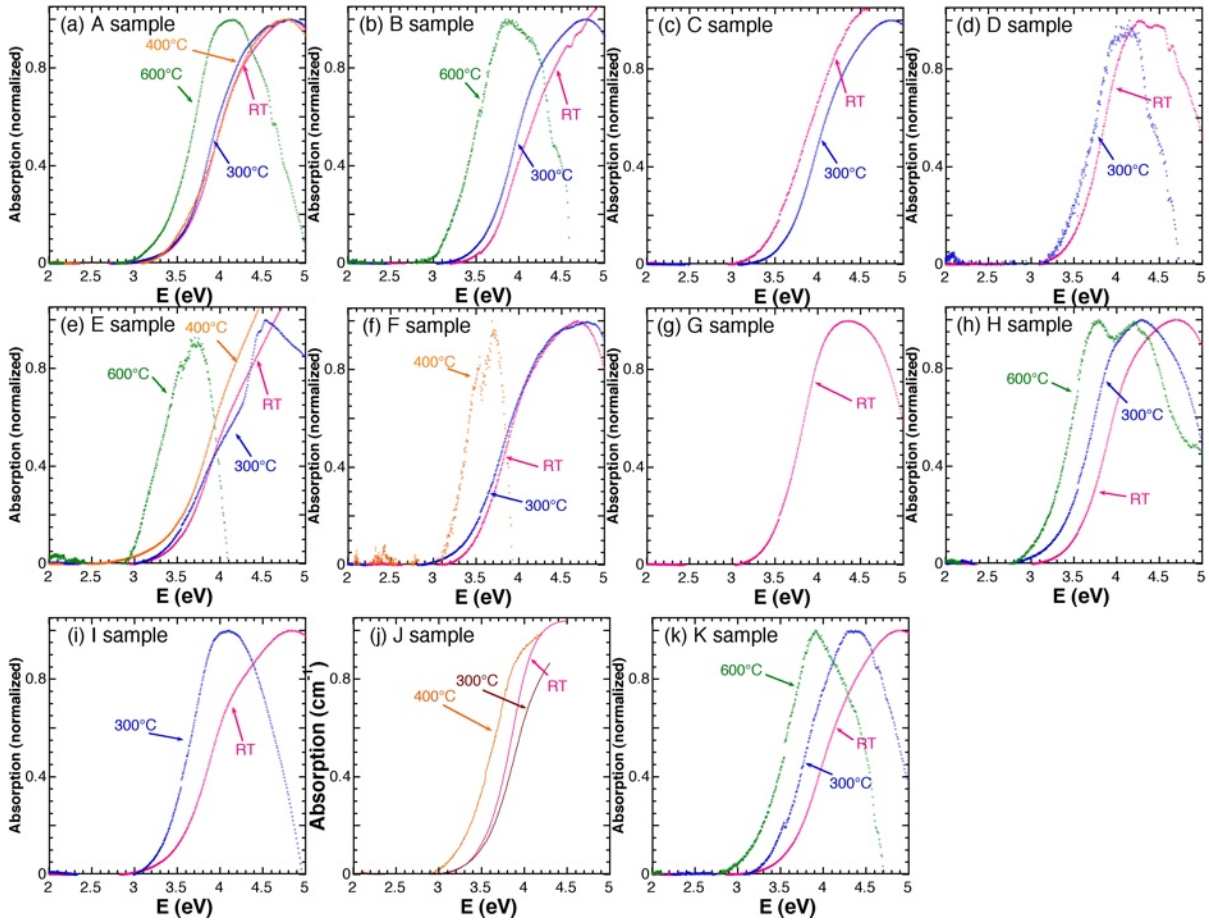

Figure 3.3. UV-vis spectra of samples A (a), E (b), H (c), selected at the corners of the studied phase diagram area, and K (d) at the centre of this area. All spectra have been normalized to facilitate comparison.

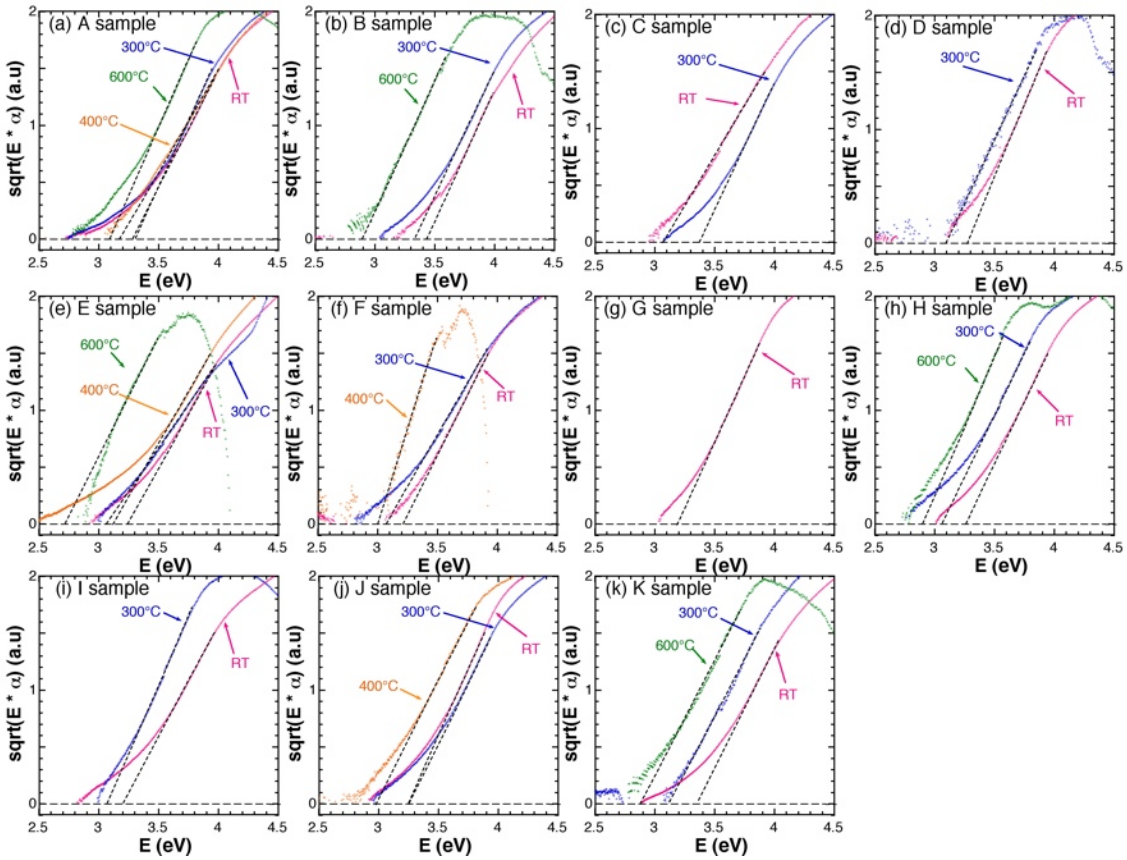

Figure 3.4: Evolution of $(\alpha.E)^{1/2}$ as a function of the energy for all samples treated at different temperatures. The extrapolation of the edge down to α = 0 provides the value of the band gap Eg, for indirect band gaps.

These values were injected into the mixture design model to obtain a response map for the expected value of E_g within the phase diagram area used for this study. This response map is displayed in Figure 3.5 for the as-synthesized samples (see also Figure 3.4). The values of E_g (in eV) compare well with the values observed for anatase, brookite and rutile, which are usually close to 3.2-3.3,[26] 3.4,[23a] and 3.0,[26a] respectively.

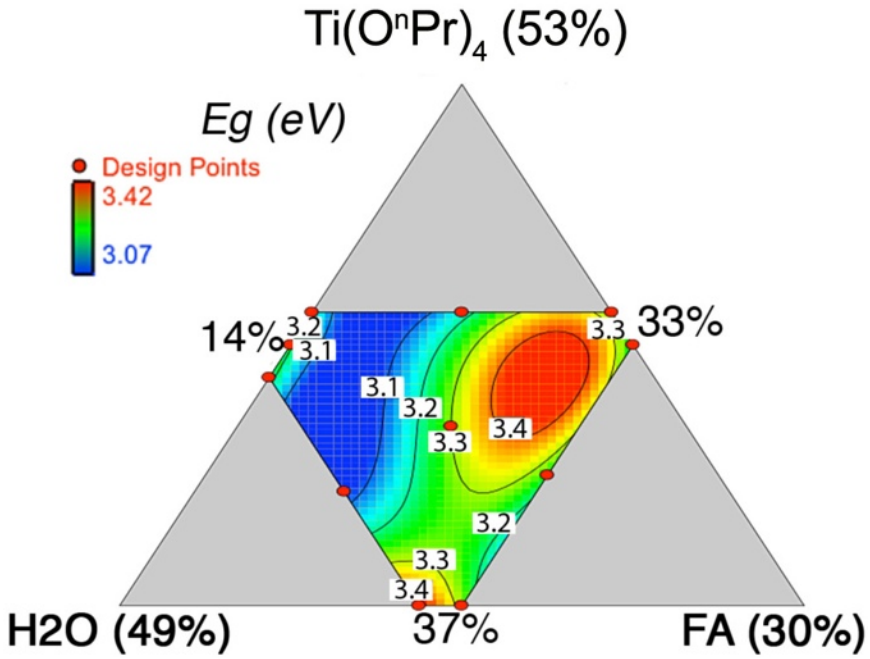

Figure 3.5. Response map for Eg, the band gap calculated with the indirect band gap model, for as-synthesized samples (RT). The % refer to the concentration range of the study, given by the apex (e.g 49% for H_2O) and the opposite side (e.g. 33% for H_2O).

The response map found for the as-synthesized samples fluctuates between 3.1 and 3.4 eV, with a minimum (blue) in the left side of the study area and a maximum (red) close to the right corner. These fluctuations may result from phase transition (anatase to brookite) and/or particle size effect, since a reduction of the crystal size leads to a wider bandgap.[16] It must be mentioned also that sol-gel syntheses of TiO_2 lead to materials with a smaller bandgap that is usually observed for anatase.[24]

The crystallization and phase transformation were investigated in parallel by using both Wide (WAXS) and Small (SAXS) Angle X-ray Scattering. Representative XRD patterns of samples (A, F, I, and K) are reported in Figure 3.6 (All samples are reported in Figure 3.7).

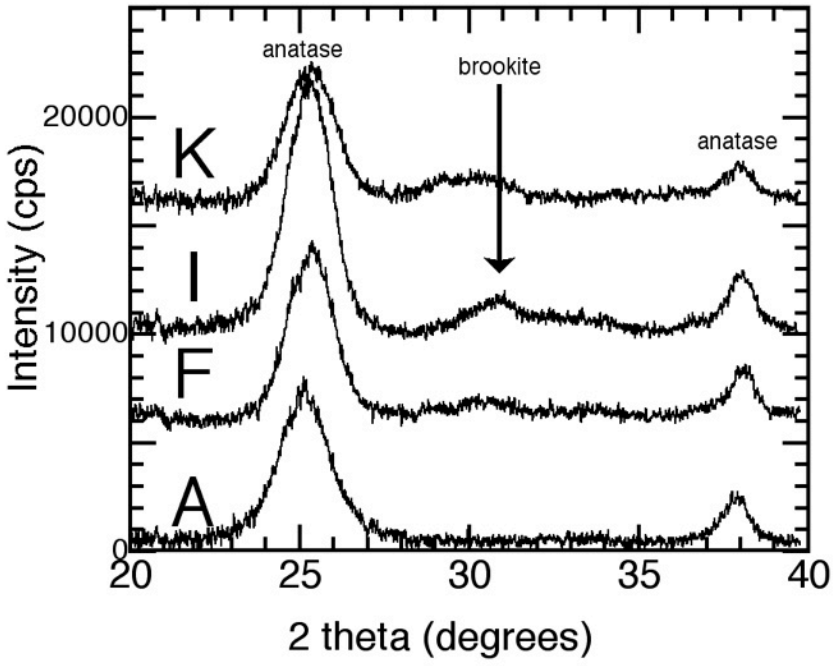

Figure 3.6. Representative X-ray diffraction patterns of samples A, F, I, and K selected at different locations of the phase diagram.

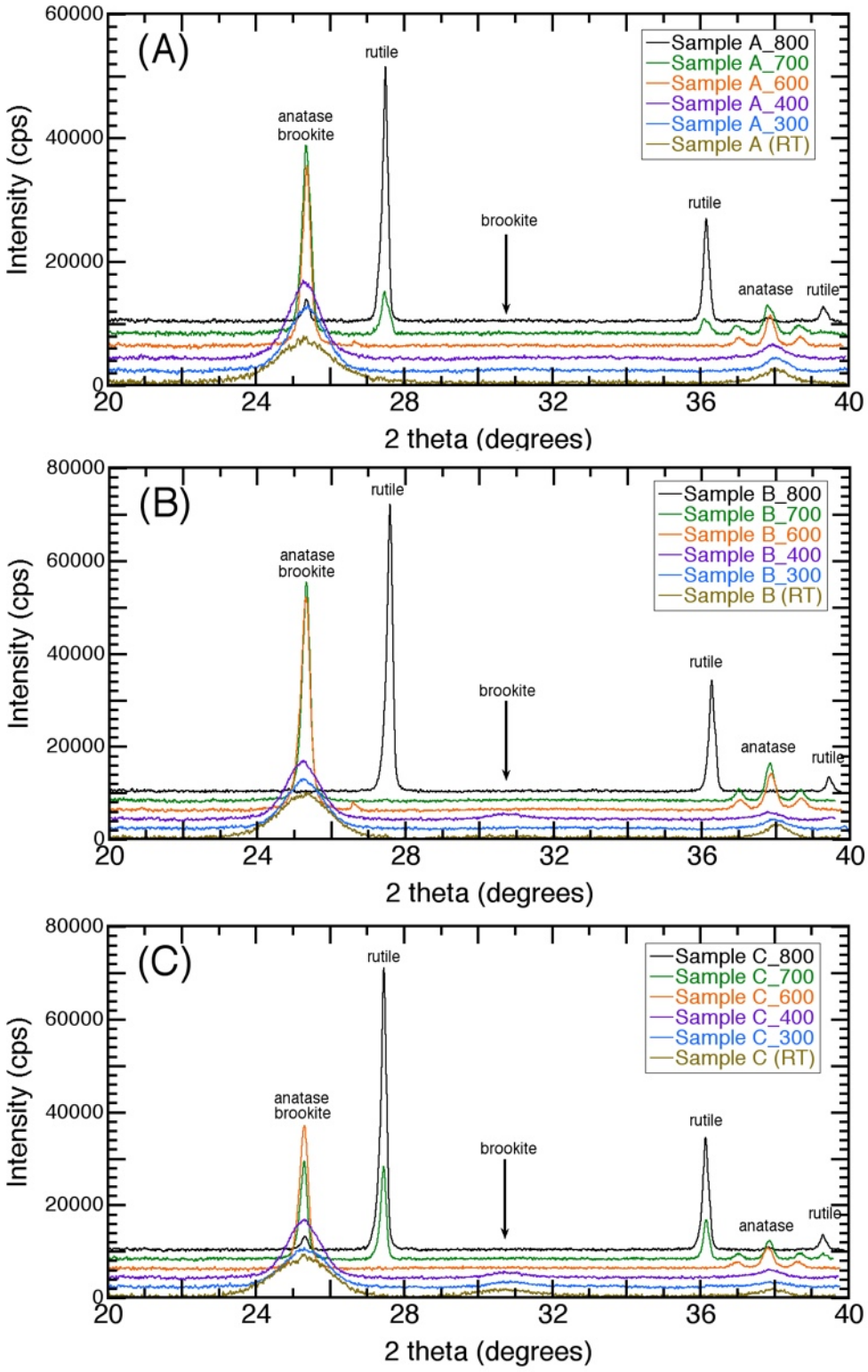

Figure 3.7.a: Evolution of X-ray diffraction pattern for the samples A, B, C, after thermal treatment between 20 and 800°C (to be continued)

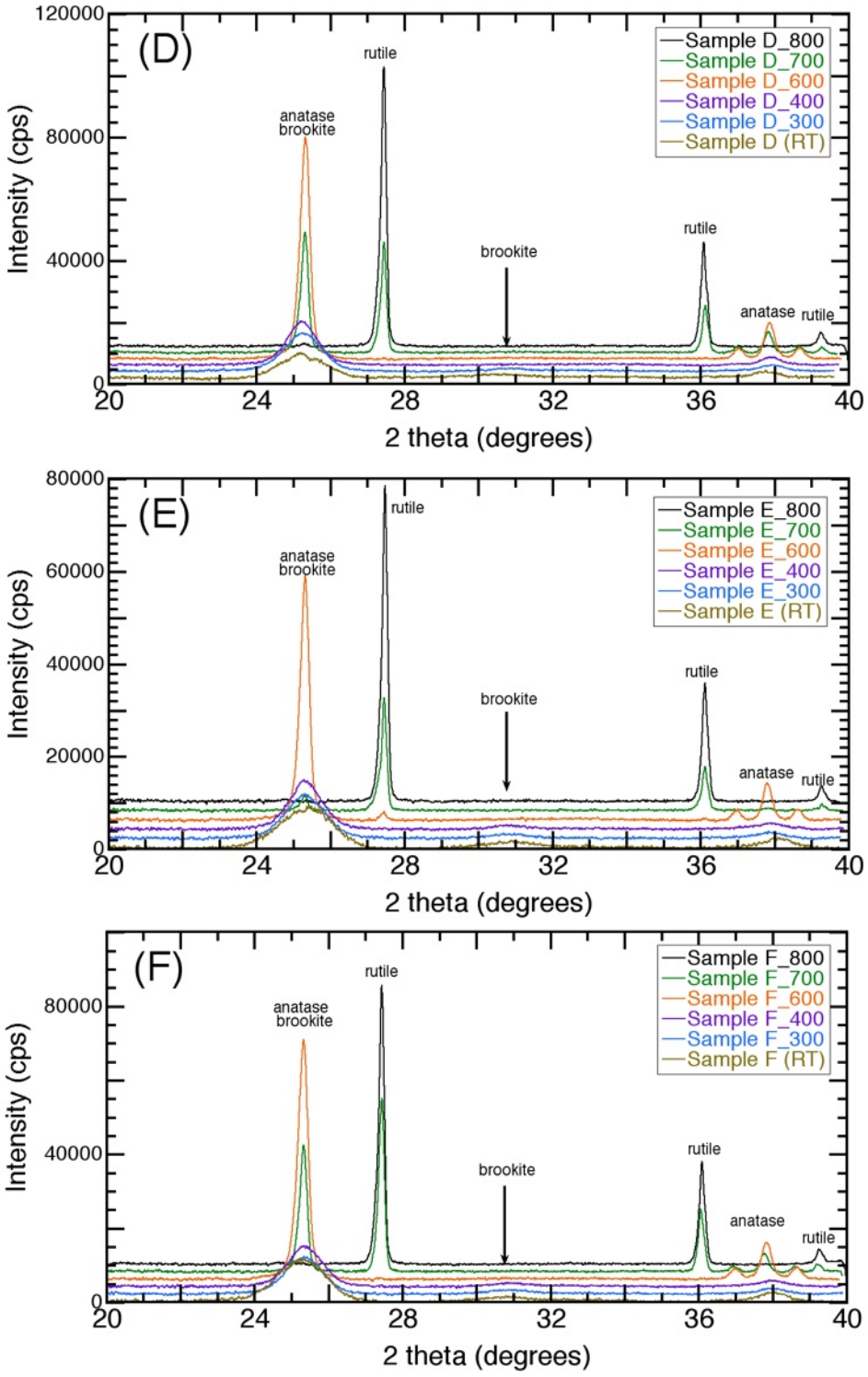

Figure 3.7.b: Evolution of X-ray diffraction pattern for the samples D, E, F, after thermal treatment between 20 and 800°C (to be continued)

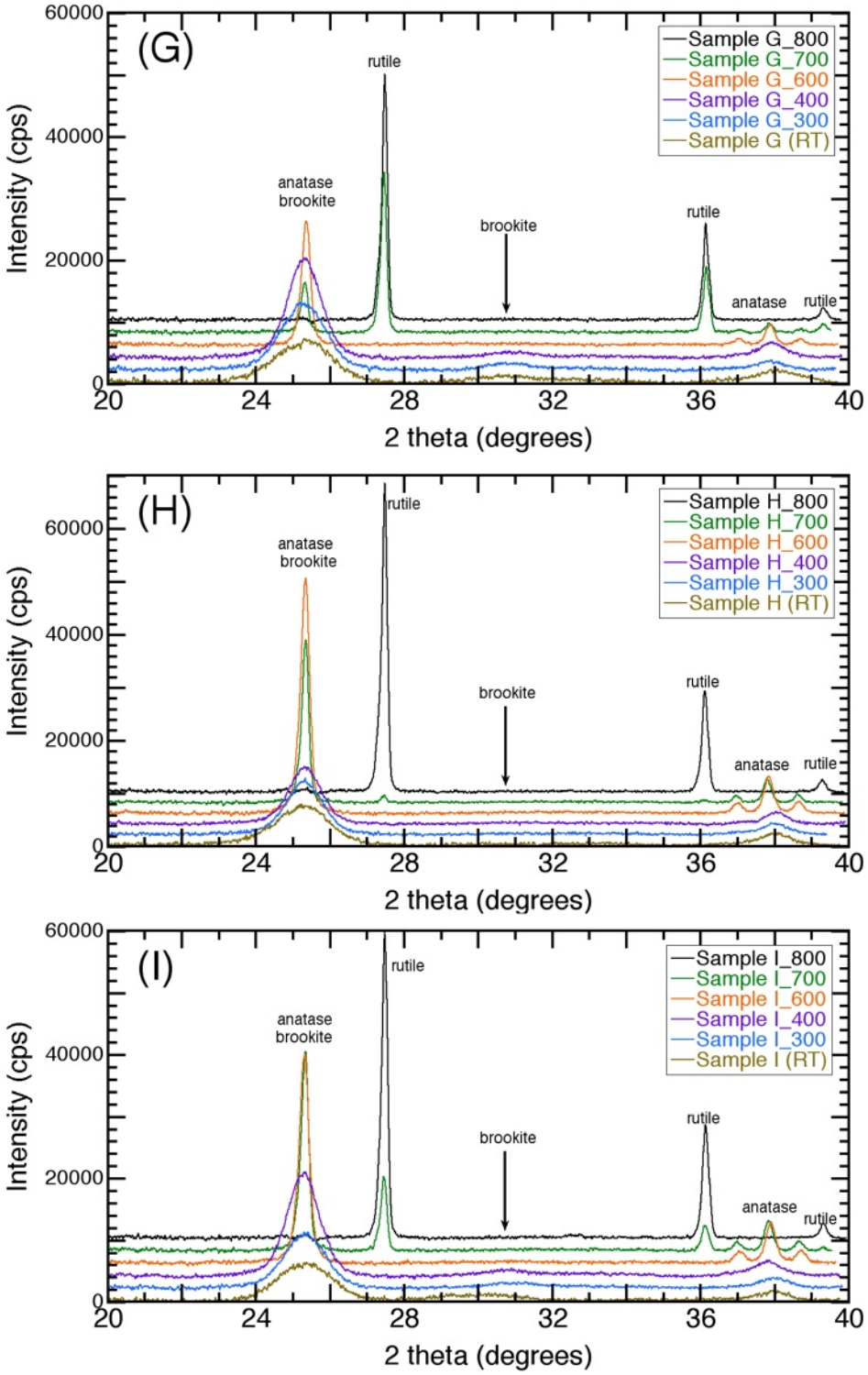

Figure 3.7. c: Evolution of X-ray diffraction pattern for the samples G, H, I, after thermal treatment between 20 and 800°C (to be continued).

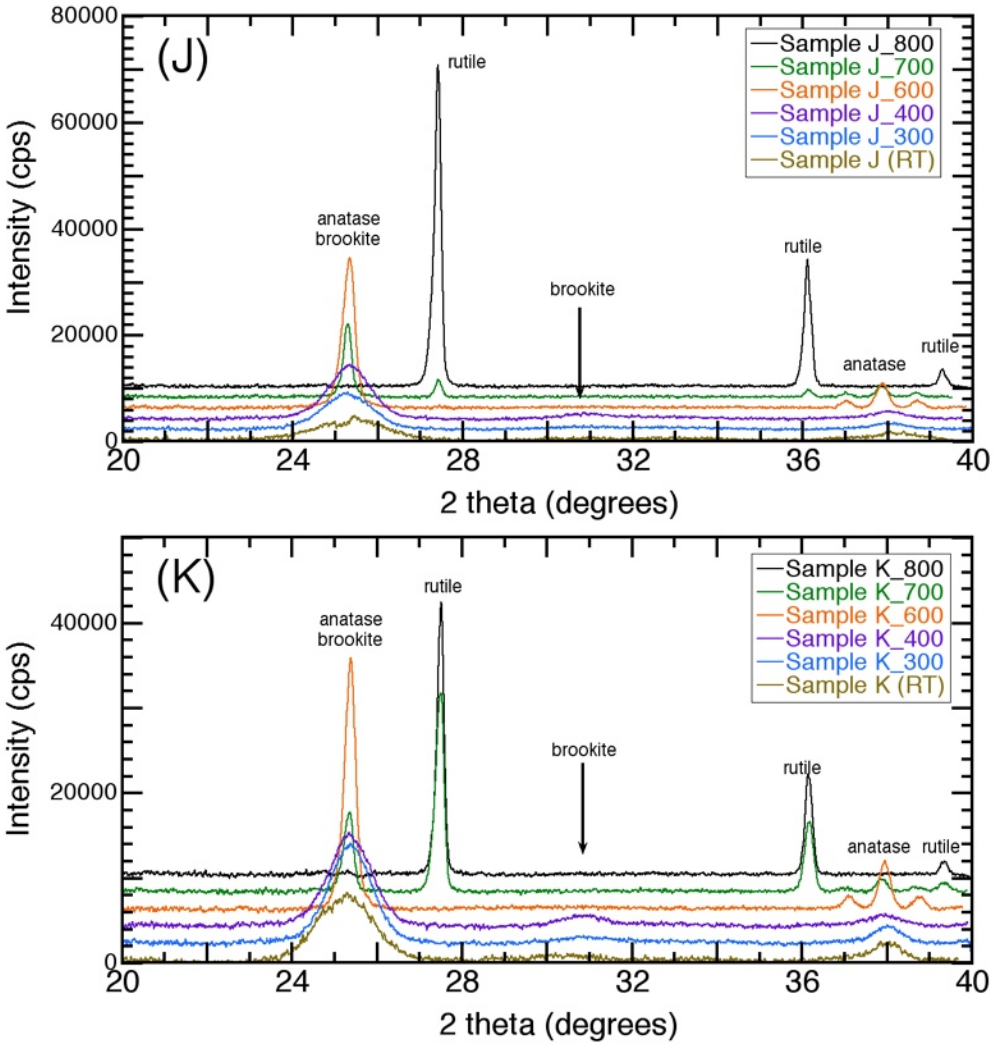

Figure 3.7.d: Evolution of X-ray diffraction pattern for the samples J, K, after thermal thermal treatment between 20 and 800°C.treatment between 20 and 800 thermal treatment between 20 and 800°C.

The existence of the anatase phase is confirmed for all samples. These diffraction patterns exhibit broad diffraction peaks at 25.3 and 37.9 degrees, as a result of small crystalline domains. When the samples are not pure anatase, additional diffraction peaks are observed from the brookite structure, especially a diffraction peak at 30.8 degrees, the other brookite diffraction peaks overlapping with the anatase peak at 25.3 degrees. For example, sample A is clearly made of pure anatase, whereas sample I contains brookite, as seen by the additional diffraction peak at 30 degrees, and a more intense peak at 25 degrees, as the result of overlap

of anatase and brookite diffraction peaks. The nature of the titanium oxide is very important for the intrinsic performance of the DSSC electrode, but many devices use commercial powders made of a mixture of anatase and rutile.[10a] We used the mixture design to plot the distribution map of anatase and brookite within the studied area and identified the anatase-rich domains in the studied phase diagram. The phase content distribution between brookite and anatase (weight fraction) was calculated using the following equation:[27]

$$W_B = (k_B.A_B)/[(k_B.A_B)+(k_A.A_A)] \qquad 3.3$$

where W_B is the weight fraction of brookite, A_A, and A_B are the integrated intensity of anatase (*101*) and brookite *(121*), and k_A = 0.886 and k_B=2.721, two experimental coefficients. The overlap between the (*101*) anatase diffraction peak and both the (*120*) and (*111*) brookite peaks was solved by numerical deconvolution.[27] The broadening of the diffraction peaks was large enough to allow a Gaussian fitting instead of the preferred Pearson VII or Pseudo-Voigt functions,[28] and the intensity of anatase (*101*), and brookite (*121*) were deduced from the respective peak areas. The weight fraction of anatase calculated from eq.(3.3) for all the as-synthesized samples is displayed in Figure 3.8.

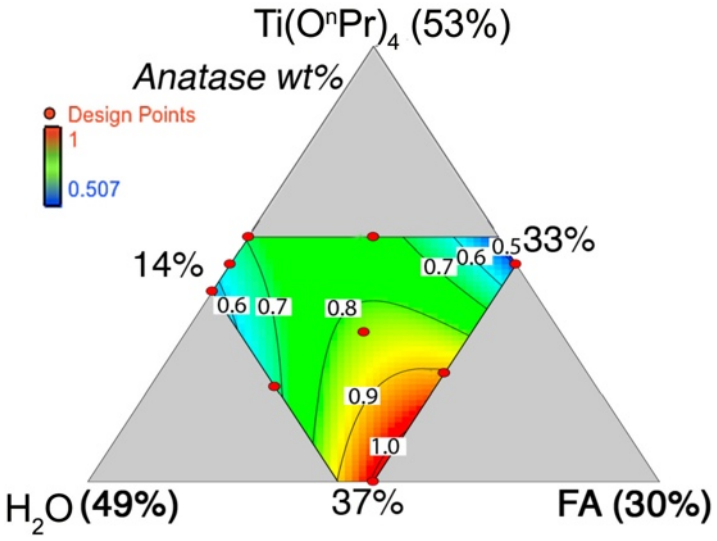

Figure 3.8. Response map for the anatase weight fraction calculated from the respective intensities of the diffraction peaks.

The distribution of the anatase/brookite weight fraction indicates clearly that samples prepared with the lowest proportion of Ti precursors give pure anatase (red area), whereas those with an increased amount of Ti(O-*n*-Pr)$_4$ contain a significant amount of brookite (blue area). However, in the whole domain, the anatase proportion always remains higher and at least equal to 60 wt % of the total material. It appears finally, that the area surrounding sample A is the region where the combination of reagents is optimized to achieve a pure anatase phase.

The evolution of the crystal size was also studied as a function of the initial concentrations and deduced from the broadening of the diffraction peak, using the Scherrer formula:

$$L(nm) = (0.9.\lambda) / (\Delta w.\cos(\Theta)) \qquad 3.4$$

with L the crystal size, λ the X-ray wavelength (0.154 nm), Δw the Full Width at Half Maximum (FWHM) (in radians), and Θ the angular position of the diffraction peak. The crystal size of the anatase phase (Figure 3.9) was calculated from the 25.3 degree diffraction peak, with the brookite contribution being removed, when required. The crystal size of the brookite phase was deduced from the 31.0 degree diffraction peak (Figure 3.10).

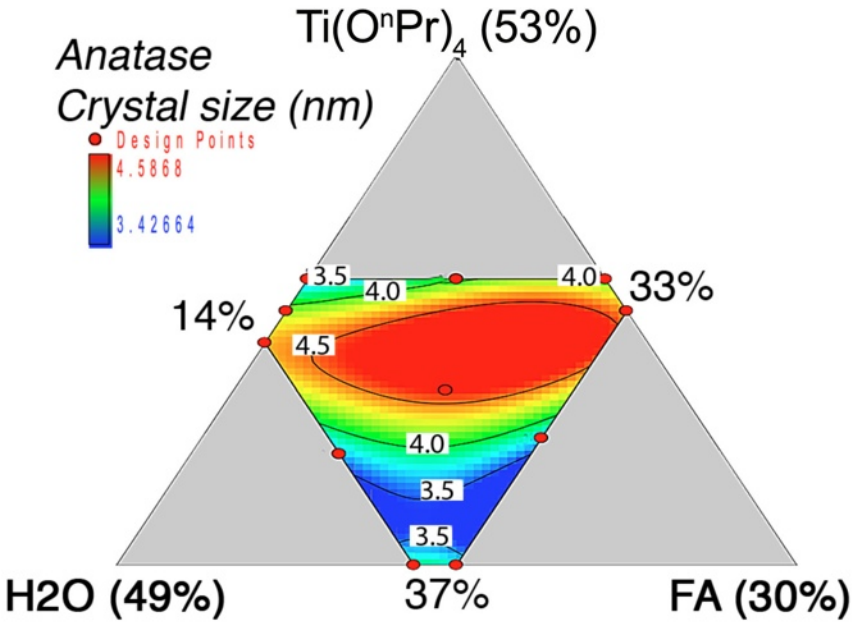

Figure 3.9. Response map for the crystal size of the anatase phase.

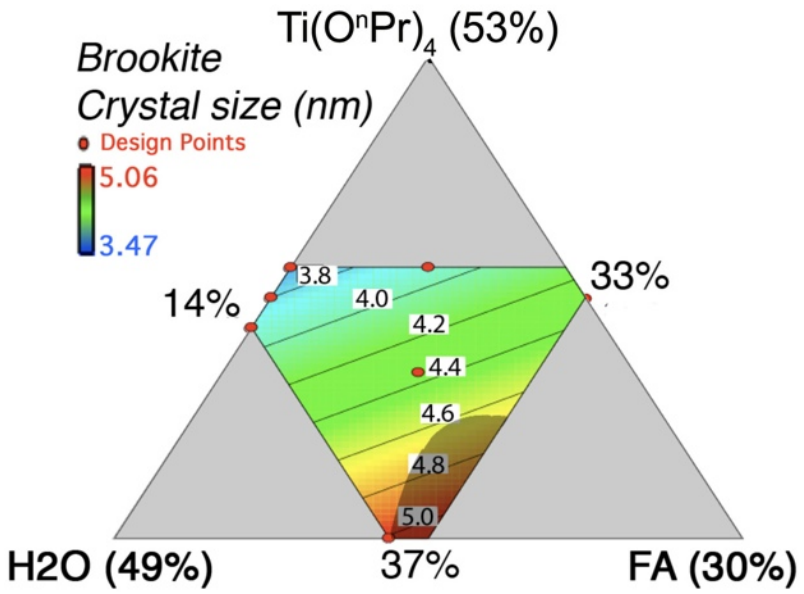

Figure 3.10. Response map for the crystal size of the brookite phase (the shadowed area corresponds to anatase >90 wt%)

The response map for the crystal size of the anatase phase reveals that very small nanocrystals, with a size ranging between 3.5 and 4.6 nm are obtained. An accurate analysis of the crystal size for the brookite phase is difficult as the intensity of the diffraction peak is low, but the same crystal size range can also be deduced. These sizes are much smaller than those observed in the Degussa P-25 nanopowder (anatase and rutile elementary particles of 85 and 25 nm, respectively),[10a] or those used for DSSC applications (16-20 nm).[29] Being able to decrease this size is a way to obtain a wider bandgap, a result of the quantum confinement, and to increase the dye loading, a result of a more opened nanostructure (see hereinafter). However, reducing the size of the photoanode particles should have also an influence on the conductivity of this photoanode, since the whole particle could be electronically depleted by the electrolyte interaction.[5] As stated previously, with 4 nm nanoparticles and the same 1.5 nm Debye screening thickness, almost all the particle should be affected by the dye and electrolyte, leading to a new volume conduction mechanism. This first part of this study demonstrates that 4 nm size anatase nanocrystals can be prepared at room temperature, with a suitable ratio of

components, and the mixture design study allowed us to identify this region in the area surrounding the A sample composition.

3.4.2.Mesostructure

Beyond the preparation of small elementary particles, the way they are assembled, especially with an optimized textural porosity and well-defined pore sizes, is another goal of achieving suitable materials for applications like DSSCs or photocatalysis.

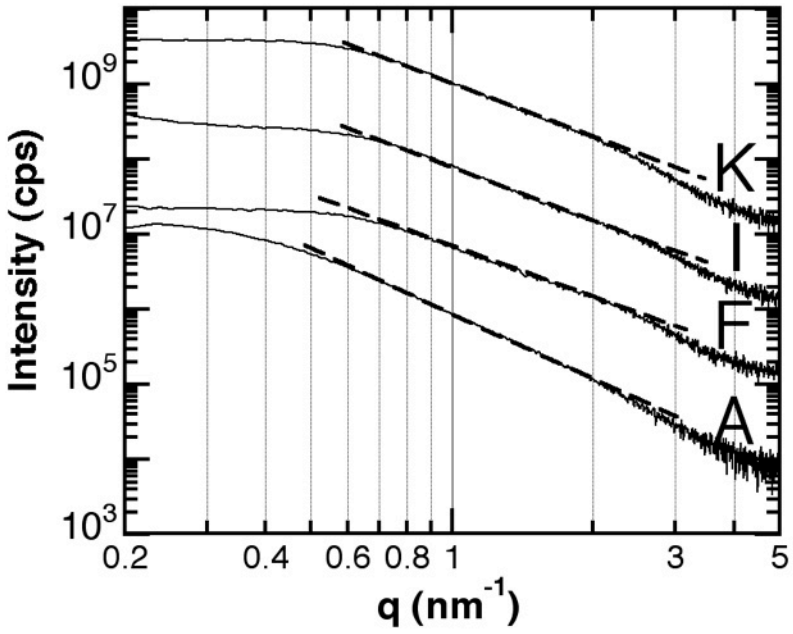

Figure 3.11 Representative SAXS patterns of samples A, F, I, and K selected at different locations of the phase diagram (SAXS patterns were vertically shifted).

We display in Figure 3.11 some SAXS patterns of as-synthesized samples selected within the phase diagram (see also Figure 3.12). All samples exhibit an intense scattering that corresponds to a porous aggregate of nanoparticles. It is observed that this high scattering curve decreases rapidly upon thermal treatment (Figure 3.12). The scattering curves exhibit three distinct regions. For most samples (F, I, K), below q = 0.6 nm^{-1}, the intensity is constant, which is consistent with a uniform, non-fractal long-range structure. For q > 0.6 nm^{-1}, a power-law regime is observed. up to 2.5 nm^{-1}, which corresponds to the Porod region, and notifies a porous structure.[30] Even though the extension of the Porod region is not large enough to justify

a true self-similar fractal structure, we decided to quantify this porous structure by using the volume fractal dimension Dv according to:[31]

$$I(q) = k.q^{-Dv} \qquad (3.5)$$

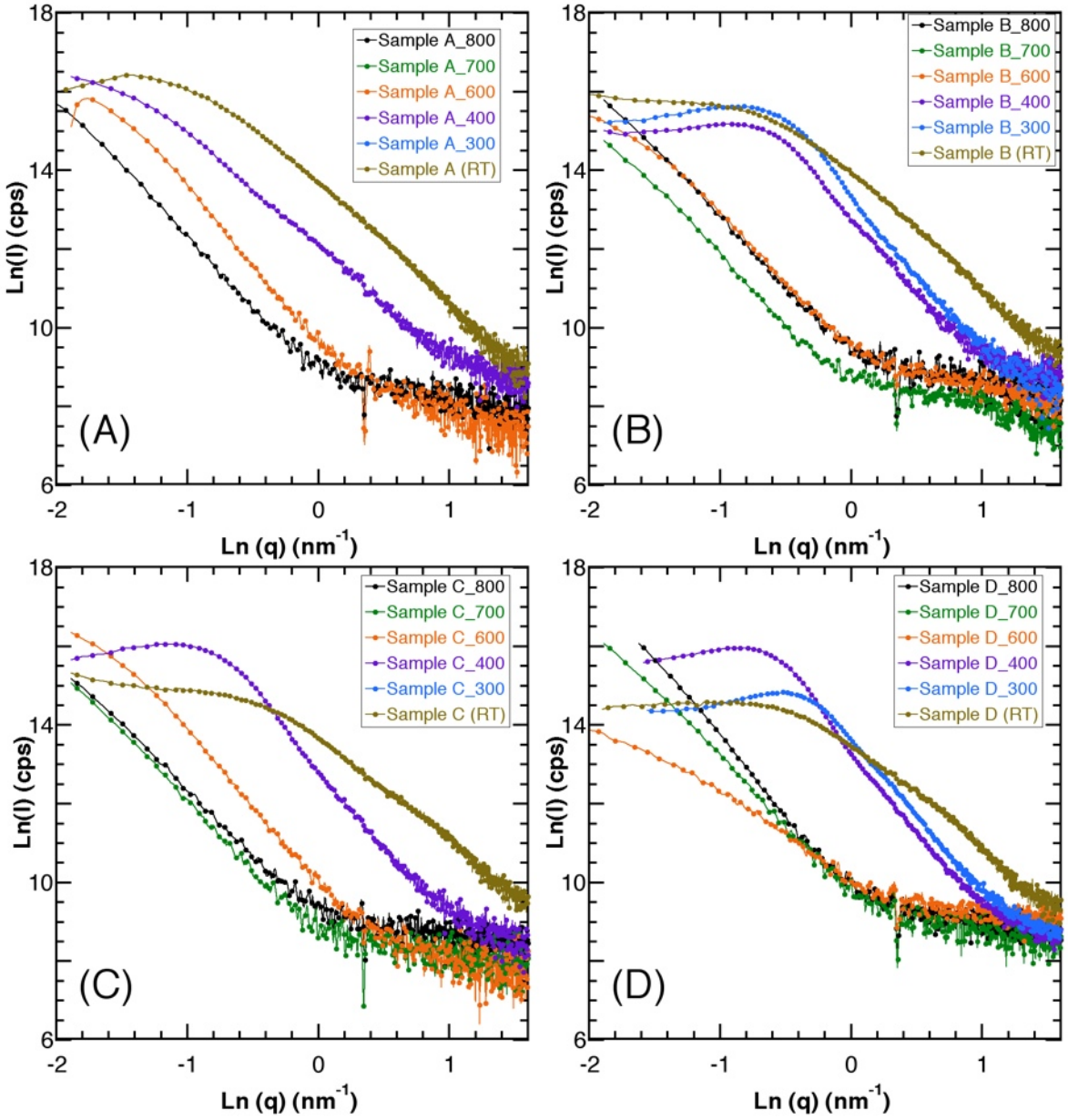

Figure 3.12.a: Evolution of the SAXS pattern for the samples A, B, C, D, after thermal treatment between 20 and 800°C (to be continued)

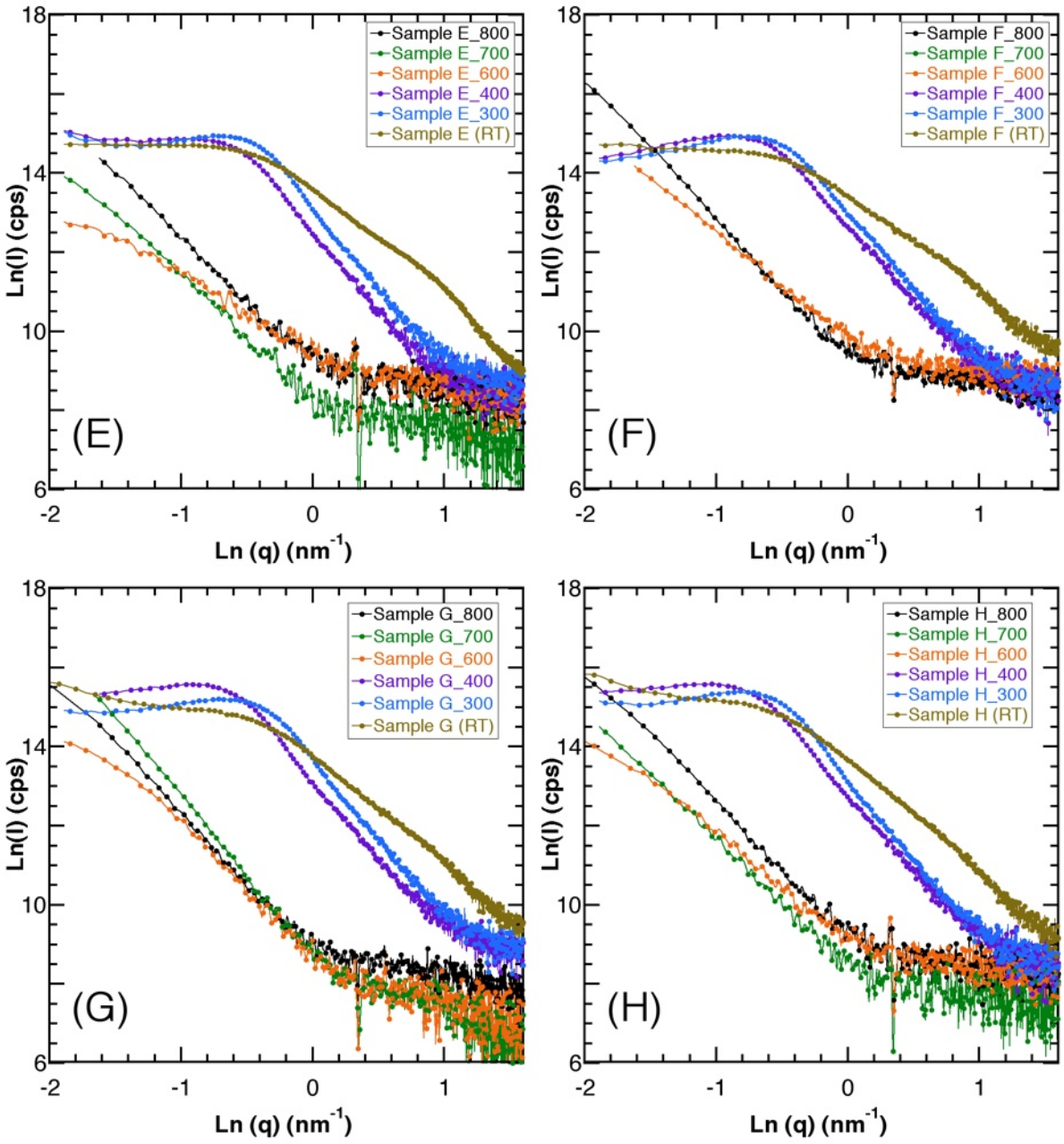

Figure 3.12.b: Evolution of the SAXS pattern for the samples E, F, G, H, after thermal treatment between 20 and 800°C (to be continued)

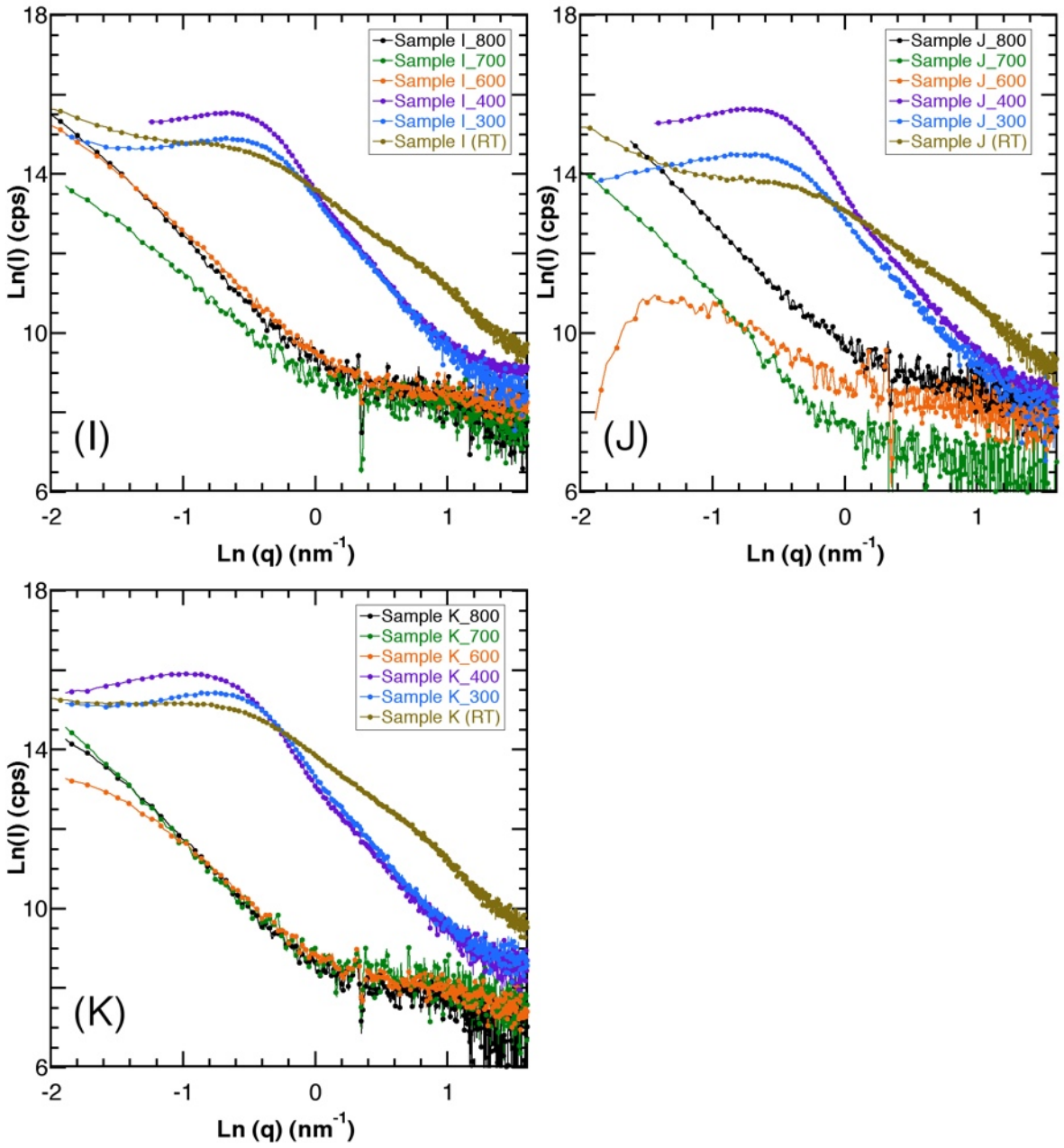

Figure 3.12.c: Evolution of the SAXS pattern for the samples I, J, K, after thermal treatment between 20 and 800°C

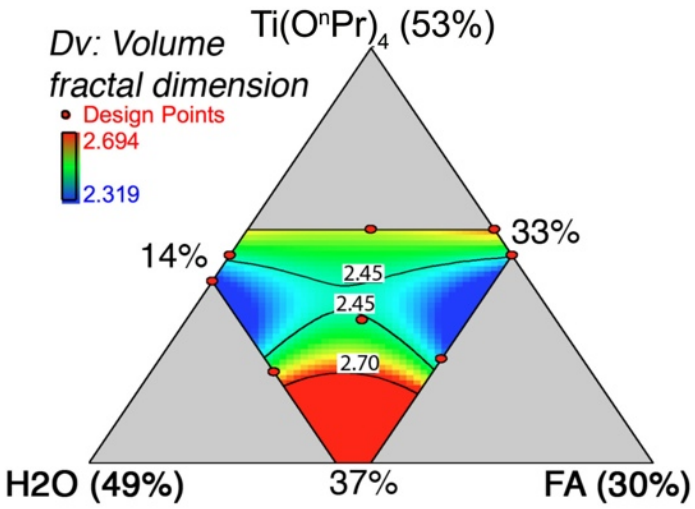

Figure 3. 13 Response map for the fractal dimension of the materials.

Figure 3.13 displays the evolution of Dv as a function of the initial composition, with Dv varying possibly from 2 (highly porous material) to 3 (fully dense material). Almost all the phase diagrams correspond to structures where Dv is below 2.7, which is the signature of opened structures. A trend is observed along the phase diagram with a region of minimum value (blue area) ranging through the whole domain, for constant concentrations in titanium propoxide. The densest structure, with Dv = 2.7, are observed in regions with a minimum concentration of titanium propoxide. As all crystals are the same size, whatever their nature (anatase or brookite), the mesoscale structure can be described as an aggregate of uniform particles. The end of the volume fractal region corresponds to the smallest object contributing to the Porod regime, that is, the particle. All SAXS patterns recorded for the as-synthesized samples exhibit about the same value, q values ranging between 2.0 and 2.7 nm^{-1}, corresponding to $d = 2\pi/q$ equal to 3.1 and 2.3 nm, respectively. The accuracy of this measurement is not very high, as it is difficult to identify clearly the slope break point, but the values found are in the same range as those deduced from XRD, which means that uniform particles (identified by SAXS) are made of single crystals(identified by XRD). The existence of very small particles is confirmed by SEM (Figure 3.14) and TEM (Figure 3.15) observations.

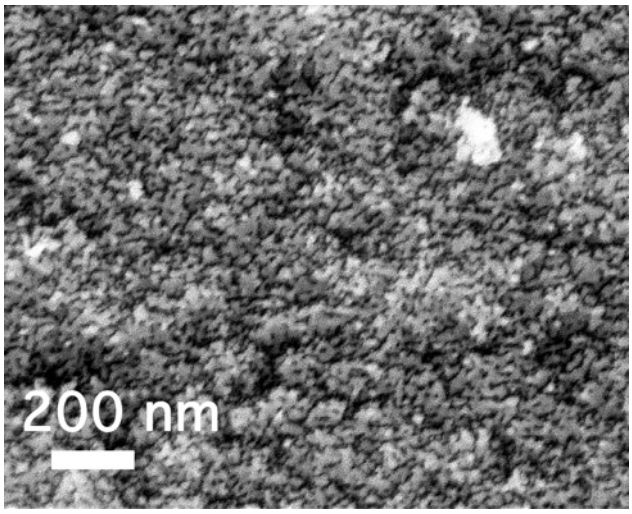

Figure 3.14. SEM observation of the sample A.

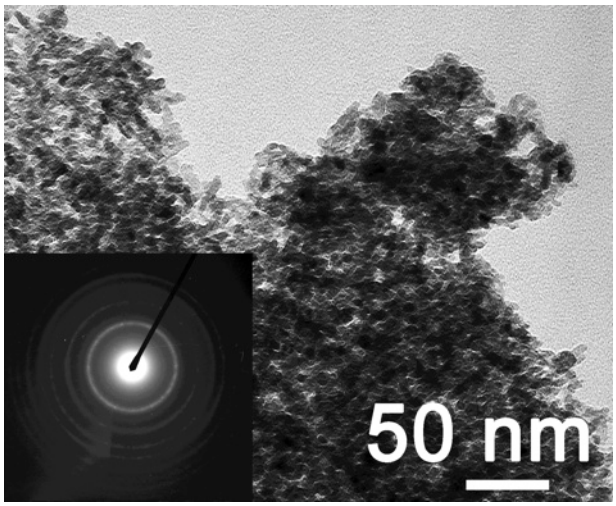

Figure 3.15 TEM observation of sample A (inset: diffraction pattern).

The N_2 adsorption isotherms for the sample A, either as-synthesized or after a 4 hour thermal treatment at 300, 400 or 500°C, is displayed in Figure 3.16.a. These curves display type IV isotherm shape, with a sharp desorption edge that corresponds to a narrow pore distribution ranging between 4 and 6.5 nm, depending on the thermal treatment (Figure 3.16.b). The as synthesized material exhibits a large 190 $m^2.g^{-1}$ specific surface area (equiv. 250 m^2/g for silica) and a 0.3 $cc.g^{-1}$ porous volume. Both values remain unchanged after treatment at 300°C, with a 176 $m^2.g^{-1}$ specific surface area, and a 0.3 $cc.g^{-1}$ total porous volume. The specific surface area drops down to 48 $m^2.g^{-1}$ at 400°C, and 20 $m^2.g^{-1}$ after the 4 hour 500°C thermal

treatment, as for the porous volume equal only to 0.07 cc.g^{-1}. The pore size increases slightly with temperature up to 400°C, before starting to collapse when densification becomes important (500°C).

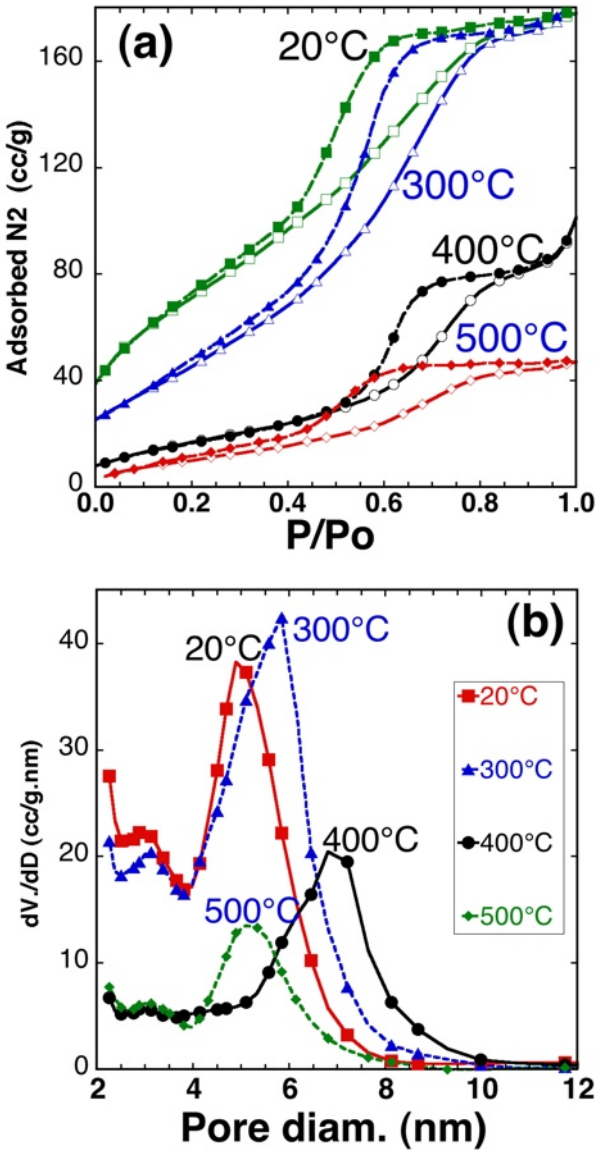

Figure 3.16 (a) N_2 isotherm, and (b) pore size distribution for the sample A at room temperature and after thermal treatment at 300°C and 500°C.

Another confirmation that the material prepared at room temperature is made of aggregates of small nanocrystals, is obtained when the material prepared by this process, was dispersed under

sonication for 10 min. in a 50:50 wt mixture of water and ethanol. The resulting suspension was studied by DLS to characterize the aggregates size. All the auto-correlation curves resulting from measurements could be analyzed with a single-size cumulant fitting model (Figure 3.17), and multi-size Padé-Laplace analysis did not reveal any polydispersity neither. We deduce from this analysis that the partial fragmentation of the initial titania gel leads to a rather homogeneous distribution of aggregates within the samples. This study through the whole phase diagram, allowed us to observe a net trend in the aggregate size distribution, with a central domain of small (around 400 nm) aggregates, and two poles where larger aggregates in the micrometer range are observed (Figure 3.18).

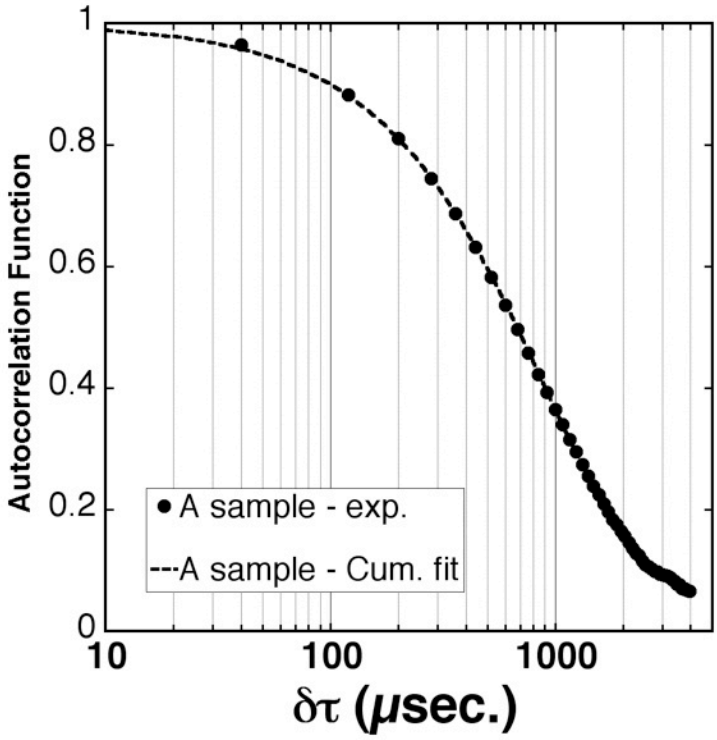

Figure.3.17: Autocorrelation curve deduced from DLS measurement, for an EtOH:water suspension of sample A sonicated at room temperature; dots: experimental function; dashed line: single size cumulant fit.

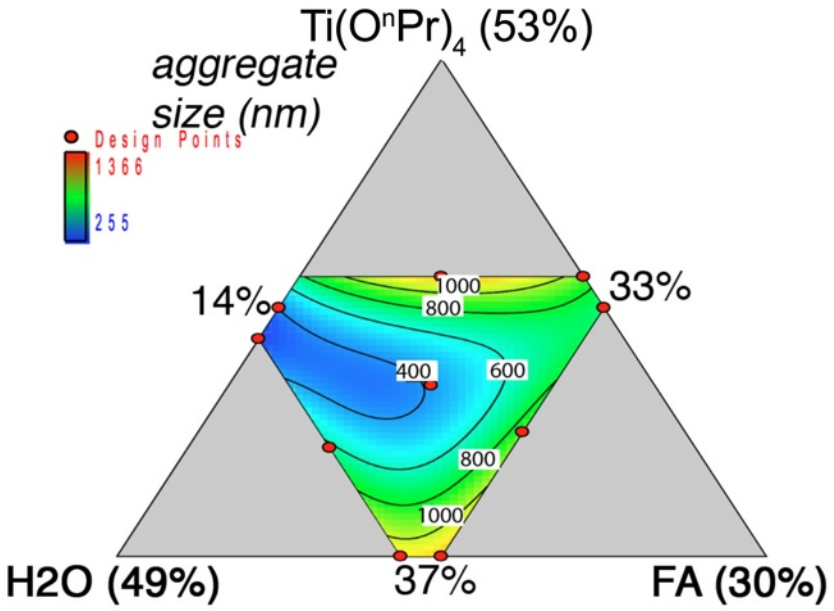

Figure 3.18 response map for the size of aggregates after sonication.

This aggregate size map overlaps well with the distribution of volume fractal dimension (Figure 3.13): the more opened structures (small Dv) observed in the middle of the phase diagram lead to smaller aggregates, as a result of an easier way to break them. In parallel, denser structures (large Dv) give larger aggregates. The sonication mode was moderate, which explains why the aggregates are rather large, but this finding let us think that the whole material could be built with a hierarchical structure, made of aggregates of nanocrystals, which would fit well with the expectations stated for new photoanode materials.[32]

The study of these materials at the mesoscale demonstrate that they possess an open mesostructure, with a well-defined porosity centered around 5 nm, in agreement with the observed size of nanocrystals. When dispersed by sonication, a uniform distribution of aggregates ranging from 400 nm to 1.0 µm, is obtained, depending on the the initial reagents proportions.

3.4.3.Thermal Evolution

The effect of thermal treatment on the crystalline nature of titanium oxide, was first studied by Temperature-Programmed XRD. The evolution of TP-XRD patterns for two representative samples (I & F) is reported in Fig.3.20.

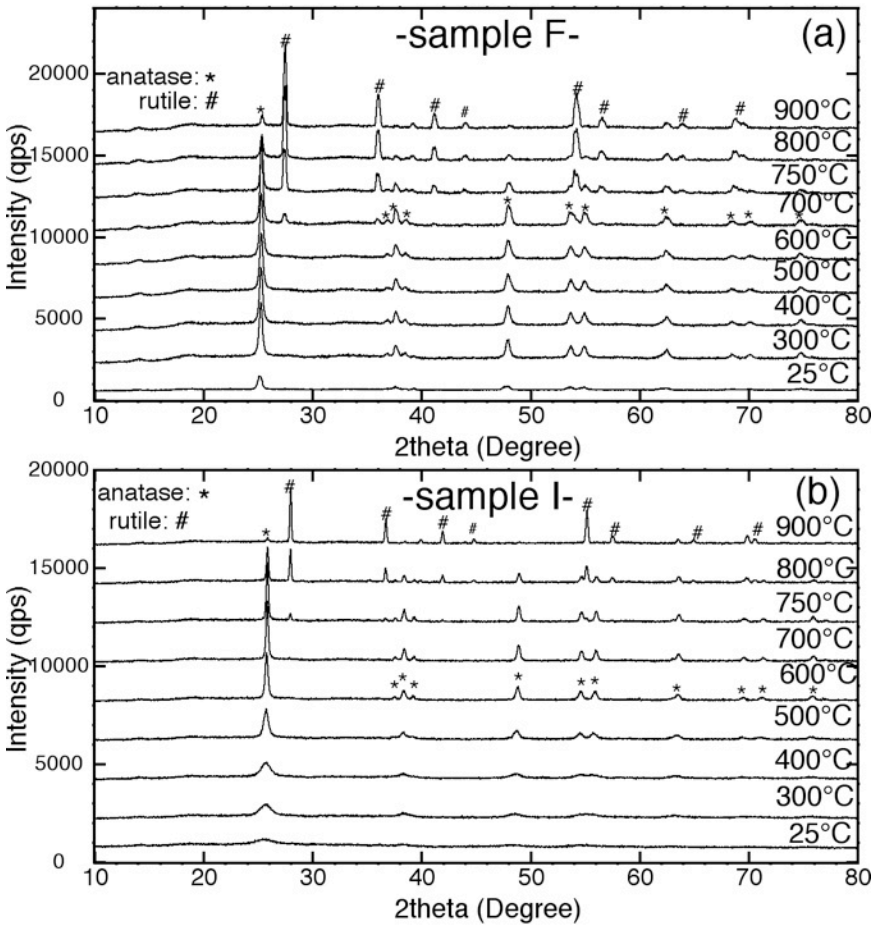

Figure 3.20 Representative HTXRD patterns for (a) sample F and (b) sample I.

The evolution of the crystalline structure follows a polyphasic transformation, with the progressive formation of rutile. As the temperature increases up to 600°C, other characteristic peaks of anatase crystals (*103*), (*112*) appear, followed by small rutile diffraction peaks; some anatase still remains at 900°C. Similar trends were observed with samples A and K (Figure

3.21). However, the temperature of rutile crystallization can vary from sample to sample, and it can be shifted up to higher temperatures, depending on the initial composition (*e.g.* 700°C for sample F and 750°C for sample I). The thermal evolution was explored further by setting different maximum temperatures (300, 400, 600, 700, 800°C) with a four hour plateau (Figure 3.21). For most of the samples, the anatase phase is still observed at 700°C, with a parallel crystallization of the rutile phase, starting at 700°C.

The phase content (weight fraction) of anatase and rutile was calculated at 700°C, using the following equation:[33]

$$f_A = \frac{1}{\left[1 + 1.26 * \left(\frac{I_R}{I_A}\right)\right]} \qquad (3.6)$$

where I_R and I_A are the integrated intensities of rutile and anatase, respectively. The mapping of the anatase distribution for samples heated at 700°C reveals a preferential area for the formation of rutile, along an axis starting on the left side of the phase diagram and expanding perpendicularly to the water apex (Figure 3.22). This domain corresponds to the more opened structure identified by higher volume fractal (Figure 3.19) and smaller aggregates (Figure 3.18), meaning that open structures are more easily converted into rutile by thermal treatment.

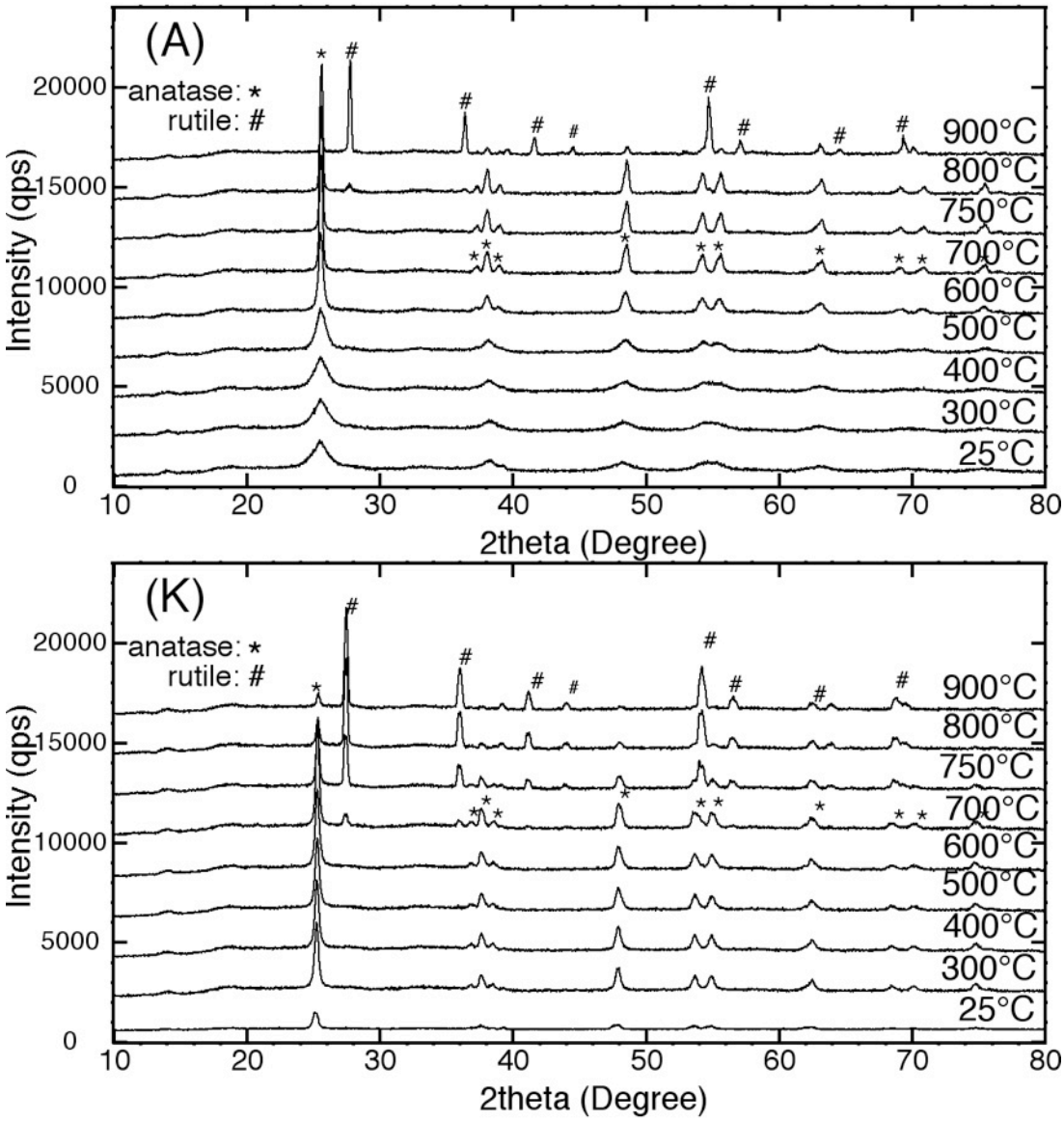

Figure 3.21: Representative HTXRD patterns for sample A and sample K.

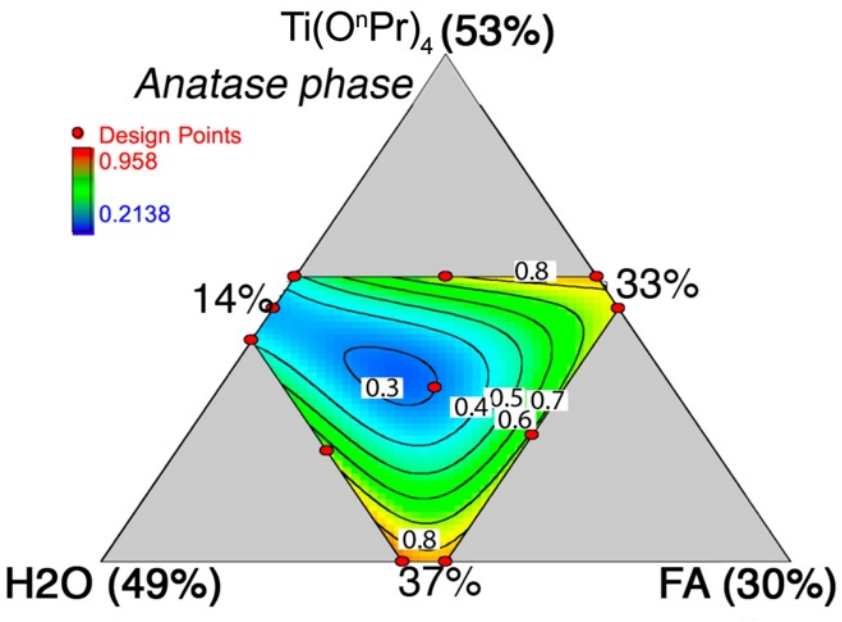

Figure 3.22: Response map for the distribution of the anatase phase at 700°C (the other phase is rutile)

The crystal size evolution as a function of the temperature is reported in Figure 3.23. The same evolution is observed for all samples, whatever their composition. The crystal size is very stable, around 4-6 nm up to 400°C, even after a four hour plateau, and the crystal growth begins only at higher temperatures. This size evolution confirms the results observed for the porous evolution of these materials (Figure 3.12), which reveals that the mesoporous structure begins to collapse at 400°C - after a four hour thermal treatment -, as indicated by the variation of the specific surface area reduction (48 $m^2.g^{-1}$ at 400°C, 20 m^2/g at 500°C, no porosity at 600°C).

The study of the thermal evolution of the nanostructured TiO_2 materials shows that the anatase phase is quite stable with temperature, since a large fraction is still found at 700°C. The critical threshold for material transformation is around 400°C: below, the nanocrystal size remains stable, and the mesoporosity is still important. Above, the crystal size increases from 5 to 30 nm, along with a concomitant loss of porosity, but the anatase phase remains present up to 700°C for most of the samples in the selected phase diagram.

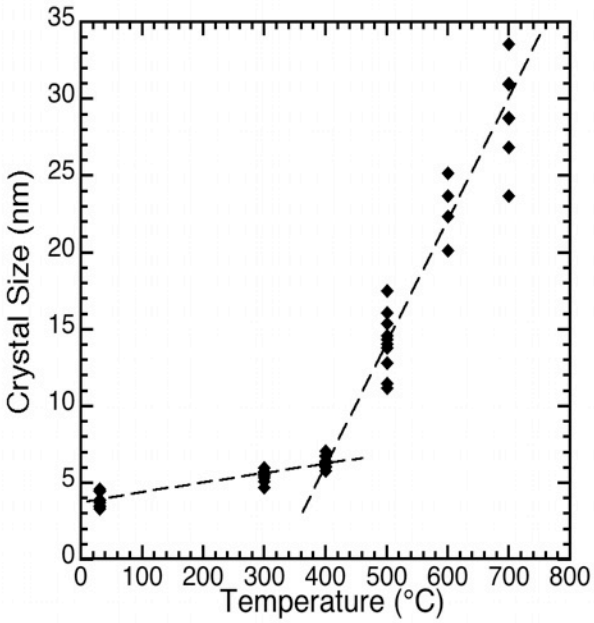

Figure 3.23 Evolution of the crystal size as a function of the thermal treatment, for the whole series of samples (A to K). (dashed lines plotted for visual help).

3.4.4. TiO_2 Anatase Band Gap Evolution

As the present synthesis, combined with the different thermal treatments, led to the preparation of anatase nanocrystals with varying sizes, it allowed us to look at precisely on the relationship between size-dependent quantum confinement and the band gap modulation.[20] As the band gap values for rutile, brookite, and anatase, are different and equal to 3.0, 3.1, and 3.2 eV, respectively,[34] we discarded any sample containing either brookite or rutile, to be sure that the crystal nature would not affect the values of the band gap. Band gap analysis was carried out by UV-vis measurements (see Figure 3.2), which confirmed that the band gap (indirect band gap model according to eq.(3.2)) decreases as the crystal size increases (Figure 3.24). All values obtained for crystals larger than 7 nm, are in the same range (3.0-3.1 eV) but smaller than what could be expected from the knowledge of bulk anatase bandgap. Such low values were observed previously,[17] but it was suggested that these surprising low values were the proof that anatase nanoparticles have a direct bandgap. Therefore, we calculated also values based on the direct bandgap model $(\alpha.E)^2 = f(E)$ to compare both trends.

The influence of size was estimated using the following equation:[11-12]

$$\Delta E_g = [h^2 / 8\mu R^2] - [1.786 \bullet e^2 R] - 0.248 E_{RY}^* \qquad 3.7$$

with ΔE_g, the bandgap shift; e=1.6021*10^{-19} C; *h* the Plank's constant = 6.62*10^{-34} (m^2.kg/s); R (in m) the radius of the particle; μ the reduced mass of the exciton ($1/\mu = [1/m^*_e + 1/m^*_h]$), with, for anatase, $m^*_e = 10\ m_e$ (m_e = 9.11.10^{-31} Kg) the effective mass of the electron, and ($m^*_h = 0.8\ m_e$) the effective mass of the hole, according to Enright *et al*.[35] ε is the dielectric constant of the material, and E_{Ry}^* = 4.3 10^{-39} J is the effective Rydberg energy. The first term in the equation represents the particle in-a-box quantum localization energy, with a simple $1/R^2$ dependence, the second term represents the Coulomb energy, with a 1/R dependence, and the third one is the result of the spatial correlation effect. This last term is size-independent, and becomes only significant for materials with a low dielectric constant. The choice of the numerical values chosen can vary.[36] We took a value usually assigned to TiO_2 anatase (ε=86),[37] and the last term of eq.(3.7) was neglected,[11] leading to the easy-to-use Eq.(3.8) applied to TiO_2 anatase:

$$\Delta E_g = (2.0328 / D^2) - (6.6976 \bullet 10^{-12} / D) \qquad 3.8$$

with ΔE_g in eV, and D the crystal diameter in nm.

We compare in Figure 3.25 the evolution of the experimental bandgap Eg calculated for both direct and indirect bandgap models, with the theoretical variation ΔE_g deduced from eq.(3.8) and E_g value for the bulk material chosen to fit with the experimental data (E_g = 3.4 eV for the direct bandgap, E_g = 3.05 eV for the indirect bandgap).

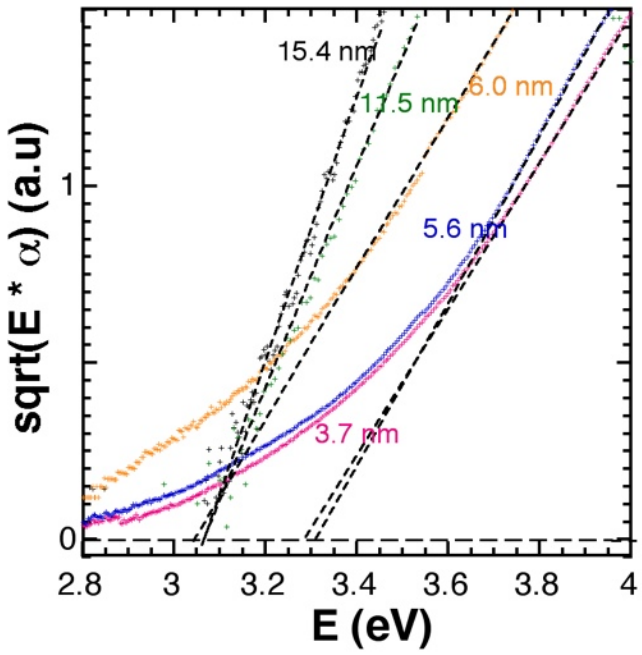

Figure 3.24: Evaluation of the indirect bandgap Eg for anatase with different crystal size

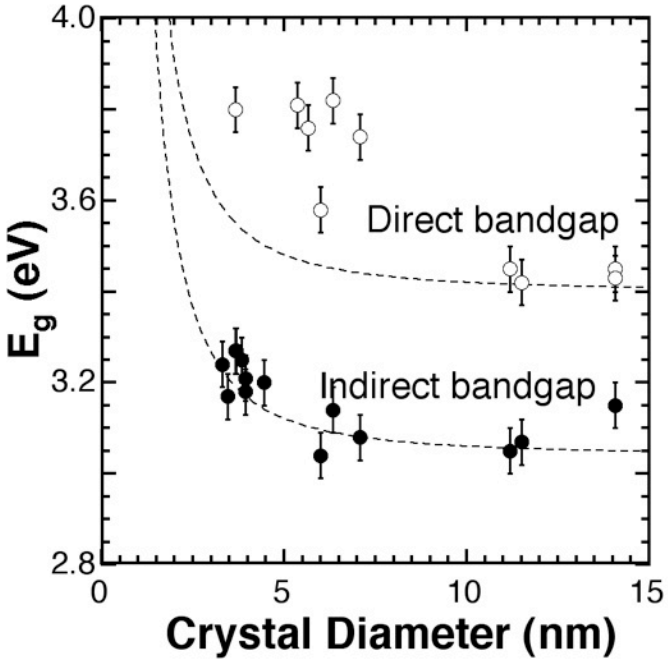

Figure 3.25. Evolution of the indirect (black) and direct (white) bandgap Eg as a function of the anatase crystal size. Lines correspond to the theoretical variation Eg + ΔEg calculated from eq 3.3, with Eg = 3.4 eV (direct) and 3.05 eV (indirect).

Despite that none of these values correspond to the expected value of 3.2 eV assigned to bulk anatase, it is however clear that the indirect band gap model gives a better agreement with the theoretical curve, than the direct one, and that the size quantum confinement effect is limited to crystals smaller than 7 nm. Hence, the difference between the value usually observed of E_g = 3.2 eV for materials prepared with high temperature methods,[14b] and ours cannot be explained by the existence of TiO_2 anatase with a direct bandgap.[17]

Lower values of bandgap for TiO_2 anatase, were already observed: Reddy *et al*. pointed out this shift,[17] but their assignment to a direct band gap is invalidated by our results. Sanchez *et al*, reported that the bandgap of titania prepared by sol-gel method can vary with the degree of hydroxylation:[24] in acidic medium (pH 3) the bandgap is smaller (2.91 eV at 200°C) than in basic medium (pH 9) (3.15 eV at 200°C). Similar results, with indirect bandgap varying from 3.04 to 2.90 eV, were also observed for nanoparticles submitted to a thermal treatment up to 900°C.[38] The possible assignment of indirect transitions at this lower energy level was described by Serpone *et al*.,[39] who noted that the electronic band structure of metal oxides like TiO_2 involves much lower energies bandgap than for fully ionic compounds, as a result of the covalent contribution. It results that the values observed for bulk rutile and anatase (3.0 and 3.2 eV, respectively), which occur from the 2p-3d separation, are sensitive to the degree of ionic versus covalent character in the bonding. This character can be affected by the degree of disorder in the TiO_2 crystalline framework, and by the degree of hydroxylation, as observed by Sanchez. They finally mentioned that the lowest indirect transitions, from the edge to the centre of the Brillouin Zone, occurs at 2.91 and 3.05 eV, which fits perfectly with our experimental observations. Our results illustrate a competitive effect between a reduced crystal size below 7 nm,[14b] which leads to higher value of E_g, and a room temperature wet synthesis,[31] which leads to lower values of E_g. However, we observe that these lower value of Eg are still observed for larger crystals that result from thermal treatment, which means that the initial synthesis history leaves behind some memory in the structure that remains disturbed enough to affect the band gap value, as mentioned previously.[39]

3.4.5. Test of the Nanostructured TiO_2 Anatase for DSSC Applications

Before carrying out deeper investigations on the integration of this new material into Dye Sensitized Solar Cells we validated first their actual efficiency as photoanodes in these cells. To this purpose, anatase TiO_2 films were prepared at room temperature as follows: the nanocrystalline TiO_2 was first calcined at 350°C for 4h, and 1g of this powder was dispersed in 5mL EtOH. After a one hour sonication, the obtained suspension was kept under stirring, and 0.3 g Pluronic P123 (MW 5800 g, Sigma Aldrich) previously dissolved in 5 mL of ethanol were added to the TiO_2 sol. The solution was stirred for one week, and the electrode prepared according to previously published methods.[40] The resulting paste was deposited onto conductive glass substrate (F-doped SnO_2 from Solaronix, 2.2 mm thick glass with ~15 Ω/ft^2 resistance) by doctor blading, followed by firing at 350°C for 4 hours. We did not selected the most commonly used temperature is (450°C) in order to avoid to induce any structural or crystalline modification, as our goal was only - at this stage - to validate the intrinsic semiconducting properties, not to optimize overall the cell efficiency. The thickness of the film was 18 nm. After cooling, the substrate along with the TiO_2 film was immersed overnight into a 0.4 mM solution of *cis*-Bis(isothiocyanato) (2,2'-bipyridyl-4,4'-dicarboxylato) (4,4'-di-nonyl-2'-bipyridyl) ruthenium(II) (known as Z907, Sigma-Aldrich) in 1:1 acetonitrile/t-butanol. Finally, the electrode was washed with EtOH and left to dry in air.

The platinized counter-electrode was prepared by pouring one droplet of a platinum catalyst (Platisol T, Solaronix) onto FTO glass and fired at 450°C for 30 min in air. The platinized electrode was placed above the working area of the photoanode and assembled by metal clips. A few drops of 50mM iodine-colored electrolyte (Iodolyte PN-50-Solaronix) was placed between the two electrodes. Assembled cells were characterized at 1.5 AM sun using solar simulator under 100 $mW.cm^{-2}$ light intensity. Tests ran with a 20 cm^2 effective surface for the dye-sensitized solar cell, validate the use of TiO_2 as an effective photoanode, but, obviously, do not compete with state-of-the art results, as the whole cell integration has not being achieved (currently under progress). The I-V curve is displayed in Figure A.1 The open circuit voltage V_{oc} is equal to 0.63V and the short-circuit current I_{sc} equal to 47.4 mA (2.37 $mA.cm^{-2}$). The cell

performance can be evaluated with the filling factor FF = $P_{max}/(V_{oc} \times I_{sc})$ = 45%, and the efficiency η = 0.68%, defined as the ratio of energy output from the solar cell P_{max} to input energy from the sun simulator. These values are obviously below those observed with current dye-sensitized solar cells, but they allowed us to verify that the new nanostructured anatase reported in this work, can be used as a future photoanode, and integration and optimization of the cells are currently under progress.

3.5. Conclusion

We have demonstrated that the study of synthesis parameters through mixture design allowed us to identify the optimum area to obtain very small nanocrystals of pure anatase at room temperature, with an opened structure that will provide the suitable structure in areas like photoanodic applications in DSSC devices. The best region for such applications lies in the A-J region of the studied phase diagram, which corresponds to the minimum percentage of titanium precursor and the maximum of formamide. We expect that the very small size of nanocrystals (4 nm) should provide a new behavior for electronic conductivity as most of the crystal volume will be affected with the charge depletion created by the dye molecules and electrolytes. Beyond the study of the synthesis parameters and thermal treatment that can lead to various nanocrystals, we illustrated the effect of quantum size modulation of this type of semi-conductors, in agreement with what has been demonstrated for other semiconductors, like CdS or CdSe.[11-12] From our experiments, we confirm the indirect nature of the band gap for anatase nanocrystals, with the limit for the size quantum effect around 7 nm.

Chapter 4:
Parameters for enhanced photocatalysis of TiO_2 anatase

4.1. Overview

New TiO_2 anatase nanocrystals (4-6 nm), prepared by our new room-temperature synthesis method have been tested in photocatalysis. This versatile synthesis technologies allowed us to explore the influence of several parameters that could improve the photocatalytic efficiency of TiO_2-based materials. This photocatalytic activity was tested by the reduction of methylene blue under UV irradiation, and compared with two commercial powders , one made of pure anatase (Sigma™), the other of mixed anatase-rutile particles (P25 Degussa™). If the as-synthesised material, despite its anatase structure, demonstrated a low photocatalytic activity, the same material after a 450°C thermal treatment, which improved the crystallinity without increasing the crystal size, led to excellent photocatalytic properties. Varying the test parameters allowed us to provide a full comparison with the commercial products. The experimental kinetic data followed a zero order reaction model where changes in dye concentrations had no effect, and the acidic media improved the degradation rate. At the optimum catalyst dosage and experimental parameters, our material treated at 450°C exhibited a higher photocatalysis than did commercial anatase, and a level similar to the commercial material used for reference (P25). This study allowed us to conclude that nanocrystalline anatase is an excellent photocatalyst if both the size and the crystallinity are optimised. It confirms also that rutile-anatase heterostructures create a true synergy that cannot be overcome by pure phases, unless we are able to improve the charge-carrier separation.

4.2. Introduction

Photocatalysis is an important domain in VOC remediation and water treatment, especially with the emerging problem of pharmaceuticals released in drinking water.[1] Photocatalysts could also solve a strategic issue in the development of energy smart grids. Indeed, "clean" energy technologies like photovoltaic or windmills face two problems: yield and fluctuating production. If the yield issue has to be solved by material science and engineering, fluctuating production without intermediate storage is a major hurdle in systems that directly convert directly sunlight or wind into electricity, because their random injection into the energy grid will require a major adaptation in grid management. Many options have been investigated to store the electricity temporarily: batteries, inflated balloons, hydrogen, pumping water.[2] All these solutions are based on a similar chain of production and delivery: (i) conversion of energy into electricity, (ii) conversion of electricity into chemical or mechanical energy, (iii) back conversion of the chemical or mechanical energy into electricity, (iv) delivery to the grid. Therefore, photocatalysts, able to convert sunlight directly into chemical energy (H_2) by water splitting, which would be used in fuel cells, could become a significant component of the whole energy grid, along with other elements, as this process would contribute to smoothing the whole energy collecting and delivery loop. In addition, large scale static production platforms would allow us to find the key to the presently unsolvable problem of hydrogen storage for mobility, as industrial static storage of hydrogen is better controlled than mobile storage. Moreover, the production of electricity could use large-scale fuel cells that are also easier to control in an industrial environment. Finally, as the car industry has definitively voted for the electric car, it seems presumptuous to postulate that two grids of fuel delivery (electricity and hydrogen) will be implemented in parallel. Therefore, hydrogen production should target toward realistic goals such as the solar light-based static production of hydrogen for further conversion on demand of electricity. However, this goal will be achieved only if the process, overall, is cost effective, which implies that the photocatalytic material has to be made with affordable raw materials, and to convert water into hydrogen with a reasonable yield. Therefore, our present contribution, adds to the understanding of material parameters that are

strategic to the photocatalysis mechanism, in order to favor a future "knowledge-based" design of efficient materials. We chose to use the photocatalysis of organics as a first and simple way to evaluate the properties of materials.

Since the discovery of the photocatalytic splitting of water by titanium oxide under UV light irradiation,[3] many works have been devoted to this development.[4] Photocatalysis uses photons as the energy source for the creation of free electrons in a semi-conducting material. The photon energy must be higher than the material bandgap to allow for generation of the electron–hole pair, and UVs are the most effective form of radiations in the solar spectrum. These electrons form hydroxyl and superoxide anionic radicals that are the primary oxidizing species in the photocatalytic oxidation processes. A dye like methylene blue is cationic, and it can react with the electron in the conduction band, forming a dye radical anion. Subsequent reactions lead to a dye degradation. Therefore it is a good tracer of photocatalysis efficiency.

As TiO_2 displays a good band gap for photon absorption, is inexpensive, non-toxic, and highly reactive in nature, it has been widely studied for applications using its semi-conducting properties, such as photovoltaics and photocatalysis, and it has been demonstrated that its crystalline phase (anatase, rutile, brookite) and crystallinity are important parameters.[5] The degradation efficiency of the dye depends upon the oxygen concentration adsorbed on the Ti (III)- surface or dissolved in water. Hence, a good photocatalyst must display adequate electronic band structure, to allow for a good absorption of light and creation of stable electron-hole pairs, and a high specific surface area, to allow for an effective transfer of these electrons to the surrounding solvent.

Among the three crystalline phases of TiO_2 anatase, brookite, and rutile, the first two are metastable and the latter is thermodynamically stable. It has been observed that pure anatase (E_G = 3.2 eV) gives better results than rutile (E_G =3.0 eV) because of the higher reduction potential of photo-generated electrons. However, this assumption is partially contradicted by the excellent activity of a mixed structure of anatase and rutile provided by P25 from Degussa™, which means that other mechanisms are involved. We have tried in this study to optimize all crystalline, structural, and processing parameters of a nanocrystalline powder of

pure TiO_2 anatase, to evaluate how much the photocatalysis is relevant to those parameters. This study has allowed us to optimize both the material and the process, endeavors validated by comparison with a pure anatase material (Sigma™), from where we compared our performances with P25 (Degussa™) made of a mixed anatase-rutile heterostructure. Our study demonstrates that the full optimization of anatase structural parameters lead to photocatalytic results as good as those obtained with the reference material from Degussa™, suggesting that future developments toward the creation of heterostructures should allow us to further improve the photocatalytic properties of titanium oxide obtained with this new method.

4.3. Experimental

4.3.1. Materials

BD BBL™ TB Methylene Blue, 250 mL (4/sp) (Becton, Dickinson and Company) buffer solution was used as received. Two types of commercial Titanium oxide (TiO_2) were used as a catalyst for comparison; the first (P25, Degussa™, Germany) is made of 75% anatase and 25% of rutile and has a mean particle size of 18 nm;[6] the other is pure TiO_2 anatase (Sigma™) with a 13 nm mean particle size. TiO_2 anatase nanoparticles (6 nm) were synthesized at room temperature, according to a method previously published.[7] This method allowed us to prepare nanocrystalline titanium oxide and to adjust, not only the crystal size within 4 and 6 nm, but also the crystalline structure from pure anatase to a mixed anatase-brookite composition. Results reported in the following deal only with pure anatase, as experiments carried out with anatase-brookite mixtures did not provide good photocatalytic results.

4.3.2. Analysis

Instruments. X-ray diffraction (XRD) was carried out on a Bruker D8-Advance powder diffractometer using Cu Kα radiation (λ = 1.5405 Å) operating from 2θ = 10–90°. Sherrer formula was applied to calculate the crystallite size for the samples, the full width at half maximum (FWHM) being determined after a Gaussian fitting. (Gaussian fit is allowed because of the large peak broadening.) The UV-vis absorption of Methylene Blue was analyzed with an

Evolution 60 Thermo Scientific UV-Vis Spectrometer. Methylene blue (MB) aqueous solution absorbs light of around 664 nm (absorption peak), and under the photocatalytic reaction of the TiO_2, this peak decreases smoothly, with a slight shift toward a shorter wavelength until the solution becomes colourless. The absorption was determined by the evaluation of the total absorption peak area, deduced after subtraction of the absorption base line (polynomial fit) from the raw data.

The N_2 adsorption isotherms were measured with a Quantachrome AUTOSORB-1. The samples were outgassed at 200°C under vacuum for 12 h before measurement. Surface area was determined by the BET method in a relative pressure range of 0.05−0.25. Pore size distribution was calculated with the Broekhoff and deBoer Model applied to the desorption branch.[13, 14] A 254nm wavelength, five 8W bulbs with a typical intensity of 3,500-4,500 μW/ cm^2 (FB-UVXL-1000, Fisher Scientific) was used as the irradiation source. FT-IR spectra were recorded from 400 to 4,000 cm-1 (16 scans, 0.2 cm^{-1}) by transmission with a Brucker Tensor 27 spectrometer (OPUS program). Absorption was adjusted by mixing the samples with KBr (Fisher Scientific).

4.3.3. Synthesis

A specific composition was chosen within the working area in the phase diagram for the preparation of pure TiO_2 anatase, described previously.[7] In a typical synthesis, 2.9 mL of HCl was added drop-by-drop within 5 min under vigorous stirring (200 rpm) to 5 mL of Ti $(O\text{-}n\text{-}Pr)_4$ left in an ice bath. Then, 2.86 mL formamide (FA) and 2.17 mL deionized water were mixed before being added drop-by-drop to the previous solution within 15 min. After full addition, the sample was left for ageing in a thermostatted bath at 30°C for 24 h. The solution experienced a phase separation during this ageing phase, with a physical gel forming at the bottom and a supernatant liquor on the top. The gel container was covered and left at 60°C for one week before drying. Ammonium chloride, a byproduct of the reaction, was removed by washing the sample three times with 100 mL of deionized water, the powder being recovered by filtration afterward. At this stage, the gel could easily be dispersed in water by sonication. The samples were finally calcined in air for 4 h

(100°C.h^{-1} ramp) at different temperatures. The samples names used are RT-TiO_2 for as-synthesised, and Txxx for RT-TiO_2 thermally treated at xxx°C.

4.3.4. Photocatalytic Test

A stock methylene blue (MB) solution of 7.48 mM was used to create an 0.063 mM solution (2.1 ml MB in 250 mL D.I water). Aliquots of 25 mL of this MB solution were used for test, and different masses of TiO_2 were added. In the following, "mass of TiO_2" refers to the amount added into these 25 mL volumes. The suspension was kept under dark conditions (over night) before experiments were carried out to allow the equilibrium to take place between the methylene blue solution and the catalyst. The methylene blue solution was exposed to the UV irradiation source, and then, every two minutes the samples were stirred for 30 sec and then re-exposed to UV. The samples were centrifuged to separate the TiO_2 from the solution, and the aliquots were taken for recording the spectra, before being poured back into the mother liquor. All experiments were conducted at room temperature, and the top surfaces of all the beakers were open to air. Atmospheric air obviously provided enough oxygen for the oxidative degradation of pollutants. The pH of the solution was changed during the experiment (pH=2, 6, and 9). The progress of the reaction (degradation of the methylene blue solution) was achieved by integrating the area under the absorbance curve. The percentage removal of MB was calculated by using the equation given below:

$$Q = (\alpha_0 - \alpha_t) / \alpha_0 \qquad (4.1)$$

where α_0 and α_t are the absorbance of the MB solutions in the 664 nm wavelength at the initial and any other time, respectively. The experimental evolution of MB degradation as a function of time was fitted with a 3rd degree polynomial:

$$(a_0 + a_1.x + a_2.x^2 + a_3.x^3) \qquad (4.2)$$

The variation of all coefficients (a_0 to a_3) was further fitted in order to provide a complete 3D map evaluation of the MB degradation as a function of time and other variables.

4.4. Results and Discussions

4.4.1. Structural Characterization

Figure 4.1 shows the XRD patterns of the TiO_2 nanoparticles treated thermally at different temperatures (RT, 350, 450, 500°C and 600°C), as well as the two types of commercial materials used as a reference in this study. A broad peak at $2\Theta = 25.6^{o}$, corresponding to the {101} plane for anatase, is observed, and crystal size increases with the temperature (6 nm, 7 nm, 10.5 nm, 10.8 nm, and 19 nm, for RT, 350°C, 450°C, 500°C, and 600°C respectively). The similar diffraction peak broadening analysis for the commercial powders, Sigma™ and Degussa™, led to values of 13 nm and 18 nm, respectively.

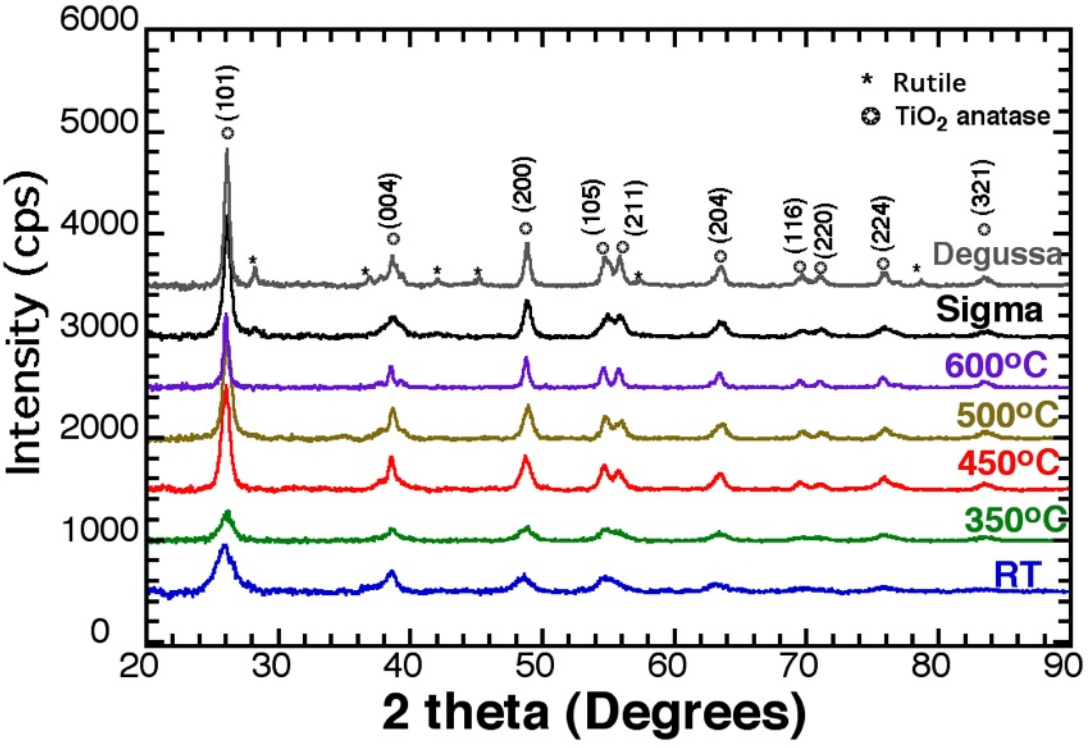

Figure 4.1: XRD patterns for TiO_2 anatase at RT, T350, T450, T500, T600, and commercial TiO_2 (Degussa™, and Sigma™).

The nitrogen isotherm (Figure 4.2) indicates that all samples, (as-synthesised, thermally treated, commercial) have a mesoporous structure with structural porosity marked by a significant specific surface area (ss) and porous volume (vol).

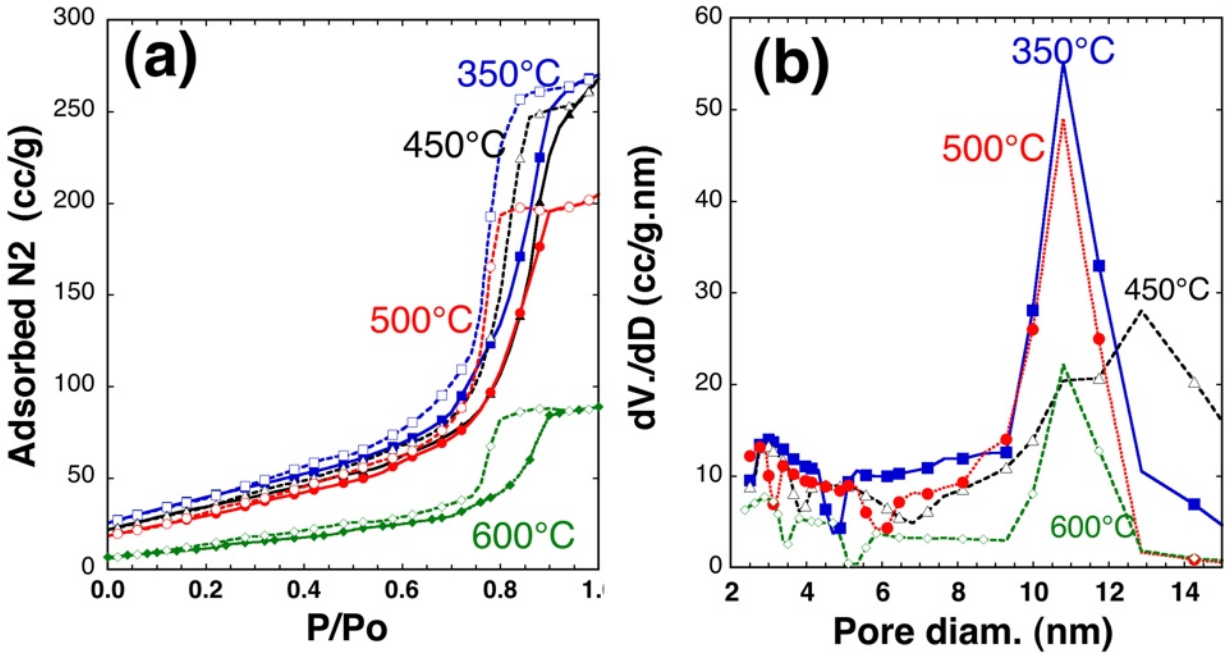

Figure 4.2: N_2 isotherm adsorption (a) and pore size distribution (b) for the TiO_2 anatase thermally treated at different temperatures.

This is observed with T350 (ss: 144 $m^2.g^{-1}$; vol: 0.4 $cm^3.g^{-1}$), T450 (ss: 123 $m^2.g^{-1}$; vol: 0.4 $cm^3.g^{-1}$), and T500 (ss: 109 $m^2.g^{-1}$; vol:0.34 $cm^3.g^{-1}$). The surface area decreased significantly after the sample was calcined at relatively high temperatures, but the major changes appears between 500 and 600°C, with a drastic reduction of specific surface area (ss: 48 $m^2.g^{-1}$) and porous volume (vol: 0.15 $cm^3.g^{-1}$) for T600. FT-IR analysis was carried out to investigate the presence of surface hydroxyl groups (Figure 4.3), and the comparison between the commercial powders and our samples did not display any major difference. FT-IR spectra show a very broad band at 3,400 cm^{-1}, characteristic of O-H stretching of adsorbed water molecules, along with one at 1,630 cm^{-1}, assigned to the H_2O bending mode. A strong and representative broad band attributed to Ti–O stretching modes is seen from 400 to 700 cm^{-1}, and an additional peak due to the O-H stretching mode of titanium-coordinated water molecules is observed at 3,840 cm^{-1}. With a rise in temperature from 25 to 500◦C, the progressive dehydration is illustrated by the reduction of the peak at 3,400 cm^{-1}, owing to the decrease in the surface hydroxyl groups on the surface of TiO_2. TEM observations confirm the nanocrystalline structure (Figure 3.15 (Chapter 3) and Figure 5.2 (chapter 5)).

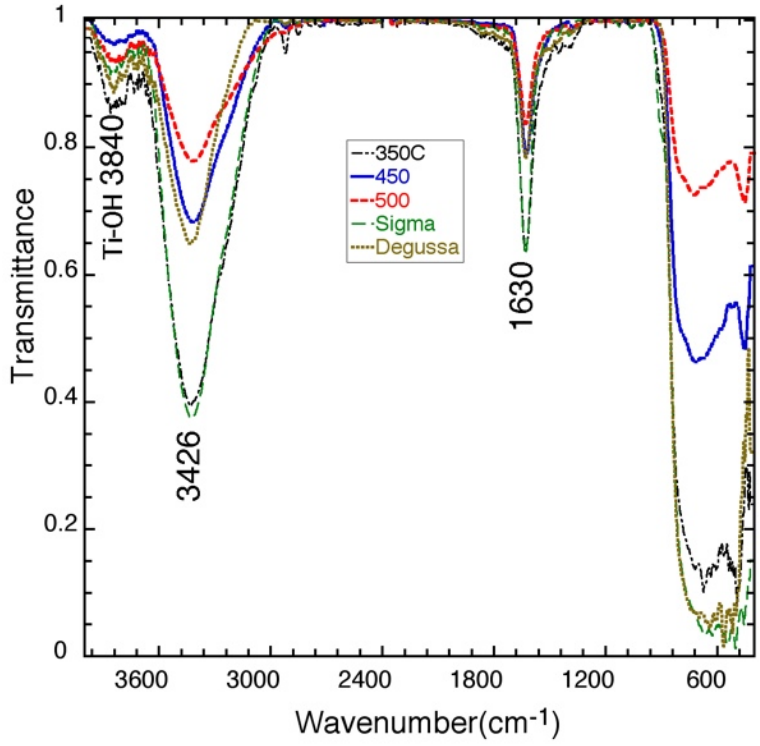

Figure 4.3: FT-IR spectra of T350, T450, T500, and Sigma and Degussa commercial TiO_2 powders

4.4.2. Photodegradation with RT-TiO_2

The potential efficiency of RT-TiO_2 nanoparticles toward MB photocatalytic degradation was verified by several tests of a 20 ppm MB solution with (5, 10, 20, 50, 100 mg in 25 mL) TiO_2, at pH=6 under atmospheric pressure. No dye degradation was observed prior to catalyst loading, as for the MB solution left under UV with no catalyst. Before testing, the MB solutions with a catalyst were kept in the dark overnight, and did not show any measurable decrease in dye absorbance. The MB solution alone, submitted to the same UV irradiation, remained unchanged. The percent of MB degradation as a function of time, for different amounts of RT-TiO_2 (in 25 mL), is reported in Figure 4.4.

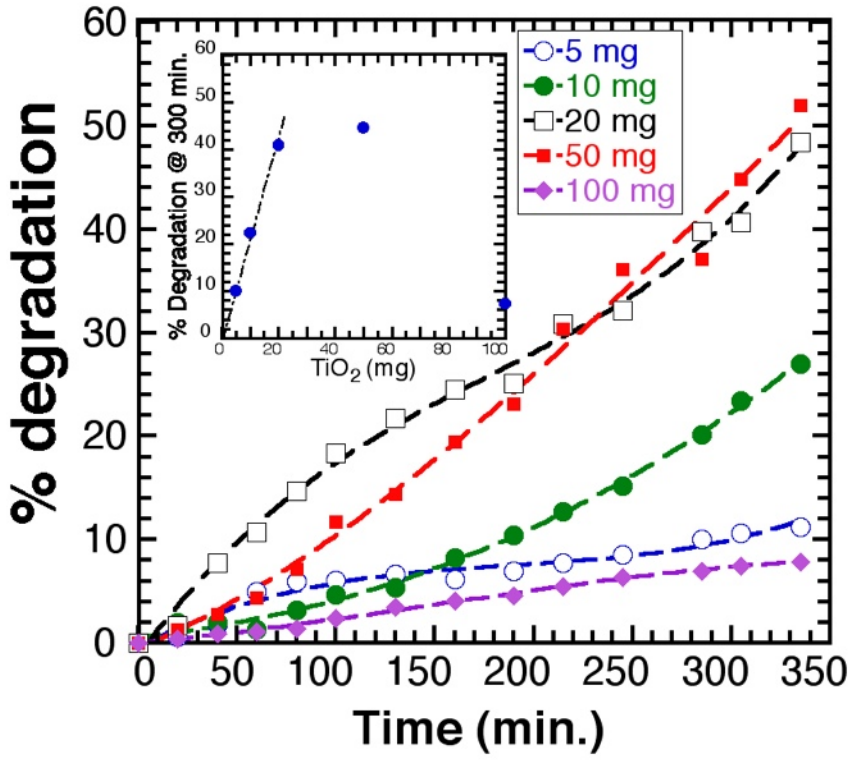

Figure 4.4 Photocatalytic degradation of RT-TiO_2 at different concentrations. Insert: % degradation after 300 min. Lines: 3rd degree polynomial fit.

All suspensions display the same, almost linearly, increasing of MB degradation with time, but the slopes of the curves depend on the amount of TiO_2.From 5 to 50 mg, this photodegradation increases with increasing TiO_2, but the photocatalytic activity of the 100 mg sample is very poor.

We plotted the MB % degradation after 300 min, as a function of the catalyst amount (Figure 4.4, insert): a linear correlation is observed up to 20 mg of TiO_2, as a proof that for the smallest amount, adding a catalyst increases the photocatalytic yield proportionally This effect remains restricted to 20 mg, as seen for the 50 mg sample that does not improve the reaction significantly Moreover, again increasing the TiO_2 concentration up to 100 mg, leads to a limited photodegradation. RT-TiO_2 offers a small particle size and a high specific surface area (190 $m^2.g^{-1}$), which plays an important role in catalytic activity, by providing a higher surface for reaction. As the catalyst concentration increases, TiO_2 will shield light, which will prevent light penetrating further into the reaction vial (the

reacting medium thickness was 0.5 cm, with the UV light on the top). As photocatalysis is a surface phenomena and very sensitive to chemical species attached to the surface or part of the TiO_2 framework, an excess of OH groups not only affects the material band gap,[12] but also causes a detrimental effect on photocatalytic oxidation. However, small quantities are essential for a sustained reaction.[9]

As illustrated in Figure 4.4, MB degradation can be fitted with a 3rd degree polynomial [% (degrad)=f(t)], according to eq.(4.2), and a_0 to a_3 parameters were fitted as a function of the mass of catalyst (Figure B1), and the combination of both fits allowed us to report the 3D modeling of [%(degrad)=f(t, m)] (Figure 4.5). This figure illustrates very well the limits in photocatalysis efficiency of the RT-TiO_2 sample, with a maximum of degradation at 45% after 280 min. and an optimum of catalyst mass around 50 mg.

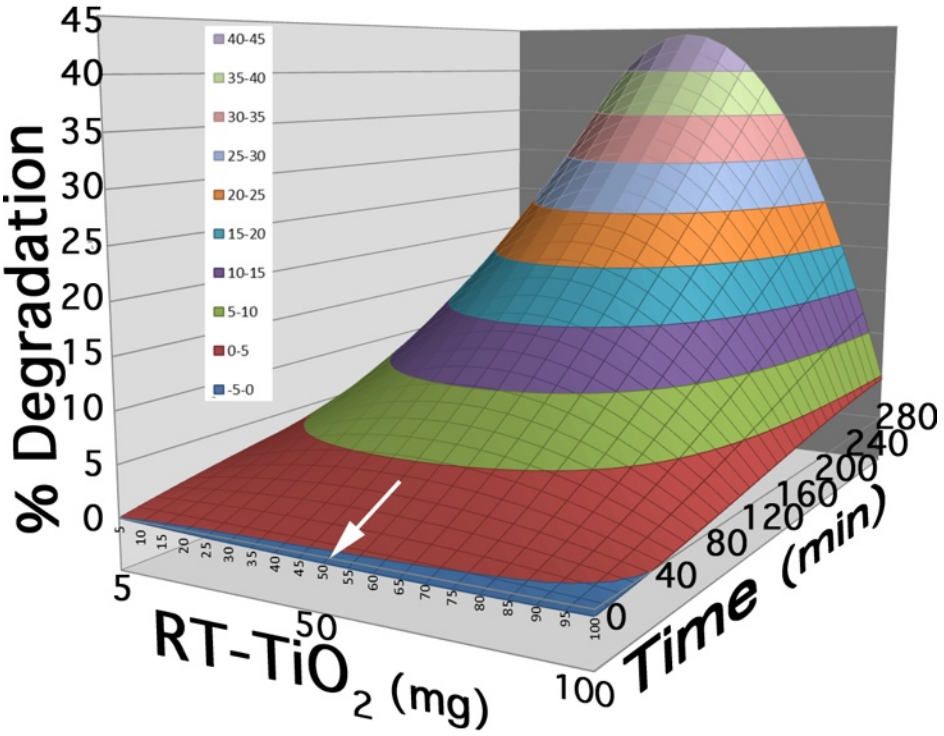

Figure 4.5: Modeling of the MB Degradation as a function of time (0 to 280 min) and mass of catalyst (5 to 100 mg), for RT-TiO_2.

4.4.3. Photodegradation with Thermally Activated TiO_2

The band gap and the number of surface hydroxyl groups have a major effect on photocatalytic activity, and it was demonstrated that TiO_2 prepared with a lower band gap, contributed to increased catalytic activity,[10] as a result of a higher photon absorption. Quantum size effects were thought to be responsible for the high photoactivity achieved on the nanoscale TiO_2 catalysts prepared by sol–gel methods,[9b] and the influence of the semiconductor size on photocatalytic efficiency has been reported in many works.[11]

Therefore, we used our synthesis and the ability to adapt the band gap and crystal size by thermal treatment,[7] to probe the influence of these parameters on the photodegradation efficiency of MB. The relationship between the post-treatment of our material and the resulting band gap was represented in Chapter 3, Figure 3.25 (for comparison: P25 Degussa™ = 3.1 eV; Sigma™ = 3.2 eV).

Figure 4.6 displays the photocatalytic degradation of MB (20 ppm) with a 100 mg suspension of RT-TiO_2 thermally activated at 350°C (T350), 450°C (T450), and 500°C (T500), respectively. Based on previous results, the 100 mg sample was chosen as it exhibits the lowest photocatalytic activity, allowing us to better evaluate any actual improvement. The thermal activation has an effective strong influence on the photodegradation yield, with the best result after 270 min being observed with T450 (90%), to be compared with the 10% yield initially obtained with RT-TiO_2 after the same time. T350 and T500 offer a better efficiency than the RT sample, with 58% and 65.7% degradation after 270 min, respectively, and almost complete reaction after 350 min. The comparison between T450 and T500 demonstrates that the improvement based on temperature activation has a limited effect.

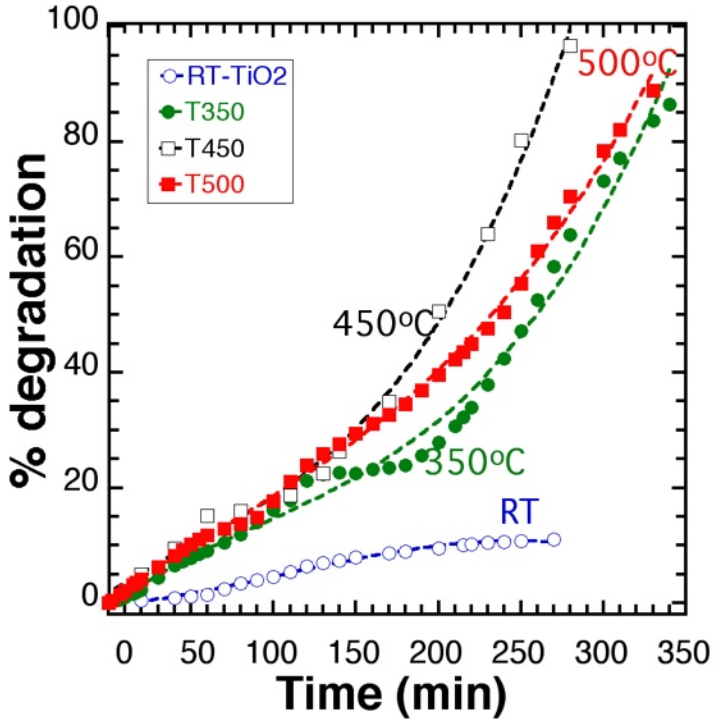

Figure 4.6 Photocatalytic degradation of a 100 mg suspension of TiO_2 (our synthesis) thermally treated at different temperatures. Lines: 3rd degree polynomial fit.

Figure 4.7 displays the whole map of the photodegradation % as a function of time and activation temperature, deduced from the 3rd degree polynomial fitting of experimental curves in Figure 4.5 (see Figure B2 for polynomial parameters fits). This model reveals that as the temperature increases, the reaction yield increases, up to 400-450°C, where it reaches an almost steady value.

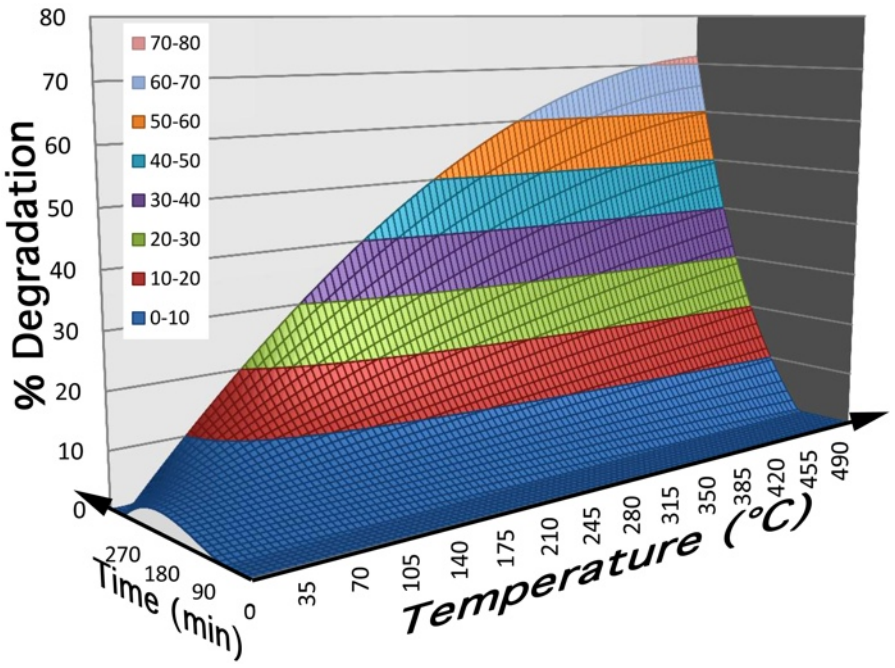

Figure 4.7 Modeling of the MB Degradation as a function of time (0 to 300 min) and temperature of catalyst activation (0 to 500°C), for an initial 100 mg RT-TiO_2 sample.

Applying temperature up to 450°C has a limited impact on crystal size the average crystal increasing only from 4 to 5 nm (Figure 3.23 Chapter 3). However, heat does affect the band gap in a more important way (Figure 3.25 chapter 3), with its value decreasing from 3.2 to 3.1 eV. In parallel, the sample crystallinity increases (Figure 4.1), with a favorable growth of the {00l} family planes (see the {004}), which was identified as the best crystalline planes for photocatalytic activity.[10] As a result, the 450°C thermal activation offers the best compromise between improving crystallinity and reducing band gap without increasing crystal size. The photocatalytic activity of nanoparticles is a surface phenomena, and very sensitive to chemical species attached to the surface of TiO_2. An excess of OH groups causes a detrimental effect of the photocatalytic oxidation, but small quantities are essential for sustained reaction.[16, 21] Hence, the catalytic activity results from a fine balance between crystallinity, surface area and surface nature. Therefore, we deduce that the anatase TiO_2 prepared according to our method and activated at 450°C offers the best compromise, with an optimal quantity of surface hydroxyl groups, and optimal surface area. Additional investigation was done for a thermally

treated sample at 600°C, and the result showed a very low degradation rate and because of the abrupt decrease in the surface area and the amount of hydroxyl groups (Figure 4.8).

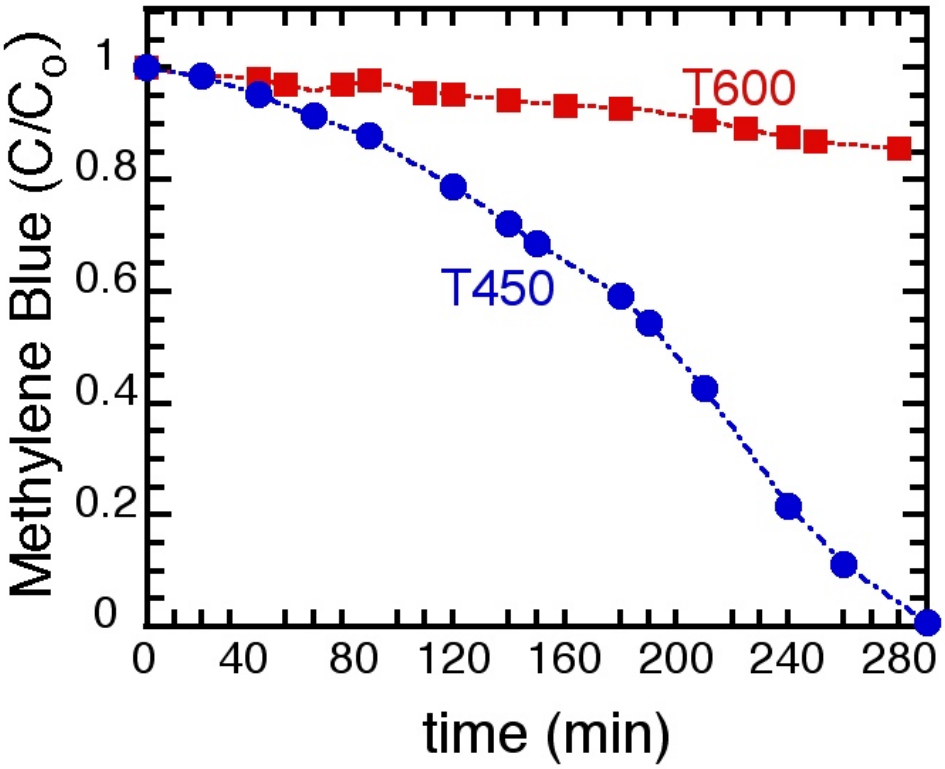

Figure 4.8: Comparison in the photodegradation of Methylene Blue between a 20 mg sample activated at 450°C and 600°C.

4.4.3.1.Influence of the catalyst amount

To determine the optimum concentration of the catalyst so that using an ineffective excess amount is avoided, a series of experiments were conducted for various catalyst concentrations, from 5 mg to 300 mg (for a 25 mL volume).

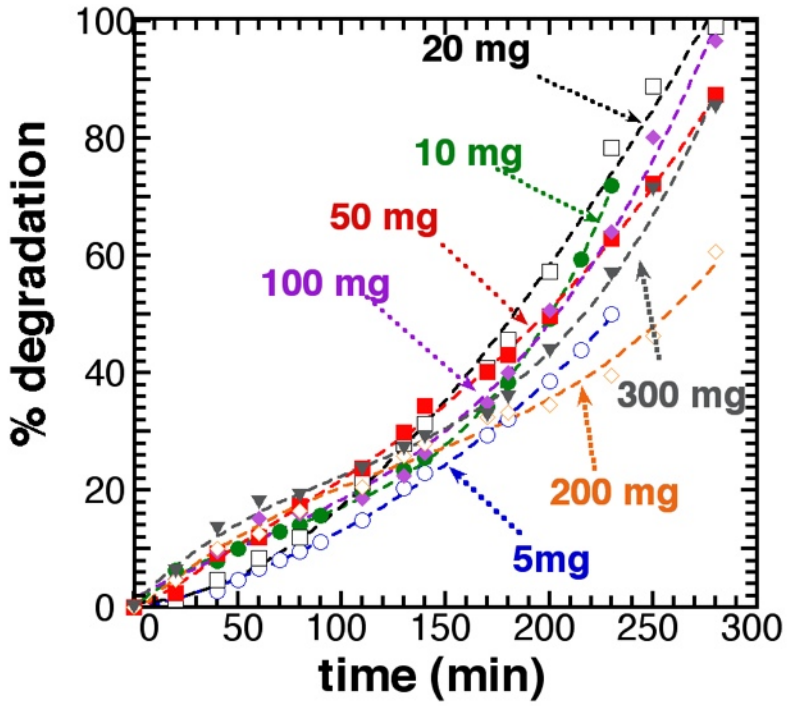

Figure 4.9 Photocatalytic degradation of different mass of T450. Lines: 3rd degree polynomial fit

Figure 4.9 illustrates the effect of catalyst concentration on the photodegradation ratio of methylene blue. Except for the 200 mg sample, which presents a small discrepancy with the whole series, all curves are rather similar, but slightly steeper curves are actually observed for mass of T450 in the 50 mg range. This trend is better illustrated with the 3D mapping deduced from the 3rd degree polynomial fitting (Figure B3) displayed in Figure 4.10.

Compared with RT-TiO_2 (Figure 4.4), the thermal activation at 450°C has almost leveled all the mass effect, and a 100% photodegradation yield is achieved with small amounts of photocatalyst, an optimum being around 20 mg (for 25 mL). Following this observation, all further analyses were carried out with a 20 mg T450 sample concentration.

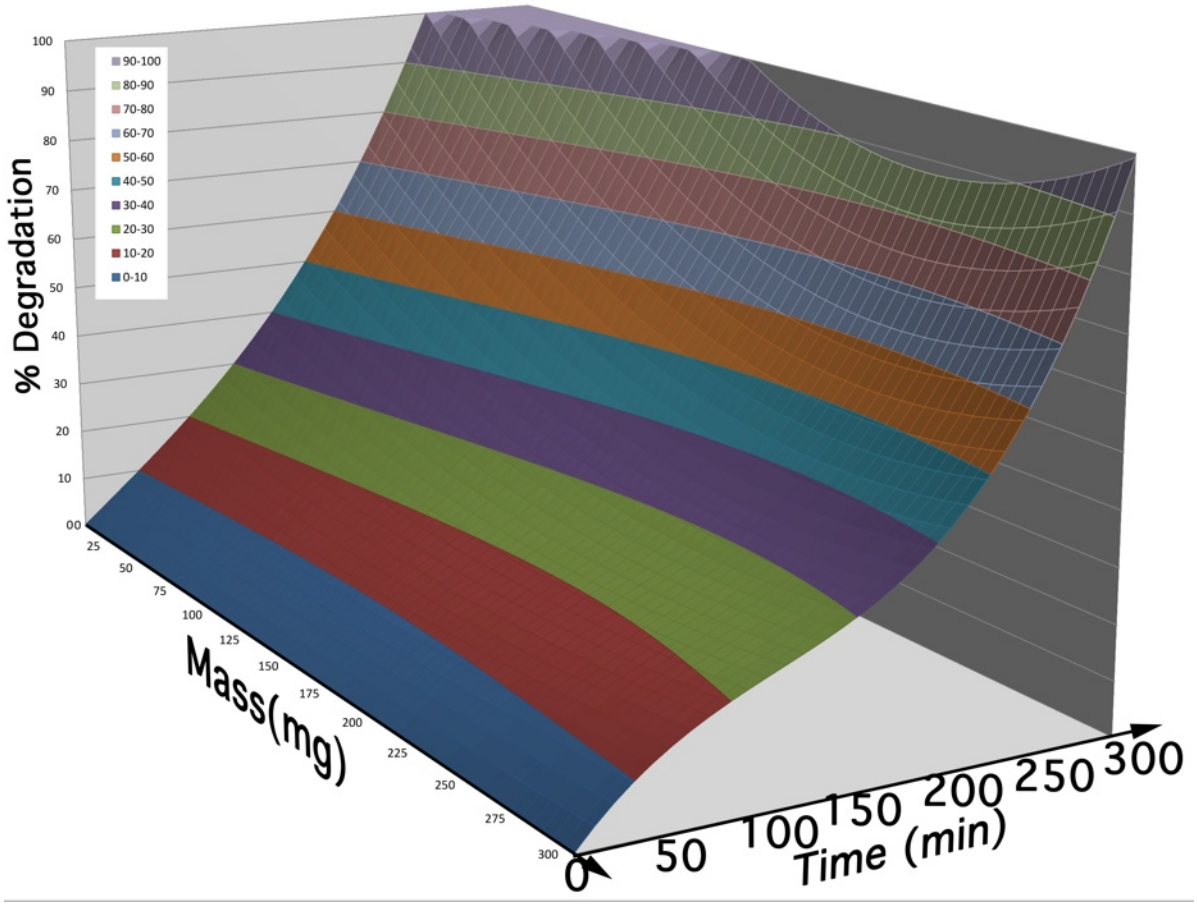

Figure 4.10: Modeling of the MB Degradation as a function of time (0 to 300 min) and mass (5 to 300 mg) , for the T450 sample.

Optimal concentration of the catalyst depends also on working conditions and the incident radiation reflux.[12] According to the rate equation (see hereinafter), the decomposition rate is expected to be directly proportional to the TiO_2 concentration, which seems to be contradicted by our results. However, the concentration of TiO_2 is not the only parameter as the reaction depends both on the availability of active sites on the TiO_2 surface which depends on the nature and structure of TiO_2, and on the intensity of light that actually reaches the surface of the catalyst, which depends on the optical path in the solution.[13] If the concentration of a given material increases, the number of active sites increases, but the light penetration decreases due to the screening effect that masks part of the photosensitive surface.[12c, 14]

4.4.3.2. Kinetic Study

The reaction kinetic of photocatalytic oxidation of dyes over illuminated TiO_2 is determined according to many parameters, for example, light intensity, concentration, and surface area. However, the combined effects of these variables are rather complex and require much in-depth analysis. These kinds of reactions are often described by first-order decay kinetics, and previous studies have shown that the photocatalytic degradation rate of textile dyes in heterogeneous photocatalytic oxidation systems under UV-light irradiation can be well explained in terms of the Langmuir–Hinshelwood mechanism:[15]

$$r = \frac{dC}{dt} = \frac{kKC}{1 + KC} \qquad 4.3$$

where r is the oxidation rate of the reactant, C the concentrations of the reactant, t the irradiation time, k the reaction rate constant, and K the adsorption coefficient of the reactant.

However, for diluted solutions ($C < 10^{-3}$ M), KC becomes <<1, and the reaction is apparently of the first order, whereas for concentrations > 5.10^{-3} M, (KC >> 1), the reaction rate is of the zero order.[32] In addition, the zero order rate was observed for different systems, such as colloidal CdS (E_G=2.4eV) for the degradation of methyl orange,[17] modified doped TiO_2 for the degradation of oxalic acid,[17] and TiO_2 doped by rare earth metals for the decomposition of nitrite.[18] The zero-order rate equation is as follows:

$$r = \frac{dC}{dt} = k \qquad 4.4$$
$$C_t = -kt + C_0$$

where r is the degradation rate of the methylene blue; C_0 and C_t are the methylene blue concentrations at t = 0 and at any time, respectively; and k is the apparent reaction rate constant.

We used a set of experiments, with reaction parameters being [MB]= 20ppm, pH= 6, T=25°C, and T450, and we tested the different kinetic orders expected from the evolution in MB

concentration as a function of time, for a catalyst load, varying from 5 mg to 300 mg (in 25 mL). According to the kinetic order, a linear evolution of Ct=f(t) will mark a zero order kinetic, a linear evolution of Ln(Ct)=f(t) a first order, and a linear evolution of 1/Ct=f(t) a second order. All curves and linear fits are displayed in Figure B4 (A to D), and the reliability parameter R^2 in Table 4.1. Except for the 200mg sample, whose a different behavior was already reported (Figure 4.9), all curves are better fitted with the zero order model, which means that the concentration in MB has no influence on the reaction kinetics. Figure 4.11 displays the evolution of 10^2.k, the apparent rate constant, as a function of the mass of catalyst. This result illustrates that the best conformation for a high kinetic, is obtained by using the T450 material with a concentration of 0.8 g. L^{-1} (20 mg in 25 mL).

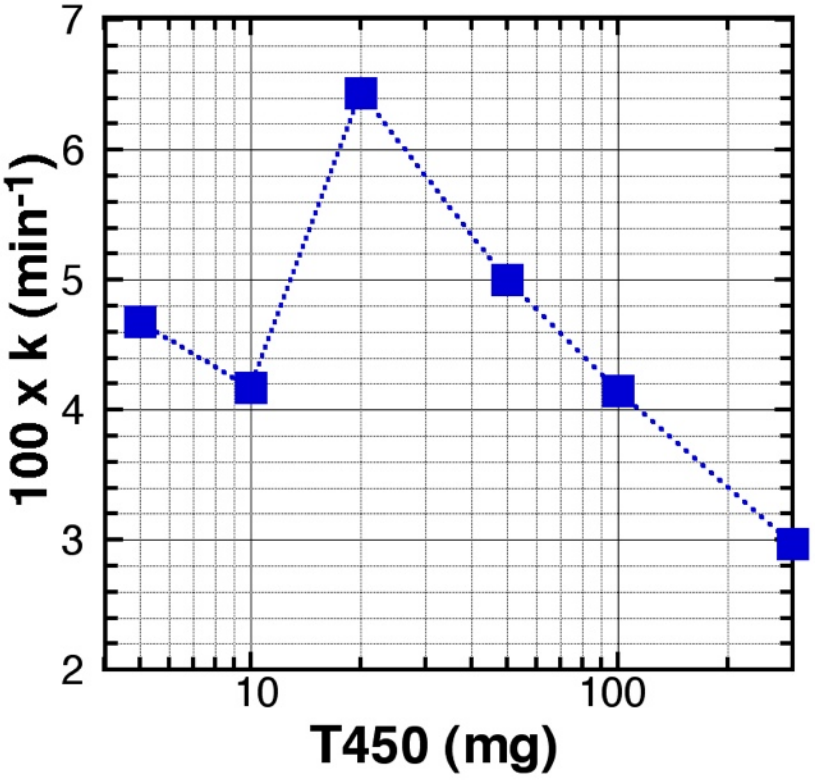

Figure 4.11 Evolution of the apparent rate constant k, calculated for a zero order kinetics, as a function of the mass of T450 catalyst used in 25 mL.

Table 4.I: Reliability Coefficients R^2 of the linear fits for the modeling of a zero-order (Ct=f(t)), first order (Ln(Ct)=f(t)), and second order (1/Ct=f(t)) kinetics (Graphs in Figures S9). Fits were done within the 40-200 min time range selected as the fitting range to avoid initial and final conditions.

TiO_2 (mg)	zero order	first order	second order
5	**0.986**	*0.968*	*0.963*
10	**0.967**	*0.945*	*0.917*
20	**0.966**	*0.920*	*0.867*
50	**0.989**	*0.974*	*0.959*
100	**0.872**	*0.828*	*0.777*
200	*0.981*	**0.982**	**0.982**
300	**0.9338**	*0.904*	*0.869*

4.4.3.3. Influence of the Dye Concentration

We tested the zero-order kinetic model by running photocatalytic tests with 20 mg of T450 in 25 mL, for different initial concentrations in MB (4.8, 9.6 and 20 ppm) (Figure 4.12). The zero order model is confirmed for all concentrations and similar kinetic constants (9.4 10^{-2} and 9.6 10^{-2} min^{-1} for 4.8 and 9.6 ppm, respectively) are found for low concentrations, with actually a higher value for the 9.6 ppm sample. These kinetic constants are higher than that found for the 20 ppm MB solution (6.0 10^{-2} min^{-1}). These differences are not relevant to the photocatalyst itself because it has been demonstrated that the dye concentration has a contradictory influence on the photocatalytic rate.[19] The degradation rate depends on the amount of hydroxyl radical formed on the surface of the catalyst, and the probability of these groups to react with the dye molecules. As a result, as the initial concentration of the dye increases from 4.8 to 9.6 ppm, the probability of interaction between the dye and the hydroxyl radical increases, which results in a higher constant value.

However, further increasing the dye concentration above certain levels decreases the degradation efficiency,[20] because of a higher light screening resulting from the high

concentration in methylene blue. This shielding effect reduces the quantity of effective photons accessing the catalyst surface to produce the electron-hole pairs.[21]

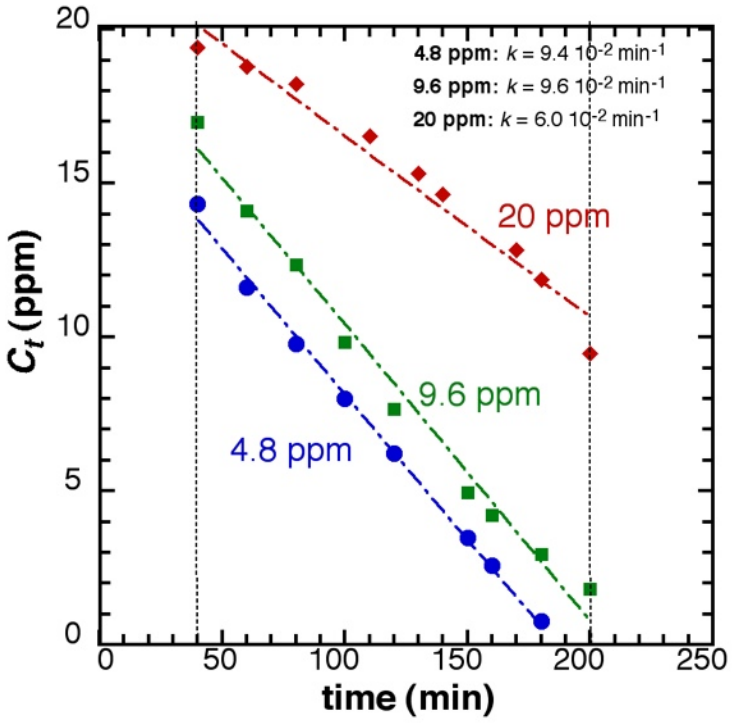

Figure 4.12: Zero order fit of the evolution of the Methylene Blue concentration as a function of time for different values of the initial concentrations in MB (4.8, 9.6, 20.0 ppm), with 20 mg (in 25 mL) of T450.

Hence, it can be concluded that higher kinetics can be achieved with 20 mg of T450 and a concentration in dye of 10 ppm. Nevertheless, it is worth mentioning that the absolute efficiency of the photocatalyst is higher for the 20 ppm solution since 10 ppm are destroyed after 200 min, whereas only 4.8 ppm are destroyed after 180 min for the lowest dye concentration.

4.4.3.4. Influence of pH

As pH is a major factor with a significant effect on the rate of photocatalytic reactions, as it can modify the rate of hydroxyl radical at the surface of the photocatalyst,[22] we carried out photocatalytic tests with solutions set at different pH values (2, 6, and 9) (Figure 4.13). All

other operative conditions remained constant; the T450 catalyst load was fixed at 20 mg in 25 mL (0.8 $g.L^{-1}$), and the methylene blue concentration was set to 20 ppm.

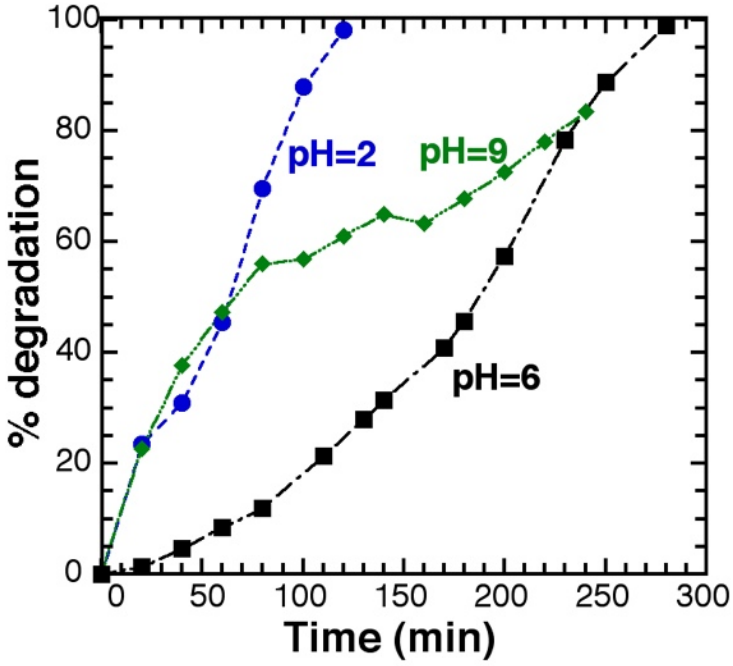

Figure 4.13: Evolution of the photodegradation for T450 (20 mg in 25 mL) at different pH values.

Photodegradation at neutral pH (pH 6), was completed after 300 minutes, and specific adsorption of dye onto the TiO_2 powder is observed (the powder remains white). The same test with basic conditions (pH 9) reveals first a steep increase of the curve, but it is the result of specific adsorption of the dye molecules onto the powder (the powder turns blue). After 120 minutes, the adsorption is completed and only photocatalytic degradation takes place, leading finally to the same reaction time for full degradation as for the neutral solution. The highest degradation efficiency is observed for pH=2, without any noticeable adsorption of the dye, and a full degradation being achieved only after 100 minutes. It is worth mentioning that the initial degradation rate with the same amount of material (RT-TiO_2) and neutral media, led only to a 48% degradation yield after 350 min (Figure 4.4).

Not only does the pH affect the surface state of titania, but also the ionization state of the ionized dye molecule.[23] Interaction between the dye molecule depends both on the pH value

and the Iso-Electrical Point (IEP) of TiO_2. The IEP value is usually reported in the 5.0-7.0 pH range, depending on the origin of TiO_2.[24] Above the IEP, the surface of TiO_2 is negatively charged, and the ammonium group (Scheme 4.1) of the Methylene Blue molecule can interact with. As a result, the dye adsorption increases in the alkaline media as the electrostatic attraction increases between the cationic MB molecules and the negative TiO_2 surface. At low pH, under the IEP, there is no adsorption, but the anionic electron donors and electron acceptors are favored.[21] This effect is limited at very low pH when an excess of H^+ induces a repulsion between the dye molecules and the positive surface of TiO_2. The positive impact of acidic pH (pH 2) combines the formation of free radicals (●$O2^-$, ●OOH) at the surface of the solid, with the creation of intermediate SO_4^{2-} groups in the MB molecule, the result being an enhanced interaction between the negative intermediate sulphate group on MB, and the positive charge on TiO2. This interaction that improves the whole photodegradation process as MB molecules are stabilized on the TiO_2 surface until full degradation.

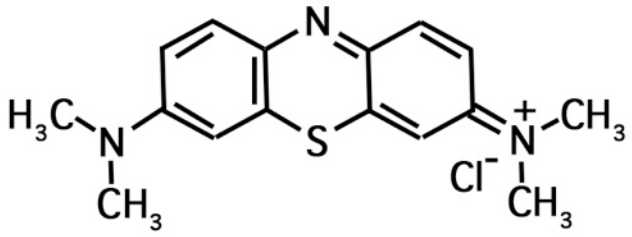

Scheme 4.1: Structure of Methylene Blue

4.4.4. Comparison With Commercial TiO_2

Experiments were carried out under UV with 20ppm dye concentration and 0.8 $g.L^{-1}$ (20 mG in 25 mL) catalyst load at two different pH values (2 and 6), over T450, and compared to two commercial titania oxides: Sigma™, which is pure anatase, from Sigma™, and a 30% rutile: 70% anatase material from Degussa™ (Figure 4.14). The commercial anatase (Sigma™) was chosen as it has the same specific surface area (126 $m^2.g^{-1}$) as T450, and as the Degussa™ product at present is the best commercial photocatalyst, and thus is always taken as a reference.

When compared with Sigma™ (Figure 4.14.a), T450 exhibits a better photocatalytic efficiency, whatever the pH, even if both the crystalline nature and the specific surface area are similar for both. Close comparison of the two XRD patterns (Figure 4.1) reveals similar diffraction patterns, except for one peak, at 38 degrees, where the crystal growth was enhanced along the [001] direction with preferred anisotropic growth perpendicular to the c-axis.[25] This growth is indicated by the strong peak intensity and narrow width of the (004) reflection for T450, whereas a relatively lower intensity and broader width for Sigma™ is reported.

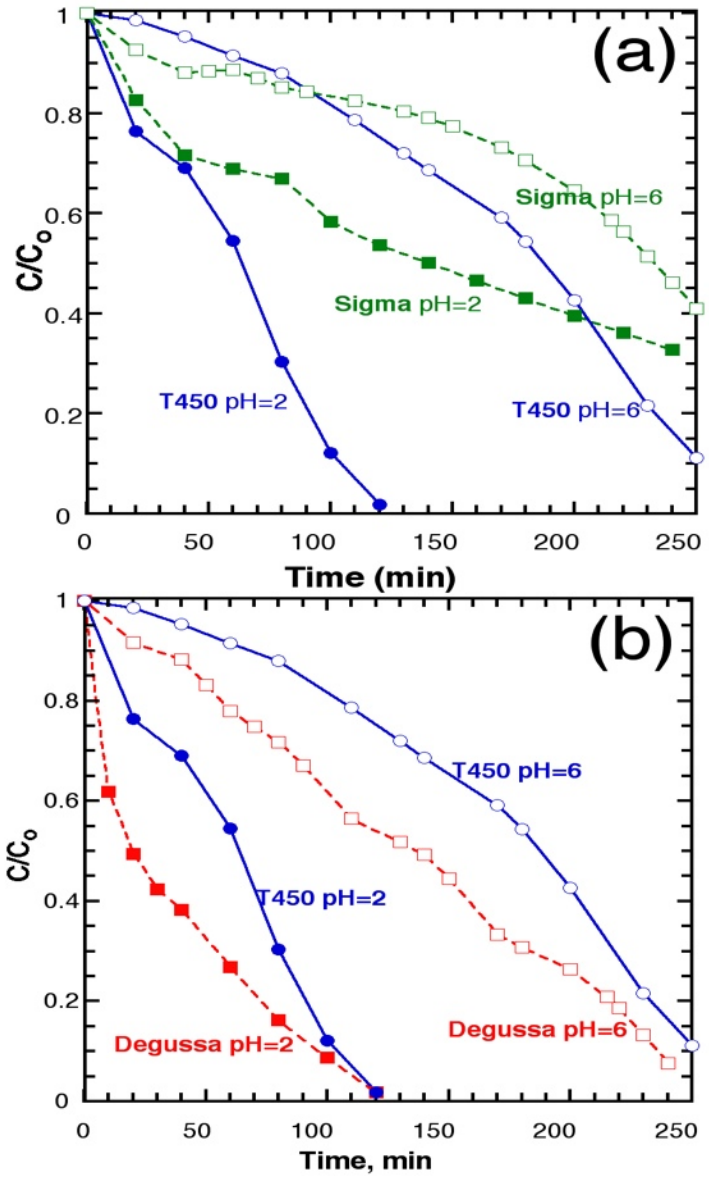

Figure 4.14 Evolution of the concentration in MB, normalized to the initial value, as a function of time, for T450 and (a) Sigma™ titanium oxide and (b) Degussa™ titanium oxide.

It has been widely reported that the (001) plan is more active than the (101) plan, owing to the low atomic coordination numbers of exposed atoms and the wide bond angle of Ti-O-Ti.[26] Zhang et al. reported that the (001) plan for anatase TiO_2 microspheres is 1.5 time more active than the (101) of the same spheres.[27] Therefore, we think that the main reason for the higher

photocatalytic activity of our sample (T450) compared to the commercial one (Sigma™) is the difference in crystal growth.

We also compared our sample T450 to another commercial TiO_2, Degussa™, which is a combination of anatase and rutile (Figure 4.14.b). This test reveals that the Degussa™ photocatalyst shows a better photoactivity throughout the reaction than T450, at pH 6, but both achieve almost full degradation after 250 min. At pH 2, the rate of reaction is higher for Degussa™ than T450, for the first 60 minutes, but again, T450 compares well with the reference, at the full completion of photodegradation.

Overall, the Degussa™ materials still offer a better photodegradation rate, especially at the beginning of the reaction, which can possibly be ascribed to the specific anatase/rutile heterostructure displayed by this material. Owing to the difference of the band edges between anatase and rutile where the anatase is more negative (0.2 eV), rutile works as an electron sink that facilitates the interfacial electron transfer. The oxygen molecules, forming superoxide radicals to oxidize the dye molecules, can scavenge the photogenerated electrons coming from the anatase conduction band to the rutile conduction band. On the other hand, the holes on the anatase valence band can also oxidize the dye molecules; consequently, the charge carrier separation efficiency increases, leading to an improvement of the catalytic activity. Moreover, rutile can play the role of an antenna that transfers the photoelectrons from rutile to anatase trapping sites that have lower energy.[28]

We also tested the effect of increasing the catalyst load to 100mg on the degradation efficiency at pH=6 and by comparing commercial powders with T450 (Figure 4.15). As we increase the catalyst load to 100mg, all activities become normalized by the light shielding effect, and the photocatalytic efficiency is limited by light instead of the material performance.

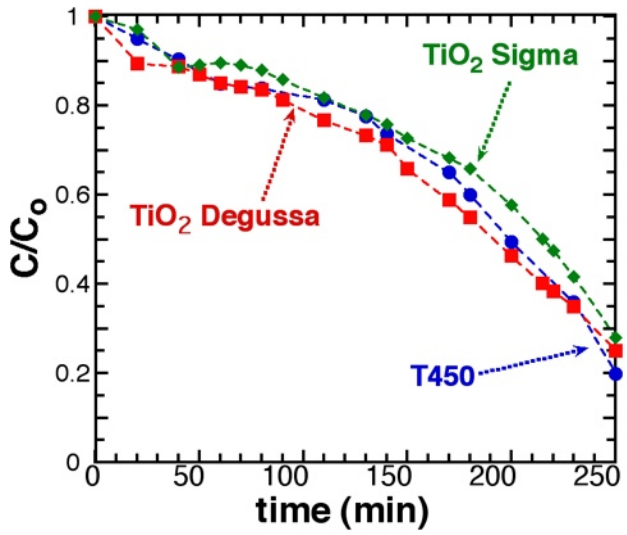

Figure 4.15: Comparison of the evolution of the concentration in Methylene Blue for TiO_2 Sigma, TiO_2 Degussa, and T450 (experimental conditions: 100 mG material in 25 mL, pH 6, MB: 20 ppm).

4.5. Conclusions

The pure anatase titanium oxide synthesized for this study has demonstrated very efficient photocatalysis, equal to that of the commercial material used as a reference, when both material and process parameters are optimized. These parameters are (i) a small size of particles that allow for a high surface access, (ii) an improvement of the crystalline structure by suitable thermal treatment that allows enhanced crystallinity without increasing the crystal size, (iii) an amount of catalyst that does not limit the whole reaction but does not shield light, (iv) if possible, a mild acidity to favor the creation of radicals. When all these parameters are optimized, the photocatalytic behavior is, overall, similar to that of the best commercial material (Degussa™ P25), which exhibits in addition a rutile:anatase heterostructure. This heterostructure is very important to improving the stability of the electron-hole pair. Therefore, our next work will explore the possibility of generating heterostructures from the pure anatase TiO_2 material tested in this study.

Chapter 5:
Testing and Assembling of DSSCs

5.1. Overview

DSSCs have attracted great attention in recent years as they possible alternatives to conventional silicon solar cells due to their low–cost raw materials, cheap production, and high conversion efficiency. To date, most of research related to increasing DSSC efficiency has been conducted to improve the components (photoanode, dye molecule) or to allow for move from laboratory settings and small–scale devices (rigid cells with liquid electrolyte) to larger scale roll-to-roll manufacturing (flexible cells with solid electrolytes). Despite tremendous advances, there is still place for specific studies dealing with the components of DSSCs: TiO_2 (the electron transporting layer), dye (the photosensitizer), electrolytes (the electron transfer mediator), and counter electrodes (including possibly a catalyst for electron transfer). We demonstrated in the previous chapters that TiO_2 plays an important role in DSSCs, because it is the core component where almost all reactions take place, which explains why not only the chemical nature, but also the nanostructure are especially important for a good synergy among components and reactions. After Chapter 3's description of a new synthesis method and how reaction parameters can modulate both the nature and structure of the material, and after Chapter's 4 complete study of the influence of the material and additional treatments on its physico-chemical properties, we now explore how this new type of nanocrystalline TiO_2 actually acts in a DSSC. At this stage, it is worth mentioning that the nature and structure of the initial material, but also the method used for shaping the photoanode, and the resulting quality of electrical contacts, are essential for successful testing. Within the timeframe allowed, we could not carry out this study with the preparation of cells that would provide statistical validity. Therefore, we tried first to confirm that our material could be used in DSSCs, and we compared its performance with those of well-known commercial materials prepared with the

same method as ours. In a second step, we started to explore how various methods of preparing the photoanode influence the final properties of the photovoltaic cell.

The influence of the TiO_2 film structure on cell performance was evaluated via different macroscopic parameters such as the current density (Jsc), open circuit voltage (Voc) and fill factor (FF). Here, the effect of the preparation method on textural, structural, and electrical properties of the photoanode were analyzed. The nature and structure of the material was checked in parallel by the usual techniques: the phase purity was characterized by XRD, porosity and surface roughness were investigated by N_2 adsorption. The amount of N907 dye adsorption onto the anatase surface was examined by FT-IR absorption spectroscopy using a multiple internal reflection technique. As the counter-electrode also plays a role in the cell efficiency , we tried to optimize its structure, and the composition and surface morphology of the Pt thin film was checked by SEM with energy dispersive X-ray spectroscopy (SEM/EDX). Cells were finally characterized at 1.5AM sun using a solar simulator under 100 mw/cm^2 light intensity.

5.2. Introduction

Dye sensitized solar cells (DSSCs) have attracted great attention in the scientific community as promising alternatives to conventional photovoltaic devices since it was demonstrated that the correct combination of materials (dye molecule and semiconductors) and their optimized assembling could allow for significant photovoltaic yields.[1] In contrast to silicon-based conventional solar cells, the light absorption and current production in DSSCs occurs though a complex multi-step mechanism: the dye-molecules are the photoactive centers where electrons are produced, but these electrons must be transferred to a photoanode made of a semiconductor material - generally TiO_2 anatase- coated onto a TCO (Transparent Conductive Oxide) electrode, that prevents the direct recombination of the electron-hole pair generated in the dye. The electrons extracted from the dye, are compensated by the oxidation of the I^-/I_3^- redox couple, present in the electrolyte. After the electrons have circulated through the external circuit, there are

injected back via the counter-electrode, into the electrolyte and reduce the I^-/I_3^- redox couple. As a result, the improvement of the photoconversion efficiency of the cell is controlled by many factors along the electron circulation loop, and all cell components must be considered for cell optimization, as well as their integration. Along with the discovery of new photoactive molecules and improvement of the electrolyte, the optimization of the titania-based photoanode, in term of nature, hierarchical structure, and electrical contact, still remains one of the major challenges in the field.[2]

Regarding the photoanode, beyond the nature of the material itself, many factors contribute to reduce the photoconversion efficiency. One of them is the poor electrical contact between the TiO_2 layer and the TCO layer. This contact can be improved by the creation of a thin interfacial layer directly onto the TCO film, before adding the nanocrystalline TiO_2.[3] Another factor is the insufficient amount of dye, which is directly relevant to the total surface area of the TiO_2 layer, and to the density of anchoring site on TiO_2. This latter can be increased by specific surface treatment that helps to protonate the TiO_2 surface before dye adsorption. The quality of the dye anchoring onto the TiO_2 surface is also increased with UV-treatment that cleans the surface from remaining organics,[4] and the strength of the dye-TiO_2 interaction is usually increased by acid treatment, as a result of TiO_2 protonation.

Nanocrystalline materials have been widely used as powerful materials for photoelectrode in DSSCs as they have astonishing physical and chemical properties, especially their nanosize and their high specific surface area that allows high dye loading.[1a, 5] Being able to reduce the size of particles used for the TiO_2 film, influences positively, not only the amount of dye adsorbed onto the surface, but also the dye-to-TiO_2 charge transfer. This affects also negatively the total internal resistance of the cell as more grain boundaries are created per unit of volume, and as the small size reduces the light internal reflection. The electronic conduction in the protonated TiO_2 film–usually made of 20 nm TiO_2 particles–is the result of a complex mechanism. First, the presence of both dye cations and iodine species, with the resulting formation of a positive layer on the surface of titania, creates a Helmoltz double layer

screening shell around the particles, which contributes to reduce the charge-hole recombination in TiO2.[6] It is also stated that the electrons are diffusing along the surface of the particles, as a result of a short screening Debye length (1.5 nm).[6] If this limits the electron diffusion to a surface process for particles larger than 10 nm, we could wander the effect of using smaller (sub-10 nm) nanoparticles, and if the whole volume will be used for conduction.

We reported previously the room temperature synthesis of pure anatase with crystalline domains in the 4-10 nm range,[7] and the semiconducting properties of this material were enhanced by the suitable thermal treatment that improves the crystallinity without increasing the crystalline domain.[8] The present work reports how this new type of titania anatase can be used in DSSC applications. We made sure by testing different methods to improve the structure and connection of the final TiO_2 photoanode, that the assembling process could lead us to a straight evaluation of our materials, and provide a comparison with commercial compounds assembled with the same method.

5.3. Experimental Work

5.3.1. Materials

Hexachloroplatinic acid hexahydrate ($H_2PtCl_6 \bullet 6H_2O$, ACS reagent, 37.50% Pt basis) was purchased from Sigma-Aldrich. FTO (Fluorine-doped Tin Oxide) glass, 2.2 mm thickness with a sheet resistance of 15 $\Omega.cm^{-2}$, Iodolyte Z-50, 50 mM of tri-iodide in methoxypropionitrile and additives of ionic liquid, alkylbenzimidazole, and guanidine thiocyanate, Platisol T(transparent platinum catalyst paint); and Meltonix 1170-60, a 60 microns thick thermoplast hot-melt sealing foil, were purchased from Solaronix. Different organic additives were tested as adhesive and plasticizers of the TiO_2 photoanode film: (i) a mixture of Span 80 (Sorbitan monooleate, d = 1.08, Mw = 428.6 g; Across) and Tween 20 (polyoxyethylene (20) sorbitan monooleate , d= 0.994, Mw =1,310 g; Sigma), (ii) polyethylene glycol 12000 (PEG 12000, Alfa Caesar), (iii) Pluronic P123 ($PEO_{20}PPO_{70}PEO_{20}$, Aldrich). The photoactive molecule was a cis-Bis(isothiocyanato)(2,2'-bipyridyl-4,4'-dicarboxylato)(4,4'-di-nonyl-2'-bipyridyl) ruthenium(II) (Z907 dye, Sigma). All were used without further purification.

5.3.2. Synthesis of TiO_2 Nanoparticles

A specific composition was chosen within the phase diagram, between the (*A*) and (*J*) data points within the working area for the preparation of pure TiO_2 anatase (Figure S1 in ESI), described previously.[7] In a typical synthesis, 2.9 mL of HCl was added drop-by-drop within 5 min under vigorous stirring (200 rpm) to 5 mL of Ti(O-n-Pr)4 left in an ice bath. Then, 2.86 mL formamide (FA) and 2.17 mL deionized water were mixed before being added drop-by-drop to the previous solution within 15 min. After full addition, the sample was left for ageing in a thermostated bath at 30°C for 24 h. The solution experienced a phase separation during this ageing phase, with a physical gel formed at the bottom and a supernatant liquor on the top. The gel container was covered and left at 60°C for one week before drying. Ammonium chloride, a byproduct of the reaction, was removed by washing the sample three times with 100 mL of deionized water, the powder being recovered by filtration afterward. At this stage, the gel could easily be dispersed in water by sonication. The nanopowder was finally calcined either at 350°C or 450°C, (4 h, 100°C.h^{-1} ramp) temperatures across the expected optimum for bandgap and crystal size with the most efficient energy absorption.[7-8]

5.3.3. Synthesis of the TiO_2 Paste

The paste was prepared by mixing the TiO_2 powder obtained during the previous step, with different organic additives. The addition of the organic additives was proceeded according to two methods. For PEG 12000 or Pluronic P123, 0.35 g was first dissolved into 5 mL EtOH, then mixed with a suspension of 1.0 g of TiO_2 dispersed into 10 mL of EtOH. The resulting mixture was left at 100°C for 24 h, in a sealed vial. The vial was further cooled down before using the paste. A mixture of Span80/Tween80 was prepared with the aim to obtain a final Hydrophilic Lipophilic Balance (HLB) of 13.6,[9] and 0.035g of this mixture (equiv. one to two drops) was directly added into a suspension of 1g TiO_2 in 10 mL acetic acid. The resulting paste was ground in a mortar to ensure good dispersion of the organics among the solid phase.

5.3.4. Preparation of the TiO_2 Film

The FTO glass was cleaned in four steps: first washing with soap then with DI water for 20 min each step. The glass was then rinsed in acetone and put in the ultrasonic bath for 10 min. The final step was to rinse the glass in alcohol (t-butanol) and sonicate for another 10 min. To clean the surface more and provide a hydrophilic effect, a UV_O3 technique was applied for 30 min. The FTO glass was immersed in 40mM TiCl4 at 70°C for 30 min to create a blocking layer (for comparison; other samples were made without it). The film was coated onto a FTO glass substrate, with doctor-blade method. The film thickness was controlled by the hight of a 17 µm *3M* adhesive tape, and the paste was spread with a glass rod over the space between the tape strips. The electrode was left to dry at 80°C for 3hrs. The electrode was calcined at 450°C for 30min, and then it was immersed in 0.1M HCl aqueous solution for 2 hours. In place of the thermal treatment, some electrodes were exposed to an intense (300 W/inch) UV light for 20 min, before being immersed in the HCl solution. All electrodes were further grafted with the Z907 dye molecule. Adsorption of the dye was undertaken by immersing the TiO_2 electrode overnight in a 0.4 mM dye in 50:50 vol. t-butanol: acetonitrile solution. The grafted electrodes was finally washed with acetonitrile to remove the excess of dye.

5.3.5. Counter Electrode Preparation

The presence of Pt nanoparticles at the surface of the counter-electrode is mandatory to achieve the reduction of the iodide/triiodide couple.[10] Two methods were used for the preparation of the Pt counter electrode. The first one used a commercial platinum paste (Platisol-T, Solaronix) used as received and fired at 450°C for 30 min in order to remove organic binders. the second method used hexachloroplatinic acid as a Pt precursor, reduced to platinum by the polyol reduction method.[10-11] In a typical synthesis, a 15 µL ethanol solution 0.01M of $H_2PtCl_6 \cdot 6H_2O$ was poured at room temperature onto a 5*5 cm^2 FTO glass substrate. The drop sprayed out spontaneously, and the solvent was totally evaporated by air drying followed by a 10 minute heating at 80°C on a heating plate. Then, 35 µl of ethylene glycol (EG) was added, and the temperature of the heating plate

was raised gradually up to 170°C. The adhesion of the Pt layer on the FTO substrate, obtained by either of these two methods, was investigated by a sonication test. The electrode was immersed in DI water, and alcohol, then sonicated for 20 minutes, without any noticeable wrenching of the Pt layer from the substrate. The thickness of the Pt layer was around 20 nm, a good compromise between conductivity and catalytic activity .[12]

5.3.6. Cell Assembly

The Pt electrode and the dye-adsorbed TiO_2 electrode were assembled as a sandwich-type. The redox electrolyte was introduce to the cell by capillary action.

5.3.7. Instruments

X-ray diffraction (XRD) was recorded on a Bruker D8-Advance powder diffractometer using Cu Kα radiation (λ = 1.5405 Å) operating from 2θ = 10–90 degrees. The N_2 adsorption isotherms were measured with a Quantachrome AUTOSORB-1. The samples were outgassed at 200°C under vacuum for 12 h before measurement. Surface area was determined by the BET method in a relative pressure range of 0.05−0.25. Pore size distribution was calculated with the Broekhoff and deBoer Model applied to the desorption branch.[13]Surface area was determined by the BET method in a relative pressure range of 0.05−0.25. Pore size distribution was calculated with the Broekhoff and deBoer Model applied to the desorption branch. [13]Porosity was calculated by using the following equation:[14]

$$P = V_p \Big/ (\rho^{-1} + V_p) \qquad 5.1$$

Where V_p is the specific cumulative pore volume calculated from desorption branch observed in the N_2 isotherm adsorption/desorption, $cm^3.g^{-1}$, ρ^{-1} is the inverse of the density of TiO_2 (anatase), ρ=3.89 $g.cm^{-3}$.

UV−vis absorption spectra were collected with a Varian Cary 5000 UV−vis-NIR spectrophotometer. Quartz cuvettes (Spectrosil, Starna Cells Inc.; transparency 170−2700 nm) and the 1 cm optical path length were used to measure the electronic absorption spectra. The UV−vis spectra were corrected from nonspecific absorption before analysis. TGA was carried

out using a Q600 TA Instrument. Measurements were taken with a heating rate of 10 °C/min, from 25 to 800 °C in air. In order to measure The relative quantity of the Z 907 dye chemisorbed on TiO_2 was measured by attenuated-total-reflection Fourier Transform Infrared spectroscopy (ATR -FTIR, Pike Technologies,),[4c, 15]using a ZnSe crystal (**n** = 2.42). Cyclic voltammetry behavior between -0.25 and 1.2 V (vs. Ag/AgCl) was recorded with a a three-electrode electrochemical cell in a 0.5 M H_2SO_4 aqueous solution, using platinum wire as the working electrode and Ag/AgCl as the reference electrode. When required, the TiO_2 films were exposed to UV light irradiation with a F300S from Fusion UV Systems Inc. (300 watt/inch microwave-powered electrodeless lamp with power supply model P300MT). TEM imaging was performed with FEI Titan 80-300 microscope (FEI company, Eindhoven, The Netherlands), operated at 300 kV. The specimens were prepared by dropping dilute suspensions of colloidal TiO_2 in methanol on a standard copper TEM grid containing lacy carbon.

The I-V measurements of the DSSCs employed an 1.5 Am solar simulator ($100mWm^{-2}$) equipped with(filter) between the sample and a 75W xenon lamp. The power of the simulated light was calibrated by using a reference Si photodiode. The Photovoltaic characteristics of the DSSC were obtained by applying an external potential bias to the cell and measuring the generated photocurrent in Keithley (source meter).

The impedance measurements were performed using SI-1287 electrochemical, and SI-1260 impedance analyzer interfaces, with a Solartron FRA, working in the potentiostate/galvanostate mode with a 0.01-10^5 Hz frequency range and 0.2V ac amplitude under dark and 100 W light conditions. The measurements were carried out after the open circuit voltage had been stabilized. The obtained spectra were fitted with Z-View software (v2.8d, Scribner Associate, Inc.) in terms of the proposed equivalent circuit. The parameters for the circuit were optimized to ensure the best fit of experimental data.

The UV-Ozone (Phantom II RIE designed by Trion Technology Inc.) working under 20m Torr pressure, 100 RF power, 0 DC power. The oxygen flow was 20 cm^3 for 900 sec.

5.4. Results and Discussion

5.4.1. Nanostructure of TiO_2

We demonstrated that the crystallinity of the TiO_2 nanoparticles synthesized according to our process,[7] can be improved without any dramatic crystal size change, if they are heated in the 400°C temperature range. In parallel, thermogravimetric analyses confirm that a thermal treatment at 350°C or above, allowed us to remove both physi- and chemisorbed water, which is compulsory for use in DSSCs (Figure 5.1). TEM analysis (Figure 5.2) confirm that the crystallinity of the TiO_2 nanoparticles increases from 350 (Figure 5.2.a) to 450°C (Figure 5.2.b) –see diffraction in the inset–, without major crystal change, and the crystal size start to increase at 500°C (Figure 5.2.c). A close observation by HR-TEM on 450°C samples (Figure 5.3) confirms the average size of 10 nm for crystallites at this temperature,[7] with high crystallinity: d-spacings are equal to 3.62 Å and 2.1 Å for the (101) and (200) planes, respectively. These values are slightly higher than those for bulk anatase, but in the usual value range reported in literature for nanocrystalline TiO_2.

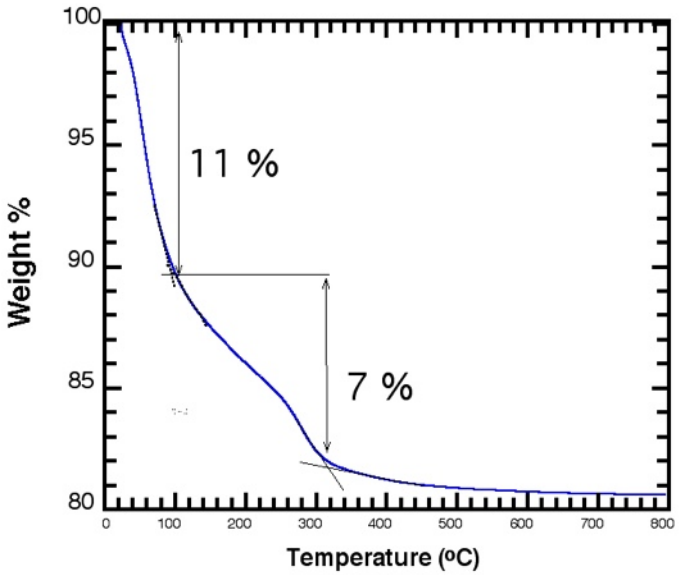

Figure 5.1: TGA analysis of the as-synthesised TiO_2 nanocrystals. The 18 wt% weight loss corresponds to the water departure.

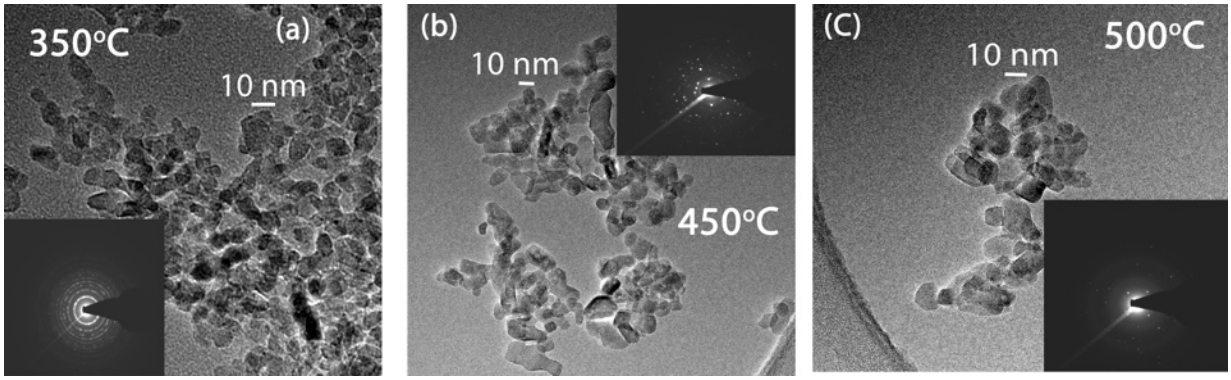

Figure 5.2: TEM micrographs of nanocrystalline TiO_2 anatase activated at (a) 350°C, (b) 450°C, and (c) 500°C. Inset: diffraction patterns.

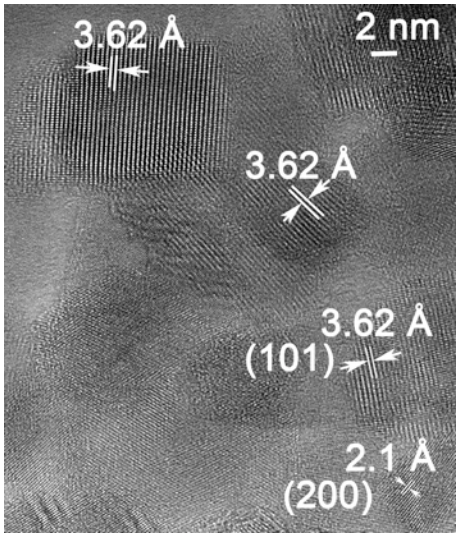

Figure 5.3: HR-TEM of TiO_2 anatase nanocrystals after the 450°C thermal treatment.

We checked also how the different treatments (thermal activation, UV treatment, different organic additives) applied to the TiO_2 layer could affect the structure of nanoparticles themselves. Figure 5.4 displays the TEM observation of titania particles initially activated at 350°C (4 h), after different additive treatments required for the film formation. Different organic additives (Pluronic P123, Polyethylene glycol 12,000 and a Tween80/Span80) were mixed with the powder to facilitate the film formation, and the films were cured by either thermal treatment (450°C, 30 min) or high intensity UV (300 W/in, 15 min). Whatever the additive, and curing treatment, the nanostructure of TiO_2 particle appears to remain stable and similar to the pristine material (Figure 5.2.a). No isolated particles were found in the

observation, indicating firm attachment of the particles, which favors the film formation and mechanical stability. The XRD was done for the film on the FTO glass substrate, relatively broad diffraction peaks of the anatase structures appeared in the mesoporous TiO_2 [identified by the (101) peak at $2\Theta = 25.2^o$] as shown in Figure 5.5. The results of both XRD and TEM prove that the TiO_2 samples are crystalline,and have anatase phase, as indicated by the presence of diffraction peaks in Figure 5.5 and the presence of an anatase diffraction rings in the insets in Figure 5.4.

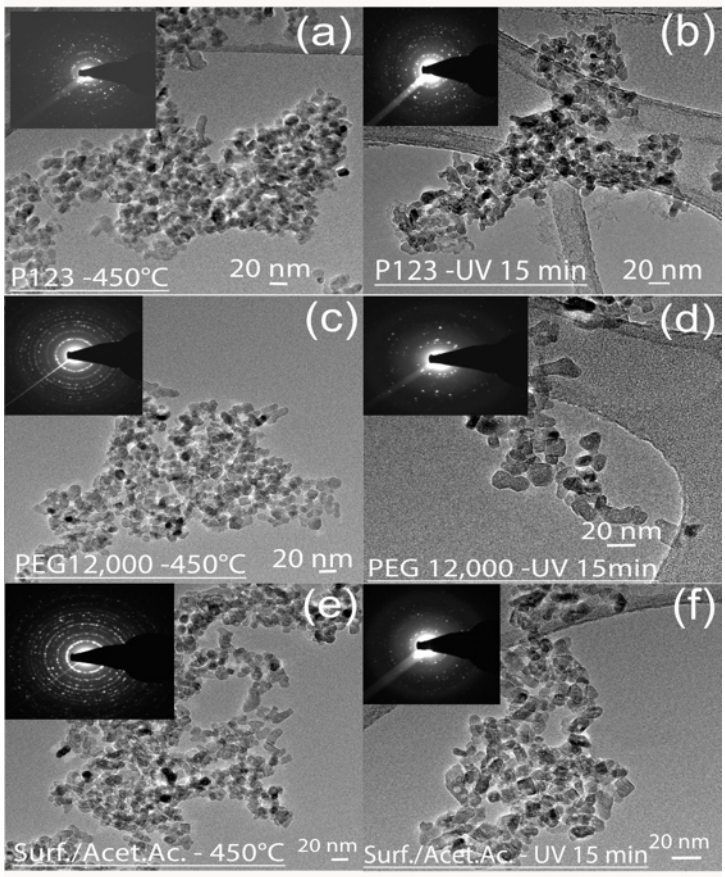

Figure 5.4: TEM images for TiO_2 used for the photoanode, after different treatment: (a) addition of Pluronic P123 and calcination; (b) addition of Pluronic P123 and UV irradiation; (c) addition of PEG 12,000 and calcination; (d) addition of PEG 12,000 and UV irradiation; (e) addition of Tween80/Span80 nonionic surfactants + acetic acid, and calcination; (f) addition of Tween80/Span80 nonionic surfactants + acetic acid, and UV irradiations. All calcinations were carried out at 450°C for 30 min, all UV irradiations were applied for 15 min.

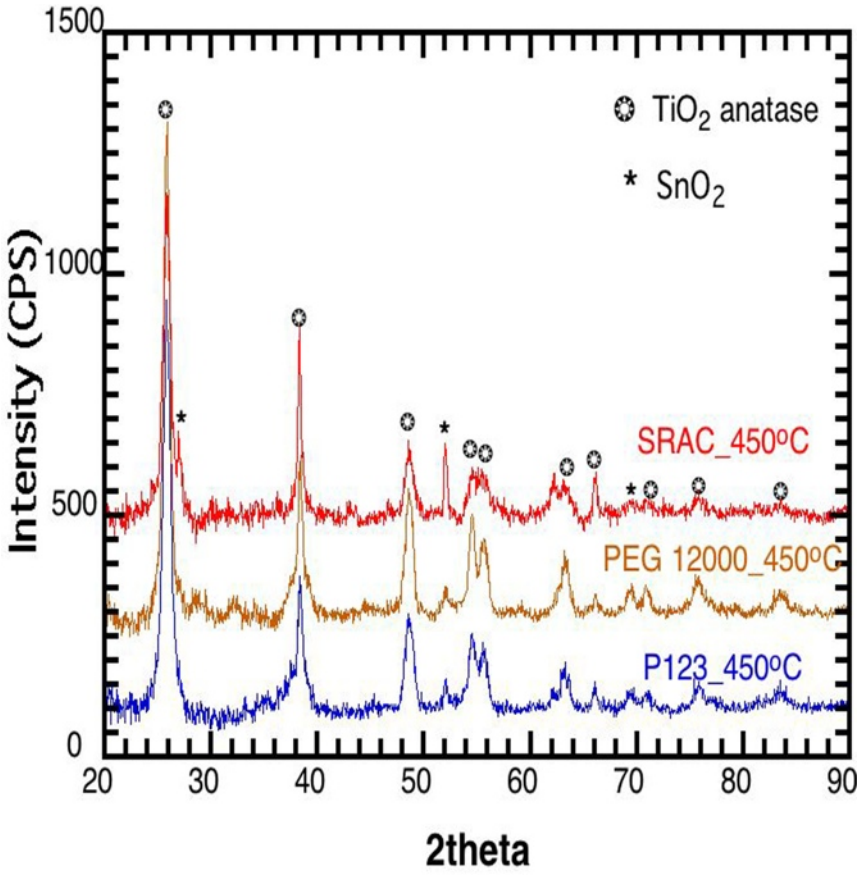

Figure 5.5 XRD patterns of TiO_2 thin films prepared by colloidal TiO_2 mixed with surfactant/ Acetic acid (red), PEG (brown), and Pluronic P123 (blue)

5.4.2. Structure of the TiO_2 layer

Figure 5.6 displays the SEM images of the surface morphology of a TiO_2 layer (TiO_2 nanoparticles initially activated at 350°C) calcined at 350°C, prepared with Pluronic P123 as an additive. Figure 5.6.a shows that the film is homogenous and had a good adhesion to the FTO substrate with no cracks or mechanical defects. The film is quite porous with globular aggregates connected well with each other and the layer thickness is 17 µm on average(Figure 5.6.b.).

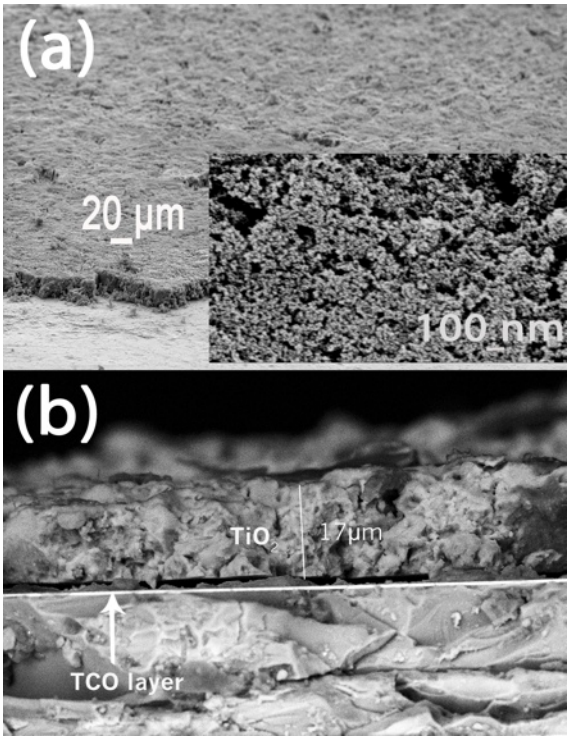

Figure 5.6: SEM images of TiO_2 films prepared by the doctor blade method with Pluronic 123 as additive after (a) calcination at 350°C for 4hr b) Cross section of TiO_2 thin film showing the thickness

Both surface area and porosity of the film are two important parameters in performance of DSSC, and porosity has to be typically in the range of 50%-65% range.[16] As it can be affected by the pre-(powder) and post- treatment (film), either treated thermally or by exposing to UV, we checked if the different treatment could affect this parameters. The BET measurement was performed to determine the Specific surface area was calculated by BET analysis of the TiO_2 film. Porosity and surface roughness factor were calculated based on the BET measurements. Three samples were tested after calcination and UV irradiation, and the description of the samples are illustrated in (Table 5.I). A typical IV isotherm was observed (Figure 5.7a,b) indicating that all samples exhibit a mesoporous structure with structural porosity marked by a significant specific surface area (ss) and porous volume (vol) (Table 5.I). For samples pretreated thermally at 350°C , the N_2 isotherm shows macroporosity revealed by an increasing adsorption branch for higher relative pressure. Although, the sample initially cured by UV irradiation showed no

presence of macroporosity, it shows the highest specific surface area and total pore volume (inset of Figure 5.7). It is also worth mentioning that the sample initially cured by UV for 30 min shows no change in the particle size as the pristine material (chapter 3).

Table 5.I. Structural parameters of TiO_2 films

sample	nanoparticle treatment	Film post treatment	Surface area (m^2/g)	Pore volume (cc/g)	porosity	Roughness factor (μm^{-1})	Particle size (nm) *	Pore size (nm)
1	350°C, 4h	450°C, 30min	116	0.35	58%	190	9.4	10.8
2	350°C, 4h	UV, 20min	154	0.44	63%	221	-	10.8
3	UV, 30 min	UV, 20min	199	0.45	63%	282	4.3	8.9

* the particle size was calculated from the XRD based on Sherrer equation

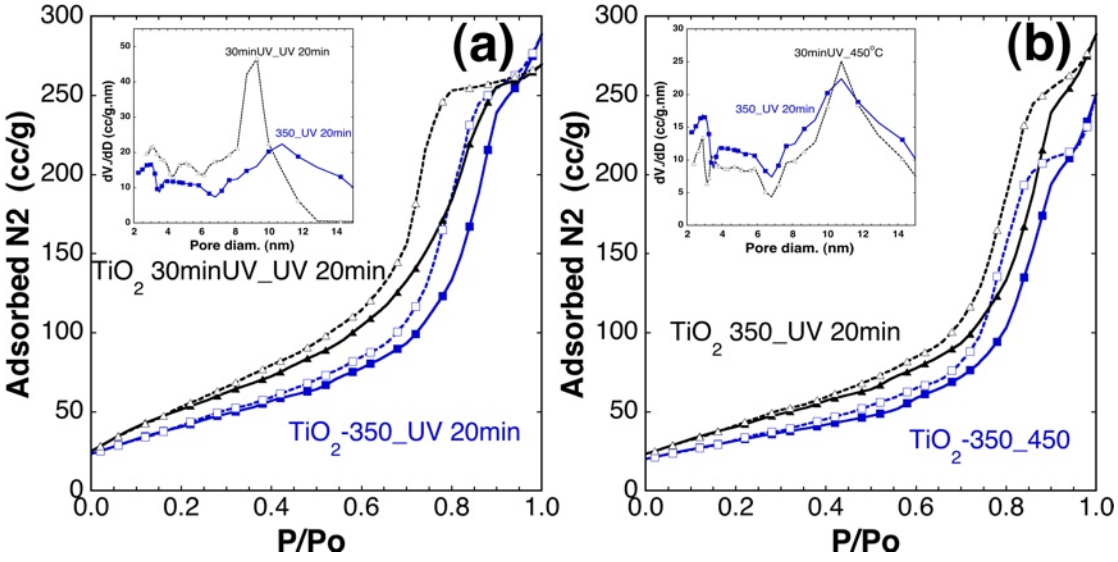

Figure 5.7. N_2 isotherm for a) TiO_2 film cured under the same condition (UV for 20min) and the nanoparticles pretreated under UV for 30min and at 350°C b) TiO_2 film cured under different conditions with (UV for 20min and at 450°C for 30min) and the nanoparticles pretreated at 350°C (inset is the pore size distribution for the samples).

Further investigation was carried out for these samples by calculating the surface fractal dimension D_s which can be used to express the surface irregularity that have a significant effect on surface reactivity. Fractal surface analysis was performed according to (Prouzet et al. 2009).[13b] For D_s =2, the surface exhibits a prefect smoothness, whereas D_s=3 indicates rough surface.[17] As can be seen from Figure 5.8 that sample post treated by UV for 20 min exhibit higher D_s=2.44, which is also very close to the calcined one(D_s=2.41). The higher surface roughness indicates that the film has good adhesion.

The roughness factor per unit film thickness is estimated using the following formula:

$$R = \rho(1-P)S \qquad 5.2$$

Where R: roughness factor (μm^{-1}); ρ: the density of TiO_2(anatase), P is the porosity (%), and S is the specific surface area (m^2/g). the roughness factor is in units of surface area per micrometer of the film thickness. In Table 5.I the sample that initially cured by UV revealed the highest roughness factor. With high roughness factor, the amount of dye adsorption is expected to be increased, and; hence, the charge harvesting efficiency will be risen.

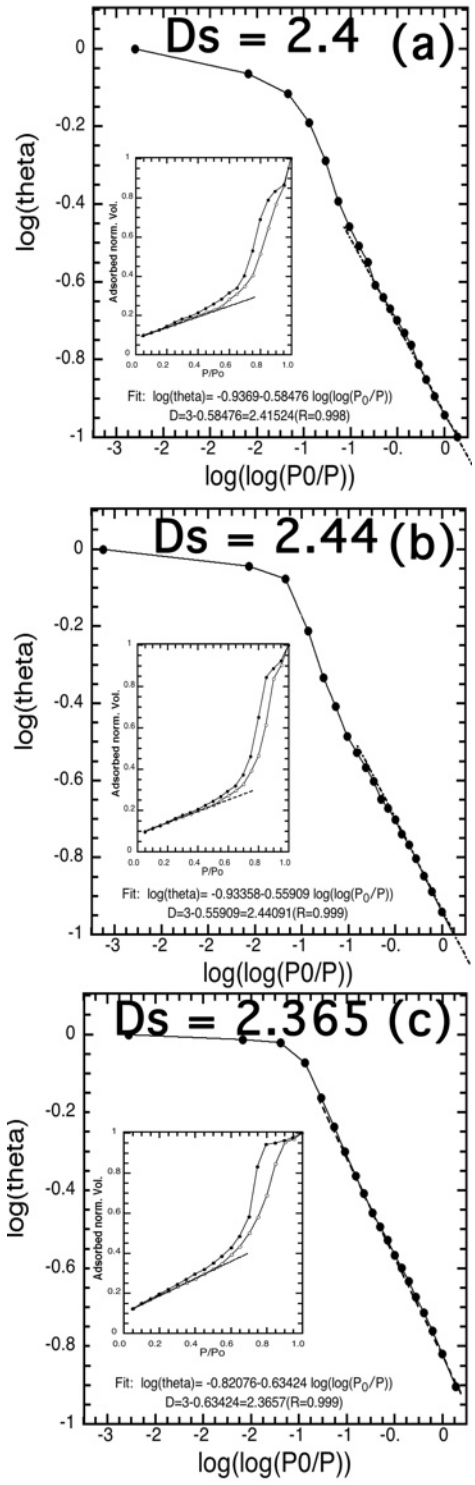

Figure 5.8 Surface fractal analysis of TiO_2 films, corresponding to samples 1, 2 and 3, respectively from top to bottom prepared by mixing TiO_2 nanoparticles with acetic acid and Span80/tween80 (Inset: comparison of the fit curve with the normalized adsorption isotherm (❍, adsorption; ●, desorption)

5.4.3. Counter Electrode

a) Structure

Scanning electron microscope (SEM) images and energy dispersive X-ray spectra (EDX) of the Pt films were taken for Pt nanoparticles prepared by Polyol and commercial hexachloro platinic acid solution. The Pt nanoparticles deposited by both methods had good adhesion on the FTO glass as observed by the cross-sectional SEM Figure 5.9 (a, b). The size of the nanoparticles are in the range of 40-400 nm and 30-200nm for polyol and thermal methods, respectively. A high specific surface area is assigned to these small nanoparticles that can be used as an effective catalyst for many chemical reactions. As indicated by EDX (Figure 5.9 b, d) no Cl signal could be observed in the EDX, and the other signals, including C, O, and Si, were from FTO or glass. The thickness of Pt layer was on average of 20nm (Figure 5.9 e) which matches well with the accepted thickness limit of Pt film according to Ma et al. 2004 that improves the cell efficiency.

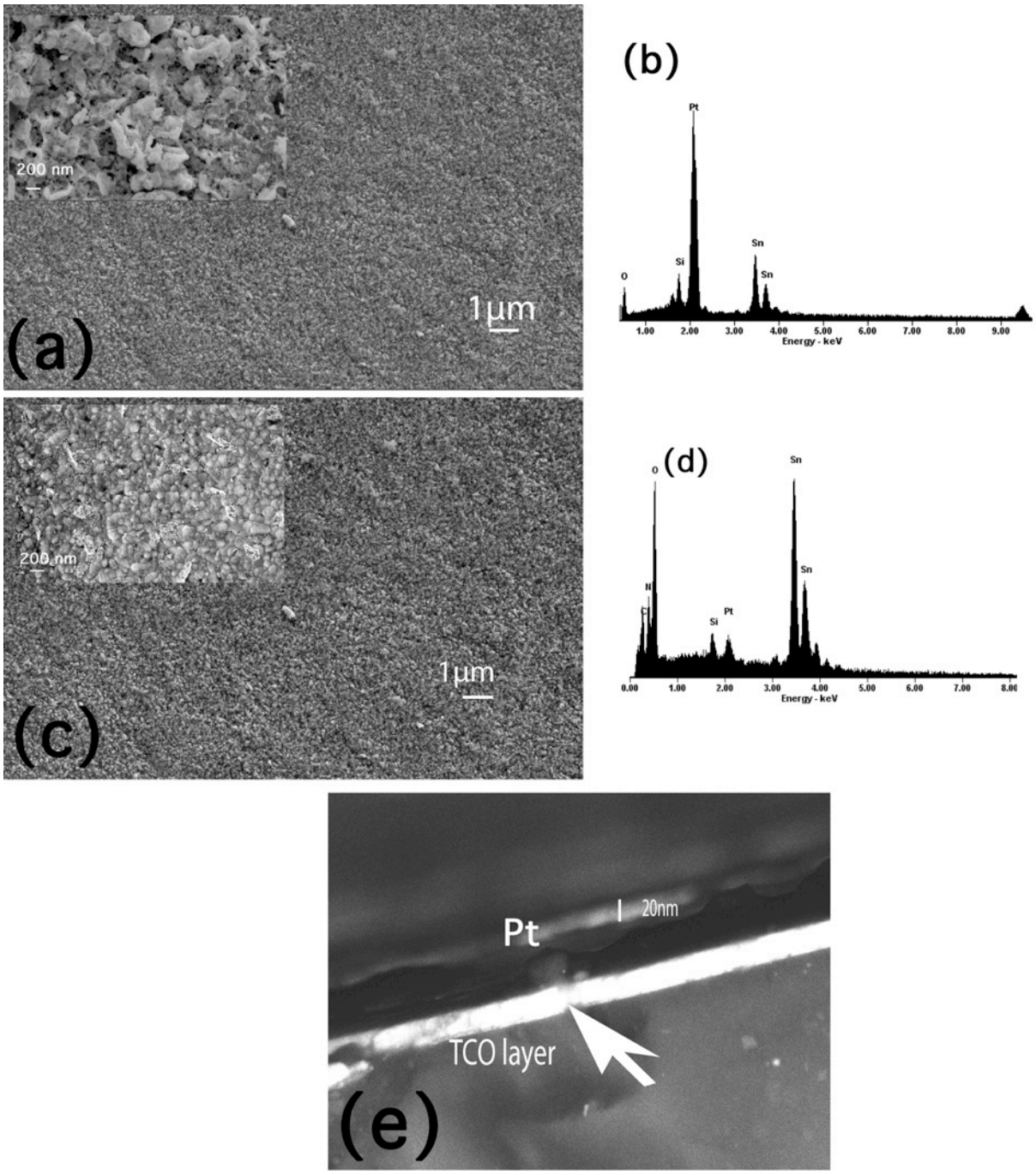

Figure 5.9 : SEM images of a Pt film deposited on FTO/glass by (a) polyol method after thermal treatment, with (b) EDAX analysis; (c) sample obtained from Solaronix after thermal treatment, with (d) EDAX analysis; (e) Cross section of Pt thin film obtained with the polyol method. (inset of (a) and (b): close view of the samples.

5.4.3.1. Electrochemical Catalysis of Pt Nanoparticles

Cyclicvoltammetry (CV) was used to study the electrochemical catalysis of Pt nanoparticles. Figure 5.10 shows a sample CV of 0.50 M H_2SO_4 in its conventional potential window (-0.25 V to +1.20 V vs. Ag/AgCl) on Pt electrode after the system has been purged with Argon. All the experiments were carried out at room temperature. The oxidation/reduction peaks were observed which indicates that the Pt electrode prepared by Polyol method has electrocatalytic activity for the hydrogen adsorption and desorption , and , hence,I_2 /I system.

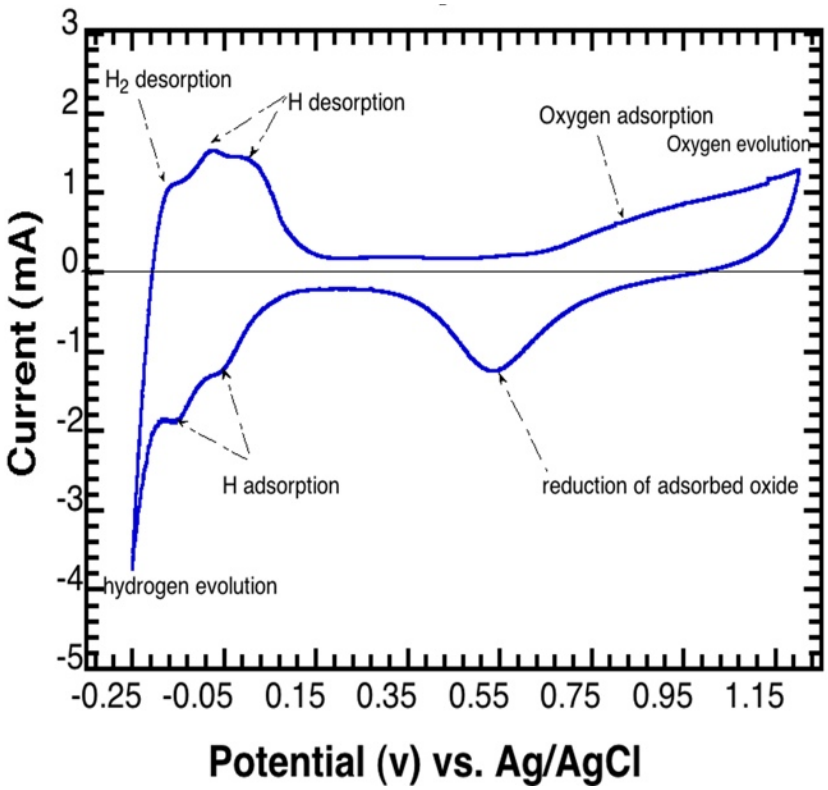

Figure 5.10 Cyclic voltammogram potentials of Pt nanoparticles on FTO glass in an electrolyte of 0.5 M H_2SO_4

5.4.4. Characterization of Complex Adsorption of Z907 Dye on TiO_2 Surface

Before checking the dye attachment to the substrate, we checked by ATR-FTIR if the film after the different treatments had any polymer left, especially the film cured with the UV treatment. We see in Figure 5.11 that none of the films (treated at 450^oC or cured by UV for 20 min.) display traces of polymer.

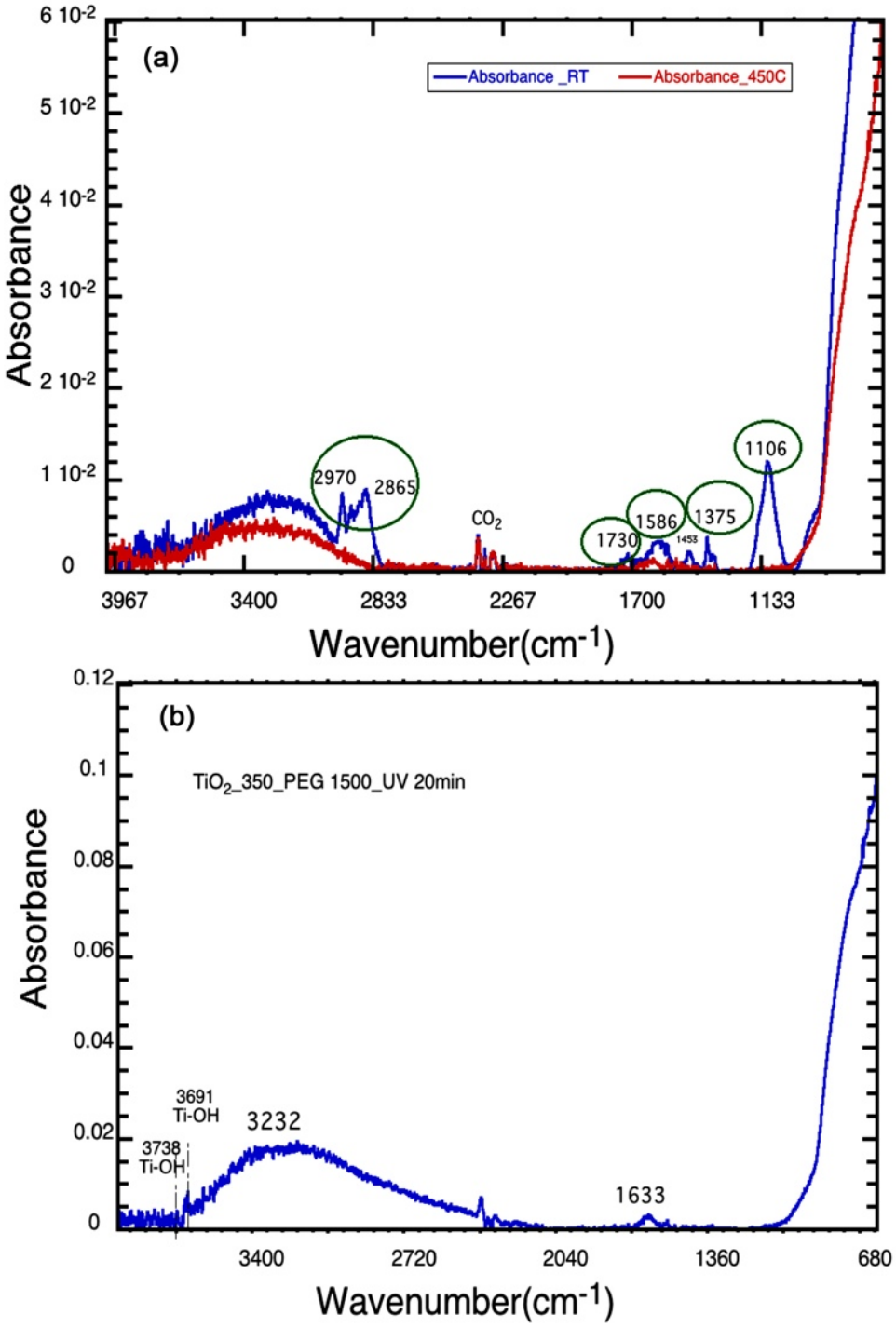

Figure 5.11 FTIR spectra of mesoporous TiO_2 prepared by mixing the preheated nanoparticles at 350°C with PEG 1500, treated (a) at 450°C for 30min (b) under UV for 20min

The cell performance is strongly affected by the efficiency of the injection of electrons from the dye to the conduction band of TiO_2, which is also the result of the quality of the dye anchoring to TiO_2 surface, both in quantity and quality. Many studies have shown that the dye anchors to the TiO_2 surface through different carboxylate coordination modes either physically adsorbed through hydrogen bonding or chemically adsorbed via chemical bond (unidentate, bidentate, and birding).[18] Among those modes, bridging and bidentate are the most stable ones.[18-19] Figure 5.12 shows the ATR-FTIR absorption spectra of the Z907 dye adsorbed onto the TiO_2 surface prepared with surfactant and acetic acid for two samples treated differently: thermally at 450°C for 30 min and UV for 45min. The spectra show strong peaks at 1380 cm^{-1} and 1607 cm^{-1} for the ν_{sym} (COO^-) and ν_{asym} (COO^-), respectively.[19b, 20] Many research groups take the difference between the symmetric and asymmetric carboxylic bands of the dyes in the free and adsorbed state, as a criterion for evaluating the quality of grafting. The spectra show no indication for the presence of carboxylic bond at 1,716 cm^{-1}, which would indicate that the dye anchored to TiO_2 surface *via* bidentate or bridging, no *via* an unidentate mode. The saturated hydrocarbon chains are identified by C-H stretch modes in the 2800-3000 cm^{-1} region with vibration modes of 2,852 cm^{-1} and 2,924 cm^{-1} for symmetric and asymmetric $-CH_2-$, respectively. The corresponding CH_3- peak is observed at 2,956 cm^{-1}. Abroad absorption range between 3,200-3,400 cm^{-1} is assigned to the intermolecular H-bond. Although the different treatments work well for the dye adsorption, the thermal treatment show an enhancement in the intensity of the peaks related to the COO^- bands and the degenerated Ti-OH at 3,785, 3,754, 3,656, and 3,698cm^{-1} (detailed explanation about the Ti-OH peaks will be covered in the following section).

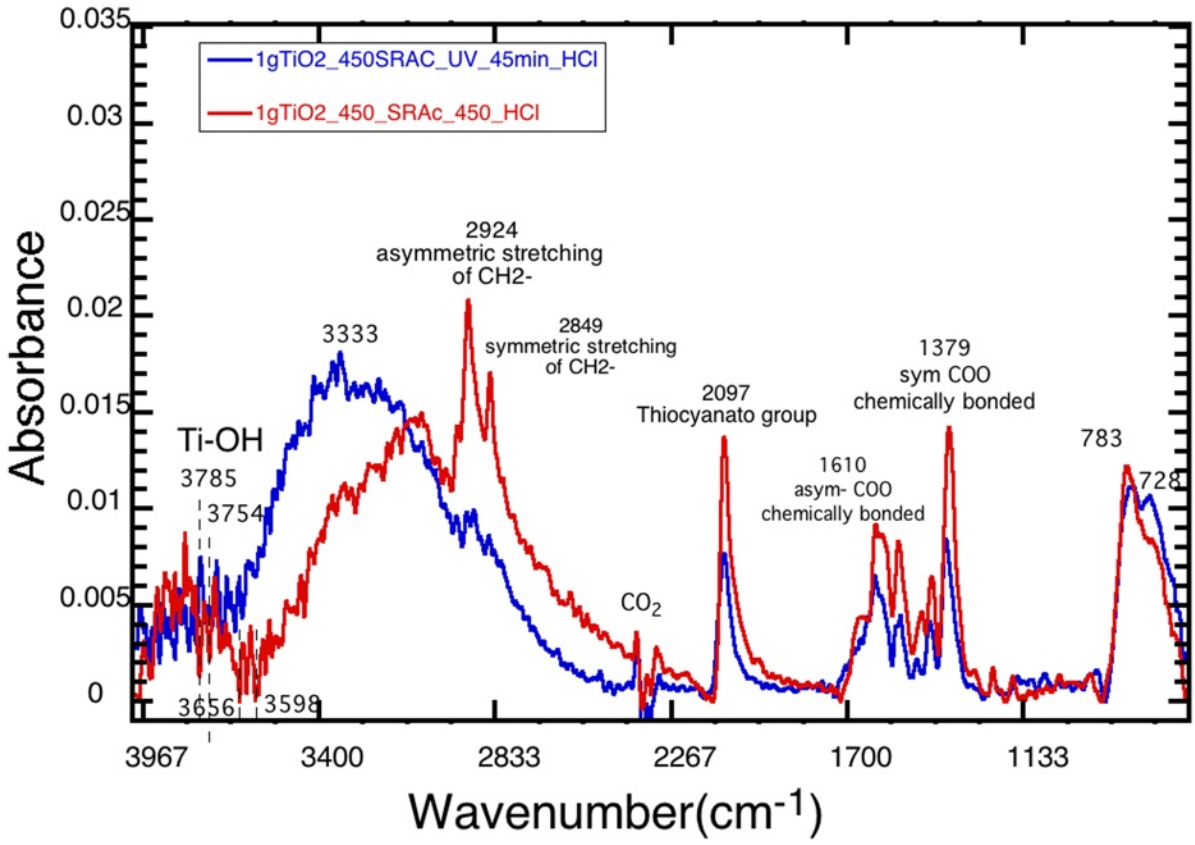

Figure 5.12 FTIR spectra mesoporous TiO_2- dye stained films prepared with preheated nanoparicles 450°C mixed with Surfactant Span 80/tween 80 and acetic acid, treated differently at 450°C for 30min and cured by UV for 45 min

5.4.5. Effect of UV and Acid Treatment on TiO_2 Layer

The UV treatment in this study was used alone without further treatment (such as thermal treatment) to investigate its effect on the cell performance. Toupance *et al*. discovered that UV treatment alone for metal oxides, such as TiO_2 and SnO_2 outperformed the calcined ones.[4c, 21]

We explored further the influence of UV treatment by studying if a thermal treatment followed by UV curing, modifies the material performance. UV removes the organic contaminants resulting from surfactant or polymer addition. In addition, several researchers stated that the major effect of UV illumination is to reversibly create a high concentration of photoactive surface states, and these surface states were described as being continuously distributed below

the conduction-band edge as shallow electron traps, which would be beneficial for electron injection from the dye and transport by thermally activated detrapping.[18a] We observed that combining UV treatment with HCl treatment gives an enhancement of the amount of adsorbed dye. It was revealed that the HCl treatment has a significant effect not only on the flat band potential of the TiO_2, but also on the adsorbed amount of the dye. The cell performance can be limited as a result of the effect of the flat band potential. Under HCl treatment (0.10 M), Huang *et al*. observed a positive shift in the flat band potential, which was attributed to large injection of electron from the excited dye energy level to the conduction band of TiO_2. The formation of new surface sites (H^+) on TiO_2, besides Ti^{4+} sites, were the main reason for the positive band shift. In most cases, it is found that after HCl treatment the Jsc of the DSC is enhanced.[18a, 22]

5.4.5.1. Bulck Material Characterization by FTIR Spectroscopy

The effect of acid treatment on the TiO_2 layer can be clearly seen through ATR-FTIR. Four TiO_2 films were prepared with an additive made of surfactants (Span 80/Tween 80) mixed with acetic acid and treated at 450^{o}C. Two of them were made with a powder initially treated at 350°C, the other two being made with a powder treated at 450˚C. an acid treatment was applied further to the films. The four films were immersed in a (0.1 M) aqueous solution of hydrochloric acid for two hours, before being fired at 450^{o}C for 30 min.

The appearance of surface hydroxyl modes can be used as an indication for the surface protonation as we expect that the dye adsorbs on OH sites on TiO_2 surface.[15] However, the assignment has to be conducted carefully because the frequencies of the Ti-OH modes depend strongly on the surface morphology and the crystallite type of TiO_2.[23] The surface of the as-synthesized TiO_2 has many hydroxyl groups as seen in Figures 5.13 and 5.14 (especially the untreated samples). The FTIR spectrum exhibits a broad band in the 3,100-3,400 region, characteristic of hydroxyl groups that are physisorbed, or weakly chemisorbed. This band disappears above T=200^{o}C. The stronger bands (insets of Figures 5.13 and 5.14) at 3,623, 3,648, and 3,680 cm^{-1}, are assigned to tetrahedral coordinated vacancies ($_4Ti^{4+}$-OH).[24] The bands at 3632 and 3670 cm^{-1} are characteristics of vicinal (hydrogen bonding one to another) and bridging Ti-OH modes. Other similar bands around 3715, 3692, 3676, and 3630 cm^{-1} are

assigned to stretching mode of the surface hydroxy species that are observed also in this work.[19b, 25] The 3,700-3,800 cm^{-1} region designated for isolated or free hydroxyl groups.[23-24, 25b]Two bands at 3,750 and 3,842 cm^{-1} are due to octahedral vacancies ($_6Ti^{3+}$-OH), but only the band at 3,842 cm^{-1} was observed for the sample made of powder initially treated at 450°C and treated with HCl (inset in Figure 5.14).[24] Additional bands are noted in this work which may be related to the appearance of other crystal faces. As mentioned before, the signature of dye connection is found at 1,380 cm^{-1} and 1,607 cm^{-1} for the ν_{sym} (COO^-) and ν_{asym} (COO^-), respectively.[19b, 20] So, any increase in these bands is an evidence of an increasing amount of adsorbed dye. A close analysis of the FTIR spectra, for both untreated samples, or those treated with HCl, there is a drop in the absorbance intensities for all bands related to the free groups, or for those related to tetrahedral vacancies, and we take this evolution considered as a strong evidence that the dye adsorbs onto OH sites on the TiO_2 surface. For samples treated with HCl , the amount of isolated OH peaks is more reduced after grafting, compared to the untreated ones, which proofs our claim about the occupation of these sites by dye molecules. It is worth mentioning that some research groups only considered the drop in the intensity of 3,751cm^{-1} position without taking into account other bands, as an indication for the dye adsorption on OH sites.[15, 26]

By comparing the samples made of a powder activated at 450°C, with or without HCl treatment (Figure 5.14), we found that all peaks for OH sites have a sharp decrease which indicates the successful attachment of the dye onto these hydroxyl sites. Other types of organic additives has been tested. Other experiments has been done to test the effect of UV and HCl treatments on the commercial TiO_2 (Degussa) and other types of organic additives has been tested (AppendixC, Figures C.4- C.10).

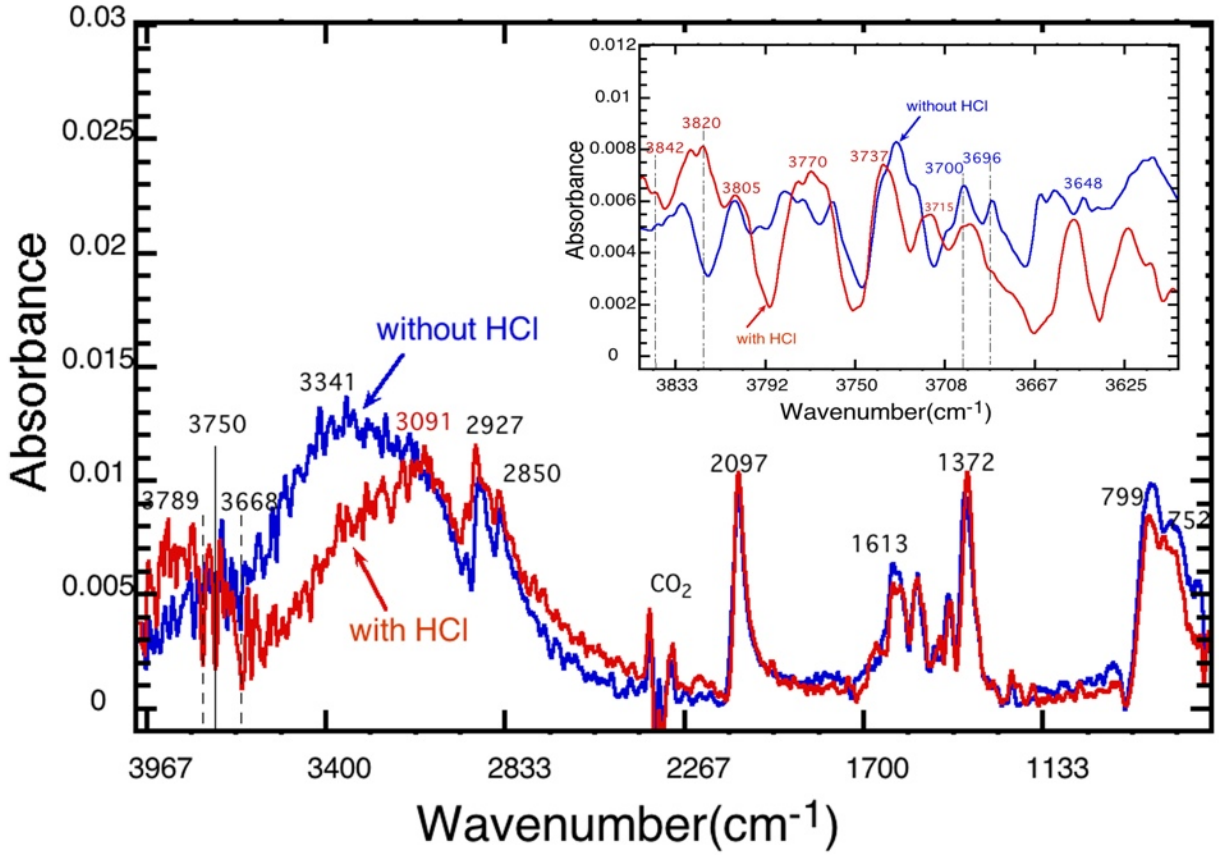

Figure 5.13 FTIR spectra for HCl and non HCl treated mesoporous TiO_2- dye stained films prepared with preheated nanoparicles 350°C mixed with Surfactant Span 80/tween 80 and acetic acid, treated at 450°C (inset : magnification at wavenumber from 3500-3850 cm^{-1})

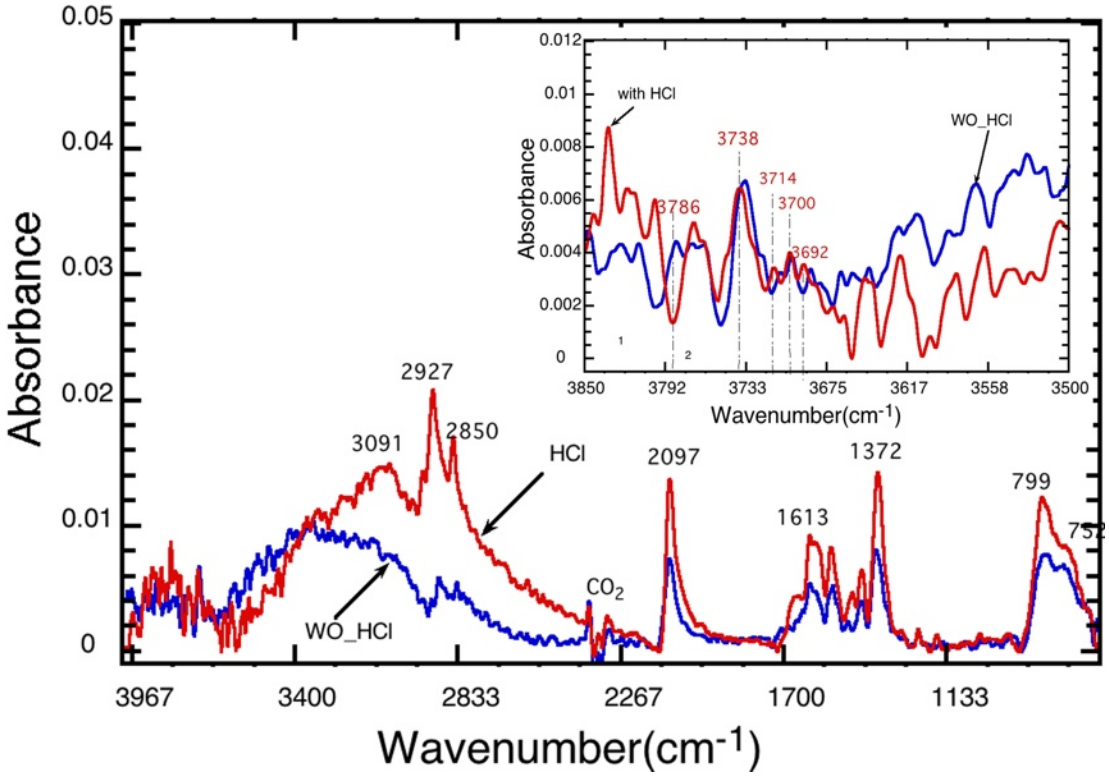

Figure 5.14 FTIR spectra for HCl and non HCl treated mesoporous TiO_2- dye stained films prepared with preheated nanoparicles 450°C mixed with Surfactant Span 80/tween 80 and acetic acid, treated at 450°C (inset : magnification at wavenumber from 3500-3850 cm^{-1})

5.4.5.2. Thin Film Characterization: UV -Vis Absorption

The UV-Vis analysis was run to gain further insight into the effect of different treatment methods (calcination, UV, and HCl) on the optical properties of TiO_2 films. TiO_2 films were prepared by following two pathways: firstly, nanoparticles were initially cured by UV for 30 min before thin film preparation, and the film was prepared by adding surfactant and acetic acid as detailed previously (Figure 5.15.a); secondly, the nanoparticles were calcined at 350°C for 8 hrs, and the film preparation used polyethylene glycol 1500 as an additive (Figure

5.15.b). Both films were further cured with a 20 min UV treatment followed by acid treatment (immersing the film in 0.1 M HCl for 2 hours).

The UV-Vis spectra display an increase in the absorbance for both films after the HCl treatment. In addition, bandgap values, which were checked for both treated and untreated films, reveal a blue shift of the band gap after HCl treatment, a proof of a change in the electronic structure of the thin films and presence of quantum confinement.

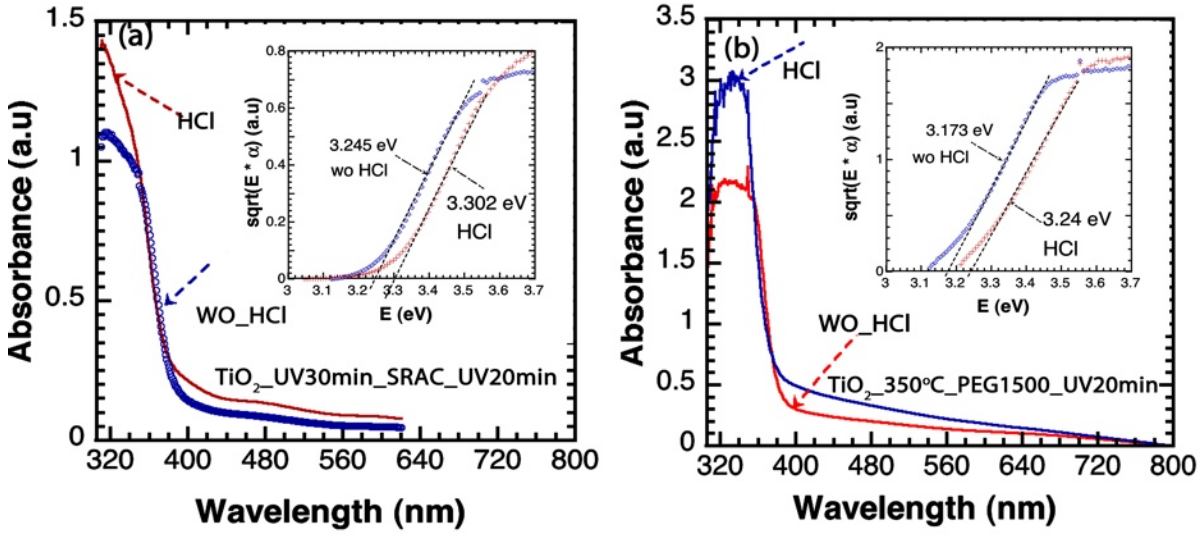

Figure 5.15 Absorbance Spectra of the photoanodes with and without HCl treatment for TiO_2 thin films prepared by different organic additives a) nanoparticles initially cured by UV for 30 min then mixed with surfactant and acetic acid b) nanoparticles treated at 350°C mixed with polyethylene glycol (PEG 12000) , under UV treatment for 20min (insets: $(\alpha.E)^{1/2}$ as a function of the energy. The extrapolation of the edge down to $\alpha = 0$ provides the value of the band gap Eg, for indirect band gaps.)

Further investigation was carried out to compare the influence of the curing thermal treatment vs the UV one. Two photoelectrodes were prepared by mixing nanoparticles activated initially at 450°C with surfactant and acetic acid. One of the film was exposed to UV

for 45 min while the other was fired at 450°C for 45 min. Both samples were finally treated with HCl 0.1 M for 2 hrs.

The UV-vis spectra (Figure 5.16) exhibit a higher absorptivity for the thermally treated film. This result matches well with the result of the FTIR and also with the IV curve (seen hereafter), in which cells treated thermally have higher overall cell efficiency. The band gap was also checked for both samples: the film treated thermally shows a slight increase in the band gap compared to the UV treated one. According to the increase of absorptivity of the calcined sample , after the HCl treatment, we believe that the effect of HCl on the calcined sample is greater than the UV treated one, which is responsible for the increase of the band gap.

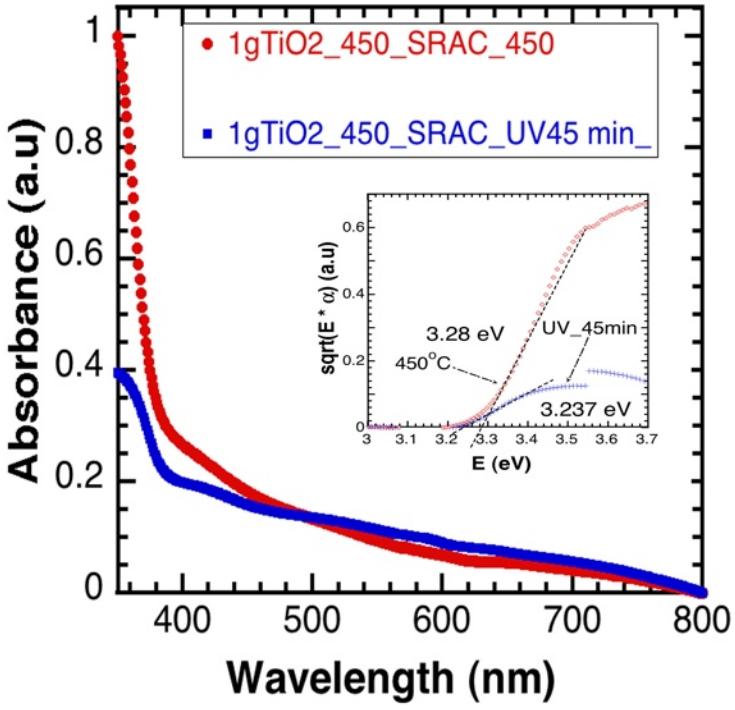

Figure 5.16 Absorbance Spectra of the TiO_2 photoanodes prepared by surfactant and acetic acid under different treatments
(inset: $(\alpha.E)^{1/2}$ as a function of the energy. The extrapolation of the edge down to $\alpha = 0$ provides the value of the band gap Eg, for indirect band gaps.)

5.4.5.3. Effect of Different Treatments (UV treatment and calcination with HCl) on Cell Performance

We compared the influence of different treatments by assembling cells that were measured. It is worth noticing that the cells were not initially fully optimized on purpose: for example, a blocking layer of TiO_2, required to avoid charge leakage, was not created onto the FTO electrode for the first tests, and that the performances of the cells were initially used as comparative within this study, not against the performances reported in literature.

a) I-V Measurement

Figure 5.17 shows the photocurrent-voltage curve of synthesized TiO_2. The fill factor and the overall energy efficiency were calculated according to the following equations

Fill factor: $$FF = \frac{I_{\max} \bullet V_{\max}}{I_{oc} \bullet V_{oc}} \qquad 5.3$$

Overall energy efficiency: $$\eta = \frac{FF \bullet V_{oc} \bullet I_{sc}}{E_{in} \bullet A} \qquad 5.4$$

with Imax, Vmax, the current and the voltage at maximum power point, respectively. Voc is the open circuit voltage and Isc is the short circuit current, It is considered that the Isc and Voc are the highest current and voltage obtained from the cell, the E_{in} is the incident irradiation power (100 mW/cm^2). A dye sensitized solar cell prepared from pluronic P123 with preheated nanoparticles at 350^{o}C gave an open circuit voltage of 0.764 volt and short circuit current density of 9.61mA/cm2 for an incident light intensity of 100 mW/cm^2. The overall power conversion efficiency of 4.93% was achieved.

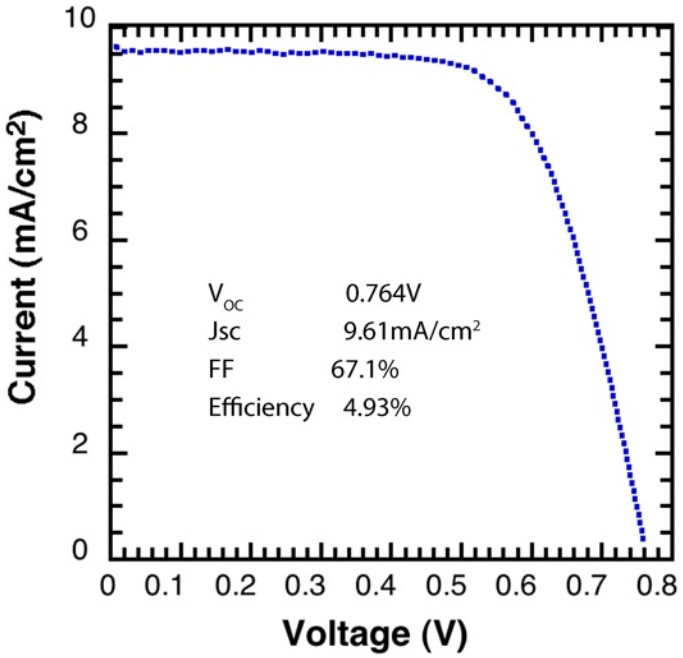

Figure 5.17 J-V curves of dye-sensitized TiO_2 films prepared on FTO/glass calcined at 450°C using Pluronic P123 with preheated nanoparticles at 350°C

The effect of HCl treatment on the cell performance can be clearly seen by measuring the J-V curve of the dye sensitized solar cells. Figure 5.18 shows the J -V characteristic of thermally treated TiO2 films with and without HCl 0.1 M prepared by initially treated nanoparticles at a) 350°C and b)450°C. As shown in Figure 5.18, the short-circuit photocurrent density J_{sc} and solar-photoelectricity conversion efficiency of treated TiO_2 films are higher than that of the untreated ones (Table 5.II); the active surface area was 5 cm^2 for all samples . After the HCl treatment, the Jsc value and efficiency increased by 28.4%and 4.5%, respectively for the 350°C sample (Figure 5.18.a). However, Voc value was slightly changed and FF was decreased. Whereas, for sample prepared with 450°C pretreated nanoparticles (Figure 5.18.b), Jsc was modified by 36.3%, the efficiency by 37.2% and Voc by 8.6%. The poor fill factor is a result of a combination of the high R_{series} and low R_{shunt} as indicated in table 5.II. The parameters for the sample initially treated at 450°C were increased, except for the FF, by higher percentage compared to the ones for the 350°C sample; the initial current density and efficiency of the 350°C were increased significantly compared to 450°C sample.

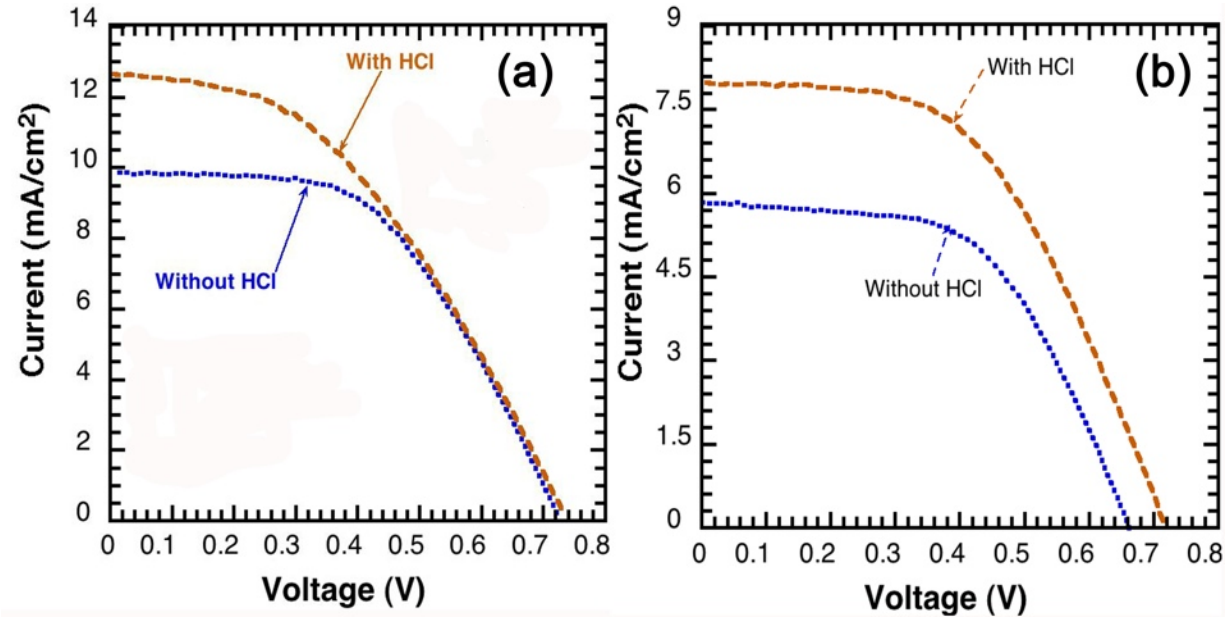

Figure 5.18 J–V curves for thermally treated TiO_2 films, at 450°C for 30 min prepared on FTO/glass before and after HCl treatment for samples prepared with nanoparticles calcined initially at a) 350°C b) 450°C, then mixed with acetic acid and surfactant.

Table 5.II Photovoltaic parameters of DSSCs prepared by surfactant and acetic acid with HCl treated and untreated cells

Sample	V_{oc} (V)	J_{sc} (mA/cm^2)	FF	Efficiency %	R_s (Ω)*	R	R_{sh} (Ω)*	R
a_HCl	0.738	12.69	42.2	3.95	5.6	0.99	125	1
a_without HCl	0.727	9.88	52.7	3.78	5.3	1	120	1
b_HCl	0.719	7.99	51.3	2.95	6.7	0.947	226	0.938
b_without HCl	0.662	5.86	55.5	2.15	6.7	1	176	1

* the shunt (Rsh) and series (Rs) resistances were calculated based on the the slope generated from the linear fitting for the illuminated J-V. The reliability coefficient- R- was added for each measurement.

5.4.5.4. Comparison Between Calcination and UV Treatments on the Performance of the Solar Cells

Two sets of experiments were conducted to study the effect of different treatments on solar cell performance. The first set was prepared as follows: nanoparticles activated at 350°C were mixed with surfactant and acetic acid and the films were exposed to either heat treatment at 450°C, or UV treatment for 45min. The other set was prepared by the same ways, but with nanoparticles initially activated at 450°C.

As can be seen in Figure 5.19 that the thermal treatment at 450°C for 30 min, for both sets, show a higher cell performance compared to the UV one: the current density was improved by almost 1.5. The open circuit voltage and fill factors were also enhanced. The films prepared by 350°C nanoparticles (Figure 5.19 a) shows better performance for the cell parameter compared to the 450°C ones. The films that stood UV treatment exhibit almost the same results, with a little improvement for the sample prepared with nanoparticles activated at 350°C. This observation for the UV treatment supports the observations by FTIR and UV-Vis in the previous sections which give the indication that curing TiO_2 films by UV alone did not improve the cell performance. One of the reasons was revealed by Deacon et al. who mentioned the change of the dye anchoring mode from bidentate or bridging, to unidentate mode after the UV treatment.[18a, 27] By looking back to the FTIR spectra (Figure 5.12), it is clear that there are weaker COO- bonds at 1,379 and 1,609 cm^{-1} for the UV treated sample, and the presence of a small peak at 1,712 cm^{-1}, assigned to C=O bond, that indicates the existence of the unidentate mode by which the electron transport is not favored. In presence of the hole, the OH^- on the TiO_2 surface is converted to ($OH\cdot$) radical that reduces other OH^- leaving them on the surface as anions that may change the coordination mode (unidentate by which the electron transport is not favored.)

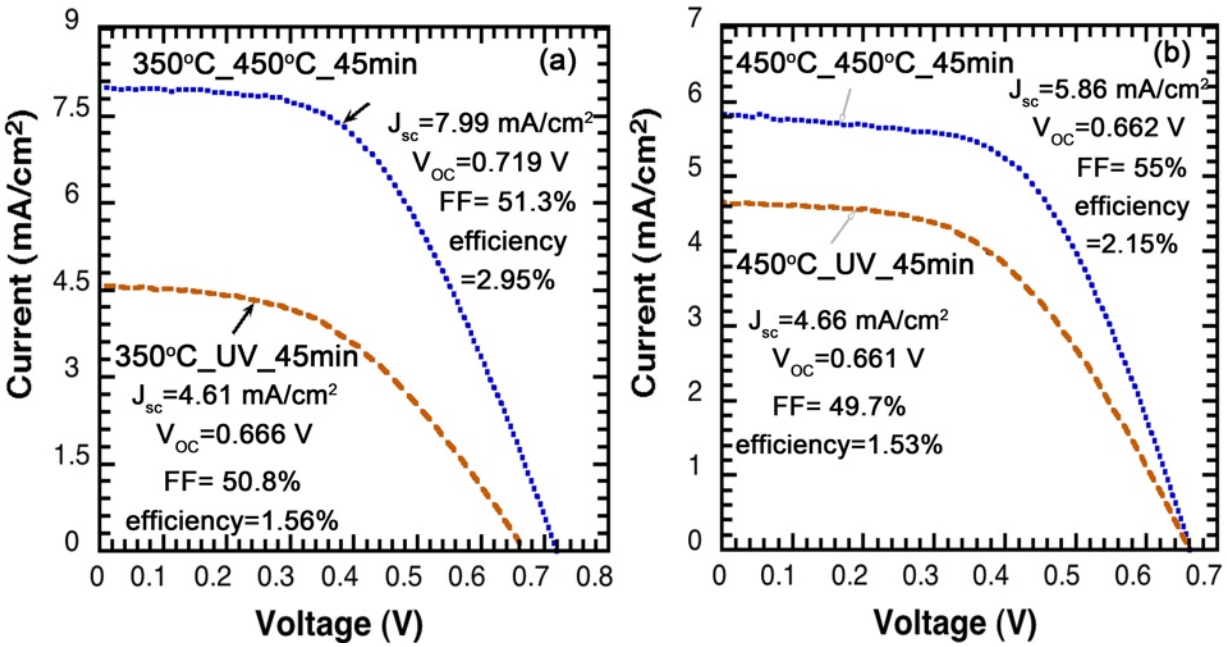

Figure 5.19 J-V curves for TiO_2 films treated differently (thermally at 450°C or UV for 45min) prepared with nanoparticles calcined initially at a) 350°C b) 450°C, then mixed with acetic acid and surfactant (active area=5 cm^2).

5.4.5.5. Improving the cell performance by adding a blocking layer

To improve the shunt resistance and decrease the series resistance a blocking layer was added by immersing the FTO glass, after exposing to the UV-Ozone for 30 min, in 40 mM solution of $TiCl_4$ in water at 70°C for 30 min. Different TiO_2 layers were prepared by mixing preheated synthesized TiO_2 at 350°C with different organic additives (surfactant/ acetic acid and Pluronic P123). The films were calcined at 450°C for 30 min then exposed to UV for 15 min. For comparison, films made from commercial TiO_2, prepared the same way for the synthesized TiO_2, were characterized. Figure 5.19 demonstrates that both samples made from synthesized TiO_2 exhibit higher cell performance compared to the commercial ones. Although, sample prepared by surfactant and acetic acid displays higher efficiency than that made from Pluronic, pluronic sample provides a higher shunt resistance (Table 5.III). The reproducibility of making solar cells with blocking layer was verified by running experiments for many cells prepared the same way but at different times (Appendix C Figure C.16 and Table C.II).

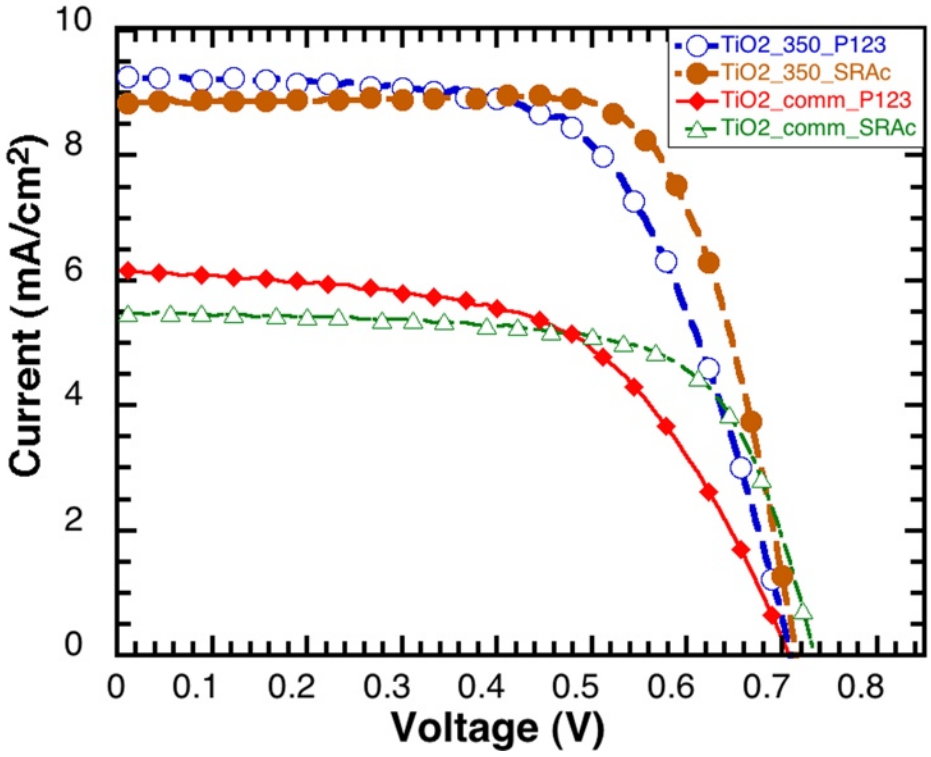

Figure 5.20 Comparison between J-V curves for TiO_2 solar cells fabricated with with different organic additives (active area=5 cm^2)

Table 5.III Comparison between photovoltaic parameters of DSSCs prepared by synthesized TiO_2 nanoparticles and commercial TiO_2

Sample	V_{oc} (V)	I_{sc} (mA/cm^2)	FF	efficiency	Series resistance (Ω)	Shunt resistance (Ω
TiO_2_350°C_P123	0.713	9.43	62.6%	4.21%	16.6	1392
TiO_2_Degussa_P123	0.707	6.16	56.7%	2.47%	15.72	462
TiO_2_350°C_SRAc	0.72	8.41	77.1%	4.67%	2.21	324
TiO_2_Degussa_SRAc	0.734	5.47	68.9%	2.77%	4.1228	606

5.4.5.6. Comparison between two treatment methods (Thermal & UV-O3 and Thermal& UV) on cell performance

UV–O3 treatment was originally used for removing organics residues from transparent conduction oxides, but it was demonstrated recently, that the UV–O3 treatment applied to remove organics residues from the TiO_2 thin films, led to a remarkable improvement in photoconversion efficiency, especially if this procedure was applied along with (before or after) thermal treatment.[28-29] Therefore, we applied two different treatments on two thin films made from nanocrystalline TiO_2 with the (surfactant/acetic acid) additive. Both films were exposed to thermal treatment (450°C for 30min), but this curing was followed by UV–O3 (15 min) for one film, and UV alone for 15 min for the second film. Figure 5.21 demonstrates that the last treatment gives higher efficiency, almost double the efficiency of the former one.

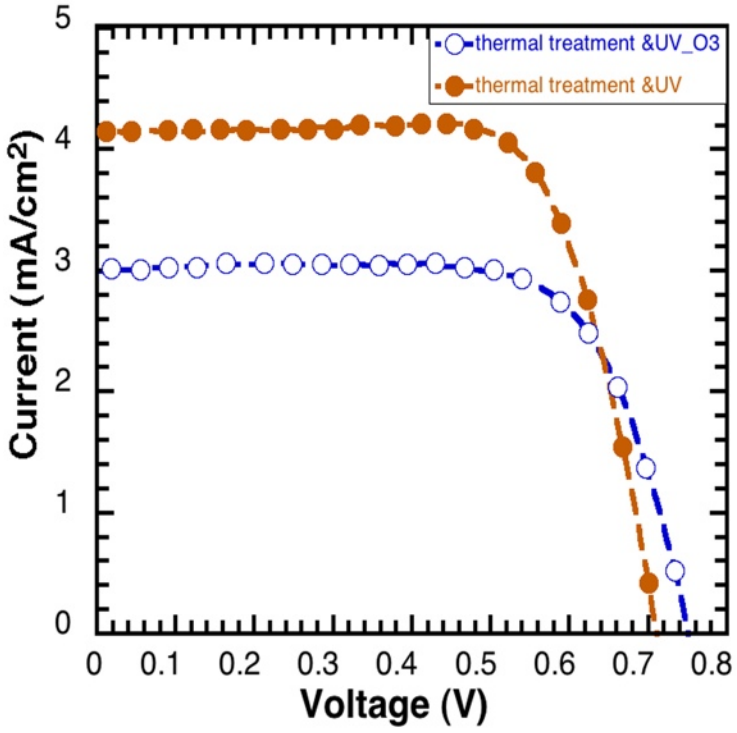

Figure 5.21 Comparison between J-V curves for TiO_2 solar cells fabricated with differently treated TiO_2 layers (TiO_2 nanoparticles with surfactant and acetic acid); the active area was 0.28 cm^2

Table 5.IV Photovoltaic Parameters for TiO_2 Solar Cells Fabricated with Differently treated TiO_2 layers

Treatment method	V_{oc}	J_{sc}(mA/cm^2)	FF (%)	Efficiency (%)
Thermal treatment + UV–O_3	0.756	2.45	68.8	1.27
Thermal treatment + UV	0.711	4.15	72.3	2.13

5.4.5.7. Amount of Dye Adsorption

Figure 5.21 shows the comparison of the UV-Vis absorption spectra of the desorbed Z907 dye of different TiO_2 films prepared by different organic additives and compared by immersing the dyed TiO_2 in a solution of 50% 0.1M NaOH and 50%EtOH overnight. The TiO_2 films were prepared by mixing the TiO_2 nanoparticles, initially preheated at 350^{o}C and then mixed with different organic additives (Pluronic or surfactant and acetic acid). All TiO_2 films were finally treated at 450^{o}C for 30min followed by UV for 15 min. Before dye anchoring, the samples were immersed in 0.1 M HCl. Different concentrations of the dye were prepared to determine the dye extinction coefficient (ε). The inset in Figure 5.21 is the calibration curve. Every dyed TiO_2 film was immersed in a definite solution volume. The dye solution in this experiment was diluted so the Lambert–Beer's law can be applied to calculate the concentration of the dye as it is proportional to the absorbance.[30]

$$A = \log(1/T) = \varepsilon c l \qquad 5.5$$

where A is the absorbance, T is the transmittance (the ratio of transmitted light to the incident one), c is the concentration of the dye, l is the thickness of the solution which is considered the thickness of the cuvette, 1cm^2, and ε is the extinction coefficient which can be calculated through the slope of the calibration curve. The calculated value of the extinction coefficient is 14 mM^{-1}.cm^{-1}

The samples prepared by surfactant and acetic acid show higher absorbance which is consistent with the overall cell efficiency. All the reference cells made from the commercial TiO_2 exhibit lower absorbance. Consequently, less amount of dye was adsorbed. The synthesized nanoprticles has the ability to adsorb dye 7 times more than that of the commercial one due to large surface area of the synthesized TiO_2. Table 5.IV shows the amount of dye adsorbed for different TiO_2 films and their cell parameters. The amount of dye adsorption was also determined for other cells treated thermally at 450^oC and was left for aging for two month (AppendixC Figure C.17 and Table C.III)

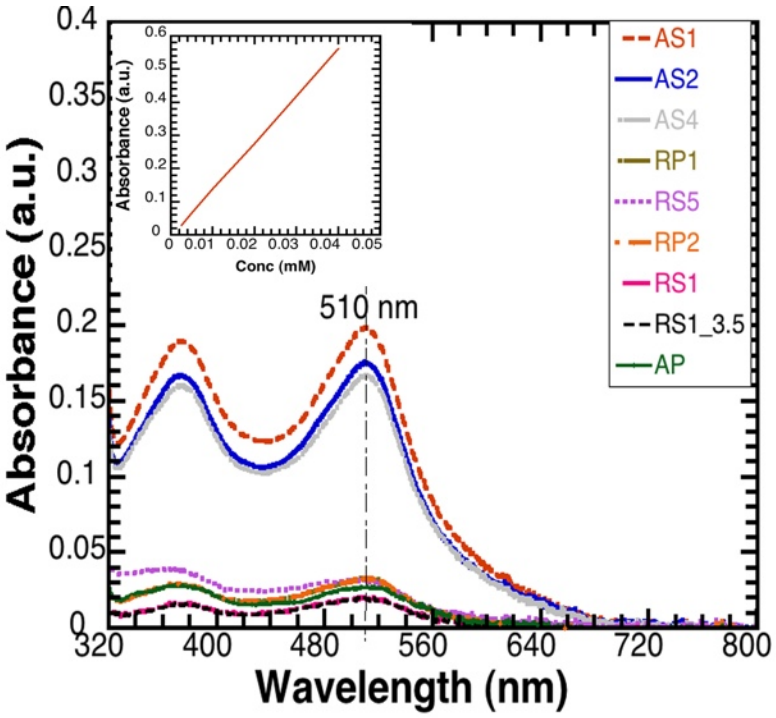

Figure 5.21 UV-Vis absorption spectra of the Z907 dye desorbed from TiO_2 films prepared with different organic additives compared to those desorbed from TiO_2 commercial. 'A' refers to the synthesized TiO_2 nanoparticles prepared with S (surfactant/ acetic acid) or P (Pluronic) additives, 'R' refers to reference electrodes prepared by TiO_2 Degussa with S or P additives. (the numbers beside each electrode refers to its order)

Table 5.V Influence of different organic additives on the performance of Z907 dye-sensitized solar cells

Sample	Film thickness µm)	J_{sc} (mA.cm^{-2})	V_{oc} (V)	Efficiency (%)	FF (%)	Amount of dye (10^{-7} mol.cm^{-2})
AS1	19	8.38	0.721	4.69	77.7	2.88
AS4	17	4.59	0.743	2.37	69.5	2.40
AP	7	8.58	0.714	3.98	65	2.30
AS2	17	6.42	0.727	2.51	53.7	1.97
RS5	3.8	5.94	0.742	2.52	58.6	0.17
RP2	4	4.71	0.709	1.94	58.1	0.36
RP1	5.2	6.18	0.706	2.47	56.6	0.46

the amount of dye adsorption for RS1 and RS1_3.5 are 0.18931and 0.16234 (10^{-7} mol .cm^{-2}), respectively.

5.4.5.8.Impedance Spectroscopy

The EIS analysis is considered an efficient tool to investigate the internal resistance of solar cells. The equivalent circuits are considered a useful tool to improve the cell performance. However, due to the complexity of fabricating a high performance solar cell, there has not been established an equivalent circuit model. In general the Nyqusit plot has three semicircles that represent the different electrochemical parameters, R_s (Ohmic resistance), R_1 (charge transfer resistance at the counter electrode/electrolyte interface), R_2 (charge transfer resistance at the photoelectrode/electrolyte), W_s (Warburg diffusion of the redox couple in electrolyte) and CPE (a constant phase element)[9]. The series resistance evaluated from the impedance spectrum depends on the preparation method of the TiO_2 film and the substrate.[32] The estimated values for the R_s for glass–FTO|TiO_2 solid-state solar cells were 35-50Ω.[32b] The sires resistance can also be estimated from the IV curve. The shunt resistance is difficult to be estimated from the EIS as it is included in R_2. The shunt resistance describes the recombination of the electron

from TiO_2 electrode to the electrolyte, a high shunt resistance indicates a slow back electron from TiO_2 electrode to the electrolyte.

General behavior of the dye–sensitized solar cells prepared by different organic additives (Pluronic P123 or surfactant and acetic acid), treated at 4500C for 30 min, and, then cured by UV for 15min, exhibit similar behavior as shown in Figure 5.22. Other layers of TiO_2 commercial films were prepared for comparison.

One big semicircle can be observed in the Nyquist plot which corresponds to the TiO_2/dye/ electrolyte triple interface interface. The interface between the high–frequency semicircle and the intermediate–frequency semicircle is difficult to distinguish due to the strong overlap of the charge transfer resistance on the TiO_2 surface and that on the Pt surface. A sub-circuit in the low-frequency response is observed which accounts for the contribution of the diffusion of the electroactive species in the liquid electrolyte.[32a] In the dark, the solar cells showed high impedance and the time constants were not well defined.

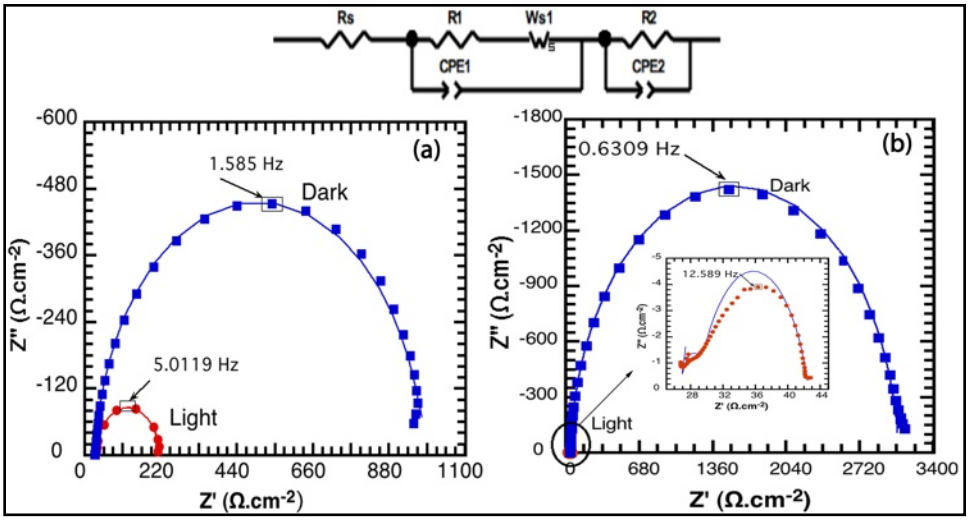

Figure 5.22 Nyquist representation of the impedance data obtained for Z907 dye–sensitized TiO_2 solar cells prepared with preheated naoparticles at 350oC mixed with a) Pluronic P123 b)surfactant and acetic acid . Experimental data are represented by symbols and solid lines correspond to fits obtained with View software using the circuit presented in figure. The inset in b) presents the magnification of circuit under light

Table 5.VI Electrochemical parameters of DSSc of different TiO_2 films prepared by different organic additives and compared to TiO_2 Degussa

sample	Area (cm^2)	Rs, Ωcm^{-2}	R1(CE), Ωcm^{-2}	R2(REC), Ωcm^{-2}	*Ws*, Ωcm^{-2}	ω_{min}/Hz	T_r/ms
AP_light	1.5	13.78	20.05	181.9	0.485	31.49	31.75
AP_dark	1.5	28.88	114.3	848.8	0.091	9.958	100.4
AP_dark	1	23.49	1.9452E-06	185.1	0.022	6.28	159
AP_light	1	17.3	42.44	12.96	0.02	62.8	15.9
AS_dark	5	0.000163	39.31	3023	14.48	3.96	252.6
AS_light	5	32.84	0.000000258	6.856	14.03	62.8	15.9
RS1_dark	4.7	42.23	7.931E-07	10.5	60.9	198.7	5
RP_light	1.2	0.000476	2.78	39.48	82.65	198.7	5
RP_dark	1.2	5.056E-08	2.091	77.15	132.2	157.82	6.33

Almost all the impedance parameters show a difference between illuminated and non illuminated cells. The response at the intermediate interface under dark condition is much higher than the one under illumination which corresponds to a high capacitance because of the expected accumulation of electrons and redox species at this interface.[32b] For these tested cells, it was found that the cells prepared with Pluronic exhibit more electron life time than those prepared with the surfactant/acetic acid additive. This observation contradicts what we have deduced from the I-V measurements. However, according to the difference in the thickness between the cells that was checked by the Profilometer, the values of the resistance are quite different.[33] The reference cells (commercial TiO_2 powder) show lower lifetime of electrons for recombination under illumination, almost six times less than the cells made with our nanocrystalline TiO_2 material. Higher electron lifetime leads to significant electron transfer, and thus, an improved Jsc. Therefore, EIS analysis confirms the promising results that we obtained with cells assembled with our nanocrystalline material, even if the cell itself is far from being optimized, and EIS reveals also being an efficient tool to understand the influence of each component and interface in DSSCs, and to improve efficiency.

5.5. Summary

In summary, we have successfully prepared an efficient dye–sensitized solar cells made from small crystalline TiO_2 prepared by novel soft chemistry and investigated their properties in dye–sensitized solar cells. We also demonstrated that different organic additives can be used to prepare the photoanode and obtain the well defined working range of the porosity. The effect of UV on the structure and crystal size of as-synthesized TiO_2 nanoparticles was tested through the XRD and N_2 isotherm characterization, which indicates no change in the crystal size and a higher surface area, respectively. Furthermore, various treatment methods (UV alone, thermal treatment alone, and combination of both) were applied. Although, UV treatment is able to clean the TiO_2 surface from organic contaminates, it is less efficient to be used alone, and leads to lower performance of solar cells, compared to thermal treatment. Interestingly, when it is used after the thermal treatment, the cells seem to show better efficiency, which will have to be confirmed in the future with more tests. The HCl treatment increases the cell efficiency by almost one to three. The enhancement was attributed to the increase of the amount of the dye. An intensive investigation on the effect of HCl on the adsorbed dye was done by the FTIR analysis. More investigation on the dye by the FTIR, demonstrates that the dye anchored chemically to TiO_2 surface. The amount of adsorbed dye for our TiO_2 films was 10 times compared to the amount of the commercial ones. The internal resistance of the cells were checked with EIS analysis, which shows higher electron lifetime, smaller charge transfer resistance for counter electrode and high recombination resistance compared to the commercial cells

Chapter 6: Conclusions and Recommendations

6.1. Conclusions

The initial goal of this research was to find preparation procedures that would allow for a room temperature cell manufacturing, in order to defined a possible future to a roll-to-roll process, required for industrial scale-up. Along this initial research, we developed a new method for the preparation at room temperature of TiO_2 anatase, a major component of the photoanode that is considered the heart of dye–sensitized solar cells. As a result, we decided to focus our research on a deep investigation of this new material, including the relation between the initial synthesis parameters and the final structure of the material, the influence of its structure on the semi-conducting properties, and how a controlled thermal treatment (named "activation" in our work) could modify the material and improve it for DSSC application.

We can conclude from this synthetic part, that we have successfully developed a new synthesis of very small (4 nm) nanocrystals of TiO_2 anatase that can be prepared with a simple room temperature method, which could be easily scaled-up. Unlike most of the syntheses reported in the literature, our study based on a mixture design method, allowed us to provide a fine description of the influence of different parameters throughout the phase diagram, on the nature and structure of the final material, with a new ability to select the initial synthesis parameters as a function of the final material structure. Beyond the intrinsic crystallographic structure of the crystals, we explored also how the mesostructure, an important feature in the optimization of the cell photoanode, was modified: a well-defined mesoporosity in the 5 nm pore range, with a rather high surface area (190 m^2/g equiv. to 250 m^2/g for SiO_2), was observed. Furthermore, the evolution of these materials as a function of temperature was explored. We have demonstrated that the anatase structure is very stable and that the thermal

evolution is closely linked to the initial nanostructure. We also have provided a new complete example of the bandgap modulation by size control in this study to:

• Confirm experimentally the theoretical model initially proposed by L. Brus in 1986 with a continuous evolution instead of spared results.

• Provide a final discussion regarding the choice between the indirect or direct band gap assignment, and discard the direct bandgap model.

• Demonstrate the limit of the quantum confinement effect to a crystal size of 10 nm

• Confirm that the usual band gap usually assigned to anatase (3.2 eV), does not always apply to nanomaterials prepared by sol-gel methods.

This first part was followed by an additional study designed to increase our knowledge in the improvement of the semi-conducting properties of our material, before using it in DSSCs. To ease the analytical part, we decided to explore these properties by the mean of photocatalytic tests, instead of solar cell testing, as the efficiency of solar cells depends on many other parameters. Besides, photocatalytic tests are more easy to run, and TiO_2 is obviously well-known as a very important material in this domain. This study was carried out to explore this domain as completely as possible, and to provide also a set of results that could be submitted for publication, which explains the rather exhaustive work.

The influence of different parameters on the efficiency of TiO_2 photocatalysis was studied. One very important parameter was the actual crystallinity of the anatase phase, and we revealed that the thermal activation of the initial RT-synthesized anatase is a very important parameter for enhancing the photocatalytic activity, if the crystal size remains unchanged. Consequently, excellent performances were obtained as a result of crystallinity improvement, without increasing the size. As the experimental optimization is also an important step, we have proved that a too high amount of catalyst, which is supposed to favor the reaction, will hamper it as a result of an additional light shielding effect.

We have also illustrated by a specific study that our material adopt a zero order kinetic, which means that the reaction does not depend on the amount of dye, if both the material quality and

amount are optimized. Another important processing parameter, which is the acidity of the solution have been explored, all parameters being optimized, and we showed that the reaction time can be divided by two when using a pH 2 solution instead of a neutral one.

Finally, this study, initially carried out to study our material, led us to investigate the comparison with commercial powders, one being also a pure anatase with the same specific area, and the other being the well-known P25 from Degussa, the current reference for photocatalysis. Our study proved that a "knowledge–based" design of materials can provide a breakthrough improvement, compared with a basic synthesis: compared with our as-synthesized material, which had been already optimized through the mixture design method, the adequate thermal activation and correct adjustment of pH 2, allowed our material to achieve the full photodegradation after half the time required for the commercial anatase to achieve only 65% of it. Comparison with the P25 from Degussa was also very positive as our material led to the same efficiency (complete photodegradation) within the same time range. It is worth noticing that the Degussa powder uses a strong "boosting" factor, that is, the anatase-rutile heterostructure that helps to increase the stability of the electron-hole pairs created by the photo-irradiation.

Hence, we could demonstrate that:

• The semiconducting properties of TiO_2 can be adjusted by the correct activation process, which is clearly demonstrated by photocatalytic tests on dye degradation.

• Compared with a commercial powder that exhibits a the same nature and surface area, our material was by far more active.

• The combination of both material improvement, and process, allow for the achievement of photocatalytic properties as high as those observed with the best commercial product.

The last goal of this study was to check the successful integration of the synthesized TiO_2 nanoparticles in the dye sensitized solar cells. We had first to explore the structure of TiO_2 at a higher scale, that is, the structure of the photoanode film made with. Accordingly, the TiO_2 film textural, structure, and electrical properties were checked via many techniques (XRD, FTIR,

N_2 adsorption, UV-Vis, SEM, TEM, impedance spectroscopy, Solar simulator, and profilometer).

Our main result, which summarizes this work, is that we demonstrated that solar cells can be assembled with these new nanoparticles, and lead to significant solar efficiency. Of course, until now, the optimization of DSSCs is based on the combination of many additive, some of them being secret, some of them being hardly defined for their actual contribution. Therefore, we explored the effect of various organic additives on the cell performance. We discovered that almost all types of organic additives show very close effect on the final performance of the solar cells. With either Pluronic P123 or mixture of Span80/Tween 80 and acetic acids, the cell efficiencies were rather high, and equal to 4.95% and 4.7%, respectively. Successful preparation of the Pt counter electrode by the polyol method, was performed. We also demonstrated the successful chemical attachment of Z907 dye to TiO_2 surface. Furthermore, different treatment methods were applied to the TiO_2 thin films. The most efficient method was to apply thermal treatment at 450°C and then curing by UV for 15 min. Adding a blocking layer did enhance the overall cell efficiency and more specifically the FF, as it helps in decreasing the series resistance and improving the shunt resistance. Finally, we used impedance spectroscopy to develop a model for our cells, and these analyses confirmed that EIS is a powerful tool that helps in identifying the deficiency in the cell by measuring utterance resistance.

6.2. Recommendations

The ultimate goal of this research was to investigate the properties of the synthesized TiO_2 nanoparticles and test their ability to be used efficiently in the dye sensitized solar cells, and we have successfully confirmed that this new material could become one of the "game changers" in the domain. However, there are still to be done in order to optimize the cell parameters, and mostly to design cells that could be really manufactured at a very large scale (our initial aim). Therefore, we provide the following recommendations for future research, these recommendation being listed in three steps:

First, the nanocrystalline TiO_2 powder, which has been demonstrated a promising material for solar cell, has to be further tested toward its successful integration into DSSC. This will regard many parameters, including the optimum film thickness, or amount of organic additives taking into account its effect on the film structure. This must obviously take into account a statistical approach, and fine EIS-based modeling. None of our cells have used the addition of a scattering layer (another important feature), which will have to be done. Exploring more about the effect of both treatments, UV-O_3/ thermal and UV/thermal, and determining parameters that affect the cell performance, will be required, too.

Secondly, this material has to be associated with new dye molecules (metal based or polymers) as the interaction between the dye and the semiconductor is very important. One can think that dedicated fine spectroscopic studies on charge transfer would help us to increase our knowledge on this strategic interaction.

Thirdly, a full analysis has to be done on the design that would be required for achieving solid-state solar cells. This analysis must include the choice and selection of components, especially the redox mediator and electrolyte, the preparation of the photoanode - where our study could take place-, and the ability to avoid using platinum at the counter electrode, as it is the most expensive component. This analysis must include from the beginning, the possible manufacturing process, like ink-jet printing, which means that the material design must integrate the possibility to elaborate "inks" with the correct viscosity.

References (Chapter 1)

1. (a) Gratzel, M., Mesoporous oxide junctions and nanostructured solar cells. *Current Opinion in Colloid & Interface Science* **1999,** *4* (4), 314-321; (b) Gratzel, M., Photoelectrochemical cells. *Nature* **2001,** *414* (6861), 338-344; (c) Gratzel, M., Conversion of sunlight to electric power by nanocrystalline dye-sensitized solar cells. *Journal of Photochemistry and Photobiology a-Chemistry* **2004,** *164* (1-3), 3-14; (d) Gratzel, M., Dye-sensitized solar cells. *Journal of Photochemistry and Photobiology C-Photochemistry Reviews* **2003,** *4* (2), 145-153.

2. (a) Snaith, H. J., Estimating the Maximum Attainable Efficiency in Dye-Sensitized Solar Cells. *Advanced Functional Materials* **2010,** *20* (1), 13-19; (b) Benkstein, K. D.; Kopidakis, N.; de Lagemaat, J. V.; Frank, A. J., Influence of the network geometry on electron transport in nanoparticle networks. In *Quantum Dots, Nanoparticles and Nanowires*, GuyotSionnest, P.; Mattoussi, H.; Wang, Z. L., Eds. 2004; Vol. 789, pp 325-330.

3. Kalyanasundaram, K.; Zakeeruddin, S. M.; Gratzel, M., Photonic and Optoelectronic Devices Based on Mesoscopic Thin Films. *Chimia* **2011,** *65* (9), 738-742.

4. Mao, X. C. a. S. S., Titanium Dioxide Nanomaterials: Synthesis, Properties, Modifications, and Applications. **2007**.

5. (a) Yip, C. T.; Mak, C. S. K.; Djurisic, A. B.; Hsu, Y. F.; Chan, W. K., Dye-sensitized solar cells based on TiO2 nanotube/porous layer mixed morphology. *Applied Physics a-Materials Science & Processing* **2008,** *92* (3), 589-593; (b) Kuang, D.; Brillet, J.; Chen, P.; Takata, M.; Uchida, S.; Miura, H.; Sumioka, K.; Zakeeruddin, S. M.; Gratzel, M., Application of highly ordered TiO2 nanotube arrays in flexible dye-sensitized solar cells. *Acs Nano* **2008,** *2* (6), 1113-1116.

References (Chapter 2)

1. Luque, A. H., S., Handbook of Photovoltaic Science and Engineering. Wiely, Ed. 2003.
2. Bai, Y.; Cao, Y. M.; Zhang, J.; Wang, M.; Li, R. Z.; Wang, P.; Zakeeruddin, S. M.; Gratzel, M., High-performance dye-sensitized solar cells based on solvent-free electrolytes produced from eutectic melts. *Nature materials* **2008,** *7* (8), 626-630.
3. Miyasaka, T.; Ikegami, M.; Kijitori, Y., Photovoltaic Performance of Plastic Dye-Sensitized Electrodes Prepared by Low-Temperature Binder-Free Coating of Mesoscopic Titania. *Journal of The Electrochemical Society* **2007,** *154* (5), A455.
4. Sugiyama, O.; Okuya, M.; Kaneko, S., Photocatalytic ability of TiO2 porous film prepared by modified spray pyrolysis deposition technique. *Journal of the Ceramic Society of Japan* **2009,** *117* (1362), 203-207.
5. Zhang, D.; Yoshida, T.; Oekermann, T.; Furuta, K.; Minoura, H., Room-Temperature Synthesis of Porous Nanoparticulate TiO_2 Films for Flexible Dye-Sensitized Solar Cells. *Advanced Functional Materials* **2006,** *16* (9), 1228-1234.
6. Gratzel, M., Mesoporous oxide junctions and nanostructured solar cells. *Current Opinion in Colloid & Interface Science* **1999,** *4* (4), 314-321.
7. Kalyanasundaram, K.; Grätzel, M., Photovoltaic performance of injection solar cells and other applications of nanocrystalline oxide layers. *Proceedings of the Indian Academy of Sciences-Chemical Sciences* **1997,** *109* (6), 447-469.
8. Zakeeruddin, S. M.; Grätzel, M., Solvent-Free Ionic Liquid Electrolytes for Mesoscopic Dye-Sensitized Solar Cells. *Advanced Functional Materials* **2009,** *19* (14), 2187-2202.
9. Wolfbauer, G.; Bond, A. M.; Eklund, J. C.; MacFarlane, D. R., A channel flow cell system specifically designed to test the efficiency of redox shuttles in dye sensitized solar cells. *Solar Energy Materials and Solar Cells* **2001,** *70* (1), 85-101.
10. Nusbaumer, H.; Zakeeruddin, S. M.; Moser, J. E.; Grätzel, M., An alternative efficient redox couple for the dye-sensitized solar cell system. *Chemistry-a European Journal* **2003,** *9* (16), 3756-3763.

11. Wang, M. K.; Chamberland, N.; Breau, L.; Moser, J. E.; Humphry-Baker, R.; Marsan, B.; Zakeeruddin, S. M.; Graetzel, M., An organic redox electrolyte to rival triiodide/ iodide in dye-sensitized solar cells. *Nature Chemistry* **2010,** *2* (5), 385-389.

12. Gorlov, M.; Kloo, L., Ionic liquid electrolytes for dye-sensitized solar cells. *Dalton Trans* **2008,** (20), 2655-66.

13. (a) Cho, S. J.; Ouyang, J., Attachment of Platinum Nanoparticles to Substrates by Coating and Polyol Reduction of A Platinum Precursor. *The Journal of Physical Chemistry C* **2011,** *115* (17), 8519-8526; (b) Sun, K.; Fan, B. H.; Ouyang, J. Y., Nanostructured Platinum Films Deposited by Polyol Reduction of a Platinum Precursor and Their Application as Counter Electrode of Dye-Sensitized Solar Cells. *Journal of Physical Chemistry C* **2010,** *114* (9), 4237-4244.

14. Papageorgiou, N.; Grätzel, M.; Infelta, P. P., On the relevance of mass transport in thin layer nanocrystalline photoelectrochemical solar cells. *Solar Energy Materials and Solar Cells* **1996,** *44* (4), 405-438.

15. Kay, A.; Grätzel, M., Low cost photovoltaic modules based on dye sensitized nanocrystalline titanium dioxide and carbon powder. *Solar Energy Materials and Solar Cells* **1996,** *44* (1), 99-117.

16. Toivola, M.; Halme, J.; Miettunen, K.; Aitola, K.; Lund, P. D., Nanostructured dye solar cells on flexible substrates-Review. *International Journal of Energy Research* **2009,** *33* (13), 1145-1160.

17. Hodes, G., *Electrochemistry of Nanomaterials*. WILEY-VCH: Federal Republic of Germany, 2001.

18. Leon, C. P.; Kador, L.; Peng, B.; Thelakkat, M., Characterization of the adsorption of ru-bpy dyes on mesoporous TiO_2 films with UV-Vis, Raman, and FTIR spectroscopies. *Journal of Physical Chemistry B* **2006,** *110* (17), 8723-8730.

19. Gratzel, M., Conversion of sunlight to electric power by nanocrystalline dye-sensitized solar cells. *Journal of Photochemistry and Photobiology a-Chemistry* **2004,** *164* (1-3), 3-14.

20. Hamann, T. W.; Jensen, R. A.; Martinson, A. B. F.; Van Ryswyk, H.; Hupp, J. T., Advancing beyond current generation dye-sensitized solar cells. *Energy & Environmental Science* **2008,** *1* (1), 66.

21. Rehm, J. M.; McLendon, G. L.; Nagasawa, Y.; Yoshihara, K.; Moser, J.; Graetzel, M., Femtosecond electron-transfer dynamics at a sensitizing dye-semiconductor (TiO2) interface. *Journal of Physical Chemistry* **1996,** *100* (23), 9577-9578.

22. Huber, R.; Sporlein, S.; Moser, J. E.; Grätzel, M.; Wachtveitl, J., The role of surface states in the ultrafast photoinduced electron transfer from sensitizing dye molecules to semiconductor colloids. *Journal of Physical Chemistry B* **2000,** *104* (38), 8995-9003.

23. Hagfeldt, A.; Grätzel, M., Light-Induced Redox Reactions in Nanocrystalline Systems. *Chemical Reviews* **1995,** *95* (1), 49-68.

24. Cahen, D.; Hodes, G.; Gratzel, M.; Guillemoles, J. F.; Riess, I., Nature of photovoltaic action in dye-sensitized solar cells. *Journal of Physical Chemistry B* **2000,** *104* (9), 2053-2059.

25. Cao, F.; Oskam, G.; Meyer, G. J.; Searson, P. C., Electron Transport in Porous Nanocrystalline TiO_2 Photoelectrochemical Cells. *The Journal of Physical Chemistry* **1996,** *100* (42), 17021-17027.

26. Park, N. G.; van de Lagemaat, J.; Frank, A. J., Comparison of Dye-Sensitized Rutile- and Anatase-Based TiO_2 Solar Cells. *The Journal of Physical Chemistry B* **2000,** *104* (38), 8989-8994.

27. Bouvard, D.; Lange, F. F., Correlation Between Random Dense Parking and Random Dense Packing for Determining Particle Coordination-Number in Binary-Number in Binary-Systems. *Physical Review A* **1992,** *45* (8), 5690-5693.

28. Ofir, A.; Dor, S.; Grinis, L.; Zaban, A.; Dittrich, T.; Bisquert, J., Porosity dependence of electron percolation in nanoporous TiO_2 layers. *The Journal of chemical physics* **2008,** *128* (6), 064703.

29. Frank, A. J.; Gregg, B. A.; Graetzel, M.; Nozik, A. J.; Zaban, A.; Ferrere, S.; Schlichthorl, G.; Huang, S. Y., Photochemical solar cells based on dye-sensitization of

nanocrystalline TiO_2. In *Future Generation Photovoltaic Technologies*, McConnell, R. D., Ed. 1997; pp 145-153.

30. Mori, S. Y., S., *Nanostructured Materials for Solar Energy Conversion*. 1st ed.; Elsevier: 2007; p 614

31. Zukalova, M.; Zukal, A.; Kavan, L.; Nazeeruddin, M. K.; Liska, P.; Gratzel, M., Organized mesoporous TiO_2 films exhibiting greatly enhanced performance in dye-sensitized solar cells. *Nano Letters* **2005,** *5* (9), 1789-1792.

32. Yanagida, S., Recent research progress of dye-sensitized solar cells in Japan. *Comptes Rendus Chimie* **2006,** *9* (5-6), 597-604.

33. Tebby, Z.; Uddin, T.; Nicolas, Y.; Olivier, C.; Toupance, T.; Labrugere, C.; Hirsch, L., Low-Temperature UV Processing of Nanoporous SnO_2 Layers for Dye-Sensitized Solar Cells. *ACS applied materials & interfaces* **2011,** *3* (5), 1485-1491.

34. Gutierrez-Tauste, D.; Zumeta, I.; Vigil, E.; Hernandez-Fenollosa, M. A.; Domenech, X.; Ayllon, J. A., New low-temperature preparation method of the TiO_2 porous photoelectrode for dye-sensitized solar cells using UV irradiation. *Journal of Photochemistry and Photobiology a-Chemistry* **2005,** *175* (2-3), 165-171.

35. (a) Lee, M.-K.; Yen, H.; Hsiao, C.-C., Efficiency Improvement of Dye-Sensitized Solar Cell with Ultraviolet and Hydrogen Chloride Treatments. *Journal of The Electrochemical Society* **2011,** *158* (5), K136; (b) Murakami, T. N.; Kijitori, Y.; Kawashima, N.; Miyasaka, T., Low temperature preparation of mesoporous TiO_2 films for efficient dye-sensitized photoelectrode by chemical vapor deposition combined with UV light irradiation. *Journal of Photochemistry and Photobiology A: Chemistry* **2004,** *164* (1-3), 187-191.

36. (a) Hoshikawa, T.; Kikuchi, R.; Eguchi, K., Impedance analysis for dye-sensitized solar cells with a reference electrode. *Journal of Electroanalytical Chemistry* **2006,** *588* (1), 59-67; (b) Wang, Q.; Ito, S.; Grätzel, M.; Fabregat-Santiago, F.; Mora-Sero, I.; Bisquert, J.; Bessho, T.; Imai, H., Characteristics of high efficiency dye-sensitized solar cells. *Journal of Physical Chemistry B* **2006,** *110* (50), 25210-25221.

37. Macdonald, J. R., Impedance Spectroscopy. *Annals of Biomedical Engineering* **1992,** *20* (3), 289-305.

38. Wang, Q.; Moser, J. E.; Grätzel, M., Electrochemical impedance spectroscopic analysis of dye-sensitized solar cells. *Journal of Physical Chemistry B* **2005,** *109* (31), 14945-14953.

39. Kim, J.-K.; Seo, H.; Son, M.-K.; Shin, I.; Hong, J.; Kim, H.-J., The analysis of the change in the performance and impedance of dye-sensitized solar cell according to the dye-adsorption time. *Current Applied Physics* **2010,** *10* (3), S418-S421.

40. Kalyanasundaram, K. E., *Dye-Sensitized Solar Cells*. Taylor & Francis: 2010; p 604.

41. Bisquert, J.; Garcia-Belmonte, G.; Bueno, P.; Longo, E.; Bulhoes, L. O. S., Impedance of constant phase element (CPE)-blocked diffusion in film electrodes. *Journal of Electroanalytical Chemistry* **1998,** *452* (2), 229-234.

42. Hauch, A.; Georg, A., Diffusion in the electrolyte and charge-transfer reaction at the platinum electrode in dye-sensitized solar cells. *Electrochimica Acta* **2001,** *46* (22), 3457-3466.

43. Han, C.-H.; Jousseaume, B.; Rascle, M.-C.; Toupance, T.; Cachet, H.; Vivier, V., Nanocrystalline F-doped tin dioxide materials: texture, morphology and photosensitization with a perylene-substituted organotin. *Journal of Fluorine Chemistry* **2004,** *125* (8), 1247-1254.

44. Fuke, N.; Fukui, A.; Islam, A.; Komiya, R.; Yamanaka, R.; Han, L. Y.; Harima, H., Electron transport in back contact dye-sensitized solar cells. *Journal of Applied Physics* **2008,** *104* (6).

45. Sugimoto, W.; Yokoshima, K.; Murakami, Y.; Takasu, Y., Charge storage mechanism of nanostructured anhydrous and hydrous ruthenium-based oxides. *Electrochimica Acta* **2006,** *52* (4), 1742-1748.

46. de levie, R., *Advances in electrochemistry and electrochemical engineering* Interscience: 1967; Vol. 6.

47. Atta, N. F.; Amin, H. M. A.; Khalil, M. W.; Galal, A., Nanotube Arrays as Photoanodes for Dye Sensitized Solar Cells Using Metal Phthalocyanine Dyes. *International Journal of Electrochemical Science* **2011,** *6* (8), 3316-3332.

48. Bisquert, J.; Garcia-Belmonte, G.; Fabregat-Santiago, F.; Bueno, P. R., Theoretical models for ac impedance of finite diffusion layers exhibiting low frequency dispersion. *Journal of Electroanalytical Chemistry* **1999,** *475* (2), 152-163.

49. Fabregat-Santiago, F.; Bisquert, J.; Garcia-Belmonte, G.; Boschloo, G.; Hagfeldt, A., Influence of electrolyte in transport and recombination in dye-sensitized solar cells studied by impedance spectroscopy. *Solar Energy Materials and Solar Cells* **2005,** *87* (1-4), 117-131.

50. Pichot, F.; Pitts, J. R.; Gregg, B. A., Low-temperature sintering of TiO2 colloids: Application to flexible dye-sensitized solar cells. *Langmuir* **2000,** *16* (13), 5626-5630.

51. Lindstrom, H.; Holmberg, A.; Magnusson, E.; Malmqvist, L.; Hagfeldt, A., A new method to make dye-sensitized nanocrystalline solar cells at room temperature. *Journal of Photochemistry and Photobiology a-Chemistry* **2001,** *145* (1-2), 107-112.

52. Park, N. G.; Kim, K. M.; Kang, M. G.; Ryu, K. S.; Chang, S. H.; Shin, Y. J., Chemical sintering of nanoparticles: A methodology for low-temperature fabrication of dye-sensitized TiO_2 films. *Advanced Materials* **2005,** *17* (19), 2349-+.

53. Zhang, Q.; Cao, G., Nanostructured photoelectrodes for dye-sensitized solar cells. *Nano Today* **2011,** *6* (1), 91-109.

54. Fujita, K.; Konishi, J.; Nakanishi, K.; Hirao, K., Monolithic TiO2 with Controlled Multiscal Porosity via Template-Free- Sol–Gel Process Accompined by Phase Separation. *Chemistry of Materials* **2006,** *18* (25), 6069-6074.

55. Nakanishi, K., Pore Structure Control of Silica Gels Based on Phase Separation. *Journal of Porous Materials* **1997,** *4* (2), 67-112.

56. Gaweł, B.; Gaweł, K.; Øye, G., Sol-Gel Synthesis of Non-Silica Monolithic Materials. *Materials* **2010,** *3* (4), 2815-2833.

57. Strathmann, H., *Introduction to Membrane Science and Technology*. Wiely-VCH: 2011; p 473.

58. Favvas, E. P. M., A. Ch. , What is spinodal decomposition? *Engineering Science and Technology Review* **2008,** *1*, 3.

59. Fujimoto, M., Dynamics of Phase Transitions. In *The Physics of Structural Phase Transitions*, Springer: 2003.

60. Kalyanasundaram, K.; Zakeeruddin, S. M.; Gratzel, M., Photonic and Optoelectronic Devices Based on Mesoscopic Thin Films. *Chimia* **2011,** *65* (9), 738-742.

61. Oonk, H.A.J., Phase Theory; The Thermodynamics of Heterogeneous Equilibria, Elsevier Scientific Publishing Company, Amsterdam (1981).

References (Chapter 3)

1. Kroon, J. M.; Bakker, N. J.; Smit, H. J. P.; Liska, P.; Thampi, K. R.; Wang, P.; Zakeeruddin, S. M.; Grätzel, M.; Hinsch, A.; Hore, S.; Würfel, U.; Sastrawan, R.; Durrant, J. R.; Palomares, E.; Pettersson, H.; Gruszecki, T.; Walter, J.; Skupien, K.; Tulloch, G. E., Nanocrystalline dye-sensitized solar cells having maximum performance. *Progress in Photovoltaics: Research and Applications* **2007,** *15* (1), 1-18.
2. (a) Oregan, B.; Grätzel, M., A Low-Cost, High-Efficiency Solar-Cell Based On Dye-Sensitized Colloidal TiO_2 Films. *Nature* **1991,** *353* (6346), 737-740; (b) Kavan, L.; Gratzel, M.; Gilbert, S. E.; Klemenz, C.; Scheel, H. J., Electrochemical and photoelectrochemical investigation of single-crystal anatase. *Journal of the American Chemical Society* **1996,** *118* (28), 6716-6723; (c) Grätzel, M., Mesoporous oxide junctions and nanostructured solar cells. *Current Opinion in Colloid & Interface Science* **1999,** *4* (4), 314-321.
3. (a) Toivola, M.; Halme, J.; Miettunen, K.; Aitola, K.; Lund, P. D., Nanostructured dye solar cells on flexible substrates-Review. *International Journal of Energy Research* **2009,** *33* (13), 1145-1160; (b) Ribeiro, H. A.; Sommeling, P. M.; Kroon, J. M.; Mendes, A.; Costa, C. A. V., Dye-sensitized Solar Cells: Novel Concepts, Materials, and State-of-the-Art Performances. *International Journal of Green Energy* **2009,** *6* (3), 245-256.
4. Goncalves, L. M.; Bermudez, V. d. Z.; Ribeiro, H. A.; Mendes, A. M., Dye-sensitized solar cells: A safe bet for the future. *Energy & Environmental Science* **2008,** *1* (6), 655-667.
5. Cahen, D.; Hodes, G.; Grätzel, M.; Guillemoles, J. F.; Riess, I., Nature of photovoltaic action in dye-sensitized solar cells. *Journal of Physical Chemistry B* **2000,** *104* (9), 2053-2059.
6. Wurfel, U.; Wagner, J.; Hinsch, A., Spatial electron distribution and its origin in the nanoporous TiO_2 network of a dye solar cell. *Journal of Physical Chemistry B* **2005,** *109* (43), 20444-20448.

7. Zhang, Q.; Cao, G., Nanostructured photoelectrodes for dye-sensitized solar cells. *Nano Today* **2011,** *6* (1), 91-109.

8. Carp, O.; Huisman, C. L.; Reller, A., Photoinduced reactivity of titanium dioxide. *Progress in Solid State Chemistry* **2004,** *32* (1-2), 33-177.

9. (a) Mao, X. C. a. S. S., Titanium Dioxide Nanomaterials: Synthesis, Properties, Modifications, and Applications. **2007**; (b) Lee, S.; Cho, I.-S.; Lee, J. H.; Kim, D. H.; Kim, D. W.; Kim, J. Y.; Shin, H.; Lee, J.-K.; Jung, H. S.; Park, N.-G.; Kim, K.; Ko, M. J.; Hong, K. S., Two-Step Sol-Gel Method-Based TiO_2 Nanoparticles with Uniform Morphology and Size for Efficient Photo-Energy Conversion Devices. *Chemistry of Materials* **2010,** *22* (6), 1958-1965; (c) Pagliaro, M.; Palmisano, G.; Ciriminna, R.; Loddo, V., Nanochemistry aspects of titania in dye-sensitized solar cells. *Energy & Environmental Science* **2009,** *2* (8), 838-844; (d) Yu, I. G.; Kim, Y. J.; Kim, H. J.; Lee, C.; Lee, W. I., Size-dependent light-scattering effects of nanoporous TiO_2 spheres in dye-sensitized solar cells. *Journal of Materials Chemistry* **2011,** *21* (2), 532-538; (e) Du Pasquier, A.; Stewart, M.; Spitler, T.; Coleman, M., Aqueous coating of efficient flexible TiO_2 dye solar cell photoanodes. *Solar Energy Materials and Solar Cells* **2009,** *93* (4), 528-535; (f) Yamaguchi, T.; Tobe, N.; Matsumoto, D.; Arakawa, H., Highly efficient plastic substrate dye-sensitized solar cells using a compression method for preparation of TiO(2) photoelectrodes. *Chem Commun (Camb)* **2007,** (45), 4767-9; (g) Zhang, H.; Han, Y.; Liu, X.; Liu, P.; Yu, H.; Zhang, S.; Yao, X.; Zhao, H., Anatase TiO_2 microspheres with exposed mirror-like plane {001} facets for high performance dye-sensitized solar cells (DSSCs). *Chemical Communications* **2010,** *46* (44), 8395-8397; (h) Koo, H. J.; Kim, Y. J.; Lee, Y. H.; Lee, W. I.; Kim, K.; Park, N. G., Nano-embossed Hollow Spherical TiO_2 as Bifunctional Material for High-Efficiency Dye-Sensitized Solar Cells. *Advanced Materials* **2008,** *20* (1), 195-199; (i) Zhu, K.; Neale, N. R.; Miedaner, A.; Frank, A. J., Enhanced charge-collection efficiencies and light scattering in dye-sensitized solar cells using oriented TiO_2 nanotubes arrays. *Nano Letters* **2007,** *7* (1), 69-74.

10. (a) Ohno, T.; Sarukawa, K.; Tokieda, K.; Matsumura, M., Morphology of a TiO_2 Photocatalyst (Degussa, P-25) Consisting of Anatase and Rutile Crystalline Phases. *Journal of Catalysis* **2001,** *203* (1), 82-86; (b) Weerasinghe, H. C.; Sirimanne, P. M.; Simon, G. P.; Cheng, Y. B., Fabrication of efficient solar cells on plastic substrates using binder-free ball milled titania slurries. *Journal of Photochemistry and Photobiology A: Chemistry* **2009,** *206* (1), 64-70.

11. Wang, Y.; Herron, N., Nanometer-sized Semiconductor Clusters - Materials Synthesis, Quantum Size Effects, And Photphysical Pproperities. *Journal of Physical Chemistry* **1991,** *95* (2), 525-532.

12. Bawendi, M. G.; Steigerwald, M. L.; Brus, L. E., The Quantum-Mechanics of Larger Semiconductor Clusters (Quantum Dots). *Annual Review of Physical Chemistry* **1990,** *41*, 477-496.

13. (a) Alivisatos, A. P., Semiconductor clusters, nanocrystals, and quantum dots. *Science* **1996,** *271* (5251), 933-937; (b) Fang, X.; Bando, Y.; Gautam, U. K.; Ye, C.; Golberg, D., Inorganic semiconductor nanostructures and their field-emission applications. *Journal of Materials Chemistry* **2008,** *18* (5), 509-522.

14. (a) Kormann, C.; Bahnemann, D. W.; Hoffmann, M. R., Preparation And Characterization of Quantum-Size Titanium-Dioxide. *Journal of Physical Chemistry* **1988,** *92* (18), 5196-5201; (b) Almquist, C. B.; Biswas, P., Role of Synthesis Method and Particle Size of Nanostructured TiO_2 on Its Photoactivity. *Journal of Catalysis* **2002,** *212* (2), 145-156.

15. Chen, S.-Y. C., Soofin Acid-Free Synthesis of Mesoporous Silica Using Triblock Copolymer as Template with the Aid of Salt and Alcohol. *Chem. Mater.* **2007,** *19* (12), 3041-3051.

16. Lee, H. S.; Woo, C. S.; Youn, B. K.; Kim, S. Y.; Oh, S. T.; Sung, Y. E.; Lee, H. I., Bandgap Modulation of TiO2 and its Effect on the Activity in Photocatalytic Oxidation of 2-isopropyl-6-methyl-4-pyrimidinol. *Topics in Catalysis* **2005,** *35* (3-4), 255-260.

17. Reddy, K. M. M., Sunkara V. ; Reddy , A. Ramachandra Bandgap studies on anatase titanium dioxide nanoparticles *Materials Chemistry and Physics* **2002,** (78), 239–245.

18. Hessien, M.; Singh, N.; Kim, C.; Prouzet, E., Stability and Tunability of O/W Nanoemulsions Prepared by Phase Inversion Composition. *Langmuir* **2011,** *27* (6), 2299-2307.

19. Fujita, K.; Konishi, J.; Nakanishi, K.; Hirao, K., Morphological control and strong light scattering in macroporous TiO_2 monoliths prepared via a colloid-derived sol–gel route. *Science and Technology of Advanced Materials* **2006,** *7* (6), 511-518.

20. Brunauer, S.; Emmett, P. H.; Teller, E., Adsorption of gases in multimolecular layers. *Journal of the American Chemical Society* **1938,** *60*, 309-319.

21. Broekhof. Jc; Deboer, J. H., Studies On Pore Systems In Catalysts .XII. Pore Distribution From Desorption Branch of A Nitrogen Sorption Isotherm In Case of Cylidrical Pores .A. An Analysis of the Capillary Evaporation Process. *Journal of Catalysis* **1968,** *10* (4), 368-374.

22. Aubard, J.; Levoir, P.; Denis, A.; Claverie, P., Direct Analysis of Chemical Relaxation Signals by A Method Based on The Combination of Laplace Transform And Pade Approximants. *Computers & Chemistry* **1987,** *11* (3), 163-178.

23. (a) Koelsch, M.; Cassaignon, S.; Guillemoles, J. F.; Jolivet, J. R., Comparison of optical and electrochemical properties of anatase and brookite TiO_2 synthesized by the sol-gel method. *Thin Solid Films* **2002,** *403*, 312-319; (b) Reyes-Coronado, D.; Rodriguez-Gattorno, G.; Espinosa-Pesqueira, M. E.; Cab, C.; de Coss, R.; Oskam, G., Phase-pure TiO(2) nanoparticles: anatase, brookite and rutile. *Nanotechnology* **2008,** *19* (14), 145605.

24. Sanchez, E.; Lopez, T., Effect of the preparation method on the band gap of titania and platinum-titania sol-gel materials. *Materials Letters* **1995,** *25* (5-6), 271-275.

25. Fatoni, R. Product Design of Wheat Straw Polypropylene Composite. Waterloo Waterloo, Ontario, Canada, 2012.

26. (a) Tang, H.; Prasad, K.; Sanjines, R.; Schmid, P. E.; Levy, F., Electrical And Optical-Properties of TiO_2 Anatase Thin-Films. *Journal of Applied Physics* **1994,** *75* (4), 2042-2047; (b) vandeKrol, R.; Goossens, A.; Schoonman, J., Mott-Schottky analysis of

nanometer-scale thin-film anatase TiO2. *Journal of The Electrochemical Society* **1997,** *144* (5), 1723-1727.

27. Zhang, H. Z.; Banfield, J. F., Understanding polymorphic phase transformation behavior during growth of nanocrystalline aggregates: Insights from TiO_2. *Journal of Physical Chemistry B* **2000,** *104* (15), 3481-3487.

28. Fragnaud, P.; Prouzet, E.; Brec, R., Structural Study of Room-Teperature Synthesized Nickel Thiophosphate A-NIPS3. *Journal of Materials Research* **1992,** *7* (7), 1839-1846.

29. Gajjela, S. R.; Ananthanarayanan, K.; Yap, C.; Graetzel, M.; Balaya, P., Synthesis of mesoporous titanium dioxide by soft template based approach: characterization and application in dye-sensitized solar cells. *Energy & Environmental Science* **2010,** *3* (6), 838-845.

30. (a) Wang, P.; Korner, W.; Emmerling, A.; Beck, A.; Kuhn, J.; Fricke, J., Optical Investigations of Silica Aerogels. *Journal of Non-Crystalline Solids* **1992,** *145* (1-3), 141-145; (b) Schaefer, D. W.; Keefer, K. D., Structure of Random Porous Materials-Silica Aerogel. *Physical Review Letters* **1986,** *56* (20), 2199-2202.

31. Mandelbrot, B. B., Fractal Geometry-What is it, And What Does it Do. *Proceedings of the Royal Society of London Series a-Mathematical Physical and Engineering Sciences* **1989,** *423* (1864), 3-16.

32. Kim, Y. J.; Lee, M. H.; Kim, H. J.; Lim, G.; Choi, Y. S.; Park, N.-G.; Kim, K.; Lee, W. I., Formation of Highly Efficient Dye-Sensitized Solar Cells by Hierarchical Pore Generation with Nanoporous TiO2Spheres. *Advanced Materials* **2009,** *21* (36), 3668-3673.

33. Spurr, R. A.; Myers, H., Quantitative Analysis of Anatase-Rutile Mixtures With an X-Ray Diffractometer. *Analytical Chemistry* **1957,** *29* (5), 760-762.

34. Li, J.-G.; Ishigaki, T.; Sun, X., Anatase, brookite, and rutile nanocrystals via redox reactions under mild hydrothermal conditions: Phase-selective synthesis and physicochemical properties. *Journal of Physical Chemistry C* **2007,** *111* (13), 4969-4976.

35. Enright, B.; Fitzmaurice, D., Spectroscopic determination of electron and mole effective masses in a nanocrystalline semiconductor film. *Journal of Physical Chemistry* **1996,** *100* (3), 1027-1035.

36. Bessergenev, V., High-temperature anomalies of dielectric constant in TiO_2 thin films. *Materials Research Bulletin* **2009,** *44* (8), 1722-1728.

37. Petrovsky, V.; Petrovsky, T.; Kamlapurkar, S.; Dogan, F., Characterization of Dielectric Particles by Impedance Spectroscopy (Part I). *Journal of the American Ceramic Society* **2008,** *91* (6), 1814-1816.

38. González-Reyes, L.; Hernández-Pérez, I.; Díaz-Barriga Arceo, L.; Dorantes-Rosales, H.; Arce-Estrada, E.; Suárez-Parra, R.; Cruz-Rivera, J. J., Temperature effects during Ostwald ripening on structural and bandgap properties of TiO2 nanoparticles prepared by sonochemical synthesis. *Materials Science and Engineering: B* **2010,** *175* (1), 9-13.

39. Serpone, N.; Lawless, D.; Khairutdinov, R., Size Effects on The Photophysical Properities of Colloidal Anatase TiO_2 Particles-Size Quantization or Direct Transitions in This Indirect Semiconductor. *Journal of Physical Chemistry* **1995,** *99* (45), 16646-16654.

40. Tinguely, J.-C.; Solarska, R.; Braun, A.; Graule, T., Low-temperature roll-to-roll coating procedure of dye-sensitized solar cell photoelectrodes on flexible polymer-based substrates. *Semiconductor Science and Technology* **2011,** *26* (4), 045007.

References (Chapter 4)

1. (a) Ohtani, B., Photocatalysis A to Z—What we know and what we do not know in a scientific sense. *Journal of Photochemistry and Photobiology C: Photochemistry Reviews* **2010,** *11* (4), 157-178; (b) Akpan, U. G.; Hameed, B. H., Parameters affecting the photocatalytic degradation of dyes using TiO2-based photocatalysts: A review. *Journal of hazardous materials* **2009,** *170* (2-3), 520-529; (c) Ahmed, S.; Rasul, M. G.; Martens, W. N.; Brown, R.; Hashib, M. A., Heterogeneous photocatalytic degradation of phenols in wastewater: A review on current status and developments. *Desalination* **2010,** *261* (1-2), 3-18; (d) Ahmed, S.; Rasul, M. G.; Brown, R.; Hashib, M. A., Influence of parameters on the heterogeneous photocatalytic degradation of pesticides and phenolic contaminants in wastewater: A short review. *Journal of Environmental Management* **2011,** *92* (3), 311-330.
2. (a) Rolison, D. R.; Nazar, L. F., Electrochemical energy storage to power the 21st century. *Mrs Bulletin* **2011,** *36* (7), 486-493; (b) Yang, Z.; Zhang, J.; Kintner-Meyer, M. C. W.; Lu, X.; Choi, D.; Lemmon, J. P.; Liu, J., Electrochemical Energy Storage for Green Grid. *Chemical Reviews* **2011,** *111* (5), 3577-3613.
3. Fujishima, A. a. H., K., Electrochemical photolysis of water at a semiconductor electrode *Nature* **1972,** *238*, 37-38.
4. (a) Osterloh, F. E., Inorganic materials as catalysts for photochemical splitting of water. *Chemistry of Materials* **2008,** *20* (1), 35-54; (b) Maeda, K.; Domen, K., Photocatalytic Water Splitting: Recent Progress and Future Challenges. *Journal of Physical Chemistry Letters* **2010,** *1* (18), 2655-2661; (c) Xing, J.; Fang, W. Q.; Zhao, H. J.; Yang, H. G., Inorganic Photocatalysts for Overall Water Splitting. *Chemistry-an Asian Journal* **2012,** *7* (4), 642-657.
5. Liu, G.; Yu, J. C.; Lu, G. Q.; Cheng, H. M., Crystal facet engineering of semiconductor photocatalysts: motivations, advances and unique properties. *Chemical Communications* **2011,** *47* (24), 6763-6783.

6. Ohno, T.; Sarukawa, K.; Tokieda, K.; Matsumura, M., Morphology of a TiO2 Photocatalyst (Degussa, P-25) Consisting of Anatase and Rutile Crystalline Phases. *Journal of Catalysis* **2001,** *203* (1), 82-86.
7. Hegazy, A.; Prouzet, E., Room Temperature Synthesis and Thermal Evolution of Porous Nanocrystalline TiO2 Anatase. *Chemistry of Materials* **2012,** *24* (2), 245-254.
8. (a) Broekhoff, J. C. P.; de Boer, J. H., Studies on Pore Systems in Catalysts. XIII. Pore Distributions from the Desorption Branch of a Nitrogen Sorption Isotherm in the Case of Cylindrical Pores. B. Applications. *J. Catal.* **1968,** *10*, 377-390; (b) Prouzet, E.; Cot, F.; Nabias, G.; Larbot, A.; Kooyman, P.; Pinnavaia, T. J., Assembly of mesoporous silica molecular sieves based on nonionic ethoxylated sorbitan esters as structure directors. *Chemistry of Materials* **1999,** *11* (6), 1498-1503.
9. (a) Kim, S.-Y.; Lim, T.-H.; Chang, T.-S.; Shin, C.-H., Photocatalysis of methylene blue on titanium dioxide nanoparticles synthesized by modified sol-hydrothermal process of TiCl4. *Catalysis Letters* **2007,** *117* (3-4), 112-118; (b) Cao, L. X.; Huang, A. M.; Spiess, F. J.; Suib, S. L., Gas-phase oxidation of 1-butene using nanoscale TiO2 photocatalysts. *Journal of Catalysis* **1999,** *188* (1), 48-57.
10. Nagaveni, K.; Hegde, M. S.; Ravishankar, N.; Subbanna, G. N.; Madras, G., Synthesis and structure of nanocrystalline TiO2 with lower band gap showing high photocatalytic activity. *Langmuir* **2004,** *20* (7), 2900-2907.
11. (a) Hoffman, A. J.; Mills, G.; Yee, H.; Hoffmann, M. R., Q-Sized CDS- Synthesis, Characterization, and Efficiency of Photoinitiation of Polymerization of Several Vinylic Monomers. *Journal of Physical Chemistry* **1992,** *96* (13), 5546-5552; (b) Hoffman, A. J.; Yee, H.; Mills, G.; Hoffmann, M. R., Photoinitiated Polymerization of Methyl-Methacrylate using Q-Sized ZNO Colloids. *Journal of Physical Chemistry* **1992,** *96* (13), 5540-5546; (c) Mills, A.; LeHunte, S., An overview of semiconductor photocatalysis. *Journal of Photochemistry and Photobiology a-Chemistry* **1997,** *108* (1), 1-35.
12. (a) Chen, D. W.; Ray, A. K., Photocatalytic kinetics of phenol and its derivatives over UV irradiated TiO2. *Applied Catalysis B-Environmental* **1999,** *23* (2-3), 143-157; (b)

Assabane, A.; Ichou, Y. A.; Tahiri, H.; Guillard, C.; Herrmann, J. M., Photocatalytic degradation of polycarboxylic benzoic acids in UV-irradiated aqueous suspensions of titania. Identification of intermediates and reaction pathway of the photomineralization of trimellitic acid (1,2,4-benzene tricarboxylic acid). *Applied Catalysis B-Environmental* **2000,** *24* (2), 71-87; (c) Zhu, C. M.; Wang, L. Y.; Kong, L. R.; Yang, X.; Wang, L. S.; Zheng, S. J.; Chen, F. L.; Feng, M. Z.; Zong, H., Photocatalytic degradation of AZO dyes by supported TiO2+UVin aqueous solution. *Chemosphere* **2000,** *41* (3), 303-309.

13. Wu, C. H.; Chern, J. M., Kinetics of photocatalytic decomposition of methylene blue. *Industrial & Engineering Chemistry Research* **2006,** *45* (19), 6450-6457.

14. (a) Epling, G. A.; Lin, C., Investigation of retardation effects on the titanium dioxide photodegradation system. *Chemosphere* **2002,** *46* (6), 937-944; (b) Madhu, G. M.; Raj, M.; Pai, K. V. K., Titamium oxide (TiO_2) assisted photocatalytic degradation of methylene blue. *Journal of Environmental Biology* **2009,** *30* (2), 259-264.

15. (a) Tang, W. Z.; Huang, C. P., Photocatalyzed Oxidation Pathways of 2,4-Dichlorophenol by CDS in Basic and Acidic Aqueous-Solutions. *Water Research* **1995,** *29* (2), 745-756; (b) Houas, A.; Lachheb, H.; Ksibi, M.; Elaloui, E.; Guillard, C.; Herrmann, J. M., Photocatalytic degradation pathway of methylene blue in water. *Applied Catalysis B-Environmental* **2001,** *31* (2), 145-157; (c) Miranda, M. A.; Galindo, F.; Amat, A. M.; Arques, A., Pyrylium salt-photosensitized degradation of phenolic contaminants derived from cinnamic acid with solar light - Correlation of the observed reactivities with fluorescence quenching. *Applied Catalysis B-Environmental* **2000,** *28* (2), 127-133; (d) Xu, N. P.; Shi, Z. F.; Fan, Y. Q.; Dong, J. H.; Shi, J.; Hu, M. Z. C., Effects of particle size of TiO2 on photocatalytic degradation of methylene blue in aqueous suspensions. *Industrial & Engineering Chemistry Research* **1999,** *38* (2), 373-379.

16. Herrmann, J. M., Heterogeneous photocatalysis: fundamentals and applications to the removal of various types of aqueous pollutants. *Catalysis Today* **1999,** *53* (1), 115-129.

17. Iliev, V.; Tomova, D.; Bilyarska, L.; Tyuliev, G., Influence of the size of gold nanoparticles deposited on TiO2 upon the photocatalytic destruction of oxalic acid. *Journal of Molecular Catalysis A: Chemical* **2007,** *263* (1-2), 32-38.

18. Xu, A. W.; Gao, Y.; Liu, H. Q., The preparation, characterization, and their photocatalytic activities of rare-earth-doped TiO_2 nanoparticles. *Journal of Catalysis* **2002,** *207* (2), 151-157.

19. (a) Saquib, M.; Muneer, M., TiO(2)-mediated photocatalytic degradation of a triphenylmethane dye (gentian violet), in aqueous suspensions. *Dyes and Pigments* **2003,** *56* (1), 37-49; (b) Sakthivel, S.; Neppolian, B.; Shankar, M. V.; Arabindoo, B.; Palanichamy, M.; Murugesan, V., Solar photocatalytic degradation of azo dye: comparison of photocatalytic efficiency of ZnO and TiO_2. *Solar Energy Materials and Solar Cells* **2003,** *77* (1), 65-82.

20. Konstantinou, I. K.; Albanis, T. A., TiO_2-assisted photocatalytic degradation of azo dyes in aqueous solution: kinetic and mechanistic investigations. *Applied Catalysis B: Environmental* **2004,** *49* (1), 1-14.

21. Yao, J.; Wang, C., Decolorization of Methylene Blue with TiO_2 Sol via UV Irradiation Photocatalytic Degradation. *International Journal of Photoenergy* **2010,** *2010*, 1-6.

22. (a) Fox, M. A.; Dulay, M. T., Heterogeneous Photocatalysis. *Chemical Reviews* **1993,** *93* (1), 341-357; (b) Hoffmann, M. R.; Martin, S. T.; Choi, W. Y.; Bahnemann, D. W., Enviromental Applications of Semicondutor Photocatalysis. *Chemical Reviews* **1995,** *95* (1), 69-96.

23. Lachheb, H.; Puzenat, E.; Houas, A.; Ksibi, M.; Elaloui, E.; Guillard, C.; Herrmann, J. M., Photocatalytic degradation of various types of dyes (Alizarin S, Crocein Orange G, Methyl Red, Congo Red, Methylene Blue) in water by UV-irradiated titania. *Applied Catalysis B-Environmental* **2002,** *39* (1), 75-90.

24. Gumy, D.; Morais, C.; Bowen, P.; Pulgarin, C.; Giraldo, S.; Hajdu, R.; Kiwi, J., Catalytic activity of commercial of TiO_2 powders for the abatement of the bacteria (E-coli) under solar simulated light: Influence of the isoelectric point. *Applied Catalysis B-Environmental* **2006,** *63* (1-2), 76-84.

25. Mao, X. C. a. S. S., Titanium Dioxide Nanomaterials: Synthesis, Properties, Modifications, and Applications. **2007**.

26. Kang, X.; Chen, S., Photocatalytic reduction of methylene blue by TiO_2 nanotube arrays: effects of TiO_2 crystalline phase. *Journal of Materials Science* **2010,** *45* (10), 2696-2702.

27. Zhang, H.; Han, Y.; Liu, X.; Liu, P.; Yu, H.; Zhang, S.; Yao, X.; Zhao, H., Anatase TiO_2 microspheres with exposed mirror-like plane {001} facets for high performance dye-sensitized solar cells (DSSCs). *Chemical Communications* **2010,** *46* (44), 8395-8397.

28. Nguyen-Phan, T.-D.; Shin, E. W., Morphological effect of TiO2 catalysts on photocatalytic degradation of methylene blue. *Journal of Industrial and Engineering Chemistry* **2011,** *17* (3), 397-400.

References (Chapter 5)

1. (a) O'Regan, B.; Grätzel, M., A low-cost, high-efficency solar-cell based on dye-sensitized colloidal TiO_2 films. *Nature* **1991,** *353* (6346), 737-740; (b) Grätzel, M., Photoelectrochemical cells. *Nature* **2001,** *414* (6861), 338-344; (c) Lenzmann, F.; Krueger, J.; Burnside, S.; Brooks, K.; Grätzel, M.; Gal, D.; Ruhle, S.; Cahen, D., Surface photovoltage spectroscopy of dye-sensitized solar cells with TiO_2, Nb_2O_5, and SrTiO3 nanocrystalline photoanodes: Indication for electron injection from higher excited dye states. *J. Phys. Chem. B* **2001,** *105* (27), 6347-6352.
2. (a) Grätzel, M., Mesoporous oxide junctions and nanostructured solar cells. *Curr. Opin. Coll. Interface Sci.* **1999,** *4* (4), 314-321; (b) Grätzel, M., Sol-gel processed TiO2 films for photovoltaic applications. *J. Sol-Gel Science Techno.* **2001,** *22* (1-2), 7-13; (c) Durrant, J. R.; Haque, S. A.; Palomares, E., Towards optimisation of electron transfer processes in dye sensitised solar cells. *Coord. Chem. Rev.* **2004,** *248* (13-14), 1247-1257; (d) Kroon, J. M.; Bakker, N. J.; Smit, H. J. P.; Liska, P.; Thampi, K. R.; Wang, P.; Zakeeruddin, S. M.; Gratzel, M.; Hinsch, A.; Hore, S.; Wurfel, U.; Sastrawan, R.; Durrant, J. R.; Palomares, E.; Pettersson, H.; Gruszecki, T.; Walter, J.; Skupien, K.; Tulloch, G. E., Nanocrystalline dye-sensitized solar cells having maximum performance. *Prog. Photovoltaics* **2007,** *15* (1), 1-18; (e) Pagliaro, M.; Palmisano, G.; Ciriminna, R.; Loddo, V., Nanochemistry aspects of titania in dye-sensitized solar cells. *Energy Environ. Sci.* **2009,** *2* (8), 838-844; (f) Zhang, Q. F.; Cao, G. Z., Nanostructured photoelectrodes for dye-sensitized solar cells. *Nano Today* **2011,** *6* (1), 91-109.
3. (a) Kim, H.-J.; Park, S. Y.; Kwak, S.-Y., Photovoltaic Performance of a Novel TiO_2 Electrode Consisting of a Mesoporous TiO_2 Layer and a Compact TiO_2 Blocking Layer for Dye-Sensitized Solar Cells. In *2010 International Conference on Biology, Environment and Chemistry, IPCBEE*, Press, I., Ed. Singapore, 2011; Vol. 1, pp 178-182; (b) Zukalova, M.; Zukal, A.; Kavan, L.; Nazeeruddin, M. K.; Liska, P.; Gratzel, M., Organized mesoporous TiO_2 films exhibiting greatly enhanced performance in dye-sensitized solar cells. *Nano Lett.* **2005,** *5* (9), 1789-1792; (c)

Yanagida, S., Recent research progress of dye-sensitized solar cells in Japan. *C. R. Chim.* **2006,** *9* (5-6), 597-604.

4. (a) Murakami, T. N.; Kijitori, Y.; Kawashima, N.; Miyasaka, T., Low temperature preparation of mesoporous TiO_2 films for efficient dye-sensitized photoelectrode by chemical vapor deposition combined with UV light irradiation. *Journal of Photochemistry and Photobiology a-Chemistry* **2004,** *164* (1-3), 187-191; (b) Gutierrez-Tauste, D.; Zumeta, I.; Vigil, E.; Hernandez-Fenollosa, M. A.; Domenech, X.; Ayllon, J. A., New low-temperature preparation method of the TiO_2 porous photoelectrode for dye-sensitized solar cells using UV irradiation. *Journal of Photochemistry and Photobiology a-Chemistry* **2005,** *175* (2-3), 165-171; (c) Tebby, Z.; Babot, O.; Michau, D.; Hirsch, L.; Carlos, L.; Toupance, T., A simple route towards low-temperature processing of nanoporous thin films using UV-irradiation: Application for dye solar cells. *Journal of Photochemistry and Photobiology a-Chemistry* **2009,** *205* (1), 70-76; (d) Tebby, Z.; Uddin, T.; Nicolas, Y.; Olivier, C.; Toupance, T.; Labrugere, C.; Hirsch, L., Low-Temperature UV Processing of Nanoporous SnO_2 Layers for Dye-Sensitized Solar Cells. *ACS Appl. Mater. Interfaces* **2011,** *3* (5), 1485-1491; (e) Lee, M.-K.; Yen, H.; Hsiao, C.-C., Efficiency Improvement of Dye-Sensitized Solar Cell with Ultraviolet and Hydrogen Chloride Treatments. *J. Electrochem. Soc.* **2011,** *158* (5), K136-K139.

5. (a) Wang, Q.; Moser, J.-E.; Gratzel, M., Electrochemical impedance spectroscopic analysis of dye-sensitized solar cells. *J. Phys. Chem. B* **2005,** *109* (31), 14945-14953; (b) Lee, K. E.; Charbonneau, C.; Shan, G.; Demopoulos, G. P.; Gauvin, R., Nanocrystalline TiO_2 Thin Film Electrodes for Dye-Sensitized Solar Cell Applications. *Jom* **2009,** *61* (4), 52-57.

6. Cahen, D.; Hodes, G.; Grätzel, M.; Guillemoles, J.-F.; Riess, I., Nature of photovoltaic action in dye-sensitized solar cells. *J. Phys. Chem. B* **2000,** *104* (9), 2053-2059.

7. Hegazy, A.; Prouzet, E., Room Temperature Synthesis and Thermal Evolution of Porous Nanocrystalline TiO_2 Anatase. *Chem. Mater.* **2012,** *24* (2), 245-254.

8. Hegazy, A.; Prouzet, E., Photocatalysis of 4 nm nanocrystals of TiO_2 anatase: parameters for an enhanced reaction. *Submitted* **2012**.

9. Hessien, M.; Singh, N.; Kim, C.; Prouzet, E., Stability and Tunability of O/W Nanoemulsions Prepared by Phase Inversion Composition. *Langmuir* **2011,** *27* (6), 2299-2307.

10. Bonnemann, H.; Khelashvili, G.; Behrens, S.; Hinsch, A.; Skupien, K. r.; Dinjus, E., Role of the platinum nanoclusters in the iodide/triiodide redox system of dye solar cells. *Journal of Cluster Science* **2007,** *18* (1), 141-155.

11. Cho, S. J.; Ouyang, J., Attachment of Platinum Nanoparticles to Substrates by Coating and Polyol Reduction of A Platinum Precursor. *J. Phys. Chem. C* **2011,** *115* (17), 8519-8526.

12. Fang, X.; Ma, T.; Guan, G.; Akiyama, M.; Abe, E., Performances characteristics of dye-sensitized solar cells based on counter electrodes with Pt films of different thickness. *Journal of Photochemistry and Photobiology a-Chemistry* **2004,** *164* (1-3), 179-182.

13. (a) Broekhoff, J. C. P.; de Boer, J. H., Studies on Pore Systems in Catalysts. XIII. Pore Distributions from the Desorption Branch of a Nitrogen Sorption Isotherm in the Case of Cylindrical Pores. B. Applications. *J. Catal.* **1968,** *10*, 377-390; (b) Prouzet, E.; Cot, F.; Nabias, G.; Larbot, A.; Kooyman, P. J.; Pinnavaia, T. J., Assembly of Mesoporous Silica Molecular Sieves Based on Nonionic Ethoxylated Sorbitan Esters as Structure Directors. *Chem. Mater.* **1999,** *11* (6), 1498-1503.

14. (a) Kang, S. H.; Kim, J.-Y.; Kim, H. S.; Koh, H.-D.; Lee, J.-S.; Sung, Y.-E., Influence of light scattering particles in the TiO2 photoelectrode for solid-state dye-sensitized solar cell. *Journal of Photochemistry and Photobiology a-Chemistry* **2008,** *200* (2-3), 294-300; (b) Shao, W.; Gu, F.; Li, C.; Lu, M., Interfacial Confined Formation of Mesoporous Spherical TiO_2 Nanostructures with Improved Photoelectric Conversion Efficiency. *Inorg. Chem.* **2010,** *49* (12), 5453-5459.

15. Hirose, F.; Kuribayashi, K.; Shikaku, M.; Narita, Y.; Takahashi, Y.; Kimura, Y.; Niwano, M., Adsorption Density Control of N719 on TiO_2 Electrodes for Highly Efficient Dye-Sensitized Solar Cells. *Journal of The Electrochemical Society* **2009,** *156* (9), B987-B990.

16. (a) van de Lagemaat, J.; Benkstein, K. D.; Frank, A. J., Relation between particle coordination number and porosity in nanoparticle films: Implications to dye-sensitized solar cells. *J. Phys. Chem. B* **2001,** *105* (50), 12433-12436; (b) Ofir, A.; Dor, S.; Grinis, L.; Zaban, A.; Dittrich, T.; Bisquert, J., Porosity dependence of electron percolation in nanoporous TiO_2 layers. *J. Chem. Phys.* **2008,** *128* (6).

17. Prouzet, E.; Boissière, C.; Kim, S. S.; Pinnavaia, T. J., Roughness of mesoporous silica surfaces deduced from adsorption measurements. *Microporous and Mesoporous Materials* **2009,** *119* (1-3), 9-17.

18. (a) Lee, M.-K.; Yen, H.; Hsiao, C.-C., Efficiency Improvement of Dye-Sensitized Solar Cell with Ultraviolet and Hydrogen Chloride Treatments. *Journal of The Electrochemical Society* **2011,** *158* (5), K136; (b) Leon, C. P.; Kador, L.; Peng, B.; Thelakkat, M., Characterization of the adsorption of ru-bpy dyes on mesoporous TiO_2 films with UV-Vis, Raman, and FTIR spectroscopies. *Journal of Physical Chemistry B* **2006,** *110* (17), 8723-8730.

19. (a) Wang, P.; Zakeeruddin, S. M.; Moser, J. E.; Humphry-Baker, R.; Comte, P.; Aranyos, V.; Hagfeldt, A.; Nazeeruddin, M. K.; Gratzel, M., Stable new sensitizer with improved light harvesting for nanocrystalline dye-sensitized solar cells. *Advanced Materials* **2004,** *16* (20), 1806-1811; (b) Finnie, K. S.; Bartlett, J. R.; Woolfrey, J. L., Vibrational spectroscopic study of the coordination of (2,2 '-bipyridyl-4,4 '-dicarboxylic acid)ruthenium(II) complexes to the surface of nanocrystalline titania. *Langmuir* **1998,** *14* (10), 2744-2749.

20. Greijer Agrell, H.; Lindgren, J.; Hagfeldt, A., Coordinative interactions in a dye-sensitized solar cell. *Journal of Photochemistry and Photobiology A: Chemistry* **2004,** *164* (1-3), 23-27.

21. Tebby, Z.; Uddin, T.; Nicolas, Y.; Olivier, C.; Toupance, T.; Labrugere, C.; Hirsch, L., Low-Temperature UV Processing of Nanoporous SnO_2 Layers for Dye-Sensitized Solar Cells. *ACS applied materials & interfaces* **2011,** *3* (5), 1485-1491.

22. Hauch, A.; Georg, A., Diffusion in the electrolyte and charge-transfer reaction at the platinum electrode in dye-sensitized solar cells. *Electrochimica Acta* **2001,** *46* (22), 3457-3466.

23. Vuk, A. S.; Jese, R.; Orel, B.; Drazic, G., The effect of surface hydroxyl groups on the adsorption properties of nanocrystalline TiO_2 films. *International Journal of Photoenergy* **2005,** *7* (4), 163-168.

24. Kumar, P. M.; Badrinarayanan, S.; Sastry, M., Nanocrystalline TiO_2 studied by optical, FTIR and X-ray photoelectron spectroscopy: correlation to presence of surface states. *Thin Solid Films* **2000,** *358* (1-2), 122-130.

25. (a) Busca, G.; Saussey, H.; Saur, O.; Lavalley, J. C.; Lorenzelli, V., FT-IR Characterization of the Surface-Acidity of the different Titanium-Dioxide Anatase Preparations. *Applied Catalysis* **1985,** *14* (1-3), 245-260; (b) Hadjiivanov, K. I. K., Dimitar G. , Surface Chemistry of Titania (Anatase) and Titania-supported Catalysts. *Chemical Society Reviews* **1996,** *25* (1), 9.

26. Hirose, F.; Kuribayashi, K.; Suzuki, T.; Narita, Y.; Kimura, Y.; Niwano, M., UV treatment effect on TiO(2) electrodes in dye-sensitized solar cells with N719 sensitizer investigated by infrared absorption spectroscopy. *Electrochemical and Solid State Letters* **2008,** *11* (7), A109-A111.

27. Deacon, G. B.; Phillips, R. J., Relationships Between the Carbon-Oxygen Stretching Frequencies of Carboxylate Coordination. *Coordination Chemistry Reviews* **1980,** *33* (3), 227-250.

28. Zhang, H.; Liu, P.; Li, F.; Liu, H.; Wang, Y.; Zhang, S.; Guo, M.; Cheng, H.; Zhao, H., Facile fabrication of anatase TiO_2 microspheres on solid substrates and surface crystal facet transformation from {001} to {101}. *Chemistry* **2011,** *17* (21), 5949-57.

29. Lee, B. K.; Kim, J. J., Enhanced efficiency of dye-sensitized solar cells by UV-O(3) treatment of TiO(2) layer. *Current Applied Physics* **2009,** *9* (2), 404-408.

30. Xu, J.; Zhai, C. W.; Zheng, B. W.; Li, H. W.; Zhu, M. W.; Chen, Y. F., Large efficiency improvement in nanoporous dye-sensitized solar cells via vacuum assistant dye adsorption. *Vacuum* **2012,** *86* (8), 1161-1164.

31. Ahn, S. H.; Jeon, H.; Son, K. J.; Ahn, H.; Koh, W.-G.; Ryu, D. Y.; Kim, J. H., Efficiency improvement of dye-sensitized solar cells using graft copolymer-templated mesoporous TiO_2 films as an interfacial layer. *Journal of Materials Chemistry* **2011,** *21* (6), 1772.

32. (a) Longo, C.; Freitas, J.; De Paoli, M. A., Performance and stability of TiO_2/dye solar cells assembled with flexible electrodes and a polymer electrolyte. *Journal of Photochemistry and Photobiology a-Chemistry* **2003,** *159* (1), 33-39; (b) Nogueira, A. F.; Longo, C.; De Paoli, M. A., Polymers in dye sensitized solar cells: overview and perspectives. *Coordination Chemistry Reviews* **2004,** *248* (13-14), 1455-1468.

33. Murakami, T. N.; Ito, S.; Wang, Q.; Nazeeruddin, M. K.; Bessho, T.; Cesar, I.; Liska, P.; Humphry-Baker, R.; Comte, P.; Pechy, P.; Gratzel, M., Highly efficient dye-sensitized solar cells based on carbon black counter electrodes. *Journal of The Electrochemical Society* **2006,** *153* (12), A2255-A2261.

Appendix A
Experimental Design: Model parameters

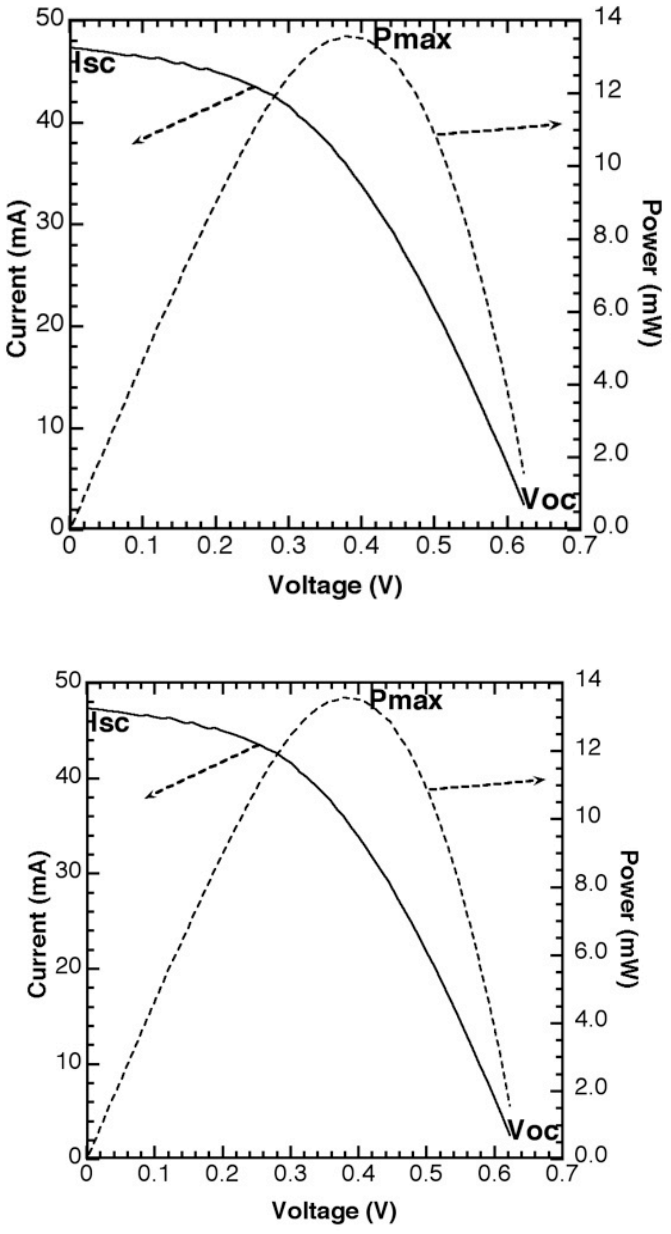

Figure A.1: Current/Voltage curve for a dye-sensitized solar cell mounted with the nanostructured TiO2 powder.

Table A.I. ANOVA Table for cubic mixture model For Eg at room temperature(cf. Figure 3.5)

Source	Sum of Squares	df	Mean Square	F value	p-value Prob > F
Total cubic mixture model	**0.076**	**9**	**8.454E-003**	**4759.56**	**0.0112**
Linear Mixture	0.020	2	9.793E-003	5513.32	0.0095
AB	3.66E-04	1	206.03	0.0443	
AC	0.042	1	23777.11	0.0041	
BC	0.018	1	9955.45	0.0064	
ABC	0.031	1	0.031	17713.44	0.0048
AB(A-B)	9.71E-03	1	9.71E-03	5464.29	0.0086
AC(A-C)	8.02E-03	1	8.02E-03	4514.87	0.0095
BC(B-C)	0.024	1	0.024	13572.79	0.0055
Residual	1.776E-006	1	1.776E-006		
Cor total	0.076	10			

The Model F-value of 4759.56 implies the model is significant. There is only a 1.12% chance that a "Model F-Value" this large could occur due to noise. Values of "Prob > F" less than 0.0500 indicate model terms are significant.

Final Equation in Terms of Actual Components:

Eg (eV) =-4.78784 * A +5.90090 * B -34.19664 * C -6.16681E-003 * A * B +0.66749 * A * C +0.54545 * B * C -6.88093E-003 * A * B * C+1.97060E-003 * A * B * (A-B) -2.23179E-003 * A * C * (A-C) - 3.86960E-003 * B * C * (B-C)

Table A.II. ANOVA Table for cubic mixture model For anatase % at room temperature (cf Figure 3.8)

Source	Sum of Squares	df	Mean Square	F value	p-value Prob > F
Total cubic mixture model	0.90	9	0.10	4.350E +007	0.0001
Linear Mixture	0.34	2	0.17	7.521E +007	< 0.0001
AB	0.12	1	0.12	5.215E +007	< 0.0001
AC	0.021	1	0.021	8.997E +006	0.0002
BC	0.11	1	0.11	4.680E +007	< 0.0001
ABC	8.649E-003	1	8.649E-003	3.774E +006	0.0003
AB(A-B)	0.056	1	0.056	2.429E +007	0.0001
AC(A-C)	0.15	1	0.15	6.586E +007	< 0.0001
AC(A-C)	0.22	1	0.22	9.764E +007	< 0.0001
Residual	2.292E-009	1	2.292E-009		
Cor total	0.9	10			

Final Equation in Terms of Actual Components:

(wt fraction of anatase_RT)$^{2.2}$ = +19.16213 * A -1.39827 * B -90.49662 * C -0.31214 * A * B +1.08593 * A * C+1.4876 * B * C-3.60773E-003 * A * B * C -4.71920E-003 * A * B * (A-B) -9.68245E-003 * A * C * (A-C) -0.011789* B * C * (B-C)

Table A.III. ANOVA Table for cubic mixture model For crystallite size of anatase at room temperature (cf. Figure 3.9)

Source	Sum of Squares	df	Mean Square	F value	p-value Prob > F
Total cubic mixture model	**0.92**	**6**	**0.15**	**2.04**	**0.1731**
Linear Mixture	0.38	2	0.19	2.53	0.1408
AB	0.38	1	0.38	5.01	0.0555
AC	0.41	1	0.41	5.49	0.0472
BC	0.44	1	0.44	5.80	0.0427
ABC	0.36	1	0.36	4.74	0.0611
Residual	0.60	8	0.076		
Lack of Fit	0.25	4	0.063	0.72	0.6188
Pure Error	0.35	4	0.088		
Cor total	1.53	14			

Final Equation in Terms of Actual Components:

crystallite size_RT= -9.27078 * A -11.03250 * B -28.95074 * C+0.41241 * A * B +0.79798 * A * C +0.87848 * B * C -0.018923 * A * B * C

Table A.IV ANOVA Table for Linear mixture model For crystallite size of brookite at room temperature (cf. Figure 3.10)

Source	Sum of Squares	df	Mean Square	F value	p-value Prob > F
Total cubic mixture model	**0.11**	**6**	**0.018**	**1550.38**	**0.0194**
Linear Mixture	0.025	2	0.013	1110.28	0.0212
AB	4.33E-04	1	4.33E-04	38.81	0.1013
AC	2.99E-03	1	2.99E-03	264.21	0.0391
BC	0.014	1	0.014	1214.49	0.0183
ABC	0.012	1	0.012	1031.19	0.0198
Residual	1.13E-05	1	1.13E-05		
Cor total	0.11	7			

Final Equation in Terms of Actual Components:

crystallite size_brookite = -0.024420 * A +0.073381* B +0.13503 * C

Table A.V ANOVA Table for cubic mixture model For fractal dimension at room temperature (cf. Figure 3.13)

Source	Sum of Squares	df	Mean Square	F value	p-value Prob > F
Total special cubic mixture model	**1.02E+06**	**6**	**1.70E+05**	**3.14**	**0.188**
Linear Mixture	4.14E+05	2	2.07E+05	3.81	0.1503
AB	2.12E+05	1	2.12E+05	3.9	0.1428
AC	2.10E+05	1	2.10E+05	3.86	0.1441
BC	1.16E+05	1	1.16E+05	2.13	0.2407
ABC	1.67E+05	1	1.67E+05	3.08	0.1775
Residual	1.63E+05	3	54322.51		
Cor total	1.19E+06	9			

Final Equation in Terms of Actual Components:

fractal volume = -1.99909 * A -3.16459 B -9.91582 * C +0.10740* A * B +0.25644 * A * C +0.32698 * B * C -7.21639E-003 * A * B * C

Table A.VI ANOVA Table for special cubic mixture model For hydrodynamic diameter at RT using DLS (cf. Figure 3.18)

Source	Sum of Squares	df	Mean Square	F value	p-value Prob > F
Total special cubic mixture model	**1.02E+06**	**6**	**1.70E+05**	**3.14**	**0.188**
Linear Mixture	4.14E+05	2	2.07E+05	3.81	0.1503
AB	2.12E+05	1	2.12E+05	3.9	0.1428
AC	2.10E+05	1	2.10E+05	3.86	0.1441
BC	1.16E+05	1	1.16E+05	2.13	0.2407
ABC	1.67E+05	1	1.67E+05	3.08	0.1775
Residual	1.63E+05	3	54322.51		
Cor total	1.19E+06	9			

Final Equation in Terms of Actual Components:

Diameter_nm_DLS= +7848.68152 * A +8415.97774 * B +21687.34256 * C -331.85416 * A * B -633.02561 * A * C -655.59479 * B * C+14.94115 * A * B * C

Table A.VII. ANOVA Table for special cubic mixture model For weight fraction of anatase at 700°C (cf Figure 3.22)

Source	Sum of Squares	df	Mean Square	F value	p-value Prob > F
Total special cubic mixture model	**0.49**	**6**	**0.082**	**4.26**	**0.0911**
Linear Mixture	0.28	2	0.14	7.16	0.0477
AB	0.14	1	0.14	7.09	0.0562
AC	0.11	1	0.11	5.84	0.0730
BC	0.098	1	0.098	5.06	0.0877
ABC	0.1	1	0.1	5.18	0.0851
Residual	0.077	4	0.019		
Cor total	0.57	10			

Final Equation in Terms of Actual Components:

wt fraction of anatase_700 =5.94594 * A+6.84097 * B +16.93320 * C -0.26006 * A * B-0.48221 * A * C-0.52136 * B * C+0.011540 * A * B * C

Appendix B: Parameters for enhanced photocatalysis of TiO_2 anatase

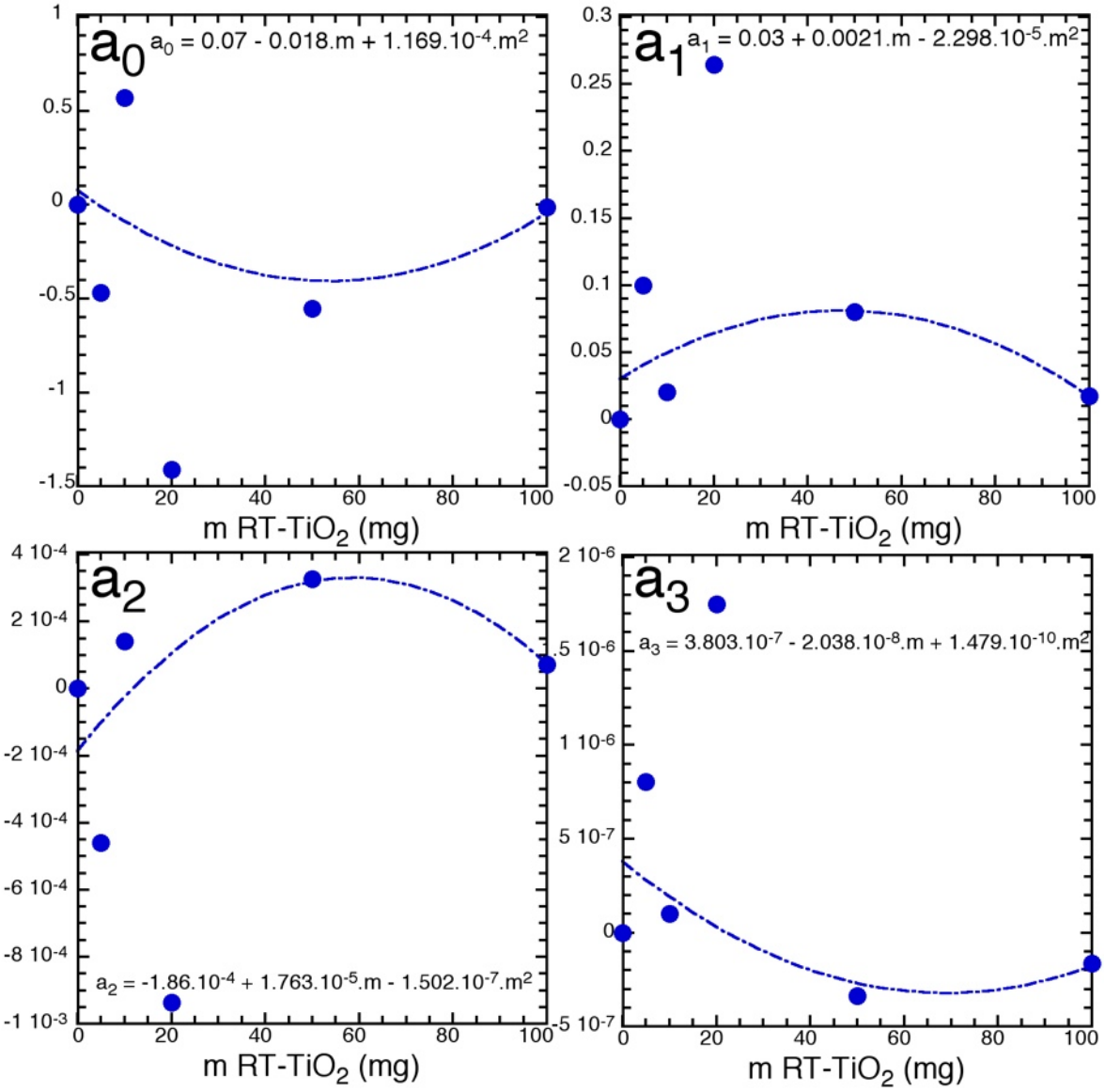

Figure B.1: Values (dots) and 2nd order fit (dashed lines) of the polynomial parameters a0(m) to a3(m), with m the mass of RT-TiO_2, and the parameters a0(m) to a3(m) being the variable of the 3rd order degree polynomial [%(degrad) = a0(m) + a1(m).t + a2(m).t^2 + a3(m).t^3]. Due to large discrepancy, the values of the 20 mg samples were not used for fitting.

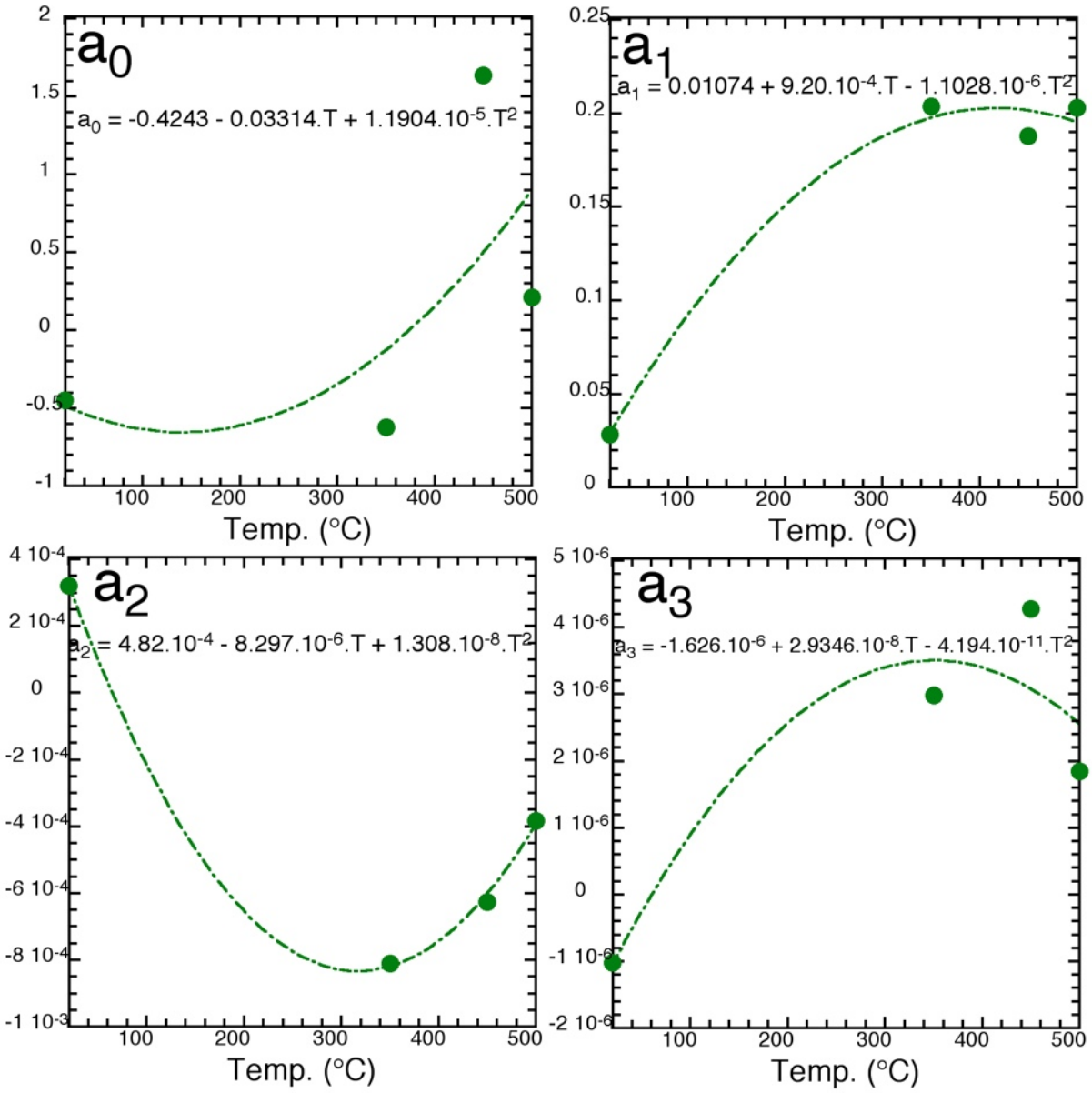

Figure B.2: Values (dots) and 2nd order fit (dashed lines) of the polynomial parameters a0(T) to a3(T), for 100 mg of RT-TiO_2, activated at different temperatures. a0(T) to a3(T) being the variable of the 3rd order degree polynomial [%(degrad) = a0(T) + a1(T).t + a2(T).t^2 + a3(T).t^3].

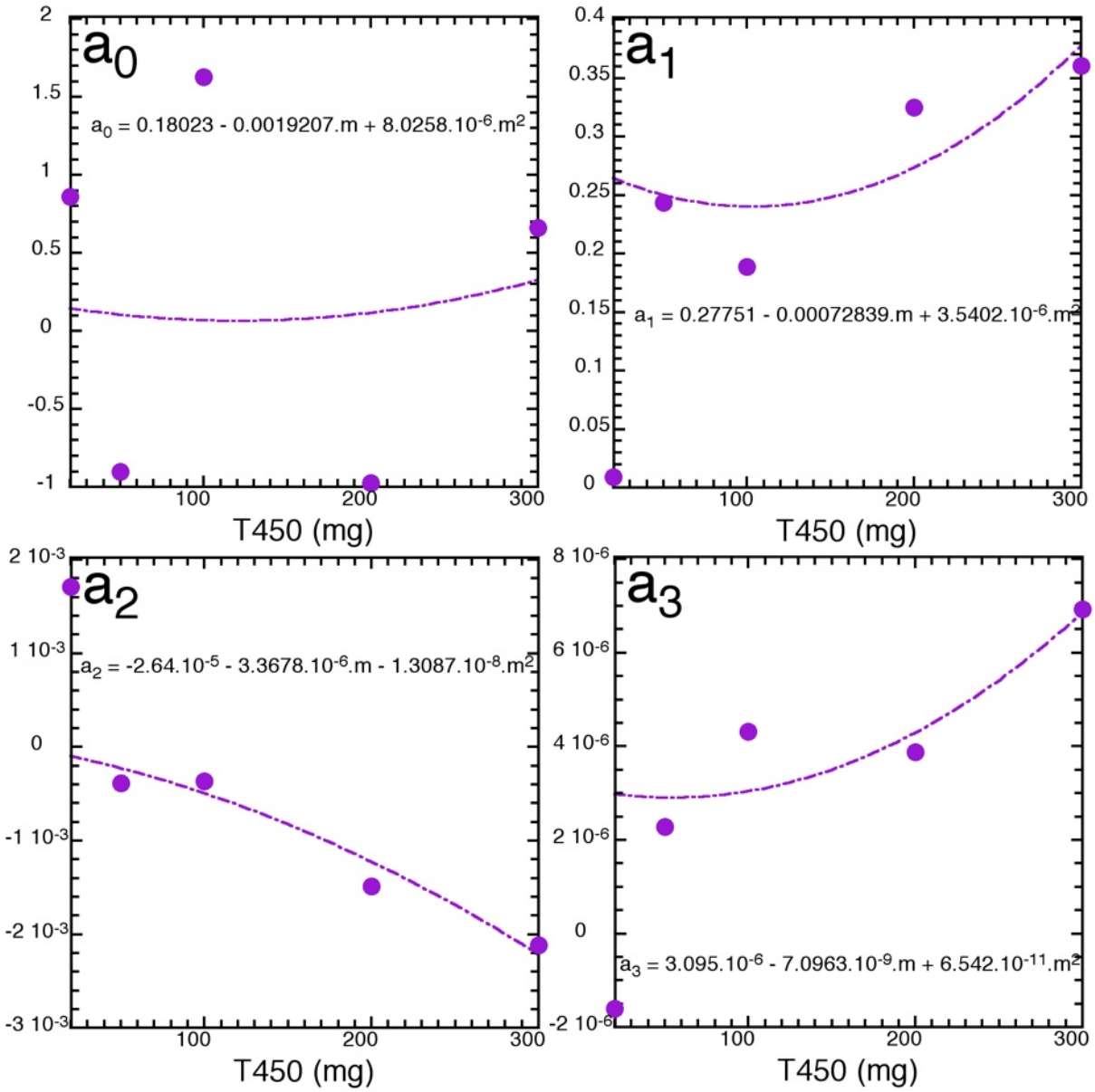

Figure B.3: Values (dots) and 2nd order fit (dashed lines) of the polynomial parameters a0(m) to a3(m), with m the mass of T450, and the parameters a0(m) to a3(m) being the variable of the 3rd order degree polynomial [%(degrad) = a0(m) + a1(m).t + a2(m).t^2 + a3(m).t^3].

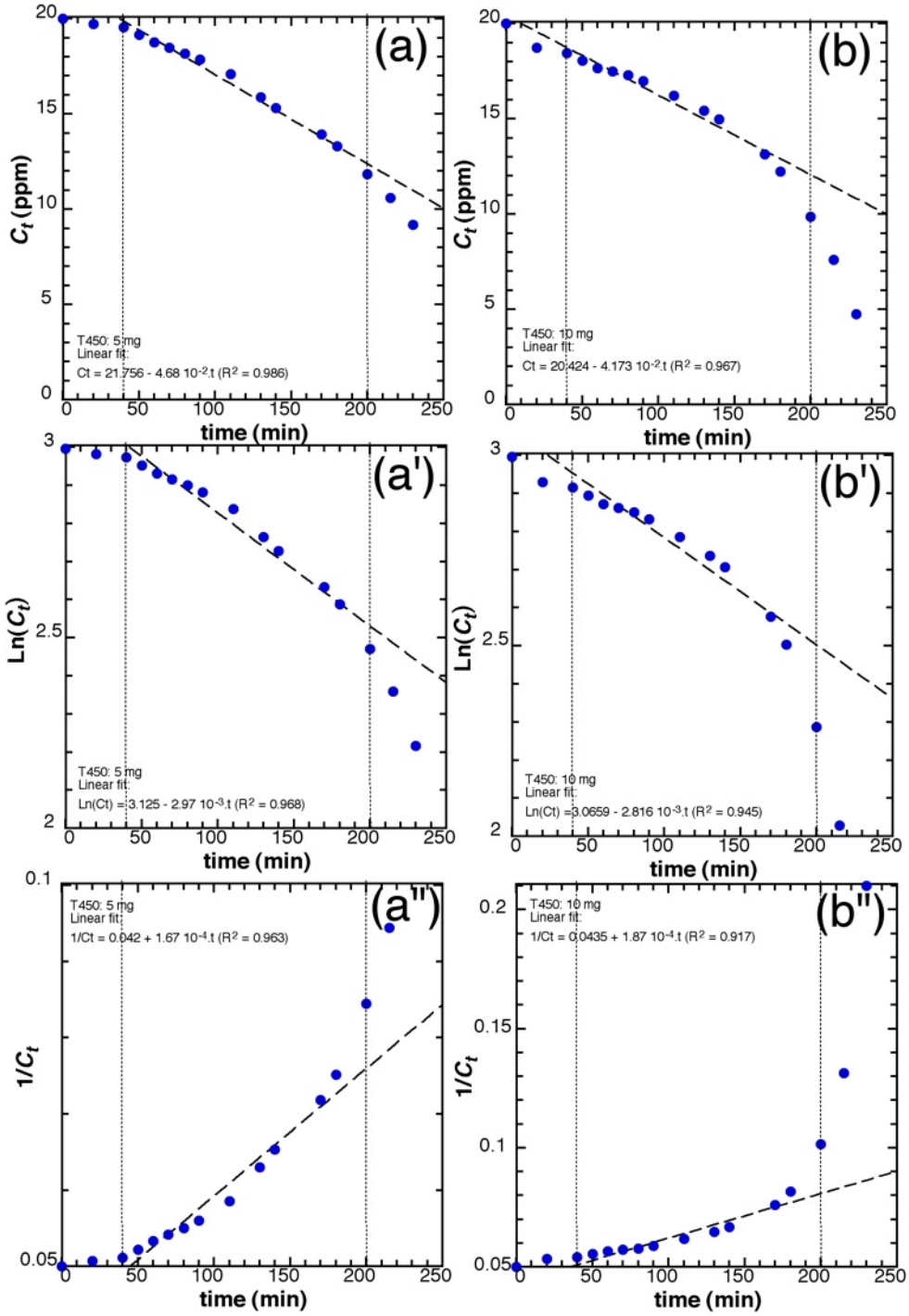

Figure B.4.A: Linear fitting of the evolution of MB (in ppm) for the different kinetics models (Ct=f(t) - zero order; Ln(Ct)=f(t) - first order; 1/Ct=f(t) - second order) for 5mg of (a; a'; a"") and 10 mg (b, b', b") of T450.

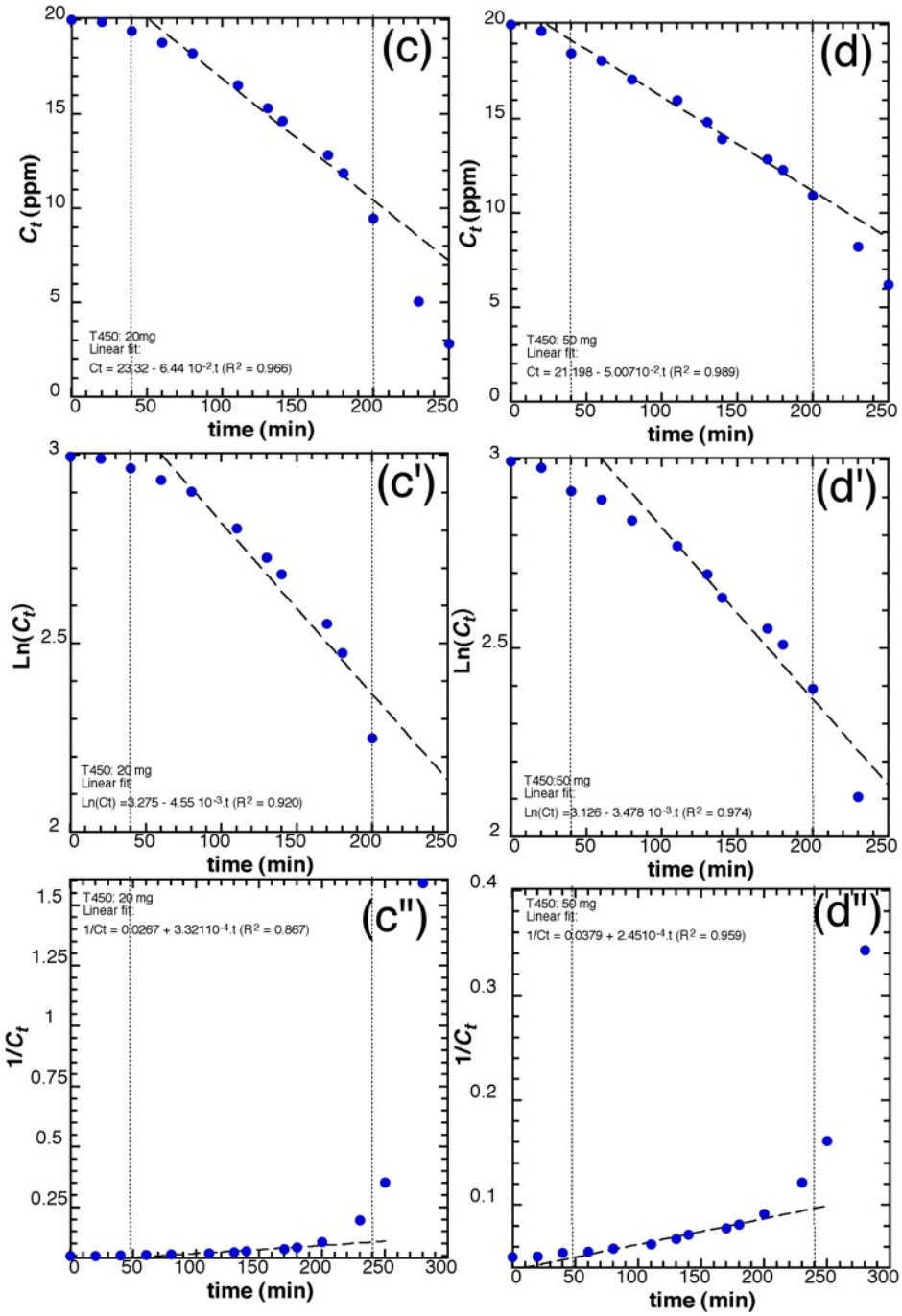

Figure B.4.B: Linear fitting of the evolution of MB (in ppm) for the different kinetics models (Ct=f(t) - zero order; Ln(Ct)=f(t) - first order; 1/Ct=f(t) - second order) for 20mg of (c; c'; c"") and 50 mg (d, d', d") of T450.

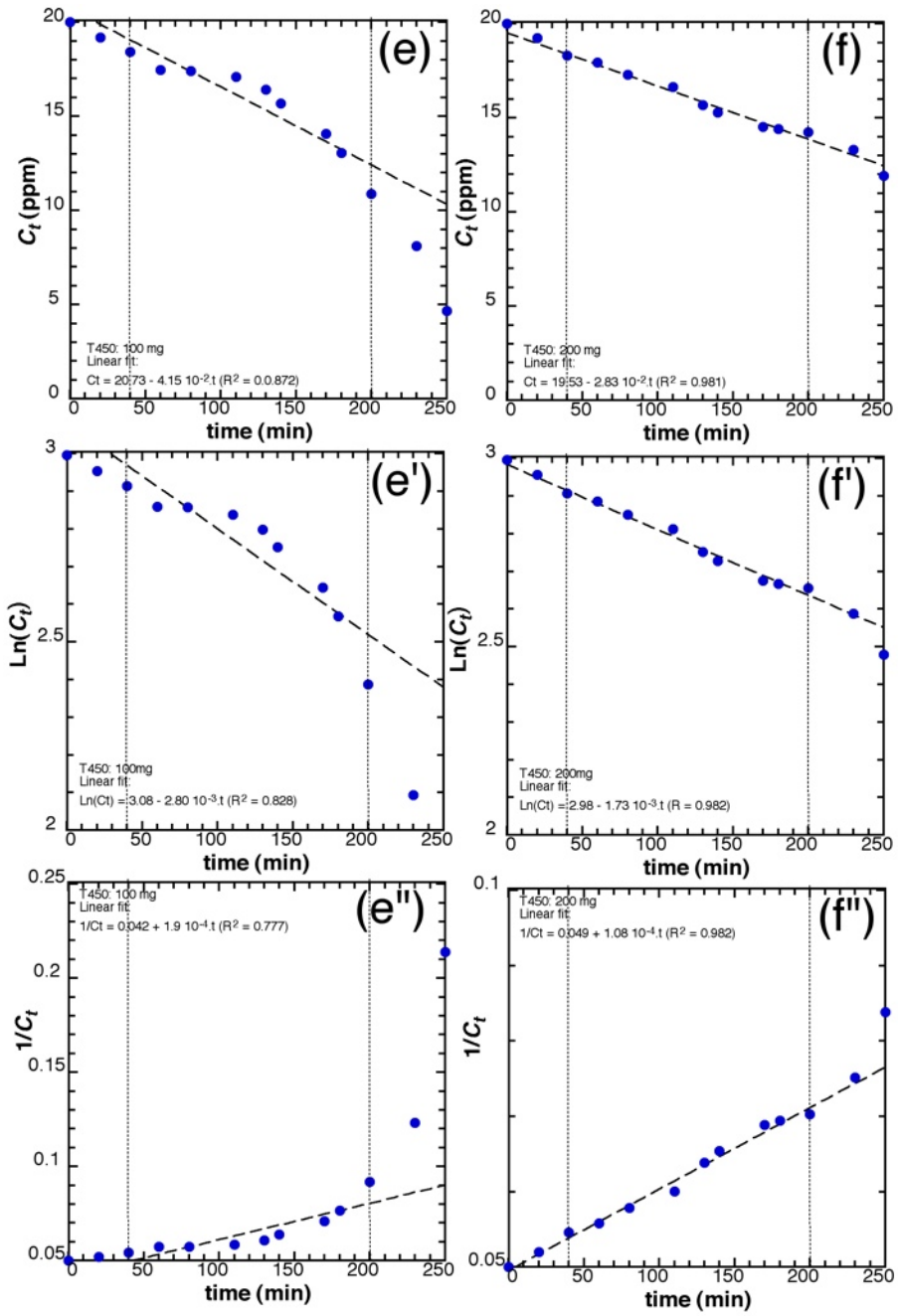

Figure B.4.C: Linear fitting of the evolution of MB (in ppm) for the different kinetics models (Ct=f(t) - zero order; Ln(Ct)=f(t) - first order; 1/Ct=f(t) - second order) for 5mg of (e; e'; e"") and 200 mg (f, f', f'') of T450.

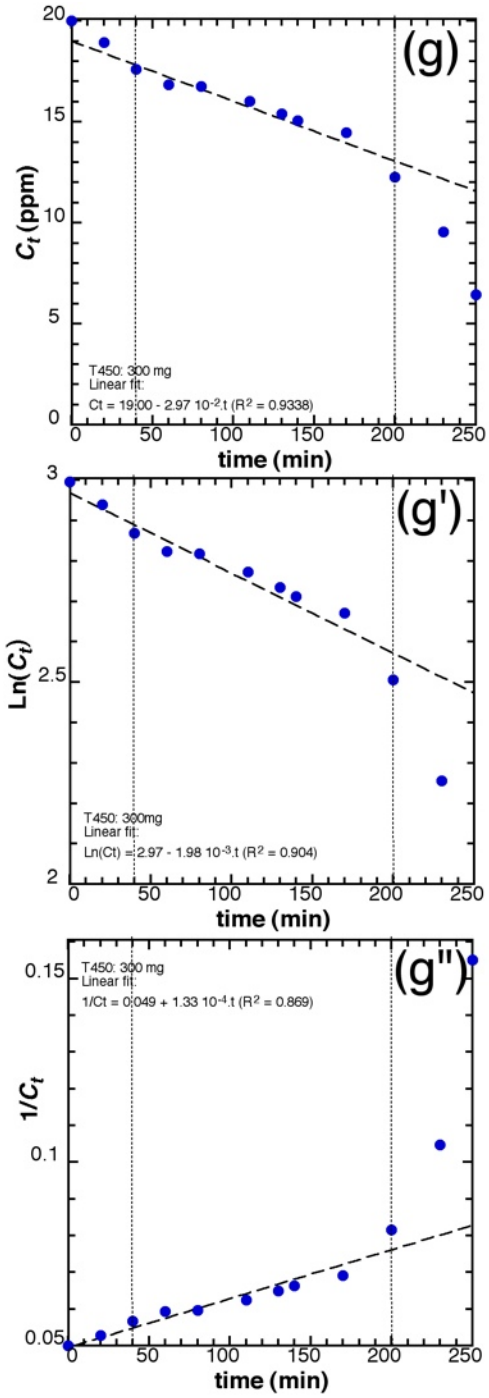

Figure B.4.D: Linear fitting of the evolution of MB (in ppm) for the different kinetics models (Ct=f(t) - zero order; Ln(Ct)=f(t) - first order; 1/Ct=f(t) - second order) for 300mg of (g; g'; g"") of T450.

Appendix C: Testing and Assembling of DSSCs

C.1. Measuring the Contact Angle

An interesting HCl treatment was done for the PET plastic substrate to solve the problem of its hydrophobicity. This work was done as a requirement for modifying the ITO/PET plastic substrate at the beginning of the thesis before moving the objective to focus on further investigation of the synthesized TiO_2 nanoparticles and applying the thermal treatment on glass substrate.

As can be seen from figure C.1 the time of exposure of ITO to the acid vapour affects drastically the shape of the water droplet poured onto the surface of the ITO layer. Figure C.2 illustrates an example of the measured contact angle. At the beginning (after 2 & 4 min) the surface of ITO shows hydrophobicity which decreased rapidly after 6 minutes. This evolution can be easily explained by the increasing protonation of the ITO layer. Surprisingly, the hydrophobicity increased after 30 minutes of acid exposure. Until further analyses, we ascribed this evolution to an increasing roughness of the film of tin oxide. This roughness, a result of acid attack, can contribute to a higher hydrophobicity, as illustrated by the structure of lotus leaves. This result indicates clearly that an optimum condition is important in order to have the desired hydrophilicity of the surface.

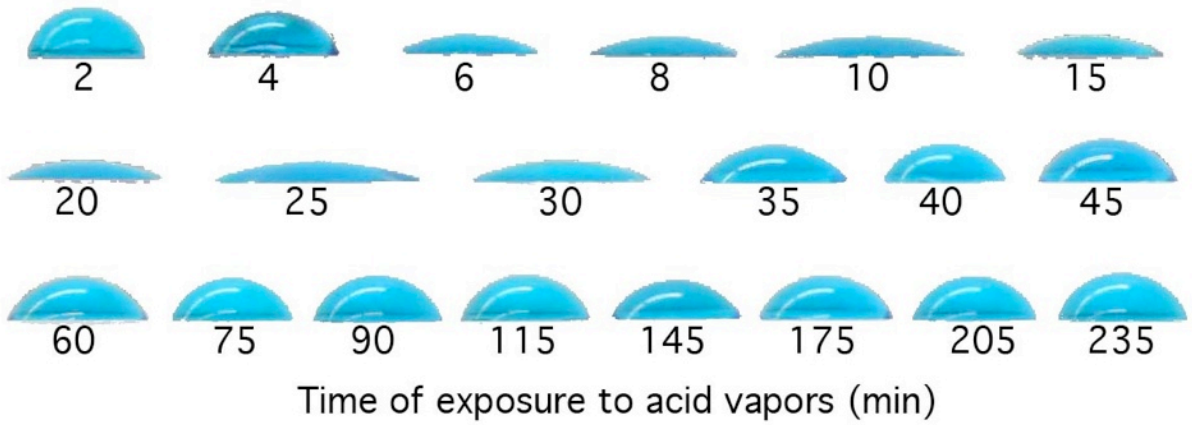

Figure C.1 the effect of the exposure time to acid vapour of ITO layer on a droplet of water

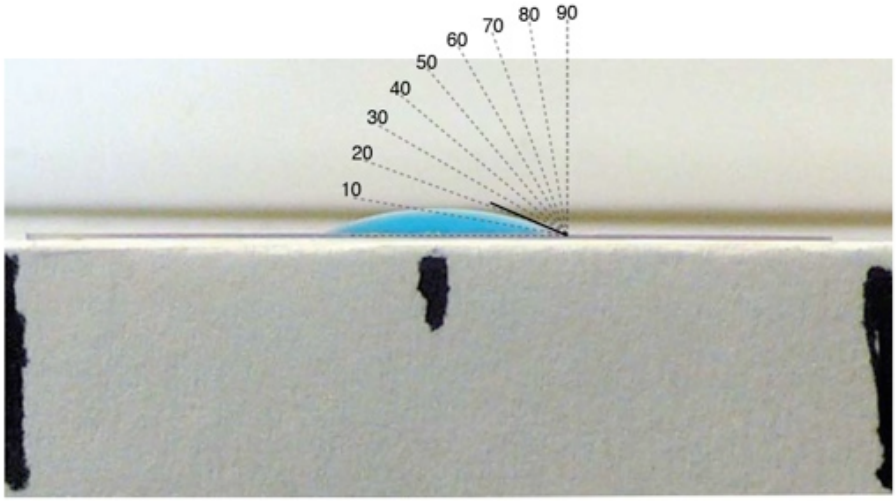

Figure C.2 Measuring of the Contact Angle

We report in Figure C.3, the evolution of the contact angle with the acid exposure time. The plot shows the optimum condition (10 min of exposure time to acid vapour) at which the contact angle shows minimum value, i.e., less surface tension.

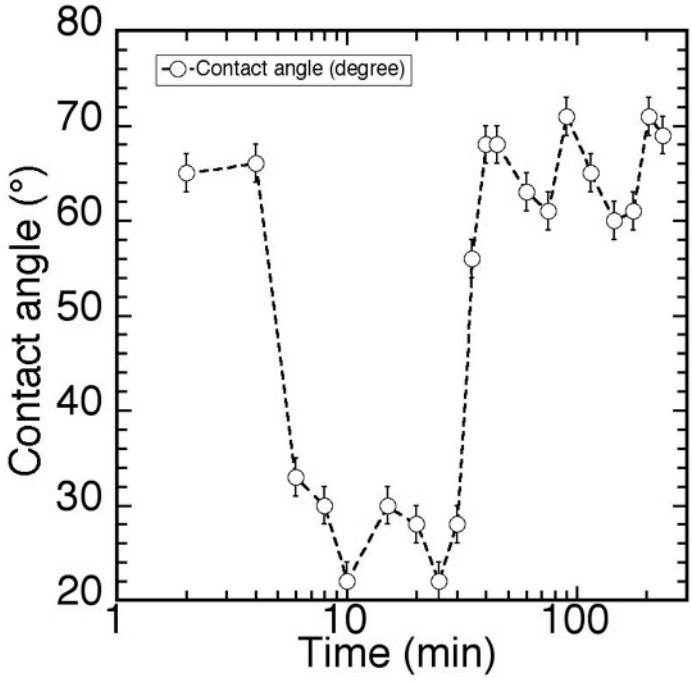

Figure C.3 The Effect of The Exposure Time of ITO To The Acid Vapour on The Contact Angle

C.2. FTIR analyses for different samples

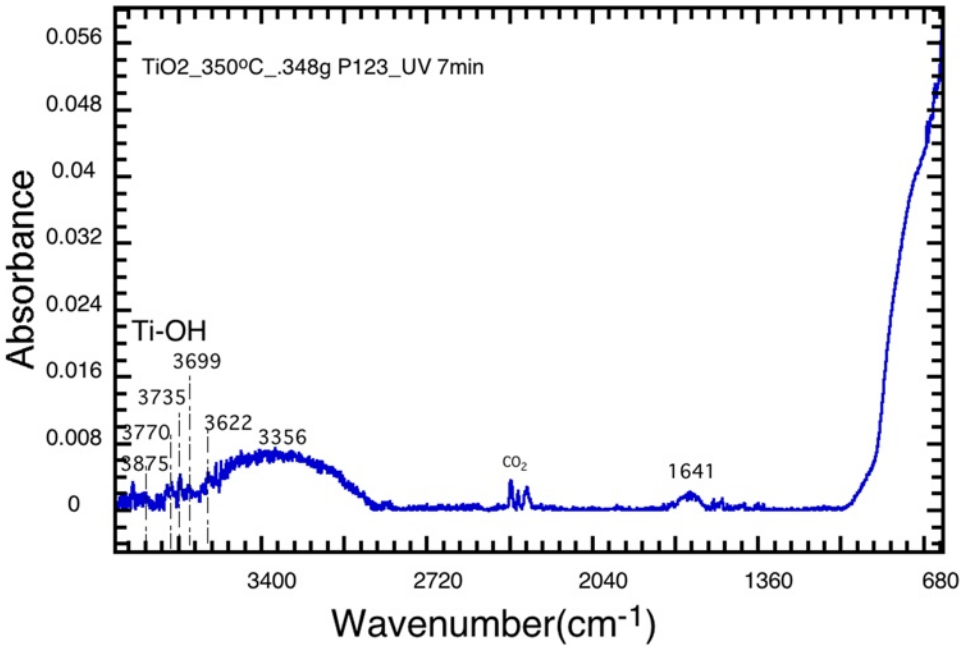

Figure C.4 FTIR spectrum for mesoporous TiO_2- dye stained film prepared with Pluronic P123, cured by UV for 7 min

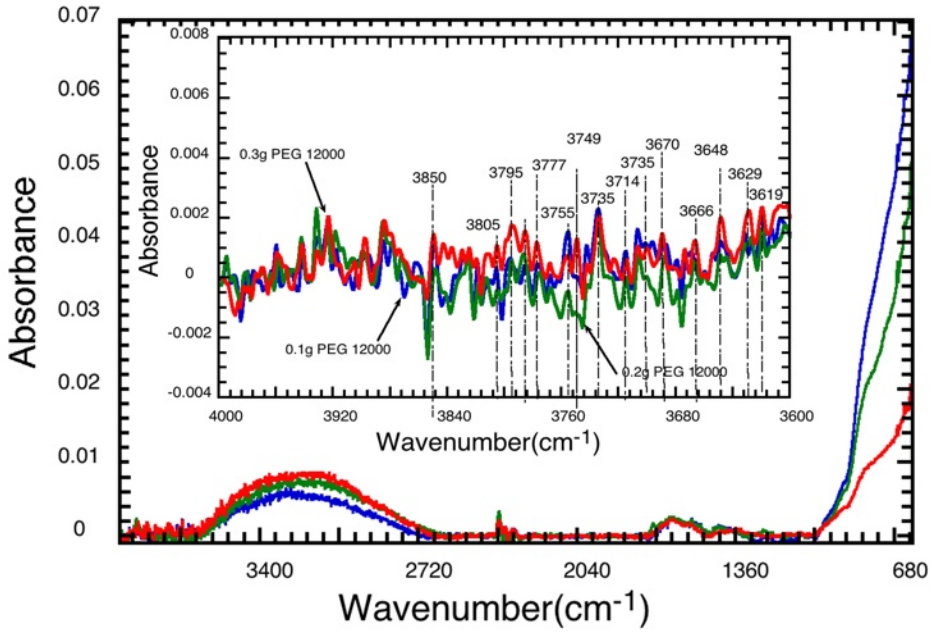

Figure C.5 FTIR spectrum for mesoporous TiO_2- dye stained film prepared with different weights of PEG 12000, cured by UV for 10 min (inset: magnification from 3500-3850cm-1)

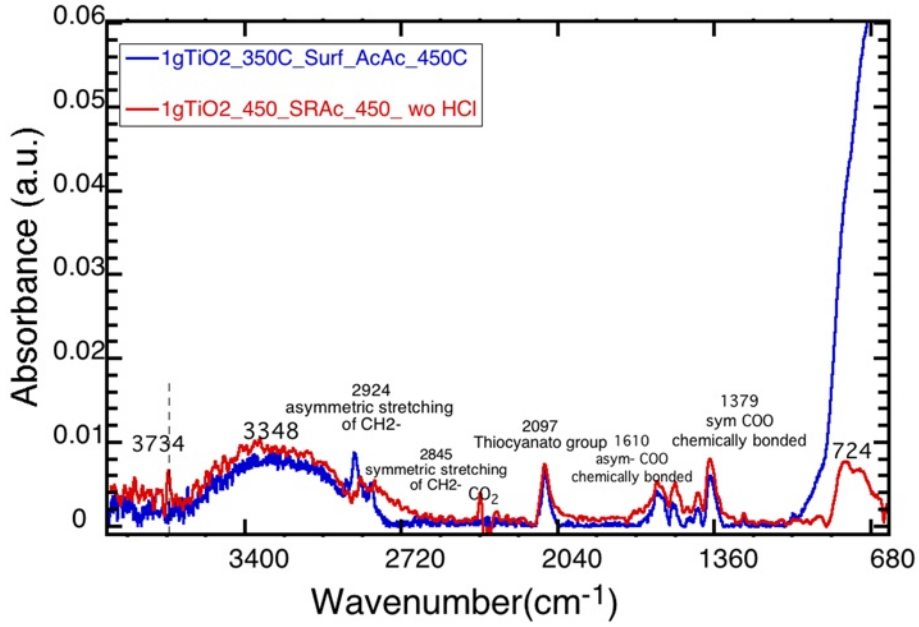

Figure C.6 FTIR spectrum for mesoporous TiO_2- dye stained film prepared with Surfactant Span 80/tween 80 mixed with acetic acid, treated at 450°C

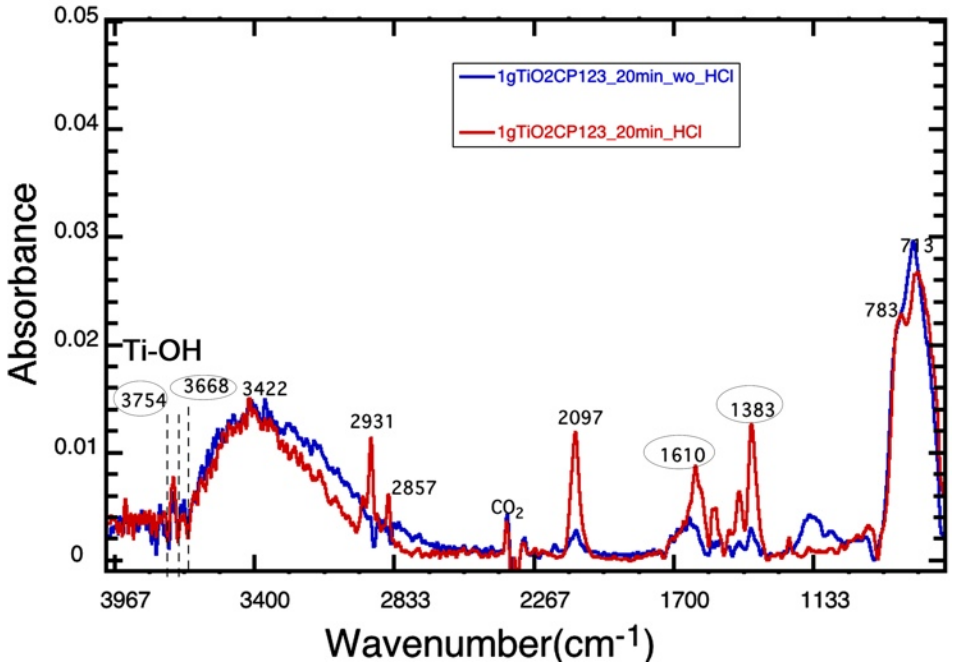

Figure C.7 FTIR spectra for HCl and non HCl treated commercial TiO_2 (Degussa)-dye stained film

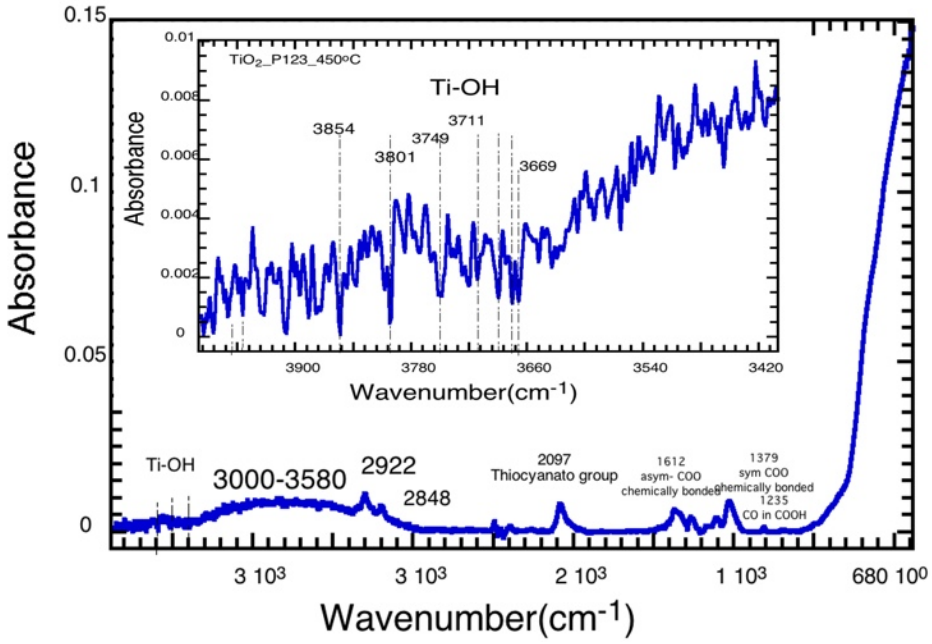

Figure C.8 FTIR spectrum for mesoporous TiO_2- dye stained film prepared with Pluronic P123, treated at 450°C

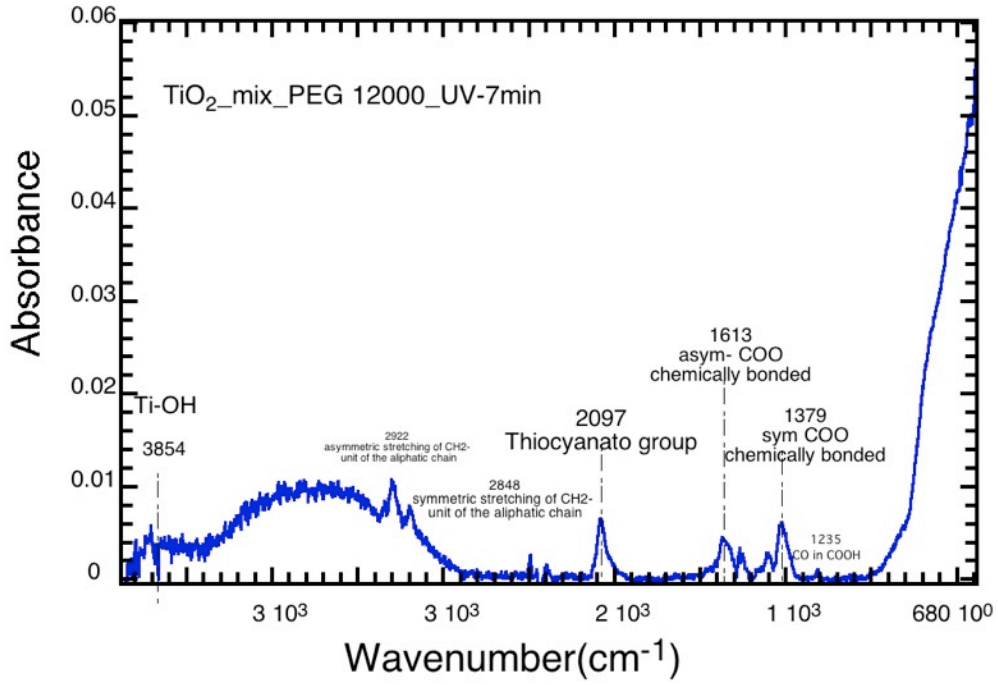

Figure C.9 FTIR spectrum for mesoporous TiO_2- dye stained film prepared by mixing the synthesized TiO_2 with TiO_2 Degussa and PEG 12000, cured by UV for 7 min.

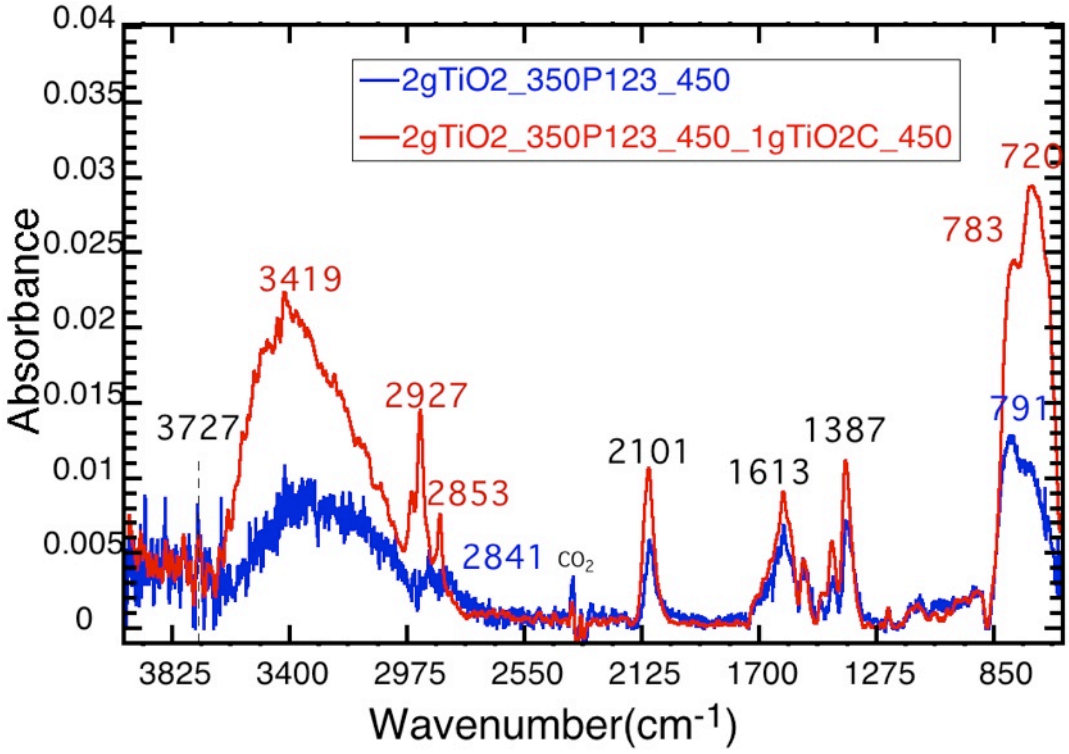

Figure C.10 FTIR spectrum of one layer of the synthesized TiO_2 mesoporous film- dye stained prepared by pluronic to two layers mesoporous TiO_2- dye stained film, the top layer prepared by mixing the synthesized TiO_2 with TiO_2 Degussa and PEG 12000, treated at 450oC for 30min

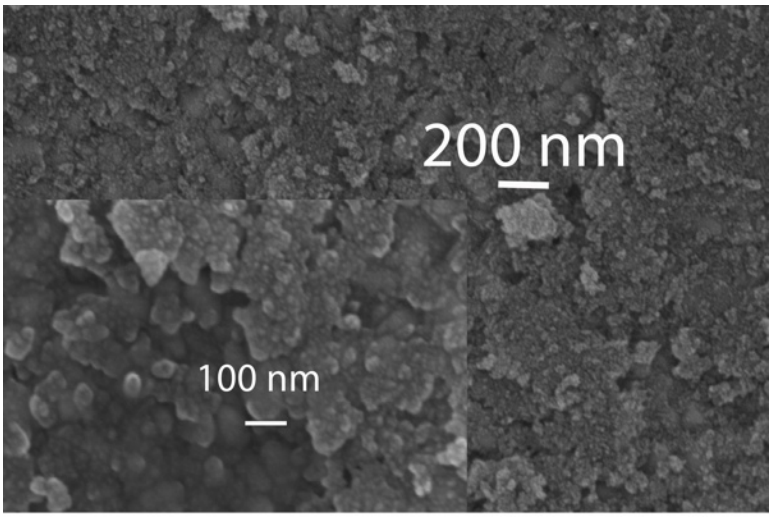

Figure C.11 SEM images of TiO_2 films prepared by the doctor blade method with PEG 12000 as additive after cured by UV for 10 min

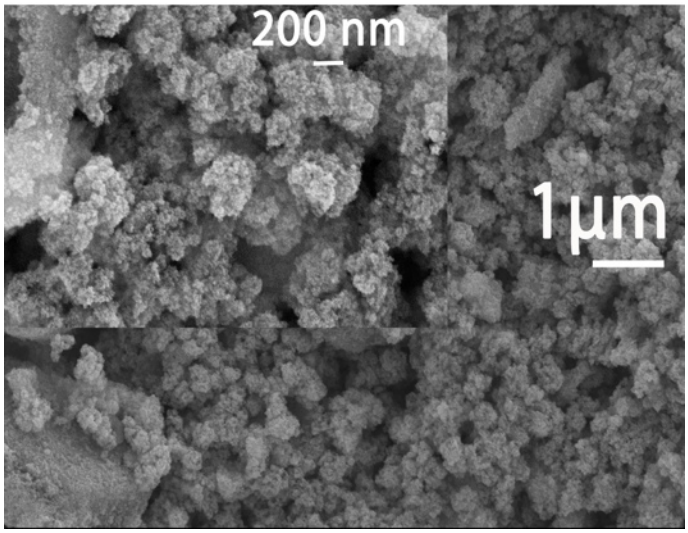

Figure C.12 SEM images of TiO_2 films prepared by the doctor blade method with PEG 8000 as additive after calcination at 450^{o}C for 30min

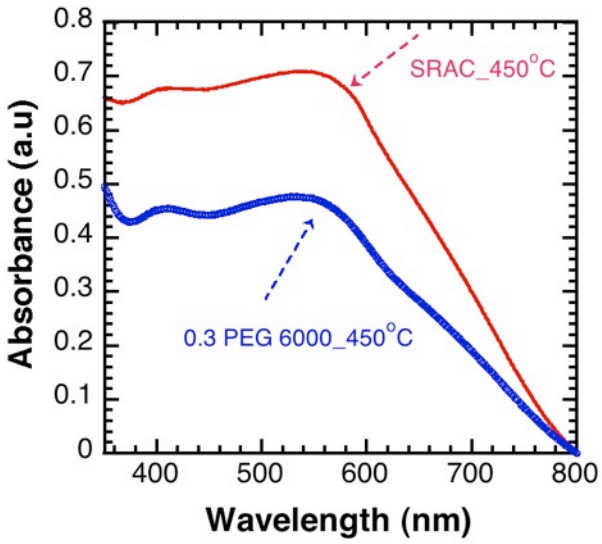

Figure C.13 Comparison between UV-Vis spectra for tow samples prepared with different organic additives

C.3. Stability of the dye sensitized solar cells

We managed to measure the cell efficiency after few months from preparation and the efficiency was decreased to its half value. It was speculated that low V_{OC} resulted from the drop in the R_{shunt} and this occurs when there is an alternate path for current to pass through the cell. The lost current is often referred to as the shunt leakage current. The low Jsc is due to the insufficient photocarrier collection and high series resistance.

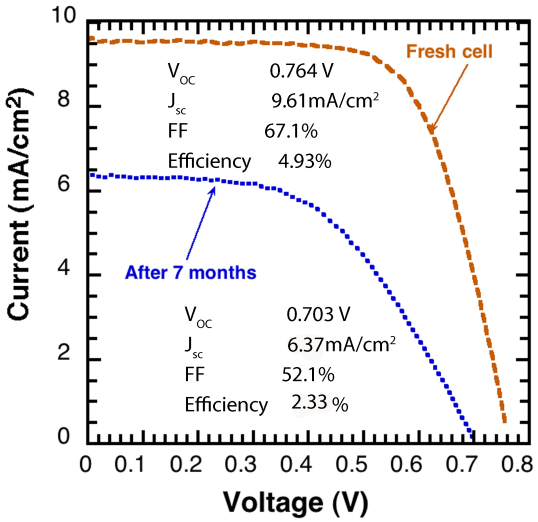

Figure C.14 J-V curves of dye-sensitized TiO_2 films prepared on FTO/glass calcined at 450°C freshly prepared sample and after 7 month of preparation at irradiance of 100 mW/cm² and 1.5 AM

C.4. Effect of adding a scattering layer on TiO_2 film on the cell performance

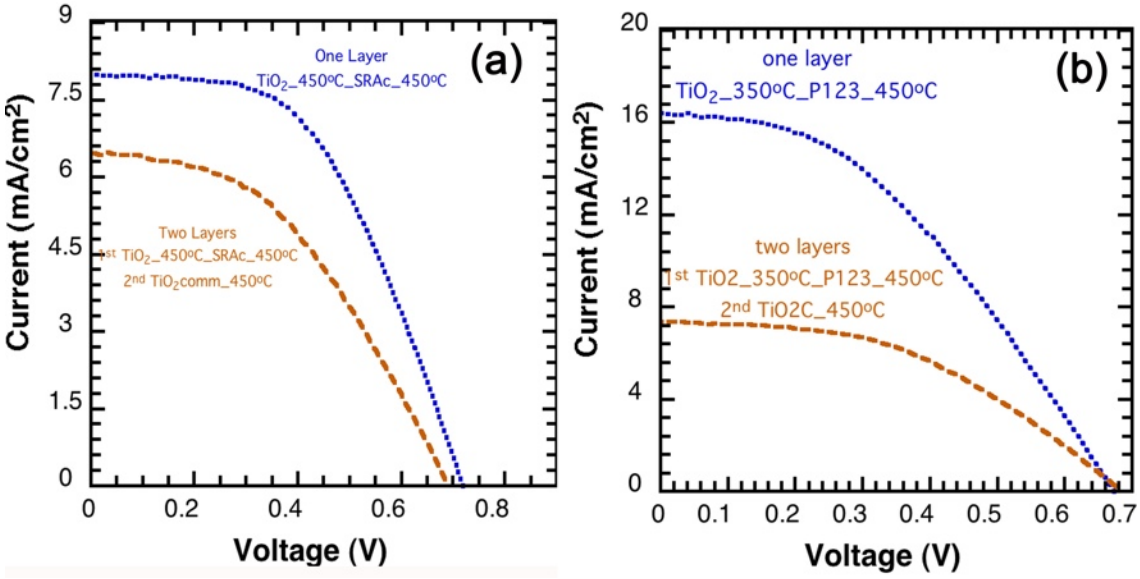

Figure C.15 J-V curves for TiO_2 films prepared on FTO/glass with first layer made of nanoparticles calcined initially at a) 450°C mixed with SRAc b) 350°C mixed with Pluronic

P123, then the thin film treated thermally at 450ºC for 30 min, and a top layer made of TiO_2 Degussa for both of them.

Table C.I Photovoltaic parameters of DSSCs prepared by different organic additives and two layers

Sample	V_{oc} (V)	I_{sc} (mA/cm^2)	FF	efficiency	Series resistance (Ω)	Shunt resistance (Ω)
A_one layer	0.719	7.99	51.3%	2.95%	6.7	226
A_two layers	0.691	6.47	43.6%	1.95%	10.05	270
B_one layer	0.67	16.4	40.3%	4.46%	4.49	136
B_two layers	0.68	8.1	44.8%	2.52%	8.43	176

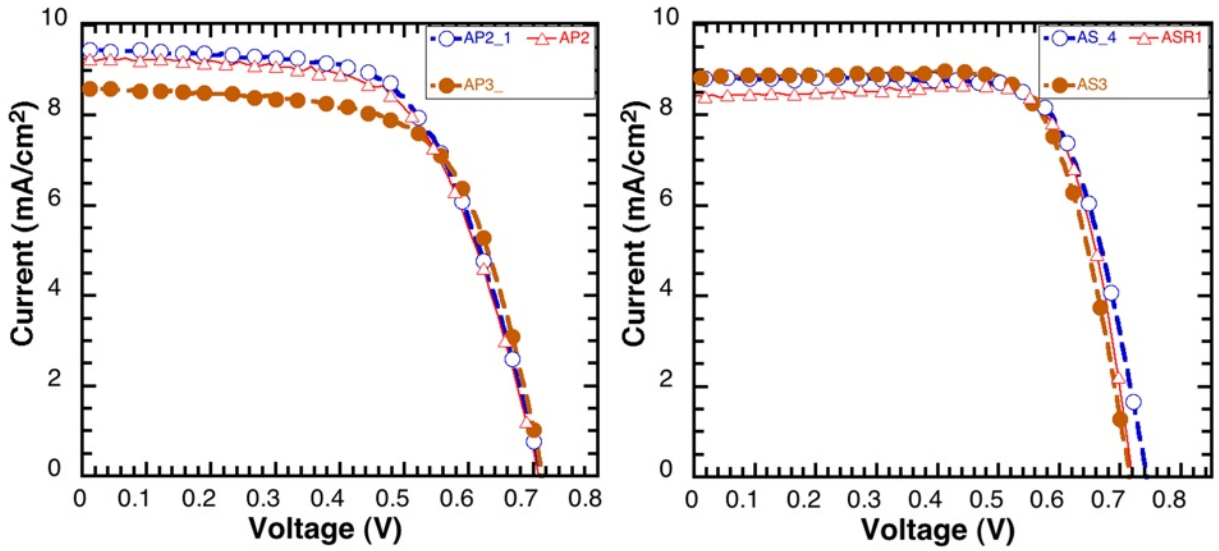

Figure C.16 J-V curves for similar TiO_2 films prepared with a) pluronic P123 b) surfactant and acetic acid, all films were fired at 450oC and then cured by UV for 15 min

Table C.II Photovoltaic parameters of DSSCs prepared by different organic additives

Sample	V_{oc} (V)	J_{sc} (mA/ cm^2)	FF (%)	Efficiency (%)	Series resistance (Ω)	Shunt resistance (Ω)
AP2_1	0.713	9.43	62.6	4.21	16.6	731
AP2	0.709	9.26	62.3	4.09	16.2	1392
AP3	0.715	8.59	64.8	3.98	29.4	1022
AS3	0.715	8.86	72.7	4.6	2.38	428
AS4	0.743	8.84	71.7	4.71	6.94	400
ASR1	0.72	8.41	77.1	4.67	2.21	324

C.5. Amount of adsorbed dye for aged cells

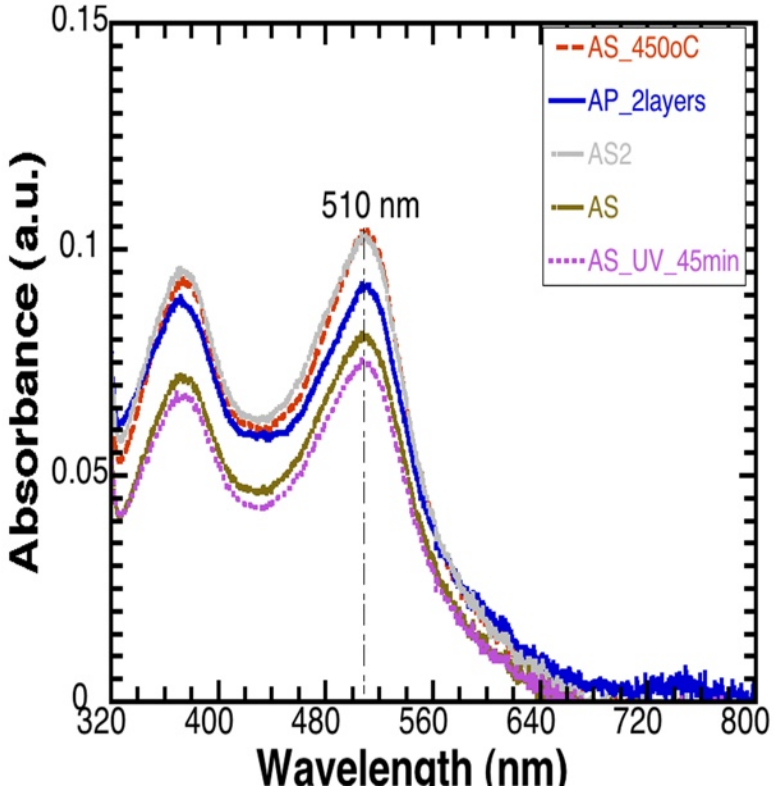

Figure C.17 UV-Vis absorption spectra of the Z907 dye desorbed from TiO_2 films prepared with different organic additives and treated differently

A refers to the synthesized TiO_2 nanoparticles prepared with (S)surfactant and acetic acid or (P) pluronic additive

R refers to reference electrodes prepared by TiO_2 Degussa with different additives S or P

Table C.III Amount of adsorbed dye for different thin films aged for two months

No.	Sample name	Film thickness µm)	Amount of dye (10^{-7} mol.cm^{-2})
1	AS_450	17	1.1528
2	AS_2g TiO_2	17	1.0790
3	AP_2layers	33	1.9756
4	AS_2g TiO_2_HCl	17	1.2377

No.	Sample name	Film thickness µm)	Amount of dye (10^{-7} mol.cm^{-2})
5	AS_UV 45min	17	0.99986
6	AS	17	1.3958

All samples treated thermally at 450oC except sample 5 cured by UV for 45min. Sample 1 was prepared by initially preheating the TiO_2 at 450°C instead of 350oC compared to other samples. Sample 4 was HCl treated compared to the untreated one (sample 2).

C.5. Quantum efficiency

The incident photon conversion efficiency was difficult to be measured as can be seen from the following curves as the response is too low. We believe that the reason behind this is the poor electrical contact. A layer of silver paste was added on the edges of both electrodes but it did not show any improvement. We tried to bond an electrical wire to the edges but the possibility to do this stuff on glass was difficult.

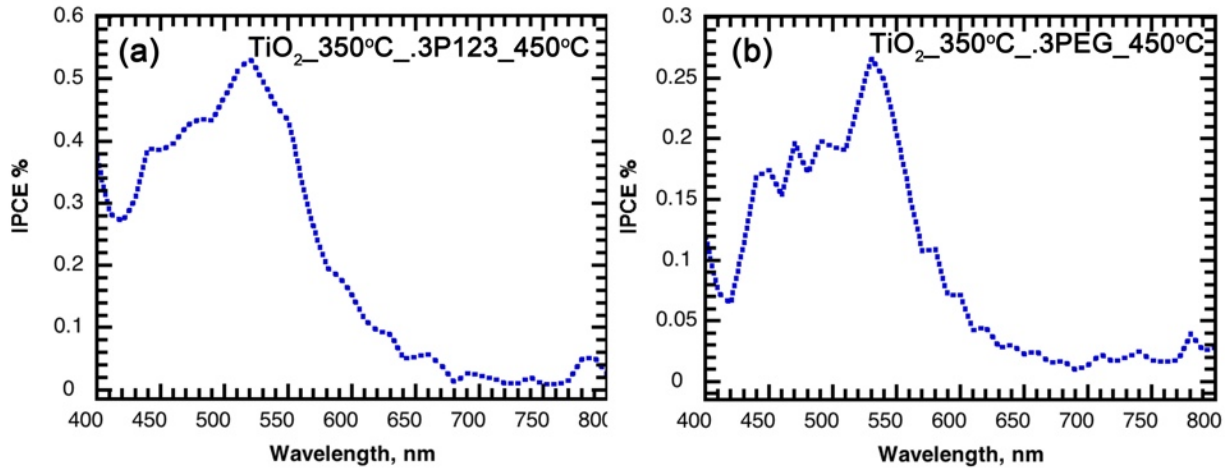

Figure 5.22 incident photon to current efficiency (IPCE) of the DSSCs fabricated with different organic additives (a) Pluronic (P123) (b) PEG 12000 prepared by preheating the nanoparticles at 350°C and the film then treated at 450°C

C.6. Impedance Spectroscopy: equivalent circuit models

TiO2_350°C_P123_450°C_1cm2_light

Element	Freedom	Value	Error	Error %
R_s	Fixed(X)	3.1082E-05	N/A	N/A
R_1	Free(+)	26.32	0.039306	0.14934
Ws1-R	Fixed(X)	12.59	N/A	N/A
Ws1-T	Fixed(X)	0.008988	N/A	N/A
Ws1-P	Fixed(X)	0.5	N/A	N/A
CPE1-T	Fixed(X)	5.278E-05	N/A	N/A
CPE1-P	Fixed(X)	0.32782	N/A	N/A
R_2	Fixed(X)	66.6	N/A	N/A
CPE2-T	Fixed(X)	0.00027203	N/A	N/A
CPE2-P	Fixed(X)	0.97568	N/A	N/A

Chi-Squared:	0.00074276
Weighted Sum of Squares:	0.089873

TiO_2_350°C_P123_450°C_1cm^2_dark

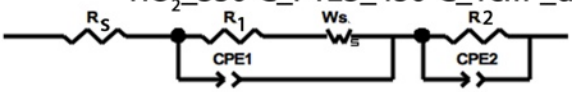

Element	Freedom	Value	Error	Error %
R S	Fixed(X)	0.00051893	N/A	N/A
R 1	Fixed(X)	1625	N/A	N/A
Ws 1-R	Free(+)	150.9	6.5231	4.3228
Ws 1-T	Fixed(X)	9.246	N/A	N/A
Ws 1-P	Fixed(X)	0.5	N/A	N/A
CPE1-T	Fixed(X)	9.656E-05	N/A	N/A
CPE1-P	Fixed(X)	0.95586	N/A	N/A
R 2	Fixed(X)	30.84	N/A	N/A
CPE2-T	Fixed(X)	0.0022911	N/A	N/A
CPE2-P	Fixed(X)	0.12064	N/A	N/A

Chi-Squared:	0.00065211
Weighted Sum of Squares:	0.091947

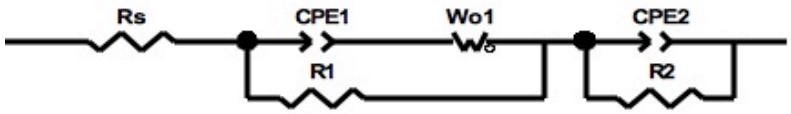

Element	Freedom	Value	Error	Error %
Rs	Fixed(X)	27.23	N/A	N/A
CPE1-T	Fixed(X)	0.00015418	N/A	N/A
CPE1-P	Fixed(X)	0.80007	N/A	N/A
Wo1-R	Fixed(X)	1.38	N/A	N/A
Wo1-T	Fixed(X)	0.00046032	N/A	N/A
Wo1-P	Fixed(X)	0.5	N/A	N/A
R1	Fixed(X)	1139	N/A	N/A
CPE2-T	Fixed(X)	0.0044835	N/A	N/A
CPE2-P	Fixed(X)	0.85676	N/A	N/A
R2	Free(+)	230.6	9.1095	3.9503

Chi-Squared:	0.00088458
Weighted Sum of Squares:	0.11411
Data File:	C:\Users\Aiat\Desktop\August 2 2012\July 1 2012\1gTiO2_350_SRACUV8min_dark.z
Circuit Model File:	C:\SAI\ZModels\Tutor3 Dummy Cell.mdl
Mode:	Run Fitting / Freq. Range (0.01 - 100000)
Maximum Iterations:	100
Optimization Iterations:	0
Type of Fitting:	Complex
Type of Weighting:	Calc-Modulus

Element	Freedom	Value	Error	Error %
R2	Free(+)	223.5	3.0867	1.3811
R1	Free(+)	166.6	9.9974	6.0008
Wo1-R	Free(+)	0.0045478	28.069	6.172E05
Wo1-T	Free(+)	0.037905	233.95	6.172E05
Wo1-P	Fixed(X)	0.5	N/A	N/A
CPE2-T	Free(+)	0.00010902	9.3391E-06	8.5664
CPE2-P	Free(+)	0.76558	0.011708	1.5293
R3	Free(+)	36.27	2.7331	7.5354
CPE1-T	Free(+)	0.099696	0.076518	76.751
CPE1-P	Free(+)	4.433	0.41453	9.351
Ws2-R	Free(+)	103.7	26.314	25.375
Ws2-T	Free(+)	2.3208E-05	3.3318E-06	14.356
Ws2-P	Fixed(X)	0.5	N/A	N/A

Chi-Squared:	0.0012556
Weighted Sum of Squares:	0.16449
Data File:	C:\Users\Aiat\Desktop\July 1 2012 - Copy \2gTiO2_350_.348P123_450_HC_darkl.z
Circuit Model File:	C:\Users\Aiat\Desktop\July 1 2012\2g TiO 2_350_.348P123_450_HCl_light.mdl
Mode:	Run Fitting / Freq. Range (0.001 - 1000000)
Maximum Iterations:	100
Optimization Iterations:	0
Type of Fitting:	Complex
Type of Weighting:	Calc-Modulus

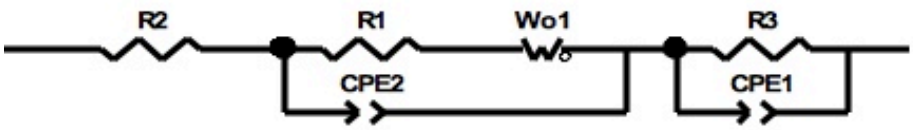

Element	Freedom	Value	Error	Error %
R2	Fixed(X)	9.5943E-07	N/A	N/A
R1	Fixed(X)	119.6	N/A	N/A
Wo1-R	Fixed(X)	84.08	N/A	N/A
Wo1-T	Fixed(X)	0.00069098	N/A	N/A
Wo1-P	Fixed(X)	0.5	N/A	N/A
CPE2-T	Fixed(X)	0.00028129	N/A	N/A
CPE2-P	Fixed(X)	0.028115	N/A	N/A
R3	Free(±)	1841	12.954	0.70364
CPE1-T	Fixed(X)	3.27E-05	N/A	N/A
CPE1-P	Fixed(X)	0.75721	N/A	N/A

Chi-Squared:	0.00059878
Weighted Sum of Squares:	0.077242
Data File:	C:\Users\Aiat\Desktop\July 1 2012 - Copy \2gTiO2_350_.348P123_450_HCl_light3.75.z
Circuit Model File:	C:\Users\Aiat\Desktop\July 1 2012\2g TiO 2_350_.348PEG12k_450_HCl_1.5_dark.mdl
Mode:	Run Fitting / Freq. Range (0.001 - 1000000)
Maximum Iterations:	100
Optimization Iterations:	0
Type of Fitting:	Complex
Type of Weighting:	Calc-Modulus

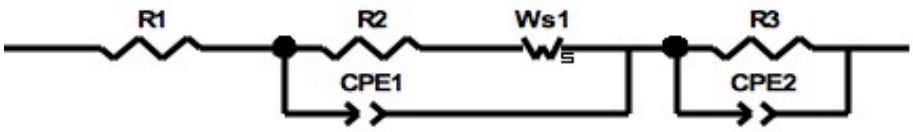

Element	Freedom	Value	Error	Error %
R1	Fixed(X)	3.1082E-05	N/A	N/A
R2	Free(+)	26.32	0.039306	0.14934
Ws1-R	Fixed(X)	12.59	N/A	N/A
Ws1-T	Fixed(X)	0.008988	N/A	N/A
Ws1-P	Fixed(X)	0.5	N/A	N/A
CPE1-T	Fixed(X)	5.278E-05	N/A	N/A
CPE1-P	Fixed(X)	0.32782	N/A	N/A
R3	Fixed(X)	66.6	N/A	N/A
CPE2-T	Fixed(X)	0.00027203	N/A	N/A
CPE2-P	Fixed(X)	0.97568	N/A	N/A

Chi-Squared:	0.00074276
Weighted Sum of Squares:	0.089873
Data File:	C:\Users\Aiat\Documents\Oct 15 2012\AP_old_1cm2_light.z
Circuit Model File:	
Mode:	Run Fitting / Freq. Range (0.001 - 1000000)
Maximum Iterations:	100
Optimization Iterations:	0
Type of Fitting:	Complex
Type of Weighting:	Calc-Modulus

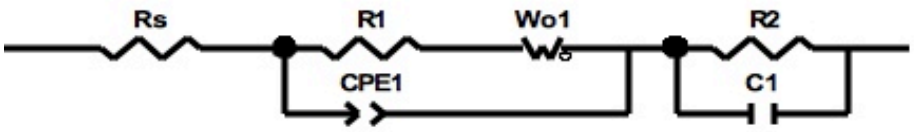

Element	Freedom	Value	Error	Error %
Rs	Fixed(X)	28.88	N/A	N/A
R1	Free(+)	114.3	5.5273	4.8358
Wo1-R	Fixed(X)	0.09143	N/A	N/A
Wo1-T	Fixed(X)	0.021441	N/A	N/A
Wo1-P	Fixed(X)	0.5	N/A	N/A
CPE1-T	Fixed(X)	0.0024559	N/A	N/A
CPE1-P	Fixed(X)	0.66461	N/A	N/A
R2	Fixed(X)	848.8	N/A	N/A
C1	Fixed(X)	0.00010498	N/A	N/A

Chi-Squared:	0.0016775
Weighted Sum of Squares:	0.20298
Data File:	C:\Users\Aiat\Desktop\Oct 15 2012\AP_1.5 cm2_old_dark.z
Circuit Model File:	C:\Users\Aiat\Desktop\Oct 15 2012\AP_1.5 cm2_dark.mdl
Mode:	Run Fitting / Freq. Range (0.001 - 1000000)
Maximum Iterations:	100
Optimization Iterations:	0
Type of Fitting:	Complex
Type of Weighting:	Calc-Modulus

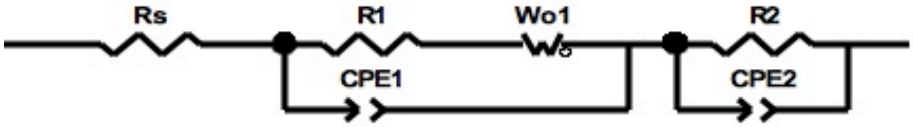

Element	Freedom	Value	Error	Error %
Rs	Fixed(X)	13.78	N/A	N/A
R1	Fixed(X)	20.05	N/A	N/A
Wo1-R	Fixed(X)	0.48539	N/A	N/A
Wo1-T	Free(+)	0.48144	0.33273	69.111
Wo1-P	Fixed(X)	0.5	N/A	N/A
CPE1-T	Fixed(X)	0.00068115	N/A	N/A
CPE1-P	Fixed(X)	0.20824	N/A	N/A
R2	Fixed(X)	181.9	N/A	N/A
CPE2-T	Fixed(X)	0.0001866	N/A	N/A
CPE2-P	Fixed(X)	0.96036	N/A	N/A

Chi-Squared:	0.00069967
Weighted Sum of Squares:	0.08466
Data File:	C:\Users\Aiat\Desktop\Oct 15 2012\AP_1.5 cm2_old_light.z
Circuit Model File:	C:\Users\Aiat\Desktop\Oct 15 2012\AP_1.5 cm2_dark.mdl
Mode:	Run Fitting / Freq. Range (0.001 - 1000000)
Maximum Iterations:	100
Optimization Iterations:	0
Type of Fitting:	Complex
Type of Weighting:	Calc-Modulus

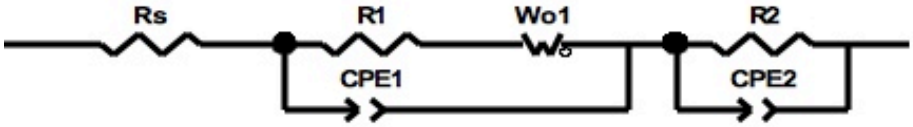

Element	Freedom	Value	Error	Error %
Rs	Fixed(X)	23.49	N/A	N/A
R1	Fixed(X)	1.9452E-06	N/A	N/A
Wo1-R	Fixed(X)	0.022068	N/A	N/A
Wo1-T	Fixed(X)	1.9305E-06	N/A	N/A
Wo1-P	Fixed(X)	0.5	N/A	N/A
CPE1-T	Fixed(X)	0.00064619	N/A	N/A
CPE1-P	Fixed(X)	0.021525	N/A	N/A
R2	Free(+)	185.1	19.992	10.801
CPE2-T	Fixed(X)	0.0072893	N/A	N/A
CPE2-P	Fixed(X)	0.4546	N/A	N/A

Chi-Squared:	0.0024016
Weighted Sum of Squares:	0.33862
Data File:	C:\Users\Aiat\Desktop\Oct 15 2012\AP_old_1cm2_dark.z
Circuit Model File:	C:\Users\Aiat\Desktop\Oct 15 2012\AP_old_1cm2_dark.mdl
Mode:	Run Fitting / Freq. Range (0.001 - 1000000)
Maximum Iterations:	100
Optimization Iterations:	0
Type of Fitting:	Complex
Type of Weighting:	Calc-Modulus

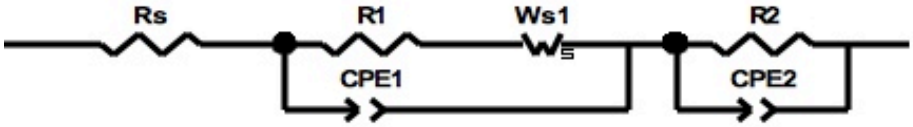

Element	Freedom	Value	Error	Error %
Rs	Fixed(X)	17.3	N/A	N/A
R1	Fixed(X)	42.44	N/A	N/A
Ws1-R	Free(+)	33.65	0.20357	0.60496
Ws1-T	Fixed(X)	0.019566	N/A	N/A
Ws1-P	Fixed(X)	0.5	N/A	N/A
CPE1-T	Fixed(X)	0.00017888	N/A	N/A
CPE1-P	Fixed(X)	0.96005	N/A	N/A
R2	Fixed(X)	12.96	N/A	N/A
CPE2-T	Fixed(X)	0.0045936	N/A	N/A
CPE2-P	Fixed(X)	0.20671	N/A	N/A

Chi-Squared:	0.00080464
Weighted Sum of Squares:	0.097361
Data File:	C:\Users\Aiat\Desktop\Oct 15 2012\AP_old_1cm2_light.z
Circuit Model File:	C:\Users\Aiat\Desktop\Oct 15 2012\AP_old_1cm2_dark.mdl
Mode:	Run Fitting / Freq. Range (0.001 - 1000000)
Maximum Iterations:	100
Optimization Iterations:	0
Type of Fitting:	Complex
Type of Weighting:	Calc-Modulus

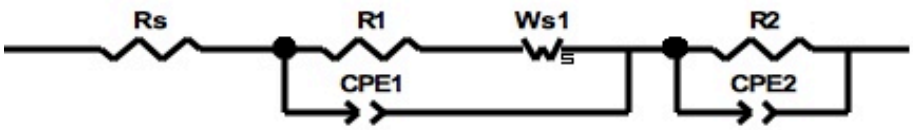

Element	Freedom	Value	Error	Error %
Rs	Fixed(X)	0.00016395	N/A	N/A
R1	Fixed(X)	39.31	N/A	N/A
Ws1-R	Fixed(X)	14.48	N/A	N/A
Ws1-T	Fixed(X)	0.2094	N/A	N/A
Ws1-P	Fixed(X)	0.5	N/A	N/A
CPE1-T	Fixed(X)	6.4322E-05	N/A	N/A
CPE1-P	Fixed(X)	0.28534	N/A	N/A
R2	Free(+)	3023	4.6891	0.15511
CPE2-T	Fixed(X)	9.093E-05	N/A	N/A
CPE2-P	Fixed(X)	0.9688	N/A	N/A

Chi-Squared:	0.00024312
Weighted Sum of Squares:	0.032821
Data File:	C:\Users\Aiat\Desktop\Oct 15 2012\AS1_5cm2_old_dark.z
Circuit Model File:	C:\Users\Aiat\Desktop\Oct 15 2012\AS1_5cm2_old_dark.mdl
Mode:	Run Fitting / Freq. Range (0.001 - 1000000)
Maximum Iterations:	100
Optimization Iterations:	0
Type of Fitting:	Complex
Type of Weighting:	Calc-Modulus

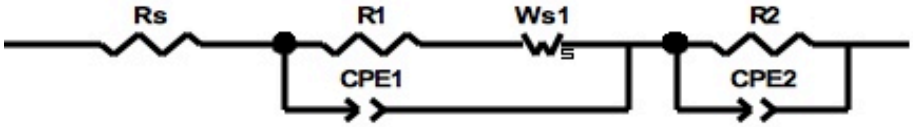

Element	Freedom	Value	Error	Error %
Rs	Fixed(X)	0.00047677	N/A	N/A
R1	Fixed(X)	2.78	N/A	N/A
Ws1-R	Fixed(X)	82.65	N/A	N/A
Ws1-T	Fixed(X)	0.0055211	N/A	N/A
Ws1-P	Fixed(X)	0.5	N/A	N/A
CPE1-T	Fixed(X)	5.8017E-05	N/A	N/A
CPE1-P	Fixed(X)	0.90876	N/A	N/A
R2	Free(+)	39.48	0.025676	0.065035
CPE2-T	Fixed(X)	2.7348E-06	N/A	N/A
CPE2-P	Fixed(X)	0.49899	N/A	N/A

Chi-Squared:	0.00019323
Weighted Sum of Squares:	0.02338
Data File:	C:\Users\Aiat\Desktop\Oct 15 2012\RP4 _1 .2cm2_light.z
Circuit Model File:	C:\Users\Aiat\Desktop\Oct 15 2012\RS2_4. 7cm2_old_dark.mdl
Mode:	Run Fitting / Freq. Range (0.001 - 1000000)
Maximum Iterations:	100
Optimization Iterations:	0
Type of Fitting:	Complex
Type of Weighting:	Calc-Modulus

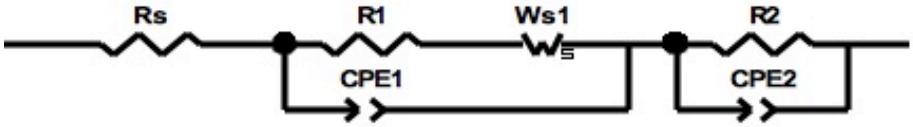

Element	Freedom	Value	Error	Error %
Rs	Fixed(X)	42.23	N/A	N/A
R1	Fixed(X)	7.9319E-07	N/A	N/A
Ws1-R	Fixed(X)	60.9	N/A	N/A
Ws1-T	Fixed(X)	0.0074853	N/A	N/A
Ws1-P	Fixed(X)	0.5	N/A	N/A
CPE1-T	Fixed(X)	4.1977E-05	N/A	N/A
CPE1-P	Fixed(X)	0.92075	N/A	N/A
R2	Free(+)	10.5	0.083876	0.79882
CPE2-T	Fixed(X)	0.021134	N/A	N/A
CPE2-P	Fixed(X)	0.16438	N/A	N/A

Chi-Squared:	0.00025472
Weighted Sum of Squares:	0.032349
Data File:	C:\Users\Aiat\Desktop\Oct 15 2012\RS2_4.7cm2_old_dark.z
Circuit Model File:	C:\Users\Aiat\Desktop\Oct 15 2012\RS2_4.7cm2_old_dark.mdl
Mode:	Run Fitting / Freq. Range (0.001 - 1000000)
Maximum Iterations:	100
Optimization Iterations:	0
Type of Fitting:	Complex
Type of Weighting:	Calc-Modulus